Deeply virtual Compton scattering at Jefferson Lab

Frédéric Georges

NNT : 2018SACLS391

Thèse de doctorat

Deeply Virtual Compton Scattering at Jefferson Lab

Thèse de doctorat de l'Université Paris-Saclay
préparée à l'Université Paris-Sud

Ecole doctorale n°576 Particules hadrons energie et noyau : instrumentation, image, cosmos et simulation (PHENIICS)
Spécialité de doctorat : Physique hadronique

Thèse présentée et soutenue à Orsay, le 25/10/2018, par

Frédéric Georges

Composition du Jury :

Franck Sabatié Docteur, CEA/Irfu/DPhN-Saclay	Président du Jury
Krešimir Kumerički Professeur, University of Zagreb	Rapporteur
Gunar Schnell Professeur, University of the Basque Country	Rapporteur
Simona Malace Docteur, Jefferson Laboratory	Examinateur
Béatrice Ramstein Docteur, Institut de Physique Nucléaire d'Orsay	Examinateur
Carlos Muñoz Camacho Docteur, Institut de Physique Nucléaire d'Orsay	Directeur de thèse

Acknowledgment

I performed my thesis in the Physique des Hautes ENergies (PHEN) group at the Institut de Physique Nucléaire d'Orsay, and first of all, I would like to address my most heartfelt appreciation to Franck Sabatié, Michel Guidal, and my supervisor Carlos Muñoz Camacho who spared no time nor effort to make this thesis possible.

I would like to express my deepest gratitude to my thesis supervisor, Carlos Muñoz Camacho, for his trust, support and guidance. He was always available to offer advices or answer my questions whenever I needed his help. His support and encouragements during the difficult and stressful last year of my PhD have been truly invaluable, and his careful reading of my thesis and his suggestions have greatly improved the quality of this document. His dedication was truly inspiring, and I am extremely glad to have been able to work under his supervision.

My gratitude also goes to my IPN colleagues for their warm welcome and the exciting three years spent among them. I would like to extend special thanks to Raphael Dupré, Eric Voutier, Dominique Marchand, Michel Guidal, Silvia Niccolai, Mostafa Hoballah and Gabriel Charles for their very appreciated help and the many interesting discussions that we have shared, be it about physics or not. I also would like to thank all my PhD and post-doc colleagues for the wonderful time spent with them.

Next, I would like to thank the DVCS collaboration. Over the course of my thesis, I have spent six months working at Jefferson Lab. During my stay there, or through video-conferences, I have learned a lot from Julie Roche, Charles Hyde-Wright, Paul King and Alexandre Camsonne, and I am extremely grateful for their advices and remarks that helped me tremendously to progress in my work. I extend further thanks to Malek Mazouz and Meriem Benali: our discussions about the calorimeter π^0 calibration and the π^0 contamination subtraction have been extremely helpful. I thank William Henry for his valuable assistance with the Geant4 simulation geometry. I have also enjoyed a lot working with my PhD colleagues Mongi Dlamini, Bishnu Karki, Alexa Johnson and Hashir Rashad, and I believe our many debates and discussions have been very beneficial to all of us. In addition, I would like to extend special thanks to Mongi and Bishnu for the fun we had together working late into the night in the Hall A counting house, or simply chatting at the resfac between two owl shifts.

I am much obliged to Maxime Defurne. His work on the previous Hall A DVCS experiment greatly inspired mine, and he dedicated a lot of his personal time to discuss and explain it to me so that I could improve my own work. Furthermore, by introducing me to the DVCS collaboration in 2013, he opened the door that led me, five years latter, to the redaction of this manuscript. I owe him greatly.

Further gratitude goes to the GMP collaboration. Yang Wang, Barak Schmookler, Vince Sulkosky and Eric Christy have provided invaluable help for the spectrometer optics calibration. Thir Gautam's assistance for the BPM calibration and Barak Schmookler's instructions for the raster calibration have also been greatly appreciated.

Special thanks go to Mark Jones for dedicating so much time to help us figure out corrections for the spectrometer optics.

I also acknowledge the amazing work of the Jefferson Lab staff and the Hall A collaboration who participated in the installation and the data taking of the experiment.

I would like to thank all the members of the examination committee for their time and their interest in my work. Special thanks go to Krešimir Kumerički and Gunar Schnell for their careful reading of the manuscript.

Finally, I thank my family whose unyielding support has carried me up to this day, and my friends who reminded me the importance of taking some time off.

Contents

Introduction

More than two millennia since the conceptualization of atoms by ancient Greek philosophers, and about a century since the discovery of the proton, one would think that mankind has already unraveled everything there is to know about the particles that ordinary matter is made of: the electrons, protons and neutrons. However, no statement has ever been further from the truth.

The electron is an elementary particle whose interactions are successfully described by Quantum Electrodynamics (QED). On the other hand, the proton and the neutron, more generally called nucleons and which are the building blocks of the atomic nuclei, are composite particles. The nucleons are made of elementary particles called quarks and gluons whose interactions are described by Quantum Chromodynamics (QCD).

The strong coupling constant that rules QCD has a value which depends on the energy scale of the interaction. At high energy, which is equivalent to short interaction distances, the strong coupling constant becomes very small, and the strength of the interactions binding gluons and quarks becomes weak. This phenomenon is known as asymptotic freedom. In this case, a perturbative treatment of QCD, similar to QED, becomes possible, and an accurate description of quarks and gluons interactions can be computed. However, at low energy, corresponding to interaction distances of the order of the nucleon size, the strong coupling constant becomes large and perturbative QCD can no longer be applied.

Quarks and gluons have never been observed free and are always bound within a hadron: this phenomenon is called confinement. In the case where enough energy is brought to a system to isolate a single quark or gluon, this energy is immediately converted into the creation of additional quarks and gluons to keep the particles bound inside a hadron: this phenomenon is called hadronization. Quantitatively understanding confinement and hadronization in QCD is one of the most prominent questions raised by modern physics.

In order to understand how QCD works at energy and distance scales which cannot be approached by a perturbative treatment, one has to turn towards experiments. By scrutinizing the internal structure of the nucleon, one can find clues about how hadrons are formed from the most fundamental bricks of matter: the quarks and gluons. Using electrons, whose interactions are well described by QED, in order to probe the internal structure of nucleons has already allowed to gather a large quantity of information, like nucleon Form Factors and Parton Distribution Functions. However, the pieces collected so far are not enough to complete the full QCD puzzle.

In the mid-90s, new theoretical tools called Generalized Parton Distributions (GPDs) have been developed. The GPDs are a generalization of the Form Factors and Parton Distribution Functions and provide a large quantity of additional information that was not accessible before. A deeper understanding of the nucleon structure can thus be reached from the experimental study of GPDs. For this reason, a worldwide experimental program dedicated to the study of GPDs has started. These new distributions are experimentally accessible through deeply exclusive electro-production processes, and one of the simplest channels available is Deeply Virtual Compton Scattering (DVCS).

DVCS is a very challenging process to study because of its small cross section and the difficulty to identify events of interest from the background. The first experiment dedicated specifically to DVCS took place in 2004 in the Hall A of Jefferson Lab. In its direct continuation, a new DVCS experiment, which is the subject of this document, took place between 2014 and 2016 in the same place. The manuscript is organized as follow:

- chapter 1 will briefly present the theoretical framework of GPDs and how they can be accessed through the DVCS process. Then, details will be provided about our experiment, its goals, and how it fits within the global experimental landscape;
- chapter 2 will describe Jefferson Lab and the Hall A instrumentation. The detectors setup and the data acquisition system specific to this DVCS experiment will also be presented;

- chapter 3 will focus on beam line components and detector calibrations. Emphasis will be put on the spectrometer optics and the calorimeter gain whose calibration turned out to be particularly challenging;
- chapter 4 will present in great detail the data analysis allowing to reconstruct, identify and select DVCS events from the raw data. Particular attention will be paid to the ARS waveform analysis algorithm which is a key component. The data quality analysis and various corrections to the number of DVCS events will also be described in this chapter;
- chapter 5 will describe the Monte Carlo simulation based on the Geant4 toolkit which allows to compute the experimental acceptance. Details about the event generator will be provided, and the implementation of radiative corrections will be explained as well. Then, the second part of Chapter 5 will focus on the algorithm used to extract cross sections, and the evaluation of the systematic uncertainties. Finally, the experiment preliminary results will be presented and discussed.

Chapter 1

Accessing the nucleon structure through DVCS

Quantum chromodynamics successfully describes at high energy the dynamics of quarks and gluons, the particles which compose hadrons. However, QCD computations stop working at low energy and we are unable to derive quantitative observables from this theory. Phenomena such as confinement and hadronisation, and more generally the structure of hadrons, still escape our grasp. As a consequence, experiments are needed to fill these gaps in our knowledge and reach a better understanding of QCD.

The measurement of nucleons Form Factors (FFs) through elastic scattering experiments was a huge step towards this goal. Historically, the study of elastic scattering of electrons on proton and deuteron targets performed in the 1950's by Hofstadter and his team at Stanford University was one of the very first hints of the existence of nucleon internal structure [1]. Form Factors are related to the spatial distribution of charges in the nucleon: their Fourier transform yields information about the transverse spatial distribution of partons, the constituents of the nucleon. Despite having been studied for over half a century, Form Factors are still an extremely hot topic among the hadronic physics community as they are central, for instance, to the currently unanswered proton radius puzzle [2].

The measurement of Parton Distribution Functions (PDFs) through Deep Inelastic Scattering (DIS) was another huge step towards the understanding of the nucleon structure. DIS experiments proved the existence of quarks, and PDFs yield information about the longitudinal momentum distribution of partons inside nucleons.

Despite these tremendous achievements, a complete understanding of the nucleon internal structure was still out of reach. For instance, FFs and PDFs yield no information about the correlations between spatial and momentum distributions of partons. However, introduced in the mid-90s, Generalized Parton Distributions will be able to fill many of these gaps. GPDs are a generalization of FFs and PDFs in that they encapsulate both of them and provide information about the correlations between transverse spatial distributions and longitudinal momentum distributions of partons inside the nucleon [3], thus allowing one to perform a 3-dimensional tomography of it. GPDs also give access to the quark total orbital angular momentum contribution to the nucleon spin through Ji's sum rule [4].

GPDs are experimentally accessible through deeply exclusive electro-production processes, and one of the cleanest channels is Deeply Virtual Compton Scattering [4, 5]. GPDs obey to a set of properties and sum rules from which one can build models which can then be tested against experimental DVCS cross sections.

This chapter will be divided into six parts. The first two parts will present a brief overview of FFs and PDFs measurements through elastic and inelastic scattering. The third part will deal with GPDs and their accessibility through the DVCS process. The fourth part will give an overview of the current experimental landscape regarding DVCS and GPDs measurements. Finally, the last two parts will present the experiment of interest of this thesis, which new information is expected from it, and what measurements are planned for the future.

1.1 Elastic Scattering and Form Factors

The elastic scattering of an electron off a nucleon means that the particles present in the initial and final states are identical. As all the particles in the final state are identified, this process is called exclusive. Fig. 1.1 represents the elastic scattering of an electron off a proton $ep \to e'p'$ in the one-photon exchange

approximation. Since this is an electromagnetic interaction governed by the fine structure constant $\alpha = \frac{e^2}{4\pi} \sim \frac{1}{137}$, the one-photon approximation should be accurate at the 1% level. This approximation will be kept in the whole of this document.

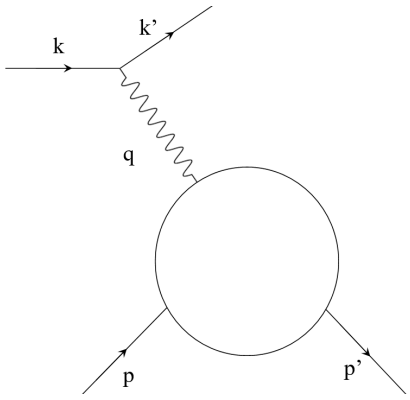

Figure 1.1: Elastic scattering diagram.

As described in Fig. 1.1, let p and p' be the initial and final nucleon four-momenta, while $k = (\overrightarrow{k}, E)$ and $k' = (\overrightarrow{k'}, E')$ are respectively the incident and scattered electron four-momenta. The nucleon is at rest in the laboratory frame and has the mass M, while the electron mass is neglected. Let us call θ the electron scattering angle in the laboratory frame, and $q = k - k' = p' - p$ is the four momentum transfer to the nucleon. One can then define the virtuality $Q^2 = -q^2 > 0$, which can be interpreted as the scale with which the internal structure of the nucleon is probed: higher values of Q^2 will allow to scrutinize shorter distances and smaller structures.

Elastic scattering is a constrained system: conservation of energy and momentum implies that the scattered electron energy E' is related to its initial energy E and the scattering angle θ by the relation:

$$E' = \frac{E}{1 + \frac{2E}{M}\sin^2\left(\frac{\theta}{2}\right)}, \tag{1.1}$$

and the virtuality Q^2 is given by:

$$Q^2 = 4EE'\sin^2\left(\frac{\theta}{2}\right). \tag{1.2}$$

In the laboratory frame, the scattering of a spin $\frac{1}{2}$, relativistic electron off a point like and spin-less nucleon is described by the Mott cross section [6]:

$$\left(\frac{d\sigma}{d\Omega}\right)_{Mott} = \frac{\alpha^2}{4E^2\sin^4\left(\frac{\theta}{2}\right)}\frac{E'}{E}\cos^2\left(\frac{\theta}{2}\right). \tag{1.3}$$

Then, if the nucleon has a spin $\frac{1}{2}$, with an anomalous magnetic moment and an extended structure, the Mott cross section (Eq. (1.3)) becomes the Rosenbluth cross section [7]:

$$\left(\frac{d\sigma}{d\Omega}\right)_{Rosenbluth} = \left(\frac{d\sigma}{d\Omega}\right)_{Mott}\left\{F_1^2(Q^2) + \frac{Q^2}{4M^2}\left[F_2^2(Q^2) + 2\left(F_1(Q^2) + F_2(Q^2)\right)^2\tan^2\left(\frac{\theta}{2}\right)\right]\right\}, \tag{1.4}$$

with $F_1(Q^2)$ and $F_2(Q^2)$ the Dirac and Pauli Form Factors, respectively. Additional information about elastic cross sections can be found in appendix A.

It is sometimes more convenient to express $F_1(Q^2)$ and $F_2(Q^2)$ in terms of the Sachs electric and magnetic Form Factors ($G_E(Q^2)$ and $G_M(Q^2)$ respectively):

$$G_E(Q^2) = F_1(Q^2) - \tau F_2(Q^2), \tag{1.5}$$

$$G_M(Q^2) = F_1(Q^2) + F_2(Q^2), \tag{1.6}$$

where τ is defined as:

$$\tau = \frac{Q^2}{4M^2}, \tag{1.7}$$

and the Rosenbluth cross section in Eq. (1.4) can be rewritten as:

$$\left(\frac{d\sigma}{d\Omega}\right)_{Rosenbluth} = \left(\frac{d\sigma}{d\Omega}\right)_{Mott} \left\{ \frac{G_E^2(Q^2) + \tau G_M^2(Q^2)}{1+\tau} + 2\tau G_M^2(Q^2) \tan^2\left(\frac{\theta}{2}\right) \right\}. \tag{1.8}$$

In the Breit frame, where the nucleon has the same energy before and after interaction, and in the case of elastic scattering, where the incoming electron has the momentum $\overrightarrow{k} = +\frac{\overrightarrow{q}}{2}$ and the initial nucleon has the opposite momentum $\overrightarrow{p} = -\frac{\overrightarrow{q}}{2}$, the Sachs Form Factors can be interpreted as Fourier transforms of the transverse electric charge $\rho(\overrightarrow{r})$ and magnetic current distributions, as shown in Eq. (1.9):

$$\rho(\overrightarrow{r}) = \int G_E(\overrightarrow{q}^2) \frac{M}{E} e^{-i\overrightarrow{q}.\overrightarrow{r}} \frac{d^3\overrightarrow{q}}{(2\pi)^3}. \tag{1.9}$$

From the Sachs Form Factors, one can also define the nucleon charge and magnetic radii (Eq. (1.10) and Eq. (1.11) respectively):

$$\langle r_E^2 \rangle = -6 \frac{dG_E(Q^2)}{dQ^2}\bigg|_{Q^2=0}, \tag{1.10}$$

$$\langle r_M^2 \rangle = \frac{-6}{G_M(0)} \frac{dG_M(Q^2)}{dQ^2}\bigg|_{Q^2=0}. \tag{1.11}$$

Eq. (1.10) and the proton charge radius puzzle is one of the reasons why elastic scattering and Form Factors measurements are still a subject of extremely high interest nowadays despite having been studied for over half a century and being well known [8].

Indeed, the proton charge radius puzzle arises from a 7σ discrepancy between the radius measured by elastic scattering experiments (0.879 ± 0.008 fm) [9] and from the Lamb shift of muonic hydrogen (0.84184 ± 0.00067 fm) [10]. Several hypothesis have been made to explain this discrepancy, ranging from issues with the extrapolation of $G_E(Q^2)$ at $Q^2 = 0$ to potential physics beyond the Standard Model. As a consequence, the high precision measurement of elastic Form Factors at extremely low Q^2 is of great interest to answer these questions [2].

1.2 Deep Inelastic Scattering and Parton Distribution Functions

The inelastic scattering of an electron off a nucleon means that the particles present in the final state are not identical to the ones in the initial state. When the particles in the final state are not all identified, this process is called inclusive. Fig. 1.2 (left) represents the deep inelastic scattering of an electron of a proton $ep \to e'X$ in the one-photon exchange approximation, with X symbolizing the various particles present in the final state, except for the electron. One can define W, the invariant mass of the initial hadronic state as $W^2 = (p+q)^2$. The deep inelastic regime is characterized by $W \gg M$ and $Q^2 \gg M^2$.

One will also notice that, while Q^2 and $\nu = E - E'$ were connected through the relation $\nu = \frac{Q^2}{2M}$ for elastic scattering, they are now independent for Deep Inelastic Scattering (DIS).

The DIS cross section is parametrized by two structure functions W_1 and W_2 and can be written as:

$$\frac{d^2\sigma}{d\Omega dE'} = \frac{\alpha^2 \cos^2\left(\frac{\theta}{2}\right)}{4E^2 \sin^4\left(\frac{\theta}{2}\right)} \left(W_2(\nu, Q^2) + 2W_1(\nu, Q^2) \tan^2\left(\frac{\theta}{2}\right) \right). \tag{1.12}$$

It is worth mentioning that the DIS cross section (Eq. (1.12)) looks similar to the Rosenbluth cross section (Eq. (1.8)), with the form factors being replaced by the structure functions W_1 and W_2. One will also remark that the structure functions have an additional dependence in ν.

It is usually more convenient to work with the structure functions $F_1(x_{Bj}, Q^2)$ and $F_2(x_{Bj}, Q^2)$:

$$F_1(x_{Bj}, Q^2) = MW_1(\nu, Q^2), \tag{1.13}$$

$$F_2(x_{Bj}, Q^2) = \nu W_2(\nu, Q^2), \tag{1.14}$$

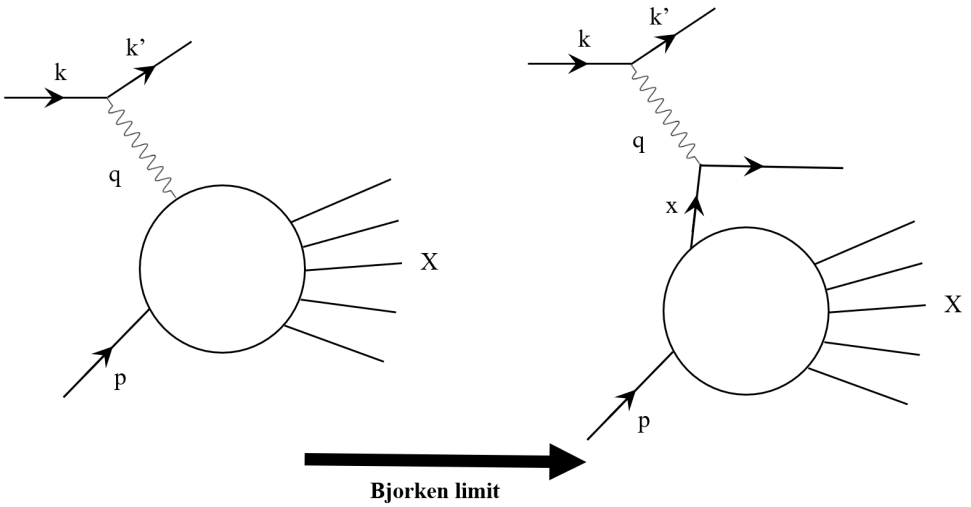

Figure 1.2: Deep Inelastic Scattering diagram in the Bjorken limit.

with the Bjorken variable x_{Bj} defined as:

$$x_{Bj} = \frac{Q^2}{2M\nu}. \tag{1.15}$$

Eq. (1.12) can then be written as Eq. (1.16):

$$\frac{d^2\sigma}{d\Omega dE'} = \frac{\alpha^2 \cos^2\left(\frac{\theta}{2}\right)}{4E^2 \sin^4\left(\frac{\theta}{2}\right)} \left(\frac{F_2(x_{Bj}, Q^2)}{\nu} + \frac{2}{M} F_1(x_{Bj}, Q^2) \tan^2\left(\frac{\theta}{2}\right) \right). \tag{1.16}$$

Experiments made at SLAC (Stanford) in the late 1960s showed that these structure functions F_1 and F_2 are independent of Q^2 [11]. This phenomenon is called scaling. In the parton model developed by Feynman [12], the scaling feature is the sign that electrons are incoherently scattering off point-like particles (partons), since an object with a finite size should have a form factor describing its structure which would then introduce a Q^2 dependence. This is an evidence of the existence of "quarks", introduced earlier by Gell-Mann, inside the nucleon. The experimental verification of the Callan-Gross relation (Eq. (1.17)) at a later date proved that these partons had a spin $\frac{1}{2}$, further evidence in favor of quarks:

$$F_2(x_{Bj}) = 2x_{Bj} F_1(x_{Bj}). \tag{1.17}$$

As the structure functions are independent of the chosen frame, Feynman's parton model can be considered in an infinite momentum frame. For instance, one of such frames can be defined as the frame in which the nucleon is moving with almost infinite momentum. In the infinite momentum frame, time dilatation means that the particles inside the nucleon do not have the time to interact during the absorption of the virtual photon emitted by the scattering electron. The nucleon can thus be viewed as a collection of non-interacting point-like particles, one of which must carry a fraction x of the total longitudinal momentum of the nucleon in order to absorb the virtual photon. As shown in Fig. 1.2 (right), in the Bjorken limit ($Q^2 \to \infty$ and $\nu \to \infty$ at fixed x_{Bj}), the electron is scattering off a single quark of the nucleon, carrying longitudinal momentum fraction x. Furthermore, in the DIS case, it turns out that x can be related to the Bjorken variable x_{Bj}. Indeed, after absorbing the virtual photon, as the quark does not interact with other partons and its mass is negligible against Q^2 and ν, one has:

$$(xp + q)^2 = x^2M^2 - Q^2 + 2xpq = x^2M^2 - Q^2 + 2xM\nu \approx 0, \tag{1.18}$$

and further neglecting x^2M^2 against Q^2 and ν one gets:

$$-Q^2 + 2xM\nu \approx 0, \tag{1.19}$$

$$x \approx \frac{Q^2}{2M\nu} = x_{Bj}. \tag{1.20}$$

As a consequence, the DIS cross section can be reduced to the sum of cross sections for scattering off individual partons i, weighted by the density of partons i with longitudinal momentum fraction x_{Bj}. The structure function F_2 can thus be expressed as:

$$F_2(x_{Bj}) = x_{Bj} \sum_i e_i^2 q_i(x_{Bj}), \tag{1.21}$$

where e_i is the charge of the parton i, in units of the proton charge, and $q_i(x_{Bj})$ is the density of partons i with longitudinal momentum fraction x_{Bj}. These functions q_i are called Parton Distribution Functions (PDFs).

However, when extracting the structure functions F_1 and F_2 over a large range of x_{Bj}, experiments showed that the scaling feature did not hold true for very large or very small values of x_{Bj} (see Fig. 1.3): this is the scaling violation. The scaling violation is explained by QCD radiative corrections: the struck quark of the nucleon may radiate gluons, much like electrons may radiate photons in Quantum Electrodynamic. The QCD evolution (variation with Q^2) of structure functions obey the DGLAP equations (Dokshitzer, Gribov, Lipatov, Altarelli and Parisi), resulting in a logarithmic dependence of the PDFs in Q^2, as can be seen in Fig. 1.3.

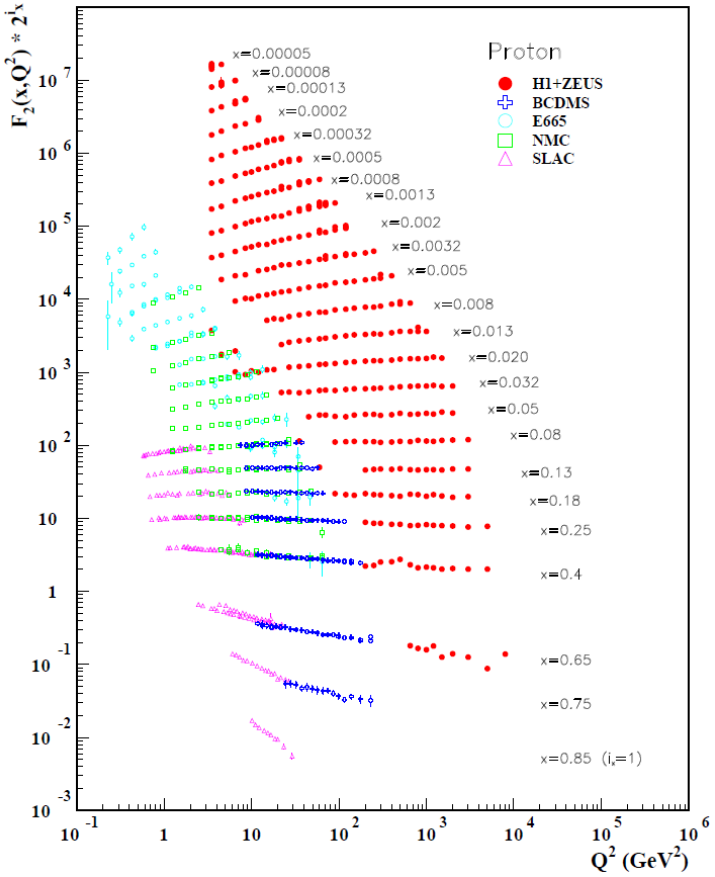

Figure 1.3: Structure function F_2 against Q^2 for several values of x_{Bj}. (Figure extracted from [13]).

1.3 Deeply Virtual Compton Scattering and Generalized Parton Distributions

While Form Factors and Parton Distribution Functions provide precious information about the nucleon internal structure, they are far from being enough to fully describe and understand it. Introduced in the mid-90s, Generalized Parton Distributions, also called "Off-Forward Distributions", are experimentally accessible through Deeply Virtual Compton Scattering and provide a higher level of information than FFs and PDFs, as will be described in the following section. Additional information about GPDs can be found in [14].

1.3.1 Accessing GPDs through the DVCS process

Deeply Virtual Compton Scattering is an exclusive process in which an electron (or a muon) scatters off a nucleon, with a photon emitted by the nucleon in the final state[1]. More precisely, in the Bjorken limit ($Q^2 \to \infty$ and $\nu \to \infty$ at fixed x_{Bj}), the electron scatters off a single quark which then emits a real photon before going back to the nucleon. Fig. 1.4 represents the DVCS process on a proton $ep \to e'p'\gamma$ in the one-photon exchange approximation. The squared momentum transfer to the nucleon t is defined as $t = (p' - p)^2 = \Delta^2$. In the infinite momentum frame, $x + \xi$ and $x - \xi$ are respectively the fractions of the nucleon longitudinal momentum carried by the struck quark before and after the interaction[2] and ξ is the skewness, which can be related to x_{Bj} by the relation:

$$\xi = \frac{x_{Bj}(1 + \frac{t}{2Q^2})}{2 - x_{Bj} + x_{Bj}(\frac{t}{Q^2})} \xrightarrow{\frac{|t|}{Q^2} \ll 1} \frac{x_{Bj}}{2 - x_{Bj}}. \tag{1.22}$$

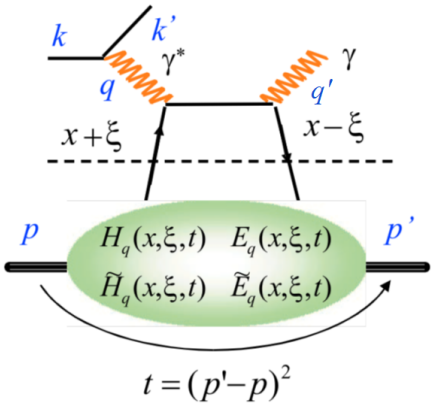

Figure 1.4: The "handbag diagram" of the DVCS process.

The angle ϕ is the azimuthal angle between the leptonic plane, defined by the scattered electron and the virtual photon, and the hadronic plane, formed by the recoil nucleon and the virtual photon (see Fig. 1.5). The azimuthal angle ϕ follows the Trento convention [15], defined by:

$$\cos\phi = \frac{q \times k}{|q \times k|} \cdot \frac{q \times p'}{|q \times p'|}, \tag{1.23}$$

$$\sin\phi = \frac{(k \times p') \cdot q}{|q \times k||q \times p'|}. \tag{1.24}$$

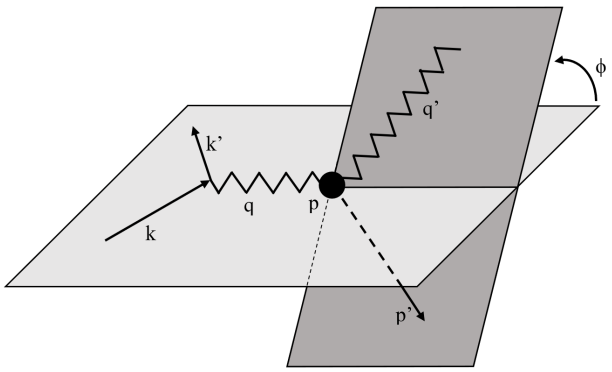

Figure 1.5: Three dimensional representation of the DVCS process.

[1]Technically, lepto-production and DVCS are two different processes since DVCS has a virtual photon in the initial state. However, DVCS being used as the part of the lepto-production process where the final photon is emitted from the hadron is a jargon widely accepted, and will be used in this manuscript.

[2]NB: unlike DIS, x is no longer equal to x_{Bj} for DVCS.

Finally, as shown in Fig. 1.4, the nucleon structure is parametrized by the quark GPDs H_q, E_q, $\widetilde{H}_q$, and $\widetilde{E}_q$, with q denoting the quark flavor. These structure functions correspond to the Fourier transform of QCD non-local and non-diagonal (off-forward) operators. The operators are non-local because the initial and final quarks have different space-time coordinates, and non-diagonal because the momenta of the initial and final quarks are different [14].

1.3.1.1 Twist and factorization

In perturbative QCD, a single tree-level leading-order Feynman diagram is usually not enough to describe a process with a satisfying precision. More complex diagrams must be taken into account, and higher order corrections need to be added. These Feynman diagram amplitudes are expressed as series in powers of α_s, the QCD strong coupling constant, which depends on Q^2: the higher Q^2 is, the smaller α_s becomes. When $\alpha_s \ll 1$, the process is called "hard", perturbative QCD computations can be applied, and higher order corrections are suppressed by powers of α_s with respect to the leading order. When $\alpha_s > 1$, the process is called "soft" and perturbative QCD computations cannot be applied. One then has to introduce structure functions such as FFs, PDFs or GPDs to parametrize the soft part.

The DVCS amplitude, which contains both hard and soft parts, can be expressed as an operator product expansion. The twist is then defined as the dimension minus the spin of these operators and is used to sort the terms of the series in growing power of $\frac{1}{Q}$. For DVCS, the leading twist of the series is twist-2, and higher twists corrections are suppressed in powers of $\frac{1}{Q}$ with respect to the leading twist (for instance, twist-3 terms are suppressed by a factor $\frac{1}{Q}$, twist-4 terms are suppressed by a factor $\frac{1}{Q^2}$, etc...).

The so-called "handbag diagram" in Fig. 1.4 is the leading twist, leading order diagram of the DVCS process. The factorization of the DVCS process has been proved at leading twist and all orders of perturbative QCD [16, 17]. As such, the diagram in Fig. 1.4 can be factorized into two parts: a hard part (upper half) which can be fully computed by perturbative QCD, and a soft part (lower half) parametrized by the GPDs, and the DVCS cross section can be expressed as a convolution of both. A consequence of the factorization is that GPDs are universal, as the differences between different processes are contained in the hard part. However, this "handbag diagram" formalism requires the conditions $Q^2 \gg M^2$, $\frac{|t|}{Q^2} \ll 1$ and W large for fixed values of x_{Bj}.

Thus, in the "handbag diagram" formalism, GPDs can be accessed at leading twist in the DVCS process through the measurement of its cross section and asymmetries. Although other hard exclusive lepto-production processes can allow access to GPDs in the same way, DVCS is the cleanest channel because it is the simplest. For instance, Deeply Virtual Meson Production (DVMP) requires the introduction of Distribution Amplitudes (DA). Nevertheless, higher twist and higher order QCD corrections may need to be taken into account for specific experiments or kinematic settings, as recent results suggest that their contributions might not be negligible [18].

1.3.1.2 Interference with the Bethe-Heitler process

Experimentally, it is not possible to distinguish DVCS from the Bethe-Heitler process. Indeed, both have the same initial and final state, though in the Bethe-Heitler case, the photon is radiated by the electron instead of the struck quark of the nucleon (see Fig. 1.6). As a consequence, contributions from the Bethe-Heitler process and its interference with DVCS will need to be taken into account in exclusive photon electro-production cross-section measurements.

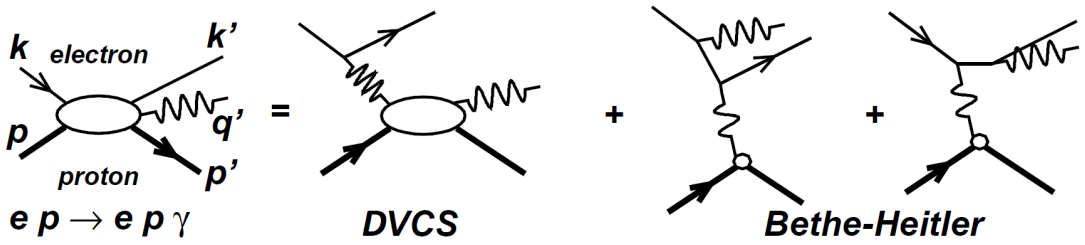

Figure 1.6: The exclusive photon electro-production $ep \to e'p'\gamma$ has contributions from both the DVCS process and the Bethe-Heitler process.

1.3.2 The Generalized Parton Distributions

GPDs are an extremely rich and complex framework which can be very hard to disentangle. This section will briefly present the GPDs and their main properties interesting either for their physics interpretation or for constraining models.

1.3.2.1 GPDs nomenclature

At twist-2, the nucleon structure is parametrized by four quark GPDs H_q, E_q, $\widetilde{H}_q$, and $\widetilde{E}_q$. GPDs depend on quarks flavor q. However, flavor separation requires DVCS data on both the proton and the neutron at the same kinematic settings, which is not the subject of this thesis. There also exist higher twist quark GPDs, whose contributions may need to be taken into account in order to properly extract the twist-2 ones [19].

H_q, E_q, $\widetilde{H}_q$, and $\widetilde{E}_q$ are chiral-even quark GPDs: the helicity of the struck quark is always conserved. There also exist four chiral-odd quark GPDs H_{qT}, E_{qT}, $\widetilde{H}_{qT}$, and $\widetilde{E}_{qT}$, also called quark transversity GPDs, which flip the quark helicity. DVCS is not sensitive to the chiral-odd quark GPDs, but they can be measured in other exclusive processes such as pseudo-scalar mesons production, for instance [20].

There also exist gluon GPDs. However, our DVCS experiment was performed in the valence quarks region, which is in principle insensitive to gluon GPDs. At leading twist, gluons contribute at next-to-leading order in the strong coupling constant α_s (double helicity-flip transversity gluons), which is believed to be negligible. Nevertheless, recent estimates [21] and results [18] seem to challenge this view and indicate that corrections for gluon contributions might be significant and should be taken into account as well.

Unless stated otherwise, "GPDs" will now refer to the four twist-2 chiral-even quark GPDs H_q, E_q, $\widetilde{H}_q$, and $\widetilde{E}_q$.

The GPDs E_q and $\widetilde{E}_q$ are associated with the flip of the nucleon helicity, while H_q and $\widetilde{H}_q$ conserve it. The GPDs H_q and E_q are related with averages over the quark helicity and are called "unpolarized" while $\widetilde{H}_q$, and $\widetilde{E}_q$ are tied with differences of quark helicity and are called "polarized". The correlations between GPDs and helicity are summarized in Fig. 1.7.

1.3.2.2 GPDs properties

GPDs depend on four variables: Q^2, x, ξ and t. However, like for DIS, GPDs also show a scaling feature and their Q^2 dependence can be predicted by QCD evolution. Therefore, the Q^2 dependence of GPDs is not relevant to the non-perturbative structure of the nucleon and is usually dropped in the notation.

This large number of variables reflects the wealth of information contained in GPDs compared to PDFs and FFs. On the other hand, GPDs suffer from "the curse of dimensionality", as this larger number of dependencies makes them much harder to extract.

The variables x and ξ vary between -1 and 1, but time reversal invariance states that:

$$H_q(x,-\xi,t) = H_q(x,\xi,t), \tag{1.25}$$

where H_q can be replaced by E_q, $\widetilde{H}_q$, or $\widetilde{E}_q$. As a consequence, the range of ξ can be reduced to $[0;1]$. In the DGLAP region characterized by $|x| > \xi$, GPDs represent the probability of finding a quark (or antiquark if $x < -\xi$) in the nucleon with longitudinal momentum fraction $x+\xi$ and putting it back with longitudinal momentum fraction $x-\xi$ and a transverse momentum kick t. In the ERBL (Efremov, Radyushkin, Brodsky and Lepage) region characterized by $-\xi < x < \xi$, either $x+\xi$ or $x-\xi$ is negative: GPDs behave like a Distribution Amplitude and can be interpreted as the probability of finding a quark-antiquark pair in the nucleon.

The GPDs are generalization of PDFs and FFs, and encapsulate both of them:

- in the forward limit ($t = 0$ and $\xi = 0$), GPDs allow to recover the PDFs:

$$H_q(x,0,0) = \begin{cases} q_q(x), & x > 0 \\ -\bar{q}_q(-x), & x < 0 \end{cases} \tag{1.26}$$

$$\widetilde{H}_q(x,0,0) = \begin{cases} \Delta q_q(x), & x > 0 \\ \Delta\bar{q}_q(-x), & x < 0 \end{cases} \tag{1.27}$$

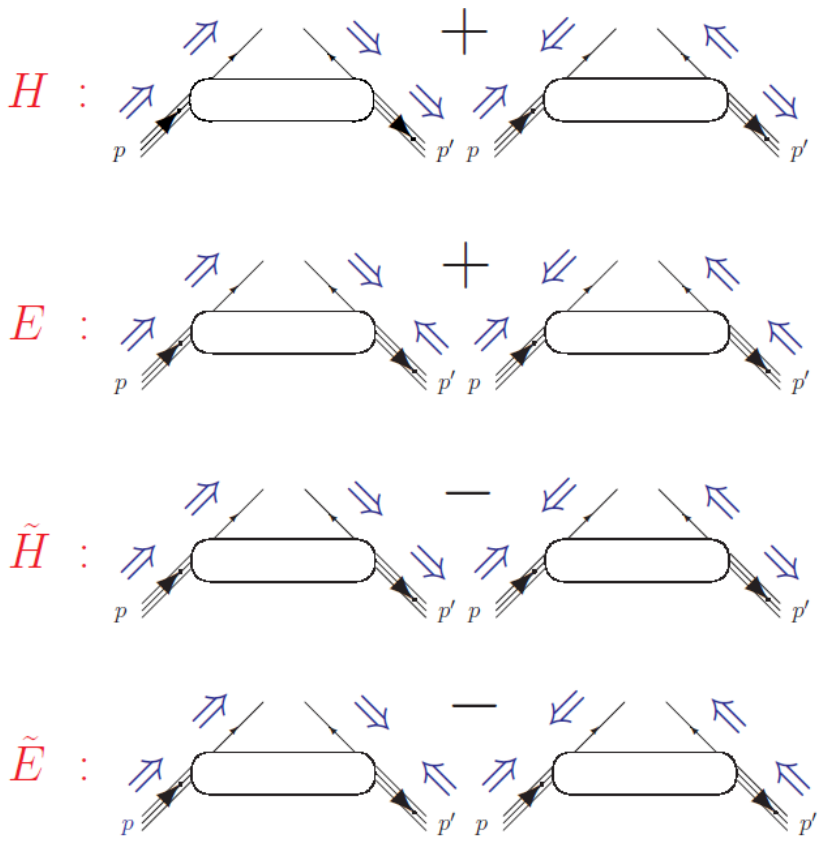

Figure 1.7: Representation of the four chiral-even GPDs H_q, E_q, $\widetilde{H}_q$, and $\widetilde{E}_q$ corresponding to different nucleon and quark helicity orientations. (Figure extracted from [14]).

where $q_q(x)$ ($\bar{q_q}(x)$) and $\Delta q_q(x)$ ($\Delta\bar{q_q}(x)$) are respectively the quark (antiquark) unpolarized and polarized PDFs for flavor q;

- at constant t, the first moment of GPDs allows to recover FFs:

$$\int_{-1}^{1} H_q(x,\xi,t)dx = F_1^q(t) \quad \forall\xi, \tag{1.28}$$

$$\int_{-1}^{1} E_q(x,\xi,t)dx = F_2^q(t) \quad \forall\xi, \tag{1.29}$$

$$\int_{-1}^{1} \widetilde{H}_q(x,\xi,t)dx = G_A^q(t) \quad \forall\xi, \tag{1.30}$$

$$\int_{-1}^{1} \widetilde{E}_q(x,\xi,t)dx = G_P^q(t) \quad \forall\xi, \tag{1.31}$$

with $F_1^q(t)$ and $F_2^q(t)$ the Dirac and Pauli Form Factors, and $G_A^q(t)$ and $G_P^q(t)$ the axial and pseudo-scalar Form Factors, for quark flavor q, respectively;

- in the infinite momentum frame and at $\xi = 0$, the variable t is the Fourier conjugate to the transverse spatial distribution of quarks as a function of x [22]. Let $GPD_q(x,\xi,t)$ be the general notation for GPDs $H_q(x,\xi,t)$, $E_q(x,\xi,t)$, $\widetilde{H}_q(x,\xi,t)$, $\widetilde{E}_q(x,\xi,t)$. At $\xi = 0$, $GPD_q(x,0,t)$ can then be interpreted as the probability amplitude of finding a quark of flavor q with longitudinal momentum fraction x at a given transverse distance from the center of momentum of the nucleon.

GPDs also allow to unveil information about the nucleon spin structure. Indeed, it has been shown in [4] that the nucleon spin can be decomposed into the quarks and gluons contributions J_q and J_g respectively:

$$\frac{1}{2} = \sum_q J_q + J_g, \tag{1.32}$$

and the quarks contributions J_q can be further decomposed into their total spin and total orbital angular momentum contributions S_q and L_q respectively:

$$J_q = \frac{1}{2} S_q + L_q. \tag{1.33}$$

The second moment of GPDs then yields the famous Ji's sum rule [4], which allows to access J_q, and thus, the total orbital angular momentum of quarks L_q:

$$J_q = \frac{1}{2} \int_{-1}^{1} x \left[H_q(x, \xi, t = 0) + E_q(x, \xi, t = 0) \right] dx. \tag{1.34}$$

A last important property of GPDs is the polynomiality, which is of great use to construct GPD models. Polynomiality states that the x^n moment of GPDs is a polynomial in ξ of order n if n is even, and order $n+1$ if n is odd. For instance, with GPD H_q:

$$\int_{-1}^{1} x^n H_q(x, \xi, t) dx = a_0 + a_2 \xi^2 + a_4 \xi^4 + ... + a_n \xi^n, n \ even, \tag{1.35}$$

$$\int_{-1}^{1} x^n H_q(x, \xi, t) dx = a_0 + a_2 \xi^2 + a_4 \xi^4 + ... + a_{n+1} \xi^{n+1}, n \ odd, \tag{1.36}$$

and Eq. (1.25) imposes that there are only even powers of ξ.

1.3.3 Compton Form Factors

In DVCS, the variables ξ and t can be computed from the kinematic variables of the particles in the initial and final states. However, x is not experimentally accessible. The DVCS amplitude is given by integrals of the form:

$$\int_{-1}^{1} \frac{H_q(x, \xi, t)}{x - \xi + i\epsilon} dx = \mathcal{P} \int_{-1}^{1} \frac{H_q(x, \xi, t)}{x - \xi} dx - i\pi H_q(\xi, \xi, t), \tag{1.37}$$

where $\mathcal{P}$ is the principal value integral and H_q is interchangeable with E_q, $\widetilde{H}_q$, or $\widetilde{E}_q$. In Eq. (1.37), x is either integrated over or evaluated at $x = \xi$. The former case is accessed by observables sensitive to the real part of the DVCS amplitude, while the latter is accessed by observables sensitive to its imaginary part.

Therefore, there are actually eight GPD-related quantities that can be extracted from DVCS:

$$\mathcal{R}e\mathcal{H}_q(\xi, t) = \mathcal{P} \int_0^1 \left[H_q(x, \xi, t) - H_q(-x, \xi, t) \right] C^+(x, \xi) dx, \tag{1.38}$$

$$\mathcal{R}e\mathcal{E}_q(\xi, t) = \mathcal{P} \int_0^1 \left[E_q(x, \xi, t) - E_q(-x, \xi, t) \right] C^+(x, \xi) dx, \tag{1.39}$$

$$\mathcal{R}e\widetilde{\mathcal{H}}_q(\xi, t) = \mathcal{P} \int_0^1 \left[\widetilde{H}_q(x, \xi, t) + \widetilde{H}_q(-x, \xi, t) \right] C^-(x, \xi) dx, \tag{1.40}$$

$$\mathcal{R}e\widetilde{\mathcal{E}}_q(\xi, t) = \mathcal{P} \int_0^1 \left[\widetilde{E}_q(x, \xi, t) + \widetilde{E}_q(-x, \xi, t) \right] C^-(x, \xi) dx, \tag{1.41}$$

$$\mathcal{I}m\mathcal{H}_q(\xi, t) = -\pi \left(H_q(\xi, \xi, t) - H_q(-\xi, \xi, t) \right), \tag{1.42}$$

$$\mathcal{I}m\mathcal{E}_q(\xi, t) = -\pi \left(E_q(\xi, \xi, t) - E_q(-\xi, \xi, t) \right), \tag{1.43}$$

$$\mathcal{I}m\widetilde{\mathcal{H}}_q(\xi,t) = -\pi\left(\widetilde{H}_q(\xi,\xi,t) + \widetilde{H}_q(-\xi,\xi,t)\right), \tag{1.44}$$

$$\mathcal{I}m\widetilde{\mathcal{E}}_q(\xi,t) = -\pi\left(\widetilde{E}_q(\xi,\xi,t) + \widetilde{E}_q(-\xi,\xi,t)\right), \tag{1.45}$$

with $C^{\pm}$ defined as:

$$C^{\pm}(x,\xi) = \frac{1}{x-\xi} \pm \frac{1}{x+\xi}. \tag{1.46}$$

The eight functions defined in Eq. (1.38) to (1.45), experimentally accessible, are called Compton Form Factors (CFFs). One can further introduce the notation:

$$\mathcal{H}_q(\xi,t) = \mathcal{R}e\mathcal{H}_q(\xi,t) + i\mathcal{I}m\mathcal{H}_q(\xi,t), \tag{1.47}$$

with $\mathcal{H}_q$ interchangeable with $\mathcal{E}_q$, $\widetilde{\mathcal{H}}_q$ or $\widetilde{\mathcal{E}}_q$.

1.3.4 DVCS cross section

As stated in section 1.3.1.2, DVCS cannot be experimentally distinguished from the Bethe-Heitler process, and the measured cross sections have contributions from both, as well as an interference term. As a consequence, the four-fold cross section can be expressed as [23]:

$$\frac{d^4\sigma}{dQ^2 dx_{Bj} dt d\phi} = \frac{\alpha^3 x_{Bj} y^2}{8\pi Q^4\sqrt{1+\epsilon^2}}\frac{1}{e^6}|T|^2, \tag{1.48}$$

where $y = \frac{p\cdot q}{p\cdot k} = \frac{\nu}{E}$ is the lepton relative energy loss (expressed in the target rest frame), $\epsilon = 2x_{Bj}\frac{M}{Q}$, and e is the elementary charge. The amplitude T can be further decomposed into the contributions from the DVCS, BH, and Interference terms:

$$|T|^2 = |T_{BH}|^2 + |T_{DVCS}|^2 + I, \tag{1.49}$$

with the interference term I being:

$$I = T_{DVCS}T^*_{BH} + T^*_{DVCS}T_{BH}. \tag{1.50}$$

Belitsky and Müller performed an harmonic expansion of the DVCS, BH and Interference terms as a function of ϕ up to twist-3 and including gluon transversity. The development from [19] will be used for the BH, while the parametrization from [24] will be applied for the DVCS and Interference terms[3].

1.3.4.1 The Bethe-Heitler term

The Bethe-Heitler amplitude is computed using pure QED and can be expressed as a function of the elastic Form Factors. By using the FFs parametrization proposed by Kelly in [8], the BH term can be computed with a precision better than 1% in the kinematic settings of this experiment.

$|T_{BH}|^2$ is given by the expression:

$$|T_{BH}|^2 = \frac{e^6}{x_{Bj}^2 y^2(1+\epsilon^2)^2 t\mathcal{P}_1(\phi)\mathcal{P}_2(\phi)}\left\{c_0^{BH} + \sum_{n=1}^{2} c_n^{BH}\cos(n\phi) + s_1^{BH}\sin(\phi)\right\}, \tag{1.51}$$

where $\mathcal{P}_1(\phi)$ and $\mathcal{P}_2(\phi)$ are the lepton propagators. The harmonic coefficients c_i^{BH} and s_i^{BH}, as well as the expressions of $\mathcal{P}_1(\phi)$ and $\mathcal{P}_2(\phi)$, are given in [19]. In the case of an unpolarized target, $s_1^{BH} = 0$.

[3]The definition of ϕ used by Belitsky and Müller is not the same as the one from the Trento convention. The transformation $\phi_{Belitsky} = \pi - \phi_{Trento}$ must be applied.

1.3.4.2 The DVCS term

The DVCS amplitude is parametrized by bi-linear combinations of CFFs. The term $|T_{DVCS}|^2$ is given by the expression:

$$|T_{DVCS}|^2 = \frac{e^6}{y^2 Q^2}\left\{c_0^{DVCS} + \sum_{n=1}^{2}\left[c_n^{DVCS}\cos(n\phi) + s_n^{DVCS}\sin(n\phi)\right]\right\}, \tag{1.52}$$

and the harmonic coefficients c_n^{DVCS} and s_n^{DVCS} are detailed in appendix B.

The first term of c_0^{DVCS} contains twist-2 quark and gluon transversity CFFs while the second term involves twist-3 quark CFFs (see Eq. (B.9)), c_1^{DVCS} and s_1^{DVCS} encompass twist-2 and twist-3 quark CFFs, and c_2^{DVCS} encloses twist-2 gluon transversity CFFs. Furthermore, the coefficient s_1^{DVCS} depends on the beam helicity, and $s_2^{DVCS} = 0$ in the case of an unpolarized target.

1.3.4.3 The Interference term

The Interference amplitude is parametrized by linear combinations of CFFs. I is given by the expression:

$$I = \frac{\pm e^6}{x_{Bj} y^3 t \mathcal{P}_1(\phi)\mathcal{P}_2(\phi)}\left\{c_0^I + \sum_{n=1}^{3}\left[c_n^I\cos(n\phi) + s_n^I\sin(n\phi)\right]\right\}, \tag{1.53}$$

where the $+$ $(-)$ case stands for a negatively (positively) charged lepton beam. The harmonic coefficients c_n^I and s_n^I are detailed in appendix B.

Each harmonic coefficient is a mixture of twist-2 and twist-3 quarks CFFs and twist-2 gluon transversity CFFs. Nevertheless, c_0^I, c_1^I and s_1^I have a twist-2 quark dominant term, while c_2^I and s_2^I have a twist-3 quark dominant term, and c_3^I has a twist-2 gluon transversity dominant term. Furthermore, the coefficients s_1^I and s_2^I depend on the beam helicity, and $s_3^I = 0$ in the case of an unpolarized target.

1.3.5 Side note on asymmetries

Beside absolute cross sections, another way to access CFFs is through the measurement of asymmetries. For instance, the beam charge asymmetry is defined as:

$$A_C = \frac{d\sigma^+ - d\sigma^-}{d\sigma^+ + d\sigma^-}, \tag{1.54}$$

where $d\sigma^+$ and $d\sigma^-$ refer to cross sections with lepton beams of opposite charge. Another example is the beam spin asymmetry, defined by:

$$A_{LU} = \frac{d\overrightarrow{\sigma} - d\overleftarrow{\sigma}}{d\overrightarrow{\sigma} + d\overleftarrow{\sigma}}, \tag{1.55}$$

where $d\overrightarrow{\sigma}$ and $d\overleftarrow{\sigma}$ designate cross sections with opposite lepton beam helicity. The first subscript, L, indicates a polarized lepton beam, while the second subscript, U, corresponds to an unpolarized target. A detailed descriptions of experimental asymmetries is available in [25].

While no asymmetry has been measured in this experiment, they represent a large fraction of the available world-wide data on GPDs. Indeed, they have the benefit that many experimental uncertainties cancel out because of the numerator over denominator ratio. On the other hand, the presence of the denominator can make the disentanglement of the different CFFs contributions and physical interpretation more difficult compared with measuring absolute cross sections.

1.4 Experimental status

Although DVCS is one of the cleanest channels to access GPDs, their measurement through this process is extremely challenging. A high luminosity is required to measure the small DVCS cross sections, and experiments need detectors able to ensure the exclusivity of the final state. Moreover, a large combination of experimental setups is needed in order to measure all the observables necessary to extract CFFs and GPDs: DVCS on the proton or the neutron, unpolarized or polarized lepton beam of positive or negative charge, unpolarized, longitudinally polarized or transversely polarized target, different beam energies and different kinematic coverages (see Fig. 1.8).

A world-wide, long-term, experiment program was started in order to extract CFFs and study GPDs. This section will present a short overview of the current experimental landscape. More detailed information can be found in [25].

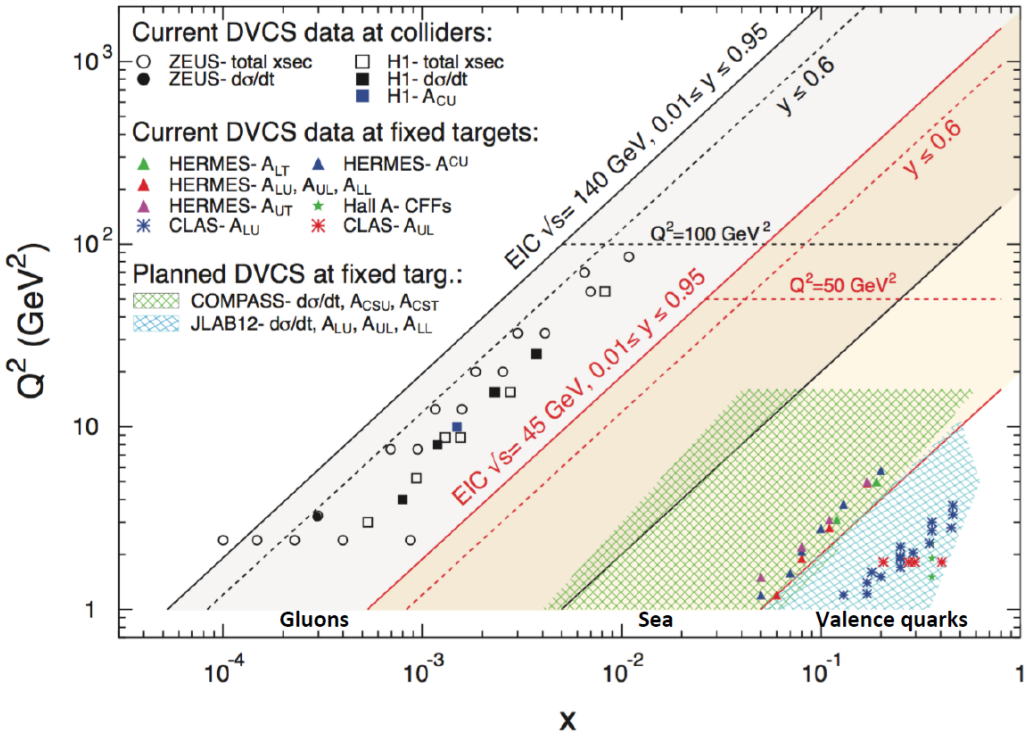

Figure 1.8: Experimental landscape (Q^2, x_{Bj}) for past and future experiments. (Figure extracted from [26]).

1.4.1 H1 and ZEUS (HERA)

The H1 and ZEUS experiments took place at the DESY laboratory (Hamburg, Germany), and were not dedicated to the sole measurement of DVCS cross sections. The HERA (Hadron-Elektron-Ring-Anlage) accelerator allowed to study high energy collisions between electrons (positrons) accelerated at 27 GeV, and protons accelerated at 920 GeV. Due to the very high energy, these experiments were able to measure pure DVCS cross sections with no contribution from the Bethe-Heitler, in kinematic regions dominated by sea quarks and gluons ($10^{-4} < x_{Bj} < 10^{-2}$).

In particular, the H1 and ZEUS experiments measured total DVCS cross sections [27, 28], their evolution as function of Q^2, W and t [29, 30, 31], and beam charge asymmetries [32, 33].

1.4.2 HERMES (HERA)

The HERMES experiment also took place at the HERA facility, between 1995 and 2007. Like H1 and ZEUS, this experiment was not dedicated to the sole study of DVCS. HERMES studied collisions between electrons (positrons) and a fixed gaseous target (protons), and did not measure total DVCS cross sections: only asymmetries, in the kinematic region defined by 1 GeV$^2 < Q^2 < 6$ GeV^2 and $0.04 < x_{Bj} < 0.2$.

What makes the HERMES experiment unique is that, even up to this date, it provided the most complete set of DVCS observables due to its flexibility: beam spin asymmetries [34, 35], beam charge asymmetries [36], beam charge-and-spin asymmetries [37, 38], target spin asymmetries and double spin asymmetries with a longitudinally polarized target [39, 40] and target spin asymmetries with a transversely polarized target [41]. It is worth noting that so far HERMES is the only experiment providing data with a transversely polarized target, but with low luminosity and limited exclusivity.

1.4.3 CLAS (JLab)

The CLAS (CEBAF Large Acceptance Spectrometer) detector is located in the Hall B of Jefferson Lab (Newport News, Virginia, USA). As its name indicates, the CLAS detector has the particularity of having

a large acceptance, covering a large solid angle, but with decreased luminosity compared to Hall A. In 2001, CLAS published the results of a non-dedicated DVCS experiment which measured the azimuthal angle dependence of beam spin asymmetries [42]. This was the starting point of an important campaign of DVCS dedicated experiments at JLab.

In 2005, the E01-113 experiment at CLAS used a polarized electron beam on an unpolarized liquid hydrogen target, and measured both unpolarized and beam helicity dependent DVCS cross sections, as well as beam spin asymmetries, in a kinematic range dominated by valence quarks, defined by $1\ \text{GeV}^2 < Q^2 < 4.7\ \text{GeV}^2$ and $0.1 < x_{Bj} < 0.6$ [43, 44]. High statistics and finely binned fourfold cross sections provided precious constraints for the GPD H_q.

In 2009, the E05-114 experiment used a 5.9 GeV polarized electron beam sent on a solid NH_3 target longitudinally polarized in order to measure beam spin asymmetries, target spin asymmetries and double spin asymmetries [45, 46], but with limited statistical precision.

1.4.4 Hall A (JLab)

The Jefferson Lab Hall A experiments are characterized by a small acceptance, but a very high luminosity for high precision results. In 2004, E00-110 was the very first experiment specifically dedicated to the measurement of DVCS cross sections. By sending a polarized electron beam on a liquid hydrogen target, the E00-110 experiment measured both unpolarized and beam helicity dependent DVCS cross sections at $x_{Bj} = 0.36$ with Q^2 ranging from 1.5 GeV^2 to 2.3 GeV^2, in the valence quark region. This experiment performed a scaling test of DVCS and showed that the factorization and leading twist dominance were valid even at relatively low Q^2 (see Fig. 1.9 and 1.10). The results published in 2006 [47] have recently been re-analyzed and the new results now supersede the previous ones [48].

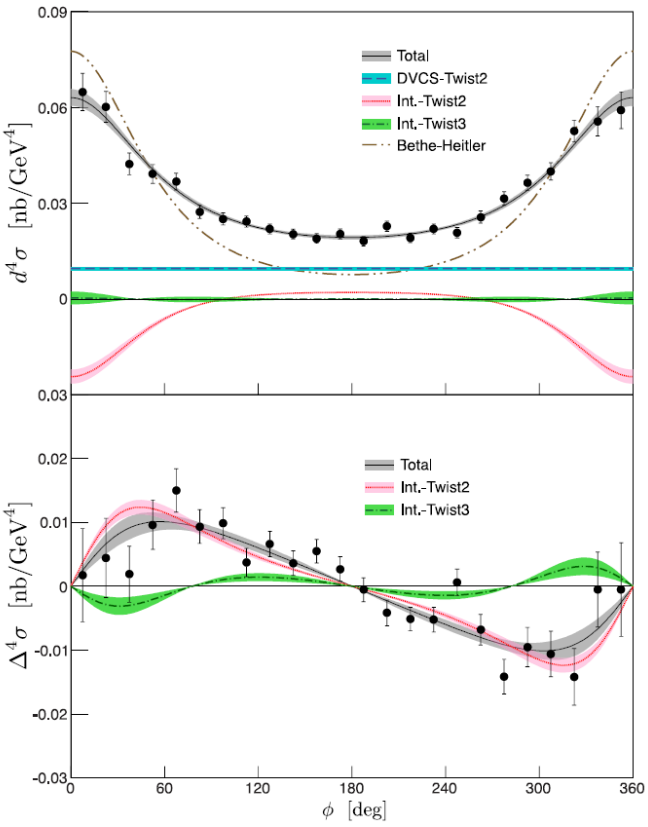

Figure 1.9: Unpolarized (top) and helicity-dependent (bottom) cross section measured in the experiment E00-110, with $Q^2 = 2.3\ \text{GeV}^2$, $x_{Bj} = 0.36$ and $-t = 0.32\ \text{GeV}^2$. The error bars and error bands are statistical uncertainties. The cross sections are dominated by the twist-2 contribution. (Figure extracted from [48]).

In the same year as E00-110, the experiment E03-106 used a liquid deuterium target instead and was the first experiment to study DVCS on the neutron, and provides the only currently available neutron results [49]. Neutrons are sensitive to E_q, the least known GPD, which is required to access quark orbital angular momentum through Ji's sum rule [4]. Neutron data also allow quark-flavor separation,

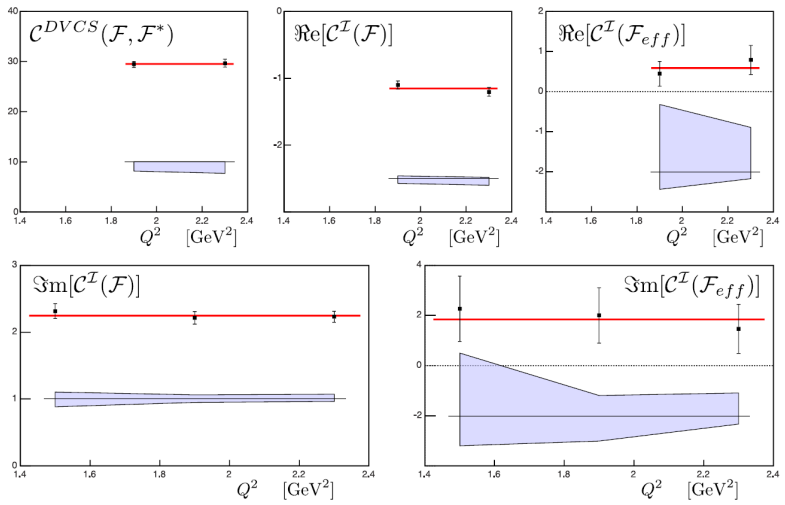

Figure 1.10: Combinations of effective CFFs extracted using the formalism developed in [23], integrated over t and plotted as a function of Q^2. The bands represent systematic uncertainties. The CFFs show no Q^2-dependence, which is a proof of scaling. (Figure extracted from [48]).

making neutron experiments invaluable. However, limited statistical precision was obtained because of the inherent difficulty of experiments on the neutron.

In 2010, a second DVCS experiment on the neutron has been performed (E08-025). Results for π^0 production have been published. The analysis for DVCS is almost complete and preliminary results are available [50].

1.4.5 COMPASS (SPS, CERN)

The COMPASS (Common Muon and Proton Apparatus for Structure and Spectroscopy) collaboration took DVCS data in 2016-2017 at CERN. Thanks to the SPS (Super Proton Synchrotron) accelerator, a polarized muon beam (μ^+ and μ^-) was sent on a 2-meters long liquid hydrogen target. The COMPASS program plans to measure charge and helicity-dependent cross sections in order to separate both the DVCS and interference cross-section terms, and the real and imaginary parts of CFF sensitive to the dominant GPD H_q. By measuring the x_{Bj} and t dependence of DVCS, COMPASS also plans to perform the tomography of the nucleon in a kinematic domain yet unexplored ($0.01 < x_{Bj} < 0.1$), between HERMES and JLab kinematic regions on the one hand, and H1 and ZEUS regions on the other hand [51].

1.5 The E12-06-114 experiment

The DVCS experiment E12-06-114 which is the subject of this document was performed at Jefferson Lab between 2014 and 2016. It is the very first experiment making use of the newly upgraded accelerator facility for the "12 GeV era" and is the natural extension of previous Hall A experiments at higher energies. Data were taken during the Fall 2014, Spring 2016, and Fall 2016. During this experiment, a longitudinally polarized electron beam was sent on an unpolarized liquid hydrogen target, and absolute polarized and unpolarized DVCS cross sections were measured for various (Q^2, x_{Bj}, t) settings. The kinematic regimes studied by this experiment are in the valence quarks region and are summarized in Fig. 1.11 and Tab. 1.1. This experiment is the first to ever cover these kinematics and its results will bring great value to the study of GPDs.

The experimental setup allowed for an extremely high luminosity, and as a consequence high DVCS counting rates. The large amount of statistics collected, combined with a good understanding of the detectors and the beam line components allow for high-precision results, which is the main asset of this experiment.

This experiment has two main goals [52]:

- to perform a scaling test with a larger Q^2 lever arm than previous Hall A experiments, taking advantage of the upgraded accelerator energy, for several values of x_{Bj} (see Fig. 1.11). This

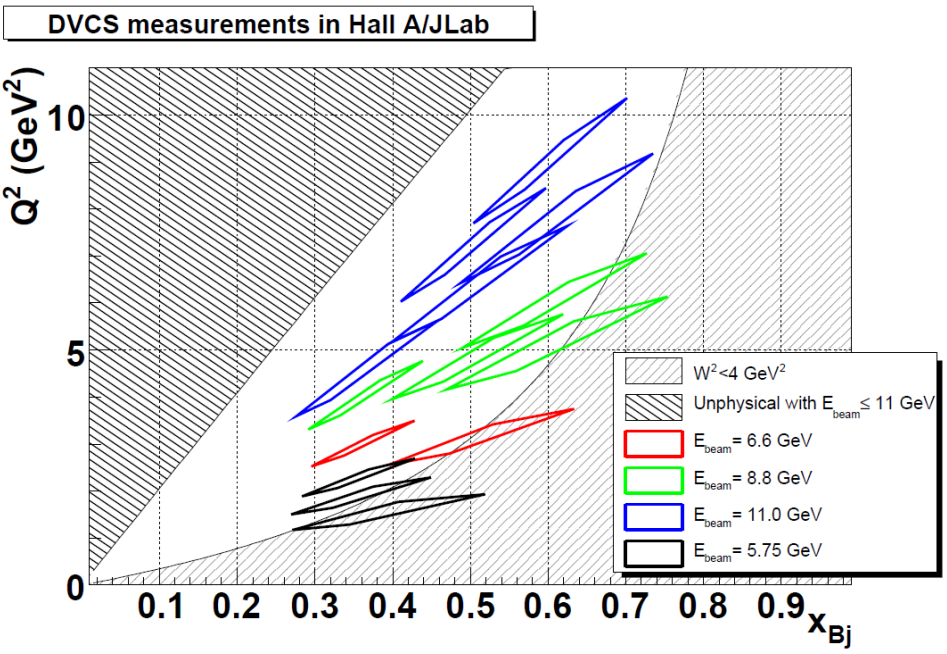

Figure 1.11: The kinematic regions (Q^2, x_{Bj}) explored by this DVCS experiment for different incoming beam energies are represented in red, green and blue. The regions in black were studied during the previous experiment in 2004, with $E_{beam} = 5.75$ GeV. The diamond shapes approximate the experiment acceptance. The limit of the unphysical region corresponds to the maximum possible Q^2 with respect to x_{Bj} for $E_{beam} = 11$ GeV. The $W^2 > 4$ GeV^2 limit is set to suppress contributions from resonances. (Figure extracted from [52]).

Kinematic setting	E_{beam} (GeV)	Q^2 (GeV^2)	x_{Bj}	t_{min} (GeV^2)	t_{max} (GeV^2)
36_1	7.383	3.200	0.36	-0.163	-0.69
36_2	8.521	3.600	0.36	-0.165	-0.54
36_3	10.591	4.470	0.36	-0.167	-0.54
48_1	4.487	2.700	0.48	-0.321	-0.58
48_2	8.851	4.365	0.48	-0.344	-0.72
48_3	8.847	5.334	0.48	-0.351	-0.71
48_4	10.992	6.900	0.48	-0.359	-0.96
60_1	8.521	5.541	0.60	-0.661	-1.47
60_2	8.521	6.100	0.60	-0.671	-1.24
60_3	10.591	8.400	0.60	-0.700	-1.41
60_4	10.591	9.000	0.60	-0.706	-1.28

Table 1.1: Summary of the experiment kinematic settings. The beam energies actually available in the accelerator at the time of the experiment differed slightly from the ones planed in Fig. 1.11. One will notice that kin60_2 and kin60_4 were not run between 2014 and 2016: they are scheduled for a later time.

will allow in particular to test the dominance of the handbag diagram, extract CFFs over large (Q^2, x_{Bj}, t) ranges, and study the t-dependence of CFFs as a function of x_{Bj};

- to separate the real and imaginary parts of the CFFs contributions to the DVCS amplitude, as can be seen in Eq. (1.56) and (1.57) in the leading twist approximation, where $d^4\overrightarrow{\sigma}$ and $d^4\overleftarrow{\sigma}$ refer to cross sections with longitudinally polarized beams of opposite helicity, and $\mathcal{R}e_{CFF}(I)$ and $\mathcal{I}m_{CFF}(I)$ refer to the contributions of the real and imaginary parts of the CFFs to the interference term. Eq. (1.56) is the unpolarized cross section while Eq. (1.57) is the polarized one.

$$\frac{d^4\overrightarrow{\sigma} + d^4\overleftarrow{\sigma}}{2} = |BH|^2 + |DVCS|^2 + \mathcal{R}e_{CFF}(I), \tag{1.56}$$

$$\frac{d^4\overrightarrow{\sigma} - d^4\overleftarrow{\sigma}}{2} = \mathcal{I}m_{CFF}(I). \tag{1.57}$$

A third goal of this experiment, which is not described in this document, is the measurement of the $ep \to ep\pi^0$ cross sections in the same kinematic regions as DVCS.

1.6 Planned future experiments

Although a lot of progress has been made in the study of GPDs, the task at hand is far from being over. This section will briefly present the planned future experiments for the study of GPDs.

1.6.1 CLAS12 (JLab)

Taking advantage of the JLab accelerator upgrade to 12 GeV, the new CLAS12 program is the natural extension of the CLAS program at 6 GeV. The E12-06-119 experiment will extend previous Hall B kinematic ranges (1.0 GeV^2 < Q^2 < 9 GeV^2 and $0.1 < x_{Bj} < 0.7$) and provide higher statistics for DVCS on the proton [53]. The kinematic range is very similar to that of experiment E12-06-114 in Hall A, and their results will be complementary, Hall B having a larger acceptance, while Hall A having a higher precision.

The CLAS12 program plans to measure a very complete set of observables, like HERMES: Unpolarized and beam helicity dependent cross sections, beam spin asymmetry, target spin and double spin asymmetry on longitudinally and transversely polarized target. It is worth mentioning that the single spin asymmetry for DVCS on the proton with a transversely polarized target is the most sensitive observable, not neutron related, to the elusive GPD E_q. So far, the only available DVCS data on transversely polarized target comes from HERMES. As such, the CLAS12 program on a transversely polarized target has been labeled as a high impact experiment, although it is currently conditionally approved, pending research and development on the target.

The E12-11-003 experiment plans to extend the currently very scarce data on the neutron by measuring beam spin asymmetry on a liquid deuterium target, with high accuracy [54]. The covered kinematic region will be defined by 1.5 GeV^2 < Q^2 < 6.5 GeV^2, $0.1 < x_{Bj} < 0.6$ and -1 GeV^2 < $t < -0.1$ GeV^2.

A proposal for experiment C12-15-004, pending approval, plans to measure target spin asymmetry and double spin asymmetry on the neutron with a longitudinally polarized deuterium target [55], complementing the data from experiment E05-114.

1.6.2 Hall C (JLab)

The Hall C experiment E12-13-010 [56] will measure unpolarized and beam helicity dependent DVCS cross sections on the proton. It will complement the current Hall A experiment E12-06-114 in two ways, thanks to the higher momentum reachable by the Hall C spectrometer: on one hand, it will measure cross sections at the same kinematic regions as the Hall A experiment but with different beam energies in order to separate the DVCS and Interference terms. On the other hand, it will also extend the kinematic regions of Hall A.

The range in Q^2 will be extended to higher values (up to 10 GeV^2) to further test the experimental validity of leading twist dominance at JLab energy, and improve the current understanding of higher twists effects. In particular, at high values of Q^2, the DVCS cross section is expected to largely deviate from the Bethe-Heitler, making this kinematic range all the more interesting. While CLAS12 will cover a similar range, Hall C allows for a higher luminosity, and thus higher precision results.

The range in x_{Bj} will be extended to the lower value of 0.2 in order to overlap with data from CLAS, CLAS12 and COMPASS, in kinematic regions where these experiments have similarly high statistics. This will allow for cross checks between experiments with very different setups.

1.6.3 EIC

The desire to understand the internal structure of matter will culminate with the future Electron Ion Collider (EIC). The EIC will collide electrons and protons/ions with center of mass energies varying between 20 and 140 GeV. The lever arms in Q^2 and x_{Bj} will be extremely large (see Fig. 1.8), allowing to study the internal structure of nucleons in the regime dominated by sea quarks and gluons, or in the transition between the valence and sea quarks regimes. The electron and nucleon beams will be polarized, allowing to measure various observables of interest for the study of GPDs. In particular, a transversely polarized proton beam will allow to access the elusive GPD E. A high luminosity (10^{34} cm^{-2}·s^{-1}) and hermetic detectors will allow to perform high precision measurements of finely binned DVCS cross sections and asymmetries. Furthermore, various DVMP measurements will allow a flavor separation of the GPDs.

The EIC is proposed to be constructed either at the Jefferson Laboratory or the Brookhaven National Laboratory. "Embodying the vision for reaching the next QCD frontier", the unique features of the EIC will allow to address several topics at the limit of our current understanding of QCD [26]:

- the spatial and momentum distribution of sea quarks and gluons, and their spin, in the nucleon;
- the saturation density and regime of gluons;
- the nuclear environment effect on quark and gluon interactions in the nuclei (EMC effect).

1.6.4 DDVCS (JLab)

The DVCS process has the limitation of being unable to access the full phase space dependence of GPDs. The real part of CFFs probes GPDs integrated over x, while the imaginary part accesses the GPDs only in the phase space diagonal where the quark momentum fraction x and the skewness ξ obey the constrain $x = \pm\xi$. This is a large restriction in the study of GPDs. However, in the Double Deeply Virtual Compton Scattering (DDVCS) process, the emitted photon is virtual as well. This, unlike DVCS, allows to directly explore GPDs in the out-of-diagonal phase space $x \neq \pm\xi$, which is extremely valuable for constraining GPDs and nucleon imaging. The study of the feasibility of a DDVCS experiment at JLab is currently ongoing [57].

Chapter 2

The experimental setup

The Thomas Jefferson National Accelerator Facility, commonly called Jefferson Lab, or JLab, is located in Newport News (Virginia, USA). It was founded in 1984 with the mission of studying the internal structure of nuclear matter. To carry out this mission, a Continuous Electron Beam Accelerator Facility (CEBAF) was built and can provide a longitudinally polarized electron beam simultaneously to three experimental Halls (A, B and C) with a luminosity above 10^{38} cm^{-2}·s^{-1}. In 2014, a fourth experimental Hall (D) was added, and CEBAF's maximum energy was ramped up from 6 GeV to 12 GeV [58]. The DVCS experiment described here took place in the Hall A of Jefferson Lab.

First, a brief introduction of CEBAF will be given. Then, more details about the Hall A specific instrumentation will be provided, followed by a presentation of the DVCS experimental setup.

2.1 A Continuous Electron Beam Accelerator Facility

The electrons accelerated by the facility are provided by a photo-cathode gun placed in an ultra-vacuum chamber: the injector. The gun consists of a strained gallium arsenide cathode, illuminated by a 250 MHz Ti-Sapphire laser operated at 850 nm. The electrons escaping from the cathode are then extracted by a difference of potential, accelerated to 45 MeV by a first set of Radio-Frequency (RF) cavities, and sent to the accelerator. The laser is circularly polarized by a Pockels cell in order to provide a polarized electron beam. The beam helicity is flipped at a frequency of 30 Hz by varying the voltage applied to the Pockels cell [59]. The polarization is measured at the injector by a Mott polarimeter [60], and the polarization vector can be oriented by a Wien filter [61]. In order to provide the electron beam to the four experimental halls simultaneously, the injector cathode is, in fact, illuminated by four different lasers: one for each hall. Each laser has a phase offset with respect to the others to allow the electron beams they generate to be disentangled by an RF separator. The beam current send to each experimental Hall can also be controlled independently. At maximum energy, the combined maximum beam current sent to the Halls is 90 μA.

The accelerator is made of two linacs, comprising 25 cryo-modules each, and two sets of 5 re-circulation arcs which allow the electrons to be accelerated several times in each linac (see figure 2.1). Each cryo-module is made of 8 RF cavities made of pure Niobium. The electromagnetic field in the cavities is synchronized with the total frequency of the injector (all four lasers combined) which is equal to $4 \times 250 = 1000$ MHz. Each linac increases the electron beam energy up to $\sim$1.1 GeV, so that the maximum beam energy for Hall A, B and C is reached after 5 passes through the accelerator ($\sim$11 GeV), and 5.5 passes for Hall D (12 GeV). In each linac, the electrons are all accelerated together in the same beam pipe not withstanding their different energies which depend on the number of passes through the accelerator. However, at the end of each linac, an electromagnetic separator sort the electrons by energy to the 5 different re-circulation arcs. The electrons with less energy are bent towards the upper re-circulation arcs, whereas the electrons with more energy have a far less bent trajectory and are sent to the lower re-circulation arcs (see Fig. 2.1). At the end of the South linac, the RF separator and a set of magnets allow to extract the electron beam to send it to the experimental Halls A, B and C. At maximum energy, i.e. after 5 passes through the accelerator, all three experimental Halls can be provided with an electron beam at the same time. However, if the electron beam is extracted at a lesser energy (1 to 4 passes trough the accelerator), then only one experimental hall at a time can be be provided with said energy. But all three halls can still receive the beam simultaneously provided they use electrons of different energies.

Hall D works independently from the three other Halls since it is located at the end of the North linac. After 5.5 passes through the accelerator, the electromagnetic separator at the end of the North linac extracts the electron beam towards Hall D instead of the recirculation arcs (see Fig. 2.1) [58].

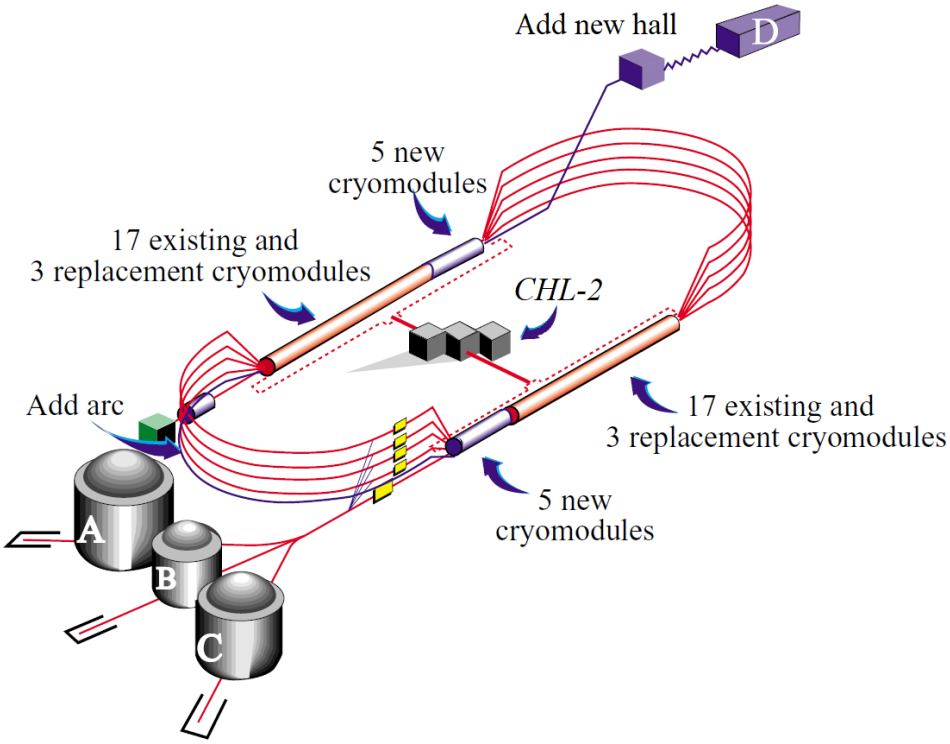

Figure 2.1: Jefferson Lab was upgraded in 2014. 5 cryo-modules have been added to each linac and a fifth re-circulation arc was constructed between the South and North linac in order to ramp the accelerator energy up to 12 GeV. A second cryogenic plant (CHL-2) was added to provide for the increased need of cryogenic power. A new experimental Hall (D) was also built at the end of the North linac.

2.2 The Hall A instrumentation

For the experiments to be able to yield high precision results, a very good understanding of the electron beam and the target is required. To provide such knowledge, the Hall A beam line is instrumented with several detectors dedicated to monitoring the electron beam, and the target has been designed to allow a careful control of its properties. Detailed information about the beam line and the detectors are given in [62] and [63].

2.2.1 The beam line

The Hall A beam line instrumentation allows the measurements of the following properties of the electron beam: current, position, polarization, and energy.

2.2.1.1 The Beam Current Monitors

The Beam Current Monitors (BCMs) are two RF cavities located at the entrance of the experimental Hall (see Fig. 2.2). These cavities are stainless steel cylindrical waveguides, tuned to the frequency of the electron beam, which output a voltage proportional to the beam current. In order to calibrate the RF cavities, a device called Unser has been installed between them. The Unser is a Parametric Current Transformer which also outputs a voltage proportional to the beam current. The Unser is calibrated by passing a known current through a wire in the beam pipe, and it can then provide an absolute reference for the calibration of the RF cavities against the beam current. The Unser itself cannot be used to monitor the electron beam current since its output signal suffers from a significant drift over time, on a time scale of a few minutes.

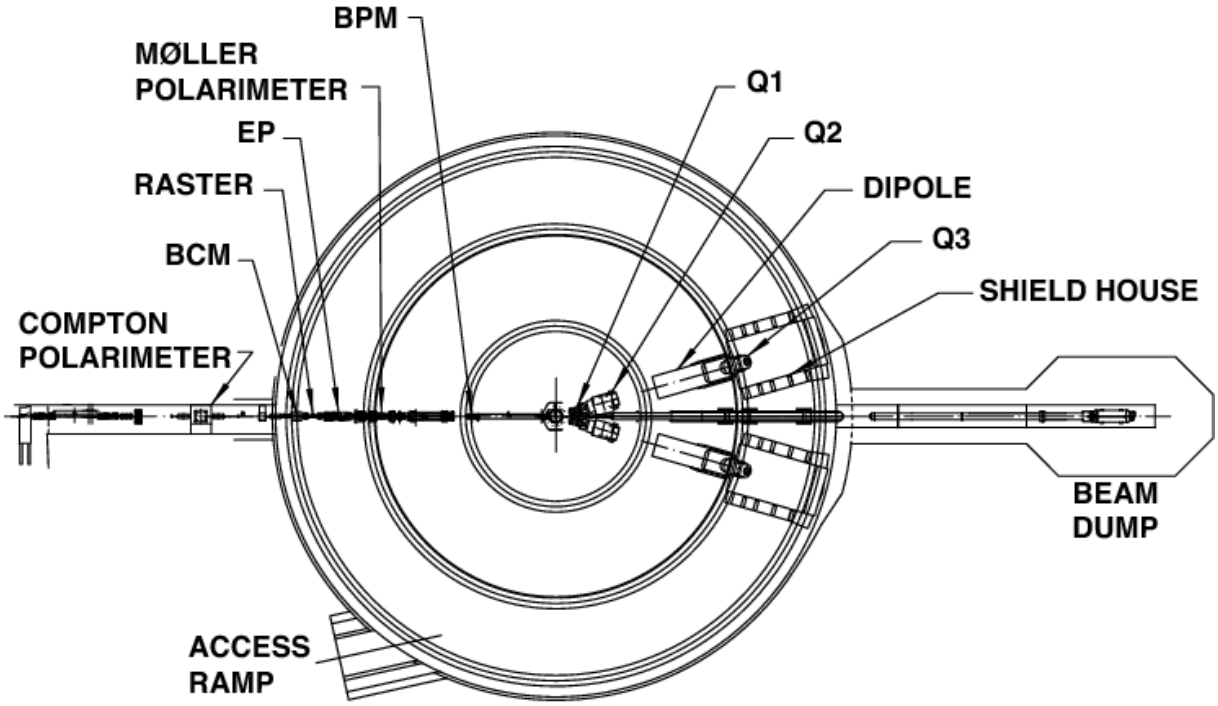

Figure 2.2: Schematic representation of the Hall A beam line.

The two RF cavities and the Unser are located in a temperature-stabilized box providing magnetic shielding in order to yield a stable beam current measurement with low noise. This measurement has also the property of being non-invasive.

Because of the wide range of beam current which can be used in Hall A, the BCMs are connected to various electronics with different amplification factors (1, 3 or 10), which are linear over different ranges of beam current. The calibration of the BCMs showed that the electronics with amplification factors 3 or 10 could be used for this experiment [64].

2.2.1.2 The Beam Position Monitors

The Beam Position Monitors (BPMs) are two devices centered at 7.524 m and 1.286 m upstream of the target (see Fig. 2.2). A BPM is made of two pairs of antennas, each antenna of the same pair being located on diametrically opposite sides of the beam pipe. The electron beam induces a current in each antenna, and by measuring the ratio of the difference of voltages over the sum of voltages induced in diametrically opposed antennas, one can determine the transverse position of the beam centroid. The relative position of the beam centroid can be measured with a precision of 100 μm for beam currents above 1 μA. This measurement is non-invasive.

The BPMs are calibrated [65] against wire scanners, called Harps, located close to each BPM. Each Harp is made of 3 wires, whose positions are known within 200 μm and which are moved transversely across the beam pipe. They provide a signal when they cross the electron beam, thus providing absolute references for the calibration of the BPMs.

2.2.1.3 The polarimeters

Two polarimetry devices allow the measurement of the longitudinal beam polarization in Hall A: the Compton polarimeter and the Møller polarimeter.

The Compton polarimeter is located just before the entrance of the experimental Hall A (see Fig. 2.2). It is installed in a chicane: if the polarimeter is not used, the chicane is by-passed entirely. If it is used, the electron beam is deflected inside the chicane by a set of two dipoles (see Fig. 2.3). The electrons can then interact with photons (Compton scattering) in a Fabry-Pérot cavity, where a circularly polarized Nd:YaG laser operated at λ=1064 nm is amplified up to 2 kW. The scattered photons are then detected in a $PbWO_4$ calorimeter, while the scattered electrons are detected in a silicon strip detector. During the summer 2016, additional shielding has been installed in front of the photon detector to reduce the background from synchrotron radiation.

The electron beam polarization is extracted by measuring the counting rate asymmetry for opposite beam helicity as shown in Eq. (2.1) and (2.2):

$$A_{exp} = \frac{N^+ - N^-}{N^+ + N^-}, \tag{2.1}$$

$$P_e = \frac{A_{exp}}{P_\gamma A_{th}}. \tag{2.2}$$

where N^+ (N^-) is the number of Compton scattering events detected with positive (negative) helicity, P_γ is the photon beam polarization, and A_{th} is the analyzing power [66].

Only a small fraction of the electrons actually scatter off the photons. The electrons that did not interact are re-injected in the beam line by another set of two dipoles located at the exit of the Compton chicane and sent towards the Hall A target (see Fig. 2.3). For this reason, this polarization measurement method is non-invasive and can be perform simultaneously to the DVCS experiment, thus providing a continuous measurement of the beam longitudinal polarization.

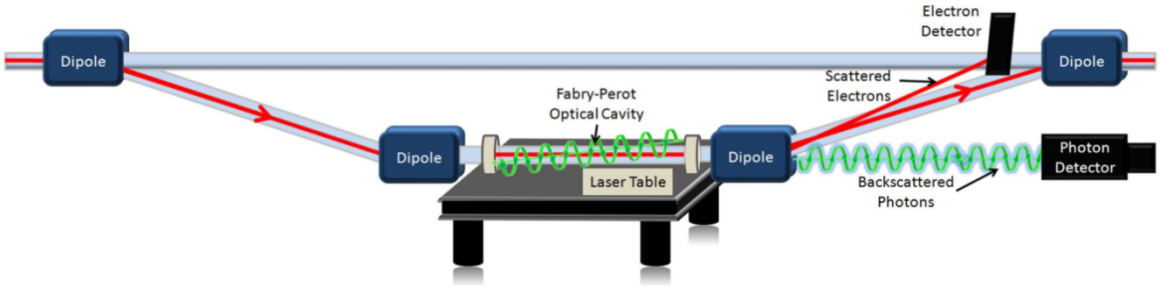

Figure 2.3: Schematic representation of the Hall A Compton Polarimeter.

The Møller polarimeter is located upstream of the BPMs in the experimental Hall A (see Fig. 2.2). There, the electrons of the beam scatter off atomic electrons (Møller scattering) of a ferromagnetic target polarized in a 24 mT magnetic field. The scattered electrons are then detected in a spectrometer made of three quadrupoles and a dipole, and PbO calorimeter crystals, divided into two arms in order to detect the two scattered electrons in coincidence (see Fig. 2.4).

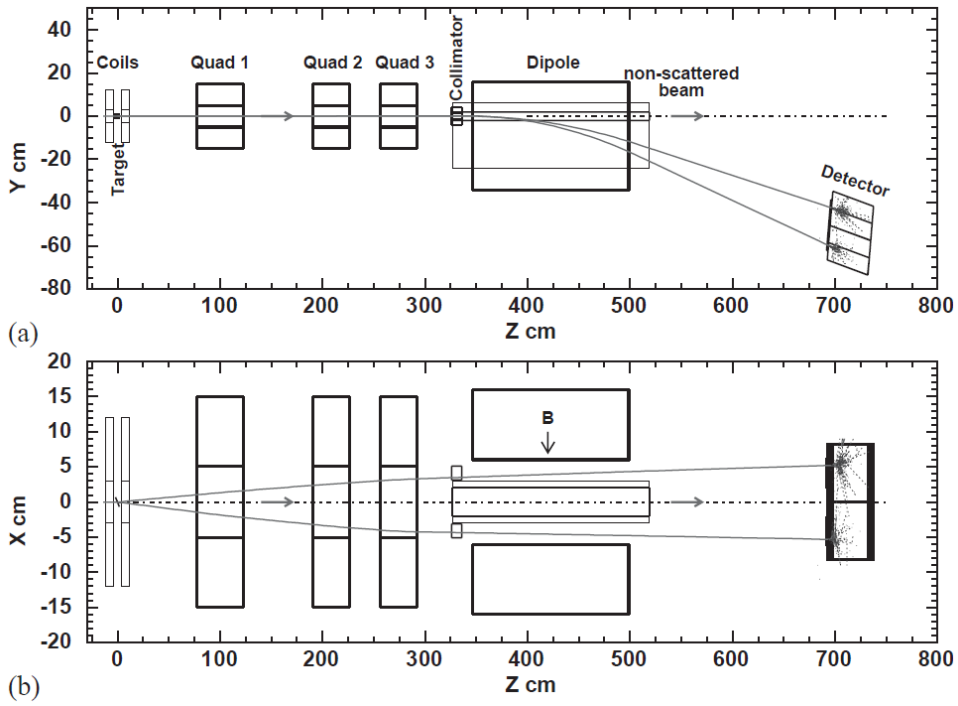

Figure 2.4: Schematic representation of the Hall A Møller Polarimeter. (a): side view. (b): top view.

Similarly to the Compton polarimeter, the beam polarization can here also be extracted by measuring counting rate asymmetry for opposite beam helicity. However, because the ferromagnetic target needs to be inserted in the beam line, this polarization measurement is invasive and cannot be performed simultaneously to the DVCS experiment. It needs dedicated beam time. The typical beam polarization delivered to Hall A is about $\sim 80\%$.

Both methods are complementary as they are not sensitive to the same systematic uncertainties. The dominant uncertainty of the Møller measurement comes from the target polarization, while for the Compton, it is its low analyzing power. The Møller also has the disadvantage that the electron beam current needs to be lowered down to 0.5 μA, which might change the beam polarization. On the other hand, the Compton method is sensitive to helicity-correlated beam parameters, to which the Møller is insensitive.

2.2.1.4 The beam energy measurement

An absolute measurement of the beam energy can be provided by what is called 'the Arc method' [62]: Hall A is connected to the accelerator by a 40 m arc section, and the beam energy can be determined by measuring its deflection in this beam line section. More specifically, the beam momentum ρ (in GeV), the field integral of the eight dipoles in the arc section $\int \vec{B} \cdot \vec{dl}$ (in Tm) and the bend angle through the arc section θ (in radians) are correlated through Eq. (2.3), with k = 0.299792 GeV·rad·T^{-1}·m^{-1}:

$$\rho = k \frac{\int \vec{B} \cdot \vec{dl}}{\theta}. \tag{2.3}$$

A simultaneous measurement of the magnetic field integral and of the beam bend angle in the arc are necessary. Wire scanners provide the measurement of the bending angle. However, the magnetic field of the dipoles in the arc cannot be measured directly. Instead, a ninth dipole located in another room, strictly identical to the eight others and powered in series, provides the required field measurement.

Because of the wire scanners and the fact that this measurement is performed with the beam tuned in dispersive mode (the quadrupoles are turned off), this measurement method is invasive.

2.2.1.5 The raster

Because of its high intensity in Hall A and its small transverse section, the electron beam will locally heat the target and possibly change its properties (cryogenic target boiling), or even damage it (solid target melting). In order to prevent these issues, a device called raster has been installed upstream of the target and the BPMs (see Fig. 2.2). The raster is made of two sets of two dipoles synchronized with each other, which deflect the beam at 25 kHz to spread the heat on the target. During this DVCS experiment, the typical spread was a 2 mm $\times$ 2 mm square at the target.

2.2.2 The target system

The target system is encompassed in a cylindrical scattering vacuum chamber, 1143 mm in diameter. Inside this vacuum chamber, several targets are mounted on a ladder controlled remotely which allows to quickly switch from one target to another during the experiment. The ladder is comprised of:

- three cryogenic targets: they are cylindrical aluminum cells, 63.5 mm in diameter and 4 cm or 15 cm long, designed to be filled with either Liquid Hydrogen (LH_2), Liquid Deuterium (LD_2) or gaseous helium. During this DVCS experiment, out of the three cells, only the 15 cm LH_2 was used. The operating temperature and pressure of this cell are 19 K and 0.17 MPa, with a density of about 0.0723 g·cm^{-3}. The liquid hydrogen is cooled by circulating it through a heat exchanger with liquid helium supplied at 15 K. The maximum cooling power available is 1 kW, which allows the electron beam current to be used up to 130 μA. Indeed, at this current, the beam deposit 700 W in the target, and upon adding the contributions from the fans and the heaters used to stabilize the target temperature, the total heat load approaches 1 kW;

- two dummy targets, which are empty replicas of the cryogenic cells. They are used to study the effects of the target walls;

- an optic target, which is made of five 1-mm thick carbon foils spaced by 3.75 cm from each other. This target is mainly used to perform the optics calibration of the spectrometer. Between Spring and Fall 2016, four additional foils were added to improve the optics calibration;

- an empty target, which is used to reduce radiation in the Hall during invasive beam studies;
- a carbon hole target, which is made of a single carbon foil with a 2-mm diameter hole at its center. This target is used to position the beam at the center of the target;
- a BeO target: this target glows when hit by the beam, which allows a direct visualization of the beam position on the target thanks to a camera. This target is used during the beam centering procedure;
- a carbon target, which is made of a single 1-mm thick carbon foil;
- a target which is made of an empty aluminum cylinder. This target is used to check that the beam is not slanted.

2.3 The DVCS experiment apparatus

Hall A is permanently equipped with two High Resolution Spectrometers (HRS), one on either side of the beam, whose polarizations can be switched to detect either negatively or positively charged particles. For this DVCS experiment, the scattered electrons are detected in the Left HRS (LHRS), while the Right HRS (RHRS) is not used.

In order to detect the photon emitted by the DVCS process, a custom electromagnetic calorimeter has been built and installed between the beam pipe downstream of the target, and the RHRS (see Fig. 2.5).

Finally, the recoil proton is not detected. However, it is identified thanks to the $M_X^2 = (e+p-e'-\gamma)^2$ missing mass technique which will be detailed in section 4.6.3.

The detectors and the data acquisition system of the experiment will now be presented in more detail.

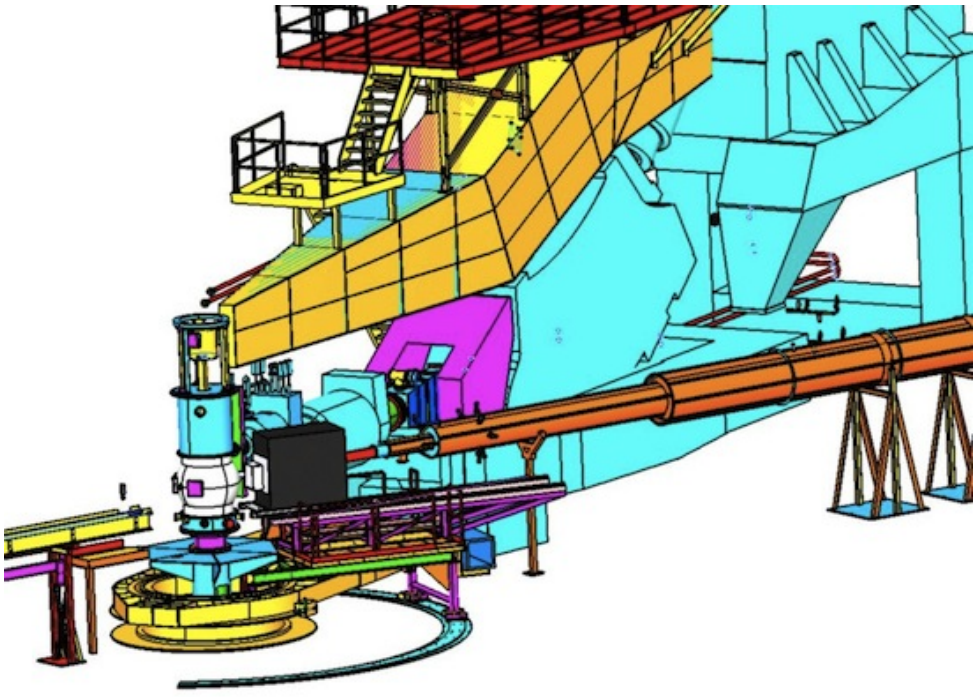

Figure 2.5: Schematic representation of the DVCS experimental setup. The target system is represented as the white sphere while the beam pipe downstream of the target is represented in orange. The scattered electrons are detected in the Left High Resolution Spectrometer (light blue) and the emitted photons are detected in a custom electromagnetic calorimeter (black). The recoil protons are not detected.

2.3.1 The High Resolution Spectrometer

The High Resolution Spectrometer is made of a set of superconducting magnets bending the charged particles trajectory at 45° upward towards a detector package. The magnet set has a QQD_nQ design: two

quadrupoles followed by an indexed dipole, followed by a final quadrupole. The quadrupoles improve the performances of the spectrometer, acceptance and resolution wise, and the dipole selects the momentum of the particles sent towards the detector package. The value of this selected momentum is called "central momentum" of the spectrometer. One will notice that compared to a uniform-field dipole, the indexed one has an additional focusing effect which allowed to reduce the number of quadrupoles compared to the initial $QQQDQQ$ design.

The spectrometer has a momentum range between 0.3 and 4.0 GeV/c, and an acceptance of $\pm 4.5\%$ relative to its central momentum. Its angular acceptance is ± 30 mr horizontally and ± 60 mr vertically.

In the detector package (see Fig. 2.6), the charged particles first travel through two sets of Vertical Drift Chambers (VDCs). The VDCs are inclined at an angle of 45° with respect to the nominal particle trajectory. Each of them is made of two wire planes oriented at 90° to one another, and are filled with an argon (62%) - ethane (38%) gaz mixture. The VDCs provide tracking information about the charged particles, which then allow to reconstruct the event vertex, the particle momentum, and the particle scattering angles at the target through the use of an optics matrix. The spectrometer optics will be explained in more detail in section 3.2.2.

The charged particles then travel through two sets of scintillators (S0 and S2) and a gas Cherenkov detector, which are used for triggering. S0 is made of a single 10 mm thick plastic paddle, while S2 is made of sixteen 5 mm thin ones. Each scintillator paddle is viewed by two photomultipliers (PMTs). The time resolution per plane is approximately 0.30 ns.

The gas Cherenkov detector is located between S0 and S2. It is filled with CO_2 at atmospheric pressure, and it has 10 spherical mirrors each viewed by a PMT. Moreover, the detector has a threshold for pions at 4.8 GeV/c while it is 17 MeV/c for electrons, so that it also allows to discriminate electrons from pions.

The final detectors of the spectrometer are two layers of electromagnetic calorimeters called Pion Rejectors (PR). Both layers are made of 34 lead glass blocks of dimensions 15 cm $\times$ 15 cm $\times$ 30 cm, optically coupled to PMTs. As their names suggest, these detectors are used to discriminate electrons from pions, as electrons and hadrons will not deposit the same amount of energy in them. Combining the gas Cherenkov detector and the Pion Rejectors provides a pion suppression factor of 2×10^5 above 2 GeV/c.

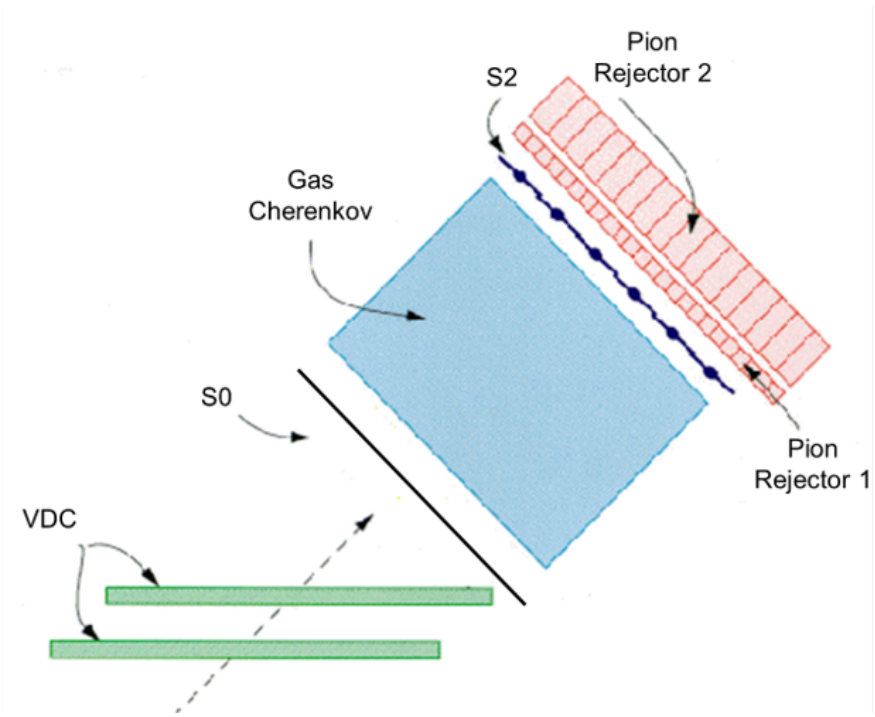

Figure 2.6: Schematic representation of the spectrometer detector package.

2.3.2 The DVCS electromagnetic calorimeter

The DVCS electromagnetic calorimeter is made of 208 PbF_2 crystals laid out in a 13 × 16 rectangular pattern (see Fig. 2.7). They are 3 cm × 3 cm × 18.6 cm large, which corresponds to 20 radiation lengths, and they are wrapped in Tyvek© (internal wrapping) and Tedlar© (external wrapping) to avoid light transmission from one block to another. Each crystal is optically coupled to a fast response PMT (Hamamatsu R7700), capacitively coupled to a pre-amplifier. The choices for this design are motivated by the following properties [52]:

- PbF_2 is a radiation hard, Cherenkov medium. Thanks to the absence of scintillation light, the calorimeter is insensitive to low energy particles. Moreover, since Cherenkov light pulses are short, coupled with fast response PMTs and appropriate electronics, it allows to greatly minimize pile-up;
- the short radiation length minimizes fluctuations in light collection;
- the small Molière radius (2.2 cm) minimizes energy leakage at the edges of the calorimeter. A shower will be contained within nine adjacent blocks, with 90% of the energy in the central block. This also allows the separation of showers from the π^0 decay into two photons without requiring the calorimeter to be too far away from the target, as this distance is chosen so that the two showers are separated by at least 9 cm (3 blocks);
- because of the large number of pile-ups from low energy γ-rays, the total energy deposited in the calorimeter averaged over time can be rather consequent. However, since the averaged pile-ups create a continuous signal, they are filtered by the capacitive coupling.

On the other hand, the energy resolution of the PbF_2 blocks is rather low, with only 1-2 photo-electron detected per MeV. The energy resolution of the calorimeter is the main limiting factor of this experiment.

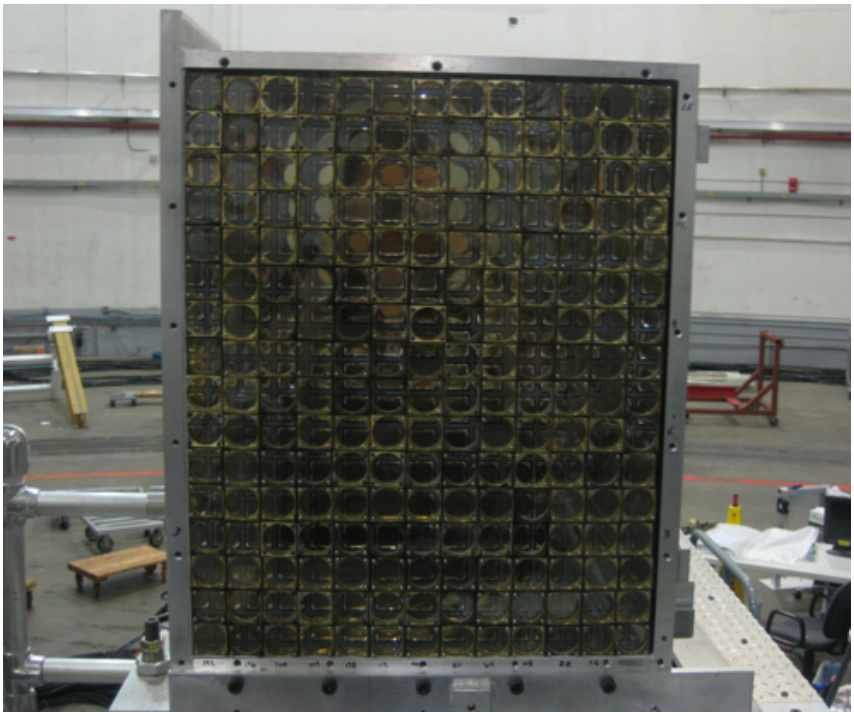

Figure 2.7: Picture of the front face of the DVCS electromagnetic calorimeter.

Several layers of shielding have been added in order to prevent damage to the calorimeter and reduce the background:

- the calorimeter is installed in a light-tight black box in order to protect the PMTs from being damaged by direct exposure to the Hall lighting;
- beam line shielding has been added in order to protect the calorimeter from radiation produced by multiple scattering from the target chamber or the beam pipes (see Fig. 2.8). The “nose shielding” is composed of a triangular and a rectangular tungsten plate located close to the scattering chamber.

The triangular plate protects the first column of the calorimeter closest to the beam line from particles coming from the target, while the rectangular plate protects the side of the calorimeter from radiation coming from the beam pipe. An additional lead half cylinder placed further downstream completes the shielding provided by the rectangular tungsten plate;

- in order to limit the number of low energy γ-rays hitting the calorimeter, two rectangular plastic plates are installed in front of the calorimeter, one of them being inside of the black box.

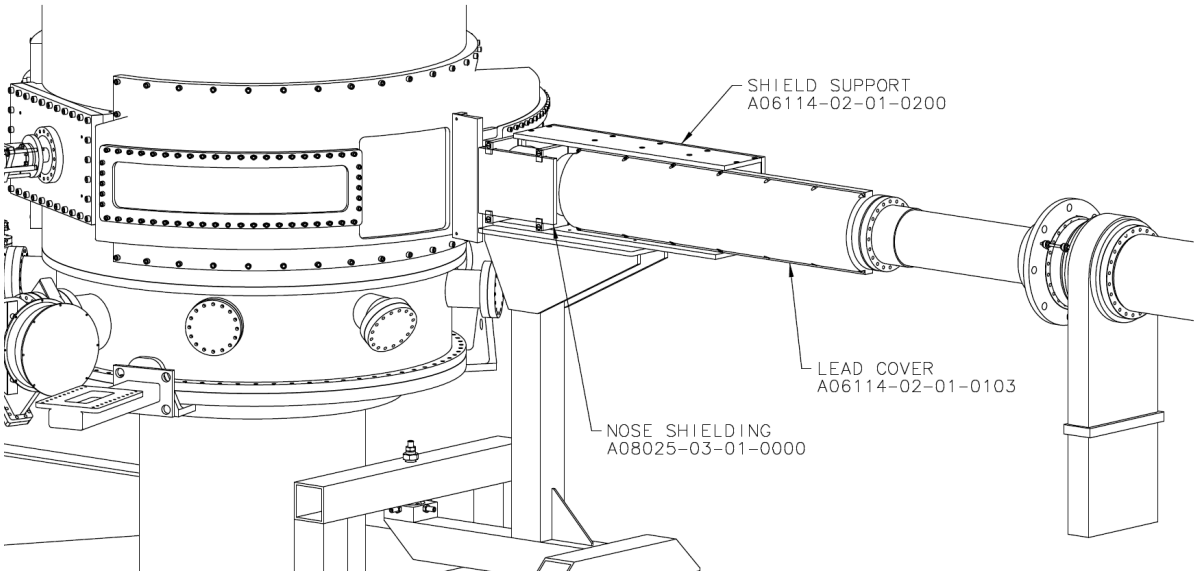

Figure 2.8: Sketch of the beam line shielding protecting the calorimeter. (Figure extracted from [67]).

2.3.3 The Data Acquisition (DAQ)

In addition to a custom detector, this DVCS experiment needs a specific data acquisition system in order to deal with background noise and high counting rates. First, the standard Hall A data acquisition system will be briefly presented, and then some additional details will be given about the DVCS custom electronics and trigger.

2.3.3.1 The Hall A data acquisition system

The DAQ is controlled by a software called CODA (CEBAF Online Data Acquisition), which has been developed at JLab. It is a toolkit of software components from which data acquisition systems can be built and customized.

As a general rule, each detector is connected to Analog Digital Converters (ADCs), and in some cases Time-to-Digital Converters (TDCs) and/or scalers, which are gathered into VME crates, one or more crates per detector depending on the number of channels the detector has. Each VME crate is controlled by a Read-Out Controller (ROC), which is connected to the Trigger Supervisor (TS) which controls several triggers depending on the experiment settings. When a trigger is fired, the Trigger Supervisor requires the recording of the data. The ROCs gather the data from the VME crates, buffer them in memory, and then send these buffers to the Event Builder (EB). The EB builds the event from the pieces sent by several ROCs, and then passes it to the Event Recorder (ER) which writes the data on a local disk. These data are subsequently copied to the Mass Storage tape Silo (MSS) for long term storage, and erased from the local disk.

The Trigger Supervisor will accept a new trigger only when all the ROCs are available. As long as one or more ROCs are busy processing data, a VETO is sent to the Trigger Supervisor which will not accept any new trigger, resulting in acquisition dead time.

2.3.3.2 The Analog Ring Samplers (ARS)

Because of the high luminosity of the experiment, and the proximity of the calorimeter to the beam pipe, high event rates and pile-ups are expected. As a consequence, a specific DAQ device has been designed

for the calorimeter, based on a chip developed at the CEA of Saclay (France): the Analog Ring Sampler (ARS) [68].

Each of the 208 calorimeter channel is connected to an ARS, which samples the data at 1 GHz. An ARS contains a circular array of 128 capacitors, and each 1 ns, the ARS stores the data in the next capacitor of the array. Each capacitor is thus overwritten every 128 ns, and at any point in time, a 128 ns data sample is stored in the ARS. This 1 GHz sampling allows to separate two pile-up photons as long as they are separated by at least 4 ns (see Fig. 2.9).

When a trigger is fired and the Trigger Supervisor requires the recording of the data, the data sampling by the ARS array is stopped, and the content of the capacitors is digitized, read-out and recorded. However, the ARS array generate a large amount of data which makes the digitization process quite lengthy and creates a large dead time of 128 μs.

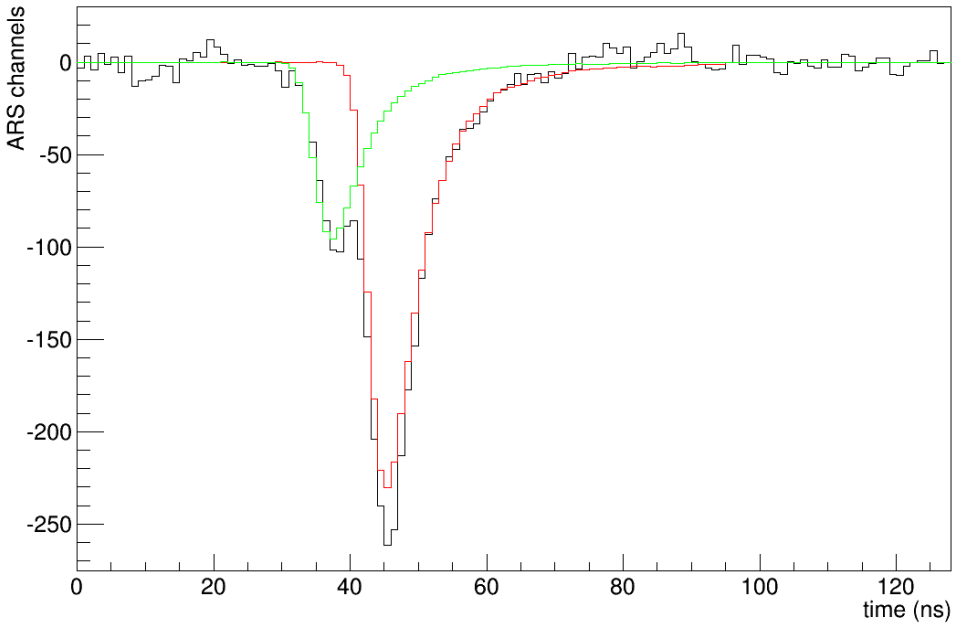

Figure 2.9: Example of an ARS signal with two piled-up photons. The black histogram is the ARS signal. The green and red histograms are the fitted signals from the two photons.

2.3.3.3 The trigger system

In order to minimize the acquisition dead time, a two-level trigger has been designed. The first level is a coincidence between the Scintillator S2 and the Cherenkov detector of the spectrometer. The second level is a coincidence between the spectrometer and the calorimeter.

The signal from each block of the calorimeter is continuously sampled by an ARS, but a copy of this signal is also sent to a flash-ADC which integrates it over 128 ns. When the first level trigger is fired, the Trigger Supervisor sends a STOP signal to the ARS array, stopping their sampling of the data, and orders the read-out of the flash-ADCs. Then, the sum of the signals integrated by the flash-ADCs over every 2x2 neighboring calorimeter blocks is computed. If at least one of the sums yields a result higher than a set threshold, a VALID signal is sent to the Trigger Supervisor which then requires the read-out of the event from the ARS array.

If the first trigger level, from the spectrometer, is not validated by the second level, from the calorimeter, a Fast Clear signal is issued to the ARS array, which are reset before resuming the data sampling. If a Fast Clear is issued, the total acquisition dead time is then only 500 ns, which is negligible compared to 128 μs.

Chapter 3

Calibration of detectors

Prior to the data analysis and the extraction of DVCS cross sections, the calibration of the detectors is a critical step that requires utmost attention. The calibration is extremely important to control the results and minimize as much as possible systematic uncertainties.

In the first part of this chapter, the calibration of a beam line component, the raster, will be presented. Then, the second part will deal with the High Resolution Spectrometer, with particular emphasis on its optics. Finally, a detailed description about the energy calibration of the calorimeter will be provided.

3.1 Beam line calibration

The calibration of most of the beam line components has been briefly described in the previous chapter. This section will only focus on the raster calibration, which has been a part of my work.

3.1.1 Raster calibration

As described in section 2.2.1.5, the raster is made of two sets of two dipoles synchronized with each other which deflect the beam at high frequency orthogonally to the target in a plane (x, y). However, the BPM electronics are not fast enough to track the beam position when deflected by the raster and they can only provide averaged values. Because of this, the BPMs reading cannot be relied on directly to measure the beam position at the target. Instead, the current in the raster coils must be used. The goal of the calibration is to compute coefficients allowing to reconstruct the orthogonal vertex position (v_x, v_y) from the current in the raster coils [69].

The raster calibration is performed against the BPMs, and relies on the assumption that the two sets of dipoles are synchronized with each other so that they may be assimilated to a single set. As the calibration method is identical for both axis x and y, and for both BPMs, the description will be limited to one BPM for the x axis.

If $\overline{I_x}$ and dI_x are respectively the mean value and the standard deviation of the current in the raster along x, and $\overline{x_{beam}}$ and dx_{beam} are respectively the mean value and the standard deviation of the beam position in x measured by the BPM, then the raster calibration computes a slope a and an offset b as shown in Eq. (3.1) and (3.2):

$$a = \frac{dx_{beam}}{dI_x}, \tag{3.1}$$

$$b = \overline{x_{beam}} - \overline{I_x}\frac{dx_{beam}}{dI_x}. \tag{3.2}$$

In Eq. (3.1), using the standard deviations dI_x and dx_{beam} allows to compute the dependence of the beam position on the raster current despite the BPM electronics being too slow compared to the raster. In Eq. (3.2), using the mean values $\overline{I_x}$ and $\overline{x_{beam}}$ also eliminates the effect of the BPM electronics slowness, and the computed offset b allows to simultaneously take into account the beam position offset and ADC pedestals.

These coefficients a and b then allow to correct the effects of the raster on the vertex position (Eq. (3.3)), and the small dependence of the invariant mass W^2 on the raster current allows to check the effectiveness of the correction as can be seen in Fig. 3.1.

$$v_x = a * I_x + b. \tag{3.3}$$

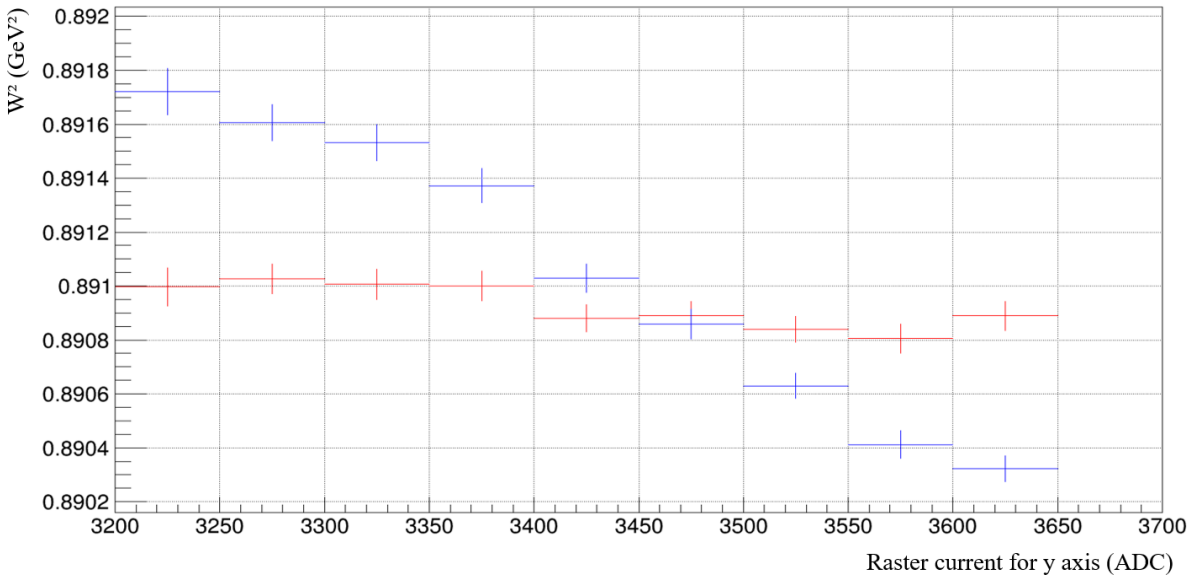

Figure 3.1: Dependence of the reconstructed invariant mass $W^2 = (e + p - e')^2$ of the elastic scattering process $ep \rightarrow e'p'$ against the current in the raster coil deflecting the electron beam vertically (y axis), before (blue) and after (red) the raster calibration. The reconstruction of the scattered electron direction depends on the vertex. The invariant mass W^2 becomes independent from the raster current after calibration.

During Spring 2016, a raster power supply failure caused the two sets of raster coils to be slightly out of synchronization with respect to each other. With no synchronization monitoring system in place at that time, this issue remained unnoticed during several days, and impacted over 50% of the statistics of one kinematic setting (kin48_3), with no solution to correct for the introduced errors. However, a Geant4 simulation study showed that the effects of this issue on the experiment variables were smaller than the experimental resolution. A monitoring system was later implemented to avoid another occurrence of the incident.

3.2 The High Resolution Spectrometer calibration

The spectrometer calibration can be separated into two main parts: the individual detectors from the detector package, and its optics. The first part of this section will give only a brief description of the calibration of the detector package as this has not been part of my work. The second part of this section will provide details about the optics calibration.

3.2.1 The detector package calibration

As described in section 2.3.1, the spectrometer detector package is made of two sets of VDCs, two sets of scintillators, a gas Cherenkov detector, and two layers of electromagnetic calorimeters called Pion Rejectors.

The VDCs rely on the relation between drift distance and drift time in order to provide tracking information. By measuring the drift time, one can deduce the distance of a particle trajectory to a VDC wire, assuming that a null drift time corresponds to a null drift distance. It is thus important that the time offset of each wire with respect to another is as close to zero as possible. The wires of the VDCs are grouped together in several TDC modules. The calibration of the time offset t_0 of the VDCs is performed by smoothing and differentiating each TDCs spectrum, and adjusting the maximum slope point of each TDC to the same value close to zero [70].

The scintillator S2 provides timing information for the detected particle. However, the sixteen scintillator paddles which compose S2 may have different time offsets with respect to each other. In order to align the different time offsets, the mean values of the time distributions of each paddle are extracted and used to shift the respective offsets to zero [71].

The gas Cherenkov and Pion Rejectors allow to discriminate electrons from pions as they do not deposit the same amount of energy in these detectors. In order to allow this identification, the PMTs

of each detector need to be calibrated so that their gains are equals. This calibration is performed by aligning the electron energy deposits seen by each PMT of a given detector. Indeed, because of the very small momentum acceptance of the spectrometer, every detected electron has roughly the same energy and thus should deposit identical amounts in each PMT of the same detector. In the specific case of the Cherenkov, the PMT resolution allows the one-photo-electron peak to be distinguished. As a consequence, the gain alignment of the Cherenkov PMTs can be done with the one-photo-electron peak instead, which is more precise.

While this calibration allowed to align the gains of each PMT within a given detector, a gain discrepancy between the two layers of the Pion Rejectors still remained. In order to further improve the calibration, two normalization factors W_1 and W_2 were computed for each kinematic setting so that the Minimum Ionizing Peak of the two layers both lie at around 500 ADC channels, and their sum (see Eq. (3.4)) is around 1000 [72]:

$$A_{PR_{sum}}^{electron} = \frac{A_{PR_1}^{electron}}{W_1} + \frac{A_{PR_2}^{electron}}{W_2}. \tag{3.4}$$

3.2.2 The spectrometer optics

A thorough description of the spectrometer optics and its calibration procedure can be found in [73]. The goal of this section is to give a simplified summary of the spectrometer optics calibration process before presenting its results for this experiment.

3.2.2.1 The optics matrix

As described in section 2.3.1, the spectrometer is made of four magnets in a QQDQ design, which guide charged particles towards a detector package. In particular, in the vicinity of the VDCs (see Fig. 2.6), there is an area called "focal plane". At the VDCs, the spectrometer measures the charged particles positions and their propagation directions which can then be transported to the focal plan where they are noted respectively (x_{fp}, y_{fp}) and $(\frac{dx_{fp}}{dz_{fp}}, \frac{dy_{fp}}{dz_{fp}}) = (\theta_{fp}, \phi_{fp})$. From these four variables, one is then able to reconstruct, at the target, the event vertex y_{tg}, the particles vertical and horizontal scattering angles θ_{tg} and ϕ_{tg}, and their relative momentum $\delta_{tg} = \frac{P-P_0}{P_0}$, where P is the particle momentum and P_0 is the central momentum of the spectrometer:

$$y_{tg} = \sum_{j,k,l} \sum_{i=1}^{5} C_i^{Y_{jkl}} x_{fp}^i \theta_{fp}^j y_{fp}^k \phi_{fp}^l. \tag{3.5}$$

The reconstruction of these variables at the vertex from the ones at the focal plane is made by the intermediate of an optics matrix, whose first order approximation can be written as:

$$\begin{bmatrix} \delta_{tg} \\ \theta_{tg} \\ y_{tg} \\ \phi_{tg} \end{bmatrix} = \begin{bmatrix} \langle \delta_{tg}|x_{fp}\rangle & \langle \delta_{tg}|\theta_{fp}\rangle & 0 & 0 \\ \langle \theta_{tg}|x_{fp}\rangle & \langle \theta_{tg}|\theta_{fp}\rangle & 0 & 0 \\ 0 & 0 & \langle y_{tg}|y_{fp}\rangle & \langle y_{tg}|\phi_{fp}\rangle \\ 0 & 0 & \langle \phi_{tg}|y_{fp}\rangle & \langle \phi_{tg}|\phi_{fp}\rangle \end{bmatrix} \begin{bmatrix} x_{fp} \\ \theta_{fp} \\ y_{fp} \\ \phi_{fp} \end{bmatrix}. \tag{3.6}$$

As one can see, the relative momentum δ_{tg} and the angle θ_{tg} mainly depend on x_{fp} and $\frac{dx_{fp}}{dz_{fp}}$ because of the spectrometer dipole momentum-dependent bending angle. On the other hand, y_{tg} and ϕ_{tg} are independent from x_{fp} and $\frac{dx_{fp}}{dz_{fp}}$.

Of course, a first order approximation would not yield results precise enough, and in practice, an expansion up to fifth order is used. In Eq. (3.5), y_{tg} (with similar equations for the other variables θ_{tg}, ϕ_{tg}, δ_{tg}) is related to the four variables in the focal plane by the optic matrix elements $C_i^{Y_{jkl}}$ ($C_i^{\Theta_{jkl}}$, $C_i^{\Phi_{jkl}}$, $C_i^{\Delta_{jkl}}$ respectively), with i+j+k+l ≤ 5. Symmetries of the spectrometer further require (k+l) to be odd for Y_{jkl} and Φ_{jkl}, and even for Θ_{jkl} and Δ_{jkl}.

3.2.2.2 The optics calibration process

The goal of the spectrometer optics calibration is to compute the matrix elements $C_i^{Y_{jkl}}$, $C_i^{\Theta_{jkl}}$, $C_i^{\Phi_{jkl}}$, $C_i^{\Delta_{jkl}}$. For this purpose, the following calibration process has been performed:

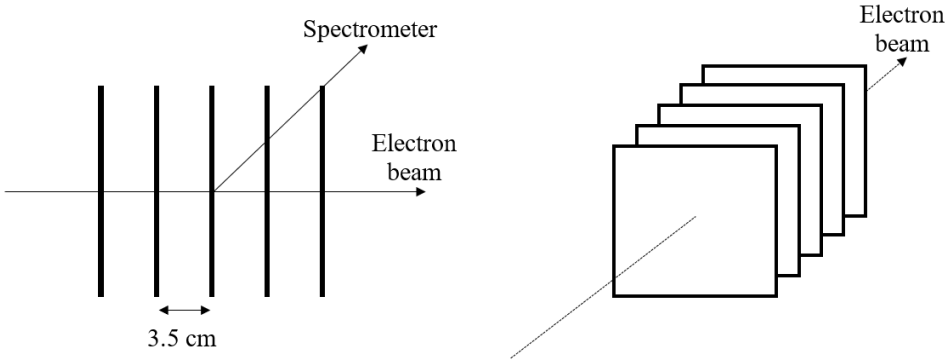

Figure 3.2: Schematic representation of the optics target made of five thin carbon foils. This target was used during the Spring 2016 optics calibration.

- step 1 is the vertex reconstruction. Data are taken on the optics target, made of 5 or 9 thin carbon foils (see Section 2.2.2 and Fig. 3.2). Each foil provides an expected vertex value y^0_{tg} while being correlated to different areas of the focal plane. The optics matrix coefficients $C_i^{Y_{jkl}}$ are then computed in order to minimize the difference between expected and reconstructed vertex values, which is done by minimizing the aberration function in Eq. (3.7):

$$\Delta(y) = \sum_{events} \left(\sum_{j,k,l} \sum_{i=1}^{5} C_i^{Y_{jkl}} x^i_{fp} \theta^j_{fp} y^k_{fp} \phi^l_{fp} - y^0_{tg} \right)^2 ; \tag{3.7}$$

- step 2 is the electron scattering angle reconstruction. Data are taken with a thick metal plate with holes, called sieve, inserted in front of the spectrometer entrance[1] (see Fig. 3.3). Each hole provides expected values θ^0_{tg}, ϕ^0_{tg} for the electron scattering angles, while being correlated to different areas of the focal plane. Similarly to step 1, the optics matrix coefficients $C_i^{\Theta_{jkl}}$ and $C_i^{\Phi_{jkl}}$ are then computed by minimizing the aberration functions $\Delta(\theta)$ and $\Delta(\phi)$ (similar to Eq. (3.7));

- step 3 is the electron momentum reconstruction. Elastic scattering data $ep \rightarrow e'p'$ are taken on the liquid hydrogen target with the spectrometer at a fixed angle, while varying the central momentum of the spectrometer. Elastic scattering has the interesting property that scattering angles and momenta are correlated. The angle of the spectrometer fixes the expected momentum of the detected particle, and changing the central momentum allows to scan different values of relative momentum δ_{tg} while illuminating different areas of the focal plane. As a consequence, each central momentum value selected provides expected values δ^0_{tg} correlated to different areas of the focal plane. Similarly to steps 1 and 2, the optics matrix coefficients $C_i^{\Delta_{jkl}}$ are then computed by minimizing the aberration functions $\Delta(\delta)$.

3.2.2.3 The Spring 2016 calibration

Prior to the start of the Spring 2016 run period, a critical issue was detected with the first quadrupole (Q1), of the spectrometer. It was discovered that the aging superconducting magnet properties were degraded to the point that its critical current threshold, above which Q1 would quench, was too low for most of the required settings of the experiment. More precisely, out of all the kinematic settings of the experiment, only kin48_1 had setting requirements that could be met by Q1. Every other kinematic settings would need a current too high in the magnet, which would make it quench.

Without the ability to replace Q1 by a new magnet before the start of the Spring 2016 run period, it was decided to run Q1 with its maximum current attainable without quenching. This effective detuning of Q1 with respect to the other three magnets of the spectrometer, which were run at their proper settings, resulted in a quite large modification of the detector optics properties and acceptance, which then needed to be carefully studied and calibrated. Details about the acceptance will be given in section 4.5.2.3.

[1] In practice, the data acquisition for step 1 and 2 can be performed in one go, by using both the optics target and the sieve plate at the same time.

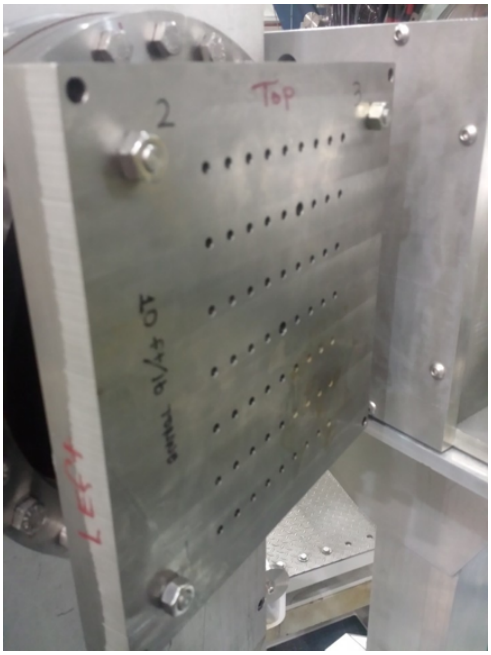

Figure 3.3: Picture of the sieve used during the Spring 2016 optics calibration.

Because the detuning of Q1 was different for each kinematic setting, a separate optics calibration had to be performed for each of them. In total, during the spring 2016 run period, four kinematic settings have been studied, with the settings of Q1 being, in percentage of current actually used over the nominal current which should have been utilized: 100.0%, 85.6%, 74.4% and 62.5% (see Tab. 3.1).

Kinematic setting	$\frac{I_{Q1}^{used}}{I_{Q1}^{nominal}}$
48_1	100.0%
48_2	62.5%
48_3	85.6%
48_4	74.4%

Table 3.1: Summary of the Q1 current tuning for each kinematic settings of Spring 2016.

In order to accelerate the optics calibration process and save beam time for the acquisition of actual DVCS data, it was decided to set the spectrometer at a small angle (16.632°) to increase counting rates. However, this had the consequence of worsening the optics reconstruction on the edges of the target for DVCS data which were taken with the spectrometer at a larger angle. Indeed, when set at a small angle, the target seen by the spectrometer looks shorter and the focal plane area illuminated is smaller. As a consequence, the focal plane areas illuminated by the edges of the target in DVCS data were not illuminated during the optics calibration (see Fig. 3.4), and thus could not be properly calibrated.

In order to correct this effect, the solution which was devised consisted in lowering the expansion of the optics matrix down to 2^{nd} order. Indeed, a high order polynomial expansion would give very good results inside illuminated areas of the focal plane, but would very quickly diverge outside. On the other hand, while a lower order polynomial expansion yields a less precise calibration, the divergence outside of the illuminated areas will be attenuated.

As can be seen in Fig. 3.5, the use of a 2^{nd} order polynomial expansion allowed to greatly improve the optics reconstruction at the target edges compared to the 5^{th} order expansion.

However, as can be seen in Fig. 3.6 (left), the calibration of the optics matrix with a 2^{nd} order polynomial expansion alone is not completely satisfactory, as there is a remaining dependence between the vertex[2] v_z and the angle ϕ_{tg} for the three kinematic settings for which Q1 had to be operated with a suboptimal current. Furthermore, the reconstructed target length turned out to be slightly shorter than the expected 15 cm.

[2] y_{tg} is the vertex expressed in a plane orthogonal to the spectrometer direction whereas v_z is expressed along the beam direction.

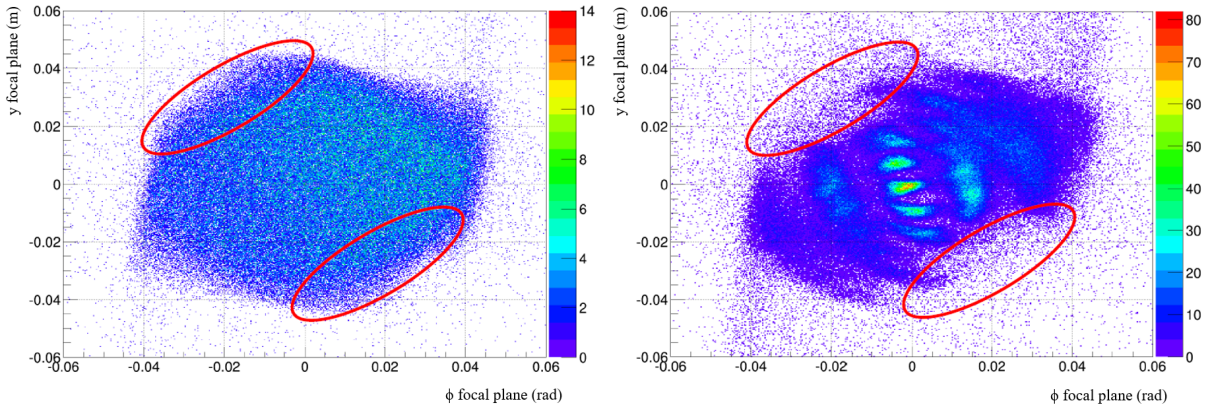

Figure 3.4: Distribution of events in the focal plane coordinates (ϕ, y) for DVCS data with the spectrometer at 37.14° (left) and for optics calibration data with the spectrometer at 16.632° (right). The areas circled in red are focal plane areas illuminated by DVCS data but missed by the optics calibration. The small areas with a higher density of events on the figure on the right side correspond to the holes of the sieve plate.

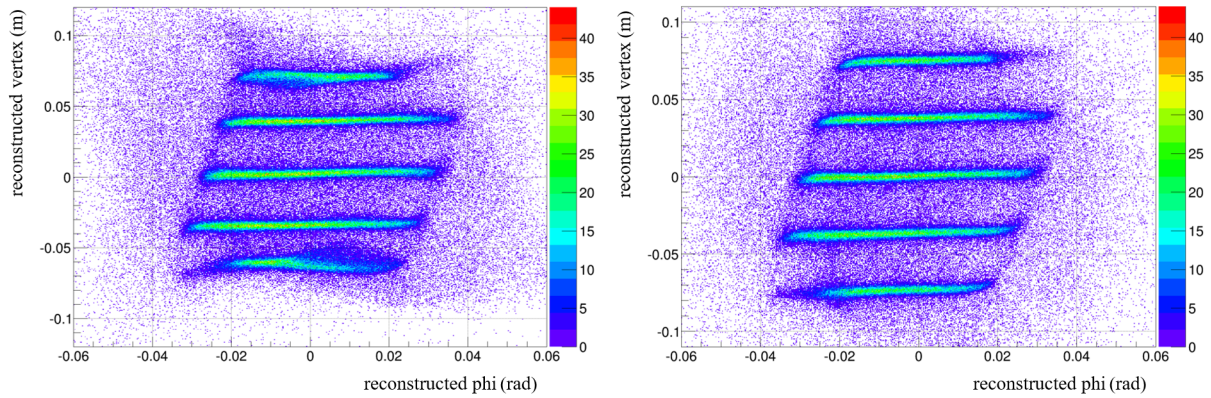

Figure 3.5: Reconstructed vertex v_z along the beam direction against reconstructed angle ϕ_{tg} for data taken on the optics target with Q1 current at 100% of its nominal value (kin48_1). Left (Right): the optics matrix calibration has been performed with a polynomial expansion up to 5^{th} (2^{nd}) order. The carbon foils at -7.5 cm and 7.5 cm are very distorted with a 5^{th} order polynomial expansion. Their reconstruction is improved with a 2^{nd} order expansion.

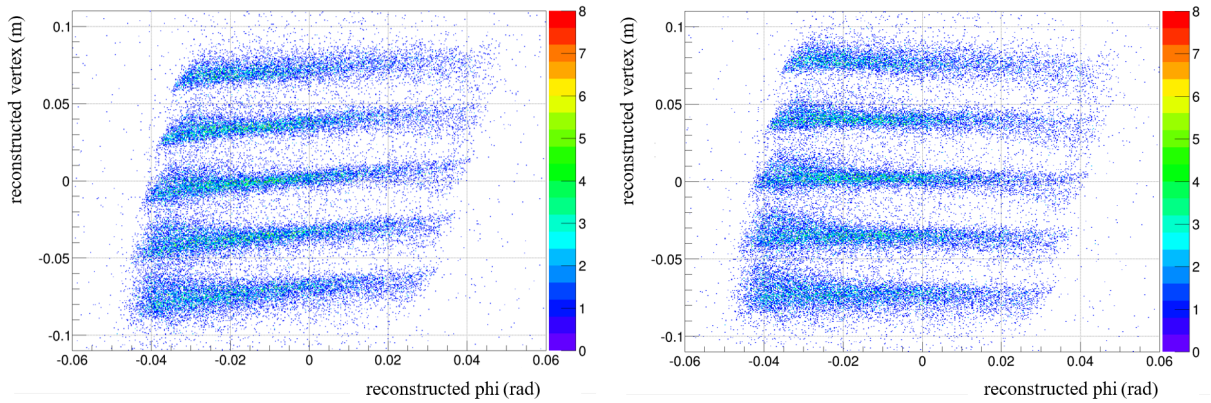

Figure 3.6: Reconstructed vertex v_z along the beam direction against the reconstructed angle ϕ_{tg} for data taken on the optics target with Q1 current at 62.5% of its nominal value (kin48_2). Left: the optics matrix calibration has been performed with a polynomial expansion up to 2^{nd} order. Right: empirical rotation and rescaling corrections have been added after the optics calibration.

It was thus decided to perform an empirical correction to the v_z–ϕ_{tg} dependence by applying a rotation in this plane, and a correction to the target length by multiplying the reconstructed vertex by a scaling factor. The corrected vertex and angle are given by the expressions:

$$v_z^{corr} = \mu_{rescale} \left\{ v_z - \phi_{tg} \left[(1 - \cos\theta_{corr}) \tan\theta_{corr} + \sin\theta_{corr} \right] \right\}, \tag{3.8}$$

$$\phi_{tg}^{corr} = \phi_{tg} \cos\theta_{corr} (1 + \tan^2\theta_{corr}), \tag{3.9}$$

with the rotation angle θ_{corr} and the rescaling factor $\mu_{rescale}$ for each kinematic summarized in Tab. 3.2. The corrected vertex y_{tg}^{corr} can then be recomputed through the expression:

$$y_{tg}^{corr} = \left[\frac{v_x \cos\left(\theta_{HRS} + \arctan\phi_{tg}^{corr}\right)}{\sin\left(\theta_{HRS} + \arctan\phi_{tg}^{corr}\right)} - v_z^{corr} \right] \frac{\sin\left(\theta_{HRS} + \arctan\phi_{tg}^{corr}\right)}{\cos\left(\arctan\phi_{tg}^{corr}\right)}, \tag{3.10}$$

with v_x the vertex along the horizontal axis orthogonal to the beam direction, and θ_{HRS} the spectrometer angle.

Kinematic setting	θ_{corr} (rad)	$\mu_{rescale}$
48_2	0.2290	1.056
48_3	0.2372	1.053
48_4	0.2051	1.042

Table 3.2: Summary of the values of the rotation angles θ_{corr} and rescaling factors $\mu_{rescale}$ for each kinematic setting.

Although not perfect, the calibration of the optics matrix with a 2^{nd} order polynomial expansion followed by the empirical correction (Eq. (3.8) and (3.9)) allowed to obtain satisfactory results, as shown in Fig. 3.6 (right) and 3.7: the v_z–ϕ_{tg} dependence is corrected and the carbon foils of the optics target are reconstructed at their expected position (up to a small offset).

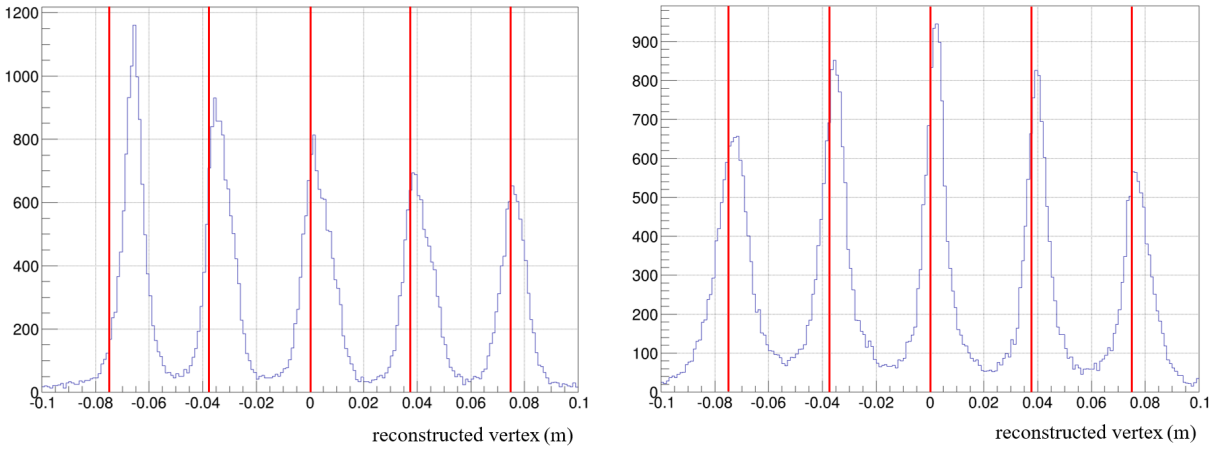

Figure 3.7: Reconstructed vertex v_z along the beam direction for data taken on the optics target with Q1 current at 62.5% of its nominal value (kin48_2). Left: the optics matrix calibration has been performed with a polynomial expansion up to 5^{th} order. Right: the optics matrix calibration has been performed with a polynomial expansion up to 2^{nd} order, followed by the application of the empirical correction of Eq. (3.8) and (3.9). The red lines represent the expected carbon foils positions if there is no offset. On the left figure, the carbon foil on the far left is not reconstructed at a correct position.

3.2.2.4 The Fall 2016 calibration

Between the Spring and Fall 2016 run periods, the faulty superconducting Q1 magnet was replaced with a classic water cooled one. Unfortunately, it was discovered after the end of the Fall 2016 run period that this magnet was saturating at the high currents required by the experiment, resulting in a magnetic field 1.6% to 7.2% lower than expected [74], depending on the kinematic setting. As the optics calibration had been performed at a lower momentum where Q1 did not saturate, this resulted in a significant degradation of the optics reconstruction.

In order to compensate for this effect, the optics matrix elements needed to be corrected. This can be done with COSY [75]. Indeed, COSY is a tool able to model the magnetic fields of the spectrometer magnets, which allows to simulate the transportation of charged particles from the target to the focal plane. While the simulation does not allow to predict precisely the optimal optics matrix from scratch, it accurately describes small variations in the optics due to magnetic fields changes [76]. Thus, the simulation allowed to compute the corrections to the optics matrix elements necessary to take into account the effect of the saturation (see Fig. 3.8 and 3.9).

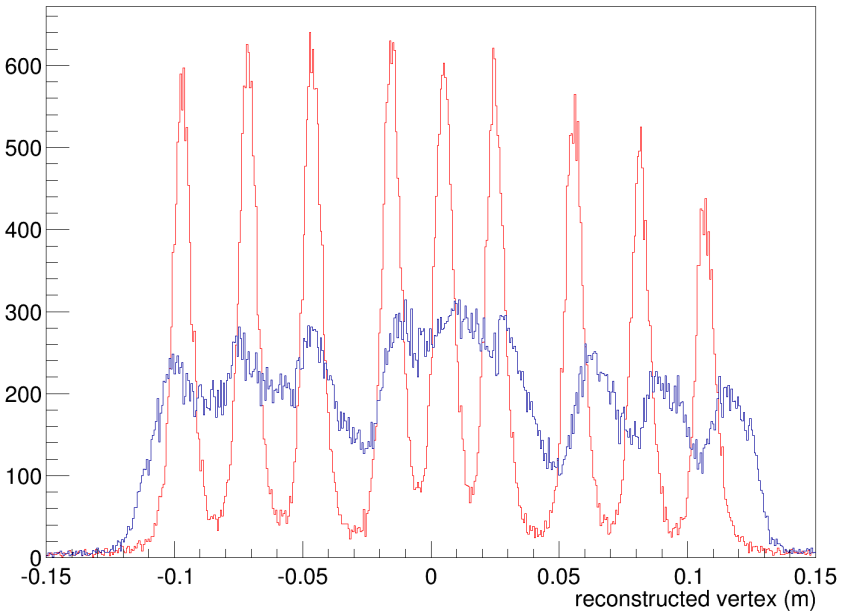

Figure 3.8: Reconstructed vertex v_z for data taken on the optics target with the Q1 magnet saturated at 7.2%, before correction of the optics for the saturation (blue) and after correction (red).

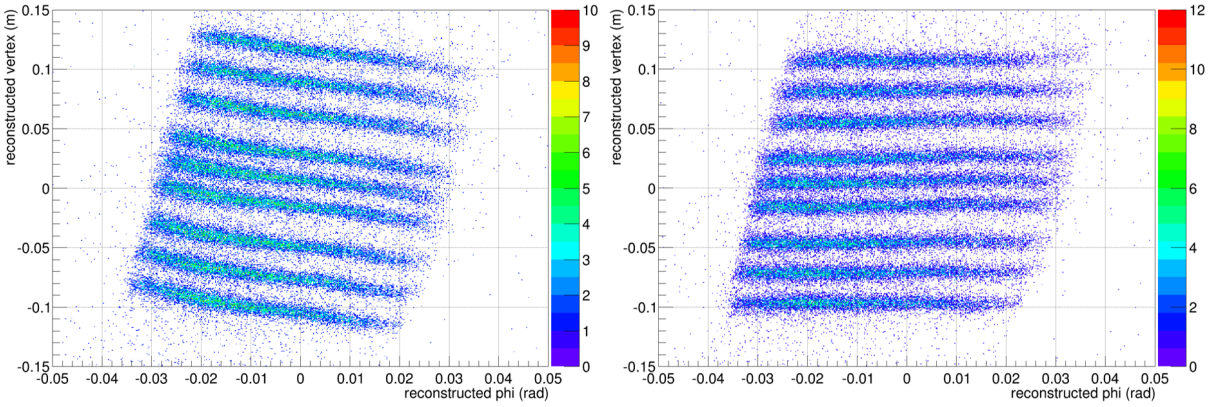

Figure 3.9: Reconstructed vertex v_z against reconstructed vertical scattering angle ϕ for data taken on the optics target with the Q1 magnet saturated at 7.2%, before correction of the optics for the saturation (left) and after correction (right). The correlation between the vertex position and the angle ϕ is successfully corrected.

3.3 The calorimeter energy calibration

As described in section 2.3.2, the DVCS calorimeter is made of 208 PbF_2 crystals optically coupled to PMTs and is used to measure the position and energy of photons emitted in the DVCS process. Because its energy resolution is quite low, it will be the main limiting factor of the experiment, which makes its calibration all the more important.

The calibration of the calorimeter is performed in three steps: cosmic rays, elastic scattering, and π^0-based calibrations. As it will be described in the following sections, the nomenclature comes from the processes involved in the different calibrations.

3.3.1 Cosmic rays calibration

First comes the cosmic rays calibration, though it is better described as being only a preliminary step. This calibration is based on the measurement of cosmic rays which travel across the calorimeter vertically.

To trigger the data acquisition of the calorimeter during this calibration, two plastic scintillators are used. One scintillator paddle is placed above the calorimeter, while the other is placed below. When a cosmic ray travels across the calorimeter, it will be detected by both scintillators in coincidence. Selected cosmic rays need to be vertical to ensure that they travel across the same distance in the calorimeter blocs and thus deposit the same amount of energy in each of them. The selection of vertical cosmic rays is preformed by requesting a sufficiently large amount of energy deposit in the top and bottom blocks of a calorimeter column.

The detected cosmic rays are Minimum Ionizing Particles (MIP). The calibration process then consists of adjusting the High Voltages (HV) of each individual PMT, using Eq. (3.12), so that the signal amplitude measured by the ADCs in each calorimeter block are roughly equal. α and β are constants, and β is correlated to the number of dynodes in the PMT: in this case, $\beta \approx 7$.

$$Gain_{PMT} = \alpha * HV_{PMT}^{\beta}, \tag{3.11}$$

$$\frac{Gain_{PMT}}{Gain'_{PMT}} = \left(\frac{HV_{PMT}}{HV'_{PMT}}\right)^{\beta}. \tag{3.12}$$

As the energy deposited by MIPs in each crystal is expected to be around 35 MeV, this also provides a preliminary energy calibration for the calorimeter and allows to estimate the High Voltages that will need to be used for GeV photons. This preliminary calibration is performed in order to provide a starting point for the elastic calibration.

Another important goal of the detection of cosmic rays is to check that every calorimeter channel is working and properly wired before the actual data taking of the experiment. A simple check-up is usually performed every time an intervention is done on the calorimeter or the DAQ and is suspected to have been able to disturb some components. This is most important when the calorimeter is being re-stacked (re-installed) in the experimental Hall at the beginning of a run period, as there is always a risk for a faulty channel (loose connector, damaged cable, miswired channels, etc...).

3.3.2 The elastic calibration

Second comes the elastic calibration. It is based on the detection of elastic scattering events $ep \rightarrow e'p'$, where the scattered proton is detected in the spectrometer (whose polarity is reversed), and the scattered electron in the calorimeter. Since it is a kinematically constrained reaction, one can compute the expected momentum of the scattered electron from the momentum of the scattered proton. Then, calibration coefficients for the calorimeter can be computed in the following way.

If E_n is the electron energy for the nth event, $A_{n,i}$ is the signal amplitude in the i^{th} bloc of the calorimeter for the n^{th} event, and C_i is the calibration coefficient associated with the i^{th} bloc, then one gets:

$$E_n = \sum_{i=1}^{208} C_i A_{n,i}. \tag{3.13}$$

In order to determine the calibration coefficients, one as to minimize the following χ^2:

$$\chi^2 = \sum_{n=1}^{N_{events}} \left(E_n - \sum_{i=1}^{208} C_i A_{n,i}\right)^2, \tag{3.14}$$

where, by energy conservation, $E_n = E_b + M_p - E_n^p$, with E_b the beam energy, M_p the proton mass, and E_n^p the recoil proton energy. This leads to:

$$\frac{\partial \chi^2}{\partial C_j} = -2C_j \sum_{n=1}^{N_{events}} \left(E_n - \sum_{i=1}^{208} C_i A_{n,i}\right) A_{n,j} = 0, \quad \forall j = 1, ..., 208, \tag{3.15}$$

$$\sum_{i=1}^{208} C_i \left(\sum_{n=1}^{N_{events}} A_{n,i} A_{n,j} \right) = \sum_{n=1}^{N_{events}} E_n A_{n,j}, \quad \forall j = 1, ..., 208. \tag{3.16}$$

Equation (3.16) can be rewritten as the matrix equation $\mathcal{A}C = B$, with $\mathcal{A}_{i,j} = \sum_{n=1}^{N_{events}} A_{n,i} A_{n,j}$ and $B_i = \sum_{n=1}^{N_{events}} E_n A_{n,i}$. The calibration coefficients C_i can then be computed as $C = \mathcal{A}^{-1} B$.

Because of the very small acceptance of the spectrometer and the kinematic constrains of the elastic process, it is necessary to move the calorimeter back at a distance of 5.5 to 6 m in order to illuminate its full height, and to move the calorimeter at 3 different angles in order to illuminate its full width.

An elastic calibration was performed at the beginning and a few weeks before the end of each run period. An energy resolution of 3.6% at 4.2 GeV, and of 3% at 7.0 GeV was measured [71].

3.3.3 The π^0 energy calibration

Finally comes the π^0 energy calibration. While the elastic calibration provides reliable results, the process has the downside of being quite lengthy (∼one day of dedicated beam time), so it could not be performed very often. However, because of radiation damage, the calorimeter suffered from a continuous loss of gain through the experiment, while simultaneously losing its radiation hardness. Near the end of the experiment, the reconstructed π^0 mass could decrease by ∼10 MeV within a few days (see Fig. 3.10). An accurate energy calibration faster to perform than the elastic one was thus required.

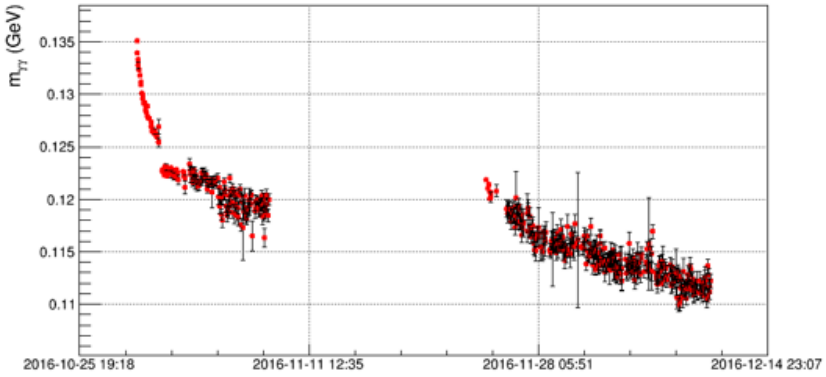

Figure 3.10: Reconstructed π^0 invariant mass against time for the Fall 2016 run period. (Courtesy of Dr. C. Muñoz Camacho).

3.3.3.1 Calibration algorithm

The π^0 calibration relies on the reconstruction of the π^0 invariant mass in the process $ep \to e'p'\pi^0$. As this electro-production of π^0 can be measured in the same kinematic conditions as the DVCS process, no dedicated beam time needs to be taken from the acquisition of DVCS data. Moreover, the π^0 production rates are such that an independent calibration can be performed approximately every day. Thus, the π^0 calibration fulfills the experiment requirements.

The calibration method described in [77] was applied. The two photons produced by the decay of the π^0 in the process $\pi^0 \to \gamma_1\gamma_2$ are detected in the calorimeter. From their energies p_{1i} and p_{2i} and the angle between them θ_i, where i refers to the event number, one can reconstruct the π^0 invariant mass m_i as:

$$m_i^2 = 2p_{1i}p_{2i}(1 - \cos(\theta_i)). \tag{3.17}$$

If $E_{ji}^{(k)}$ is the measured energy deposited by the photon j in the calorimeter block k for event number i, then the photon energy p_{ji} can be computed as the sum of the energies $E_{ji}^{(k)}$:

$$p_{ji} = \sum_{k \in cluster} E_{ji}^{(k)}, \tag{3.18}$$

with k running over the blocks (cluster) in which the photon deposited its energy. The angle θ_i is measured from the photon positions in the calorimeter, which are reconstructed from the calorimeter block positions and the energies $E_{ji}^{(k)}$.

Furthermore, if ϵ_k is the correction coefficient computed by the calibration for the block k, then the measured energy $E_{ji}^{(k)}$ is corrected as:

$$E_{ji}^{(k)} \to (1+\epsilon_k)E_{ji}^{(k)}. \tag{3.19}$$

The goal of the π^0 calibration then becomes the minimization with respect to ϵ_k of the quantity F defined as:

$$F = \sum_{i=1}^{N_{events}} (m_i^2 - m_0^2)^2 + 2\lambda \sum_{i=1}^{N_{events}} (m_i^2 - m_0^2), \tag{3.20}$$

where $m_0 = 0.1349766$ GeV [13] is the expected π^0 mass, and λ is a Lagrange multiplier. The first term of the right hand side of Eq. (3.20) represents the resolution on the reconstructed π^0 invariant mass that is being optimized, while the second term embodies the constraint $\langle m_i^2 \rangle = m_0^2$.

The minimization of F can be difficult because of the non-linear dependence of m_i^2 on the block energies $E_{ji}^{(k)}$ that appears in the reconstructed angle θ_i between the two photons (Eq. (3.17)). However, if the correction coefficient ϵ_k is small, then changing the energy $E_{ji}^{(k)}$ by ϵ_k will have a negligible effect on the angle θ_i, and will only rescale $E_{ji}^{(k)}$. From this approximation, one gets:

$$\frac{\partial m_i^2}{\partial \epsilon_k} \approx m_i^2 \frac{E_{ji}^{(k)}}{\sum\limits_k E_{ji}^{(k)}}. \tag{3.21}$$

Then from Eq. (3.20) and (3.21), one can derive:

$$\frac{\partial F}{\partial \epsilon_k} = 2 \sum_{i=1}^{N_{events}} (m_i^2 - m_0^2) \frac{\partial m_i^2}{\partial \epsilon_k} + 2\lambda \sum_{i=1}^{N_{events}} \frac{\partial m_i^2}{\partial \epsilon_k} = 0, \quad \forall k = 1, ..., 208, \tag{3.22}$$

$$\frac{\partial F}{\partial \epsilon_k} = 2 \sum_{i=1}^{N_{events}} \left(m_i^2 - m_0^2 + \lambda + \sum_k \epsilon_{k'} \frac{\partial m_i^2}{\partial \epsilon_{k'}} \right) \frac{\partial m_i^2}{\partial \epsilon_k} = 0, \quad \forall k = 1, ..., 208. \tag{3.23}$$

The solution to Eq. (3.23) is then given by:

$$\epsilon_k = \sum_{k'} [C^{-1}]_{kk'} (D - \lambda L)_{k'}, \tag{3.24}$$

where:

$$C_{kk'} = \sum_{i=1}^{N_{events}} \left(\frac{\partial m_i^2}{\partial \epsilon_k} \frac{\partial m_i^2}{\partial \epsilon_{k'}} \right), \tag{3.25}$$

$$D_k = - \sum_{i=1}^{N_{events}} \left((m_i^2 - m_0^2) \frac{\partial m_i^2}{\partial \epsilon_k} \right), \tag{3.26}$$

$$L_k = \sum_{i=1}^{N_{events}} \frac{\partial m_i^2}{\partial \epsilon_k}, \tag{3.27}$$

$$\lambda = \frac{B + L^T C^{-1} D}{L^T C^{-1} L}, \tag{3.28}$$

$$B = \sum_{i=1}^{N_{events}} (m_i^2 - m_0^2). \tag{3.29}$$

However, one will notice that the smallness of the correction coefficient ϵ_k required by the approximation in Eq. (3.21) is not directly compatible with the correction of the calorimeter gain, for which ϵ_k may need to be rather larger. As a consequence, the π^0 calibration is an iterative process. At the end of the first iteration, a set of coefficients $\epsilon_{k,1}$ have been computed to correct the calorimeter block energies

as displayed in Eq. (3.19). The second iteration of the process will then compute a set of coefficients $\epsilon_{k,2}$ so that Eq. (3.19) becomes:

$$E_{ji}^{(k)} \rightarrow (1+\epsilon_{k,1})(1+\epsilon_{k,2})E_{ji}^{(k)}. \tag{3.30}$$

The iterative process is repeated N_{it} times until $\epsilon_{k,n} \rightarrow 0, \forall k = 1, ..., 208$, and the final correction coefficients $C_k^{\pi^0}$ can then be expressed as:

$$C_k^{\pi^0} = \prod_{l=1}^{N_{it}} (1+\epsilon_{k,l}), \tag{3.31}$$

$$E_{ji}^{(k)} \rightarrow C_k^{\pi^0} E_{ji}^{(k)}. \tag{3.32}$$

3.3.3.2 Calibration precision and results

According to [77], a good convergence $\epsilon_{k,n} \rightarrow 0, \forall k = 1, ..., 208$ is obtained for a sample of 10^5 π^0 events after 8-10 iterations.

Tests with a Geant4 simulation showed that for this experiment, a day worth of data allows to compute correction coefficients with a precision of 1-2% for blocks in the middle of the calorimeter, and 4-5% for the second blocks closest to the edges. Adding more statistics would only result in a very slight improvement, while using less statistics would quickly decrease the precision. For instance, 1/4 of a day of data would result in a precision of 4-5% in the middle of the calorimeter, and 10-15% for the second blocks closest to the edges. A minimum of 3-4 iterations is required, while adding more iterations will very slightly improve the results precision as well.

It was necessary to compromise between performing π^0 calibrations as often as possible to correct for the continuous loss of gain of the calorimeter, and maintaining a precision as high as possible. It was thus decided to perform π^0 calibrations with one day worth of data each. The number of iterations of each calibration was set to 8, which is large enough to keep some margin with respect to simulation uncertainties, while not making the calibration codes unnecessarily long to run.

The Geant4 simulation also showed that the π^0 calibration does not work properly for the blocks on the edges of the calorimeter, and especially its corners. The reasons are both a lack of statistics in these specific regions, and energy losses because parts of the showers are leaking outside of the calorimeter. This leads to instabilities in the algorithm which can then diverge. It was thus decided to not calculate correction coefficients for these blocks. Instead, their coefficients were set to be equal to the mean value of the coefficients of all the other blocks.

This calibration method allowed to successfully correct the loss of gain of the calorimeter for most of the experiment running time, as can be seen in Fig. 3.11. But as shown in Fig. 3.12, the correction coefficients could vary widely from one block to another. While most blocks did not need a correction larger than 30%, a few of them very sensitive to radiation damage required corrections of the order of $\sim 200\%$ to $\sim 300\%$.

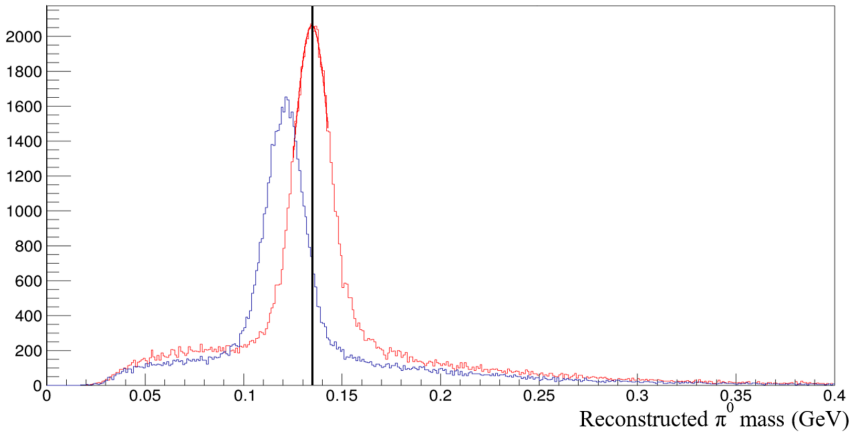

Figure 3.11: Reconstructed π^0 invariant mass before (blue) and after (red) the π^0 calibration, for data taken at the end of Fall 2016. The red curve on top of the red histogram is a Gaussian fit of the invariant mass. The black line represents the expected π^0 invariant mass. The π^0 invariant mass mean value is successfully corrected and its resolution is improved from 10.3 MeV (blue) to 10.0 MeV (red).

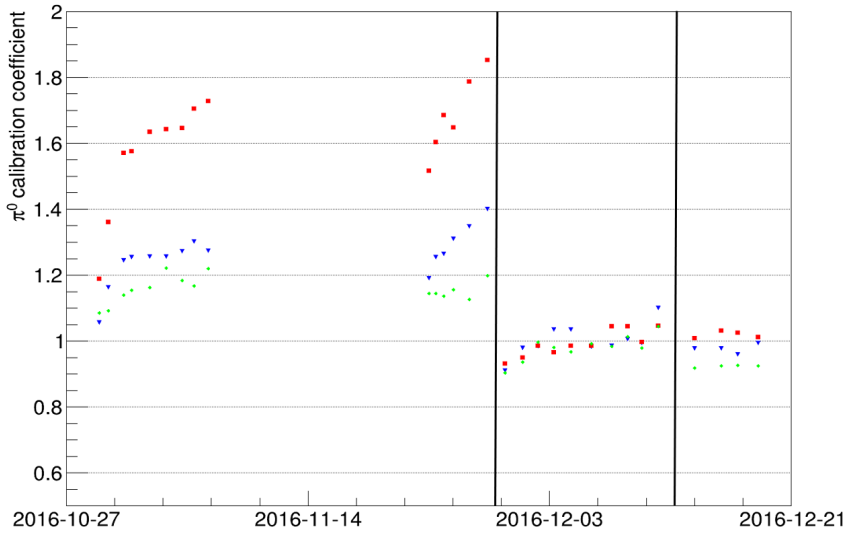

Figure 3.12: Evolution of the π^0 calibration coefficients against time (Fall 2016) for channels 147 (blue), 151 (red) and 157 (green). The black lines correspond to changes of the elastic calibration coefficients. The large gap around November 14^{th} corresponds to a beam down time during which the calorimeter blocks recovered a little from radiation damage.

3.3.3.3 Fast darkening and correction

Unfortunately, during a few time periods, the loss of gain of the calorimeter was too fast for even the π^0 calibration to correct, as can be seen in Fig. 3.13 (left): the reconstructed π^0 invariant mass drifts by $\sim$6 MeV in the span of roughly 16 hours. This happened at the beginning of the Spring and Fall 2016 run periods, and more generally after long periods of a few weeks without beam. This is explained by the fact that when the electron beam is off, the calorimeter naturally recovers from the radiation damage by itself at a slow rate, as can be seen in Fig. 3.10. However, when the electron beam is turned on again, the darkening effect comes back faster.

In order to tackle this issue, reducing the statistics used by the π^0 calibration to run it more often would be counter-productive, as this would result in a quite large loss of precision in the results. Instead, it was decided to empirically correct run by run the π^0 calibration coefficients by the ratio of the expected π^0 invariant mass over the reconstructed one (see Eq. (3.33)). This allowed to successfully correct the remaining effect of the fast loss of gain of the calorimeter, as can be seen in Fig. 3.13 (right).

$$C_k^{\pi^0} \rightarrow C_k^{\pi^0} \frac{m_0}{m_{reconstruct}} \quad \forall k = 1, ..., 208. \tag{3.33}$$

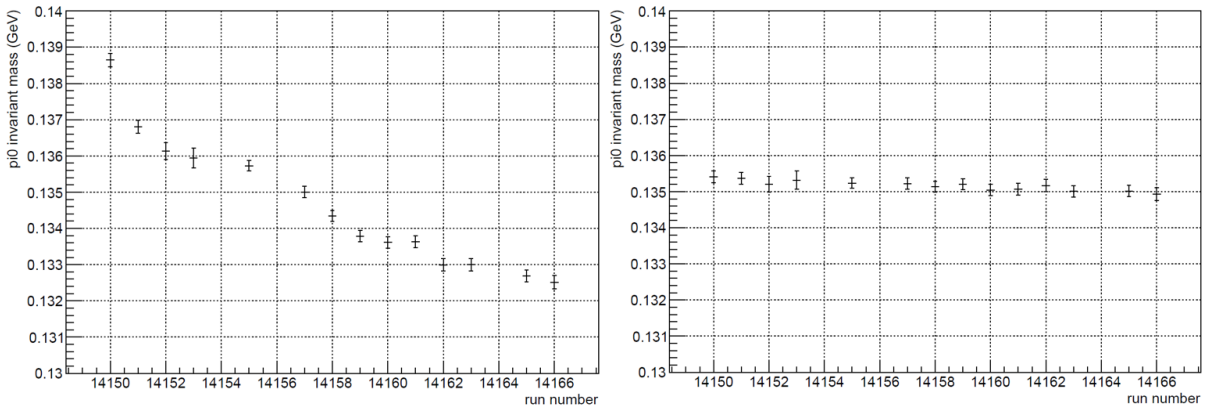

Figure 3.13: Evolution of the reconstructed π^0 invariant mass against run number before (left) and after (right) empirical correction, for data taken at the beginning of Fall 2016. Each run represents approximately one hour of beam time.

Chapter 4

The data analysis

In order to extract cross sections, unusable data because of running incidents must be identified and discarded, proper DVCS events identification and selection need to be made while background contamination has to be subtracted, and corrections are required to take into account experimental inefficiencies.

The first part of this chapter will present the data quality control. The second part will deal with time and energy information extraction from the calorimeter raw ARS signals, while the third section will briefly explain the spectrometer-calorimeter coincidence time correction. In the fourth part, the clustering algorithm which allows to reconstruct the photons detected in the calorimeter will be described. Then, the fifth section will present the DVCS event selection. Finally, the sixth part will give details about the background subtraction, while the seventh will list the corrections that need to be applied because of experimental limitations.

4.1 Data quality analysis

The first step of the data analysis is the control of the data quality. The goal is to identify and discard data sets which are unreliable, for instance, because of incidents occurring during the experiment, poor running conditions or abnormal detector readouts.

The first stage of the quality analysis consists on eliminating the runs with obvious incidents reported during the experiment by shift workers. This includes, but is not limited to: trips or failures of the power supplies of detectors and beam line components, cryogenic supply failures, unstable electron beam position or high frequency of trips, missing detector channels and DAQ crashes. Runs with too few events or a too short running time were all discarded as the vast majority of them have had an incident occurring and were stopped prematurely because of it.

In the second stage of the quality analysis, a large collection of variables are scrutinized run by run, and anomalies are singled out for further investigation. If the reason for the abnormal-looking behavior is found to be inconsequential, the run is kept. Otherwise, or if no explanation is found, the conservative decision is made to discard the suspicious run. The variables which are studied have been chosen so that there are at least one per detector. The scrutinized variables are:

- the number of hits per paddle in the scintillator S2 TDCs, normalized by the total charge of the run;
- the number of hits per PMT in the Cherenkov detector TDCs, normalized by the total charge of the run;
- the average number of blocks hit per event per Pion Rejector layer;
- the average number of VDC wires hit per event and per VDC plane;
- the average number of VDC wire clusters per VDC plane;
- the number of events with a single track in the spectrometer, normalized by the total charge of the run;
- the ratio of multi-tracks events over the total number of events with at least one track;
- the ratios of events with helicity -1, +1 or unknown over the total number of events;

- several trigger scalers, normalized by the total charge of the run;
- the dead time of the run;
- the total charge of the run;
- the synchronization of the raster magnets (see Fig. 4.1);
- the raster calibration coefficients;
- the number of events in each calorimeter block with an integrated ARS signal higher than a chosen threshold, normalized by the total charge of the run;
- the average arrival time of the ARS signal for each calorimeter block, defined here as the time when the ARS signal has maximum amplitude.

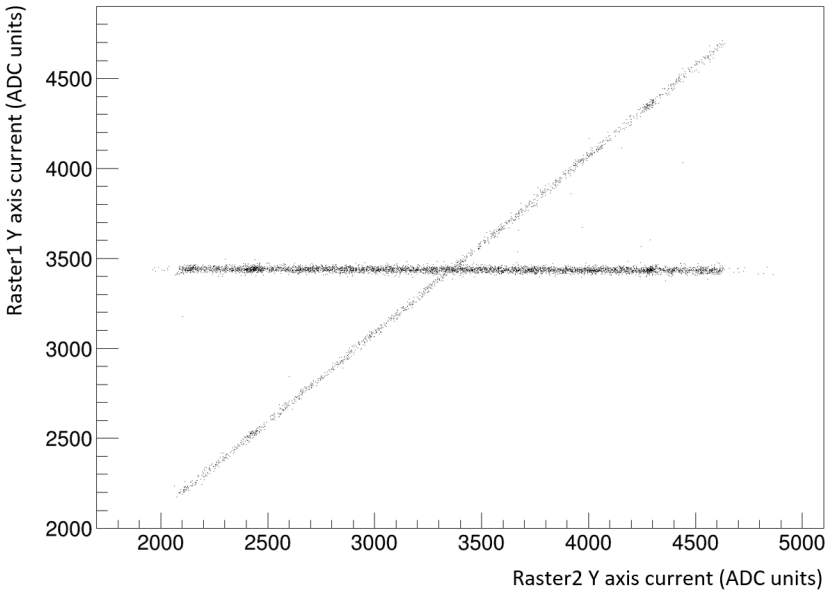

Figure 4.1: Correlation between the currents in the two rasters along the y axis for run 13370. When the two rasters are properly synchronized, their respective current along the same axis should be linearly correlated and none of them should be constant. When not properly synchronized, the correlation shape changes: in this case, the current in the first raster became constant in the middle of the run. A loss of synchronization usually occurred when the raster power supplies accumulated too much radiation damage.

Overall, the main reasons for discarding data have been runs being too short because of beam instabilities or incidents, and raster issues. Depending on the kinematic setting, between 1% to 5% of the total accumulated charge was deemed unreliable and discarded. At the end of this quality analysis, lists of reliable runs were made.

4.1.1 The spectrometer-calorimeter loss of synchronization incident

During the Fall 2016 run period, a cable carrying a 100 kHz clock signal was found wrongfully plugged into the live input of the Trigger Supervisor, resulting in random losses of synchronization between the spectrometer and the calorimeter.

Indeed, the spectrometer and the calorimeter are synchronized so that, in a run, the n^{th} event recorded by the spectrometer corresponds to the n^{th} event recorded by the calorimeter. As described in section 2.3.3, as long as a ROC is sending a VETO to the Trigger Supervisor because it is busy digitizing an event, the TS will not accept any new trigger and the data acquisition is "frozen". In fact, as the data from the calorimeter takes the most time to record, the spectrometer is always "waiting for the calorimeter". However, because of the clock plugged into the live input, the TS will wrongfully believe the calorimeter to be available when it is actually busy digitizing an event every time it receives a clock signal. If a new trigger is fired when the spectrometer is available, the calorimeter is still busy and the TS is receiving a

signal from the clock plugged in the live input, then the spectrometer will accept a new event while the calorimeter will not be able to.

This has the consequence that the $(n+k)^{th}$ event recorded by the spectrometer then corresponds to the n^{th} event recorded by the calorimeter, with k an integer growing by one unit for each additional event taken by the spectrometer. It is possible for the spectrometer to accept several events while the calorimeter is busy recording one single event. This offset could occur at any time, for any run, and happen any number of times in the same run. Unfortunately, this serious issue remained undetected for almost four days, and approximately 30% of kin60_1 total statistics were compromised.

In order to recover the data and avoid this severe loss of statistics, the following procedure was created:

- first, the identification of event windows where an offset occurred is performed by using the Electronic Dead Time Monitor (EDTM). The EDTM is a 6 Hz clock signal sent to both the spectrometer and the calorimeter to trigger an event[1]. These EDTM events are tagged with a specific identifier to be easily distinguished from other events. Because the EDTM events in the calorimeter and the spectrometer should be synchronized, a loss of synchronization of these events reveals the appearance of an offset. The event where there start to be an offset is necessarily between the first EDTM event where the loss of synchronization appears, and the previous EDTM event, where there was no issue. As the EDTM is a 6 Hz clock, this corresponds to an uncertainty window of only a few tens of events in which one cannot know where exactly the offset starts to exist and that needs to be discarded;

- then, the determination of the value k of the offset is performed by looking at the number of events waiting in a buffer to be recorded. Indeed, before being read-out and recorded, an event is first stored in a buffer. When it is actually recorded, the event is then flushed from the buffer. When the spectrometer takes additional events because of the clock plugged in the TS, they are stored in the spectrometer buffer so that several events enter it, while the calorimeter buffer contains only one event. Then, only one event is recorded and flushed from both the spectrometer and calorimeter buffers. As a consequence, the number of events in the spectrometer buffer increases compared to the calorimeter buffer. The number of additional events present in the spectrometer buffer when an offset is detected yields the value k of the offset by which the events numeration needs to be corrected.

This procedure allowed to recover all the runs affected by this issue with a negligible loss consisting only of the few tens of events in the EDTM uncertainty windows which were discarded.

4.2 The reference shapes and the waveform analysis

The next step of the data analysis is one of its core components. The goal of the waveform analysis is to extract from each raw calorimeter ARS signal the pulses arrival times and their amplitudes (see Fig. 2.9). The amplitude, once multiplied by the calorimeter calibration coefficients, corresponds to the energy deposited by photons in each PbF_2 crystal.

In order to measure these values, the ARS pulses are fitted using reference shapes. The assumption is made that the shape of a pulse is independent from its amplitude and remains unchanged. Thus, one can fit the ARS pulses with reference shapes simply by adjusting their amplitude and arrival time to match the raw data.

The reference shapes are determined individually for each of the 208 calorimeter blocks by using elastic scattering data $ep \to e'p'$, where signals are the cleanest (low probability of pile-up). The reference shapes are the average ARS pulses for each block, normalized so that their amplitude is equal to 1.

This section will now present in detail the fit algorithm, and explain the choices made for its parameters.

4.2.1 The baseline fit

The first step of the algorithm is to determine whether there is actually an ARS pulse to fit, or if the signal is flat. For this purpose, a constant baseline b is fitted to the ARS data. This is done by the χ^2

[1] the ratio of the number of EDTM events accepted by the TS over the total number of EDTM events gives an approximation of the live time (= 1 - dead time) which can be easily monitored during the experiment

minimization:

$$\chi^2 = \sum_{i=i_{min}}^{i_{max}} (x_i - b)^2, \tag{4.1}$$

which yields:

$$b = \frac{1}{i_{max} - i_{min}} \sum_{i=i_{min}}^{i_{max}} x_i, \tag{4.2}$$

with $\{x_i\}$ the ARS signal, where i designates a 1 ns sample. The analysis window $[i_{min}, i_{max}]$ is smaller than the full 128 ns width of the ARS signals as they do not contain useful information close to 0 ns and 128 ns. Additional details will be provided in section 4.2.6.

Then, in order to determine if the baseline fit is good enough, one computes χ^2_t:

$$\chi^2_t = \sum_{i=\chi^2_{min}}^{\chi^2_{max}} (x_i - b)^2, \tag{4.3}$$

with $[\chi^2_{min}, \chi^2_{max}]$ the χ^2 window. As the fit needs to be accurate only around the pulses (when they exist), the χ^2 window is smaller than the analysis one and centered around the time when the reference shape reaches its maximum amplitude. Additional details will be provided in section 4.2.6.

The computed χ^2_t is then compared to a threshold χ_0. If $\chi^2_t < \chi_0$, the baseline fit is deemed to be good enough, and there are no pulses in the ARS signal.

4.2.2 The one-pulse fit

In the case where $\chi^2_t \geq \chi_0$, the baseline fit is not enough and a pulse must be fitted alongside the baseline. This is done by minimizing the χ^2:

$$\chi^2 = \sum_{i=i_{min}}^{i_{max}} (x_i - a_1 h_i - b)^2, \tag{4.4}$$

with $\{h_i\}$ the reference shape and a_1 the amplitude parameter by which the reference shape must be multiplied to match the data. However, Eq. (4.4) assumes that the ARS signal and reference shape have exactly the same arrival time, which is not the case. To take into account the time offset t_1 between the ARS signal and the reference shape, h_i must be shifted by t_1 so that Eq. (4.4) becomes:

$$\chi^2(t_1) = \sum_{i=i_{min}}^{i_{max}} (x_i - a_1(t_1) h_{i-t_1} - b(t_1))^2, \tag{4.5}$$

whose minimization yields:

$$\begin{pmatrix} \sum_{i=i_{min}}^{i_{max}} x_i h_{i-t_1} \\ \sum_{i=i_{min}}^{i_{max}} x_i \end{pmatrix} = \begin{pmatrix} \sum_{i=i_{min}}^{i_{max}} h^2_{i-t_1} & \sum_{i=i_{min}}^{i_{max}} h_{i-t_1} \\ \sum_{i=i_{min}}^{i_{max}} h_{i-t_1} & \sum_{i=i_{min}}^{i_{max}} 1 \end{pmatrix} \begin{pmatrix} a_1(t_1) \\ b(t_1) \end{pmatrix}, \tag{4.6}$$

which allows to compute $a_1(t_1)$ and $b(t_1)$ by matrix inversion.

In order to find t_1, different values in a window $[t_1^{min}, t_1^{max}]$ are tested, by steps of 1 ns. For each possible value of t_1 in $[t_1^{min}, t_1^{max}]$, one computes:

$$\chi^2_t(t_1) = \sum_{i=\chi^2_{min}}^{\chi^2_{max}} (x_i - a_1(t_1) h_{i-t_1} - b(t_1))^2, \tag{4.7}$$

and the optimum value of t_1 is the one which minimizes $\chi^2_t(t_1)$.

The minimum $\chi^2_t(t_1)$ computed is then compared to a threshold χ_1. If $min\left\{\chi^2_t(t_1)\right\} < \chi_1$, the 1-pulse fit is deemed to be good enough (see Fig. 4.2).

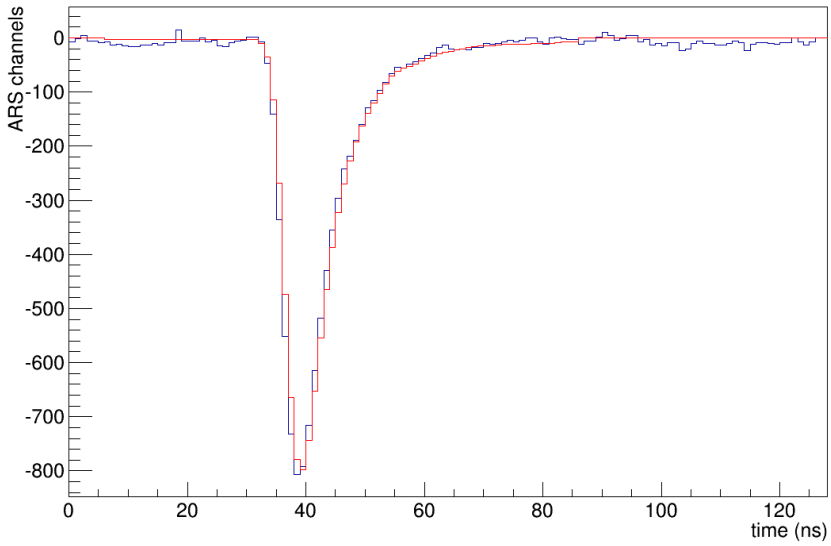

Figure 4.2: Waveform analysis of an ARS signal (blue) with a single pulse fitted (red).

4.2.3 The two-pulse fit

In the case where $min\left\{\chi_t^2(t_1)\right\} \geq \chi_1$, the one-pulse fit is not enough and a second pulse must be fitted alongside the first one. This is done by minimizing the χ^2:

$$\chi^2(t_1,t_2) = \sum_{i=i_{min}}^{i_{max}} (x_i - a_1(t_1,t_2)h_{i-t_1} - a_2(t_1,t_2)h_{i-t_2} - b(t_1,t_2))^2, \tag{4.8}$$

where t_2 and a_2 are respectively the time offset and the amplitude parameter by which the reference shape needs to be shifted and multiplied in order to match the second pulse. The minimization of Eq. (4.8) then yields:

$$\begin{pmatrix} \sum_{i=i_{min}}^{i_{max}} x_i h_{i-t_1} \\ \sum_{i=i_{min}}^{i_{max}} x_i h_{i-t_2} \\ \sum_{i=i_{min}}^{i_{max}} x_i \end{pmatrix} = \begin{pmatrix} \sum_{i=i_{min}}^{i_{max}} h_{i-t_1}^2 & \sum_{i=i_{min}}^{i_{max}} h_{i-t_1}h_{i-t_2} & \sum_{i=i_{min}}^{i_{max}} h_{i-t_1} \\ \sum_{i=i_{min}}^{i_{max}} h_{i-t_1}h_{i-t_2} & \sum_{i=i_{min}}^{i_{max}} h_{i-t_2}^2 & \sum_{i=i_{min}}^{i_{max}} h_{i-t_2} \\ \sum_{i=i_{min}}^{i_{max}} h_{i-t_1} & \sum_{i=i_{min}}^{i_{max}} h_{i-t_2} & \sum_{i=i_{min}}^{i_{max}} 1 \end{pmatrix} \begin{pmatrix} a_1(t_1,t_2) \\ a_2(t_1,t_2) \\ b(t_1,t_2) \end{pmatrix}, \tag{4.9}$$

which allows to compute $a_1(t_1,t_2)$, $a_2(t_1,t_2)$ and $b(t_1,t_2)$ by matrix inversion.

Similarly to the one-pulse fit, several values of t_1 and t_2 are tested in order to minimize the χ_t^2:

$$\chi_t^2(t_1,t_2) = \sum_{i=\chi^2_{min}}^{\chi^2_{max}} (x_i - a_1(t_1,t_2)h_{i-t_1} - a_2(t_1,t_2)h_{i-t_2} - b(t_1,t_2))^2, \tag{4.10}$$

and the couple (t_1,t_2) that minimize $\chi_t^2(t_1,t_2)$ are the arrival times of the two pulses fitted with respect to the reference shapes, and the corresponding $a_1(t_1,t_2)$ and $a_2(t_1,t_2)$ are their amplitudes (see Fig. 4.3). However, while t_1 is still sampled in the same time window $[t_1^{min}, t_1^{max}]$ as for the one-pulse fit, t_2 on the other hand is sampled in a different time window $[t_2^{min}, t_2^{max}]$, slightly larger than $[t_1^{min}, t_1^{max}]$ in order to find pile-up events.

If the two pulses are too close to each other, it can be very difficult for the waveform analysis algorithm to tell them apart. At the limit $t_1 = t_2$, an infinite number of solutions (a_1, a_2) can be found and the algorithm fails. In order to avoid those scenarios, a threshold $\Delta\tau$ is defined so that if $|t_1 - t_2| < \Delta\tau$, then the two-pulse fit is discarded, and the one-pulse fit is kept instead. The threshold $\Delta\tau$ represents the algorithm time resolution and has been chosen as $\Delta\tau = 4$ ns.

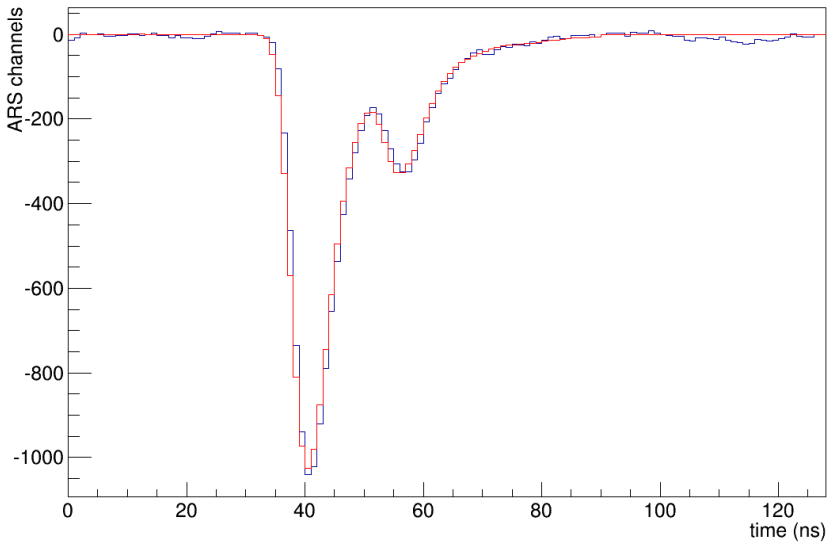

Figure 4.3: Waveform analysis of an ARS signal (blue) with two pulses fitted (red).

In the case of pile-up events for which $|t_1 - t_2| < \Delta\tau$, the energy of the photon will not be properly reconstructed, but the uncertainty created is negligible: as will be seen in section 4.2.5, the amount of pile-up events turns out to be very low, and the ones where $|t_1 - t_2| < \Delta\tau$ are even more rare.

For the same reason, the waveform analysis algorithm never looks for a third pulse: the computation time to fit a third pulse would become extremely high, for a negligible impact on the results. The effect of the two-pulse fit is already small because of the very small number of pile-up events, and a three-pulse fit would have had even less of an impact.

4.2.4 Improving the time resolution on t_1 and t_2

The time resolution on t_1 and t_2 is experimentally limited by the 1 ns resolution of the ARSs. However, it is still possible to improve it through the use of an interpolation. The process will be explained for the 1-pulse fit only, but the interpolation is identical for 2 pulses, applied separately to t_1 and t_2.

Let t_1^{opt} be the notation for the optimal value of t_1 found by the previous method which minimizes $\chi_t^2(t_1)$. Because of the 1 ns resolution of the ARSs, the true minimum of $\chi_t^2(t_1)$ is not actually reached for $t_1 = t_1^{opt}$, but rather for a value within the interval $]t_1^{opt} - 1, t_1^{opt} + 1[$. In order to obtain an approximation of this value more accurate than t_1^{opt}, $\chi_t^2(t_1)$ can be locally parametrized by a function whose minimum can be found analytically. The accuracy of the minimum found then depends on how well the parametrization actually describes $\chi_t^2(t_1)$.

In practice, χ_t^2 is locally parametrized by the second order polynomial expression:

$$\chi_t^2(t) = at^2 + bt + c, \tag{4.11}$$

whose minimization yields:

$$t_1^{interpol} - t_1^{opt} = \frac{-b}{2a} = \frac{\chi_t^2(t_1^{opt} - 1) - \chi_t^2(t_1^{opt} + 1)}{2\left(\chi_t^2(t_1^{opt} + 1) + \chi_t^2(t_1^{opt} - 1) - 2\chi_t^2(t_1^{opt})\right)}. \tag{4.12}$$

This interpolation allows to improve the time resolution on t_1 to below 1 ns.

4.2.5 Optimizing the fits thresholds χ_0 and χ_1

First, the values of χ_0 and χ_1 are converted from ADC channels to MeV using the calorimeter energy calibration coefficients. By expressing χ_0 and χ_1 in MeV instead of ADC channels, the thresholds remain constant despite the calorimeter darkening due to radiation damage.

In order to determine the value of the threshold χ_0, the evolution of several variables with respect to χ_0 has been studied:

- the calorimeter energy resolution, using elastic scattering data $ep \to e'p'$ (see Fig. 4.4);

- the invariant mass $W^2 = (p+e-e')^2$ mean value and resolution for elastic scattering data $ep \to e'p'$;
- the $ep \to e'X\gamma$ missing mass mean value and resolution;
- the $ep \to e'X\pi^0$ missing mass mean value and resolution;
- the number of events with an invariant mass compatible with π^0, normalized by the total number of events;
- the π^0 invariant mass mean value and resolution;
- the number of ARS signals with zero pulse fitted normalized by the total number of events and number of calorimeter blocks;
- the number of ARS signals with one pulse fitted normalized by the total number of events and number of calorimeter blocks;
- the computation time of the fitting process.

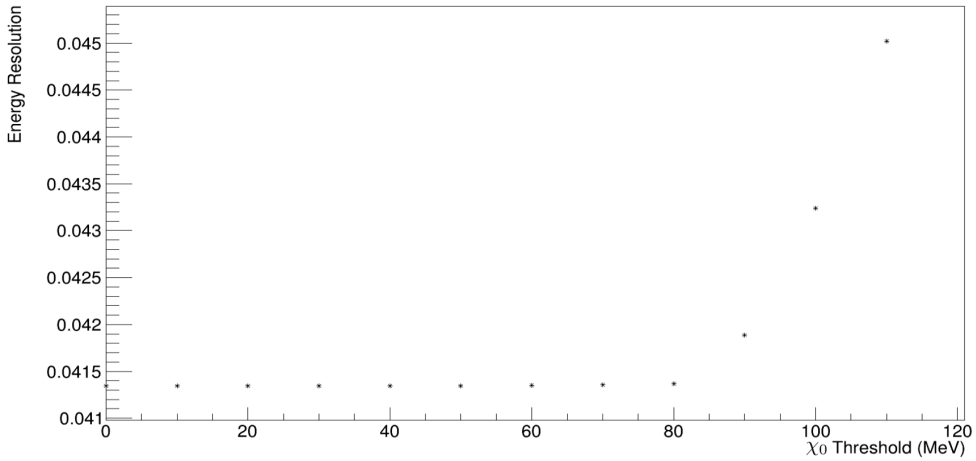

Figure 4.4: Evolution with respect to χ_0 of the calorimeter relative energy resolution. For $\chi_0 < 80$ MeV, the relative energy resolution at 4.5 GeV is stable at $\sim 4.13\%$. For $\chi_0 > 80$ MeV, the energy resolution starts degrading.

Every studied variable show a plateau for $\chi_0 \leq 60$ MeV, followed by a steep slope for $\chi_0 \geq 80$ MeV implying a degradation of the results (see Fig. 4.4). This means that for values of χ_0 larger than 80 MeV, some pulses start to be missed by the algorithm. On the other hand, choosing χ_0 lower than 60 MeV would not change anything in a significant way. As a consequence, the threshold $\chi_0 = 60$ MeV was picked as a conservative value.

In order to determine the value of the threshold χ_1, a study very similar to the one for χ_0 has been performed, with the following differences:

- the number of ARS signals with zero pulse and one pulse fitted was dropped;
- the number of events with two ARS pulses fitted normalized by the total number of events was added.

The use of the baseline in the two-pulse fitting procedure was also discussed. Indeed, in previous works [78], it was found out that if the baseline was fitted alongside two pulses, sometimes, a single pulse could be fitted by a very large baseline and two pulses with negative amplitude on each side. In order to determine whether the baseline can be used in the two-pulse fit procedure of this experiment, the evolution with respect to χ_1 of the number of events with two ARS pulses fitted with a negative amplitude, normalized by the total number of events, was added. Furthermore, every previous variable has been studied in a case with the baseline added and a case without the baseline.

However, no clear indication for an optimal value of χ_1 was found. As long as χ_1 is not too small, it has an extremely low impact, as there are actually very few piled up events. Small values of χ_1 only pick up very low energy noise or fluctuations which are of no interest.

In the end, the value $\chi_1 = 300$ MeV was chosen, as it seemed to provide a good calorimeter resolution and keep the number of pulses with a negative amplitude to a negligible level while still fitting a few two-pulse signals with a correct sign (see Fig. 4.5). The addition of the baseline to the two-pulse fit seemed to provide slightly better results than without the baseline and was thus kept in the fitting process.

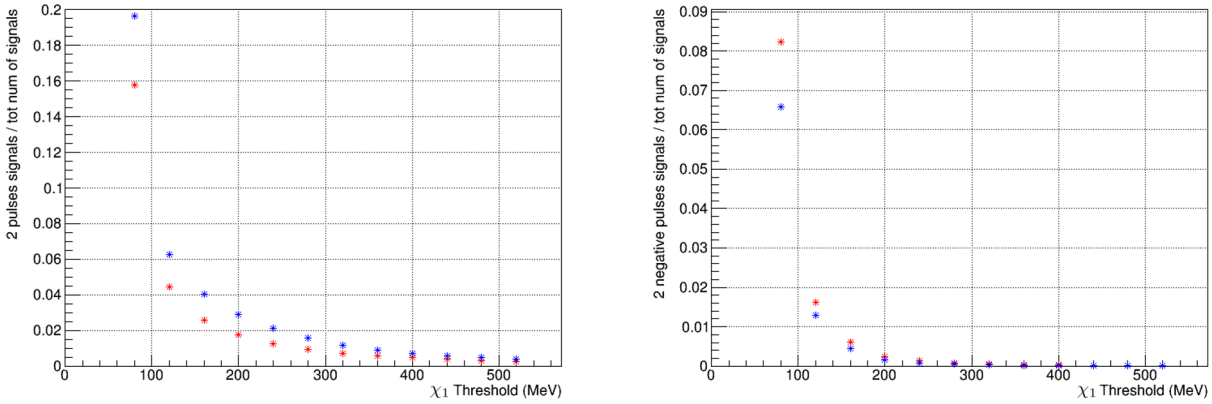

Figure 4.5: Left (Right): evolution with respect to the threshold χ_1 of the ratio of the number of events with two pulses fitted with correct (incorrect) sign, over the total number of events. The blue (red) points correspond to a two-pulse fit procedure with (without) a baseline.

4.2.6 Time windows

The analysis window $[i_{min}, i_{max}]$ could be the whole ARS sampling window [0,127], but a more optimized choice can be made. First, an ARS pulse is approximately 30 ns wide: using the whole 128 ns window would be a waste of computation time. Furthermore, reducing the window size avoids disturbances from background pulses at the edges of the 128 ns window which are of no interest. On the other hand, one wants to keep the analysis window large enough to be able to catch two pulses when required. For these reasons the analysis window has been set to be 80 ns wide, and is defined as $[20 + t^{ARS}_{offset}, 100 + t^{ARS}_{offset}]$, with t^{ARS}_{offset} the time offset between the ARS signals and the reference shapes. The offset is due to the fact that the reference shapes are computed using elastic scattering data which are taken with the calorimeter 6 m away from the target, while DVCS data are taken with the calorimeter 1.5 m to 3 m away from the target, and a photon requires approximately 13 ns to travel 4 m. In the case that t^{ARS}_{offset} is overly large, care must be taken that the edges of the analysis window do not overflow the [0,127] window. For this reason, in reality, the analysis window $[i_{min}, i_{max}]$ is defined by:

$$i_{min} = max(5, 20 + t^{ARS}_{offset}), \tag{4.13}$$

$$i_{max} = min(123, 100 + t^{ARS}_{offset}). \tag{4.14}$$

The χ^2 window $[\chi^2_{min}, \chi^2_{max}]$ could be identical to $[i_{min}, i_{max}]$. However, when there is a pulse, the fit only needs to be accurate around its maximum, while fitting the signal far from the pulse holds little interest. In the specific case of two pile-up pulses, one is interested by the second pulse only if it is close to the first one, not if it is far away. In order to avoid unimportant effects from signals far from the expected pulse, the χ^2 window size is reduced compared to the analysis window. It has been set to be 40 ns wide, centered around the time t_{ref_shape} where the reference shapes reach their maximum amplitude, and corrected for the ARS time offset:

$$\chi^2_{min} = max(5, -20 + t_{ref\_shape} + t^{ARS}_{offset}), \tag{4.15}$$

$$\chi^2_{min} = min(123, 20 + t_{ref\_shape} + t^{ARS}_{offset}). \tag{4.16}$$

The t_1 window $[t_1^{min}, t_1^{max}]$ is set so that the pulse arrival time is searched between 25 ns below and 20 ns above the reference shape one, corrected for the ARS time offset:

$$t_1^{min} = -20 + t^{ARS}_{offset}, \tag{4.17}$$

$$t_1^{max} = 25 + t_{offset}^{ARS}, \tag{4.18}$$

and any pulse outside of this time window is deemed too out of range to be in coincidence with the electron detected in the spectrometer.

The t_2 window $[t_2^{min}, t_2^{max}]$ is broadened compared to the t_1 window in order to catch the pile-up events. The t_2 window is set so that the pulse arrival time is searched between 40 ns below and 40 ns above the expected one:

$$t_2^{min} = -40 + t_{offset}^{ARS}, \tag{4.19}$$

$$t_2^{max} = 40 + t_{offset}^{ARS}. \tag{4.20}$$

4.3 The coincidence time corrections

The next step of the analysis is the coincidence time corrections. For a DVCS event, in principle, the scattered electron and the emitted photon should be detected at exactly the same time. But in reality this is not exactly the case as several effects need to be corrected for. A good resolution on the coincidence time between the electron detected in the spectrometer and the photon detected in the calorimeter is extremely important as this allows to eliminate a lot of background events.

The reference shape arrival time is usually between 40 ns and 80 ns in the 128 ns ARS window, depending mainly on the calorimeter cabling. This, along with the ARS time offset described in section 4.2.6, is corrected in order to center the ARS times of arrival around 0.

The arrival times differ from one ARS channel to another, as well as from one event to another even within the same ARS channel. The distribution of the arrival times of every pulse is a Gaussian centered on 0 and with a resolution of a few nanoseconds, which is quite large compared to the 1 GHz sampling of the the ARSs. In order to improve the time resolution, the following corrections are taken into account:

- a correction for the trigger jitter, which is the relative time between the spectrometer and calorimeter triggers;
- a correction for the scintillator S2 paddles relative time due to differences in cabling;
- a correction for the photons travel time in S2 depending on the position where the electron hit the scintillator;
- a correction for the electron travel time through the spectrometer, depending on its dispersive angle and momentum.

Fig. 4.6 shows the impact of each additional correction on the coincidence time resolution. Applying every correction listed previously allows to improve the resolution to below 1 ns.

One will notice that the time-walk effect has not been accounted for. Indeed, depending on the signal rising time, which itself depends on its amplitude, the electron trigger timing may vary slightly from one event to another. However this correction was found to have an extremely small effect, and after application of every correction listed above, it was deemed to be unnecessary.

4.4 The calorimeter clustering algorithm

The next step is to reconstruct the photons hitting the calorimeter from the results of the waveform analysis. Indeed, a photon deposits its energy in a cluster made of several blocks of the calorimeter: the PbF_2 crystals have been designed so that most of the energy is left in one block, but a non-negligible fraction remains in the adjacent ones. Thus, the goal is now to gather the time, energy and position information from each individual ARS channels and combine them together to reconstruct information on the photon.

This section will present the clustering algorithm, applied event by event, which allows to reconstruct the photons.

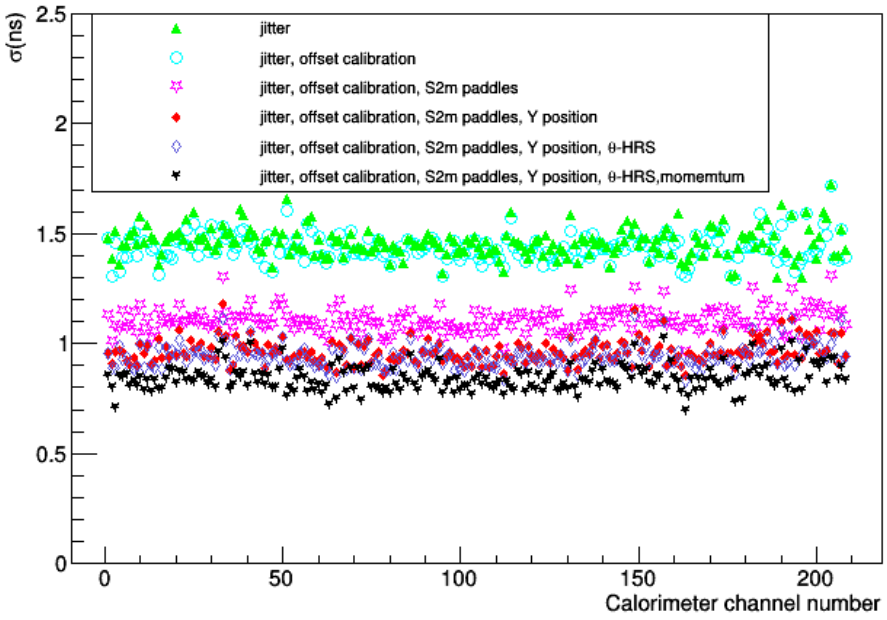

Figure 4.6: Improvement of the spectrometer-calorimeter coincidence time resolution with the progressive addition of every correction, for each of the 208 calorimeter ARS channels. Green triangles: added trigger jitter correction. Blue circles: added offset corrections to center the ARS pulses times of arrival around 0. Magenta stars: added S2 relative time correction. Red diamonds: added correction for travel time in S2. Blue diamonds: added correction for electron travel time depending on dispersive angle. Black stars: added correction for electron travel time depending on momentum. (Courtesy of Dr. M. Dlamini)

4.4.1 Cluster building: the cellular automaton algorithm

The first step of the process is to decide, for each event, which calorimeter blocks should be considered to build clusters, and which ones should be left out. A naïve choice could be to keep all the blocks. However, while this could work in an ideal case, the noise present in each block would lead to the overestimation of the photons energy. Another choice could be to apply an energy threshold to every block and keep only those with a high energy deposited in them. However, because the photon deposits most ($\sim 90\%$) of its energy in one block, the neighboring blocks might be rejected despite being relevant, leading to the underestimation of the photons energy.

A better choice is the application of an energy threshold to groups of blocks. For every possible combination of 2x2 neighboring blocks in the calorimeter, the clustering algorithm computes the group total energy as the sum of each individual block and compares it to the clustering energy threshold. If the group energy is higher than the threshold, all four blocks of the group are kept by the clustering algorithm. A block will usually belong to several groups of four (except for the corners of the calorimeter), but it only needs to belong to one group with a high enough energy to be kept (see Fig. 4.7). If two pulses are fitted in an ARS signal, the pulse with the largest amplitude is considered for this test. The clustering thresholds chosen for each kinematic are summarized in Tab. 4.1.

Kinematic setting	Clustering Threshold (GeV)	Expected DVCS photon energy (GeV)
36_1	3.0	4.6
36_2	3.8	5.2
36_3	4.8	6.5
48_1	2.0	2.8
48_2	3.0	4.6
48_3	4.0	5.7
48_4	5.8	7.4
60_1	2.8	4.5
60_3	5.0	7.0

Table 4.1: Summary of the clustering threshold and expected DVCS photon energy for each kinematic setting.

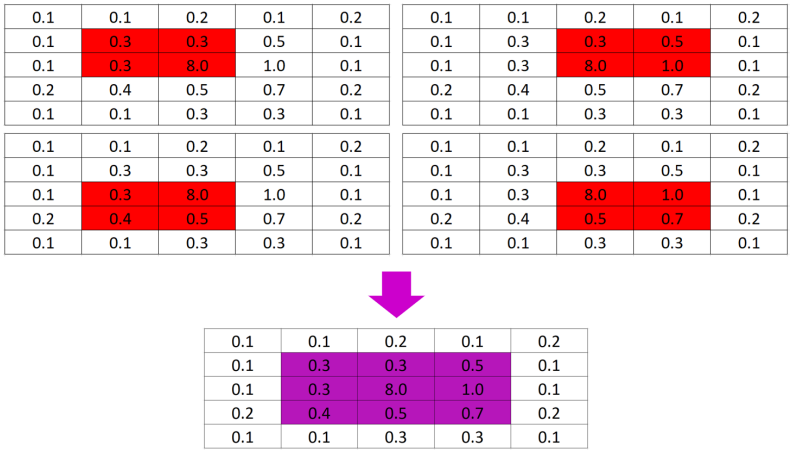

Figure 4.7: Example of possible combinations of four adjacent blocks with a clustering threshold of 4. The number written in each block represents the amount of energy deposited in them. A block only needs to belong to one group of 2x2 with a total energy larger than 4 to be kept for the next step of the clustering algorithm.

Then, the clustering algorithm looks at the corrected coincidence time of each block. If a block is out of time, then it contains energy from a photon belonging to another event, and it is thus discarded. The time resolution obtained previously allows to narrow the clustering time window to $[-3\text{ ns}, 3\text{ ns}]$. If two pulses are fitted in the ARS signal, the pulse with the arrival time closest to 0 is kept as long as it is in the $[-3\text{ ns}, 3\text{ ns}]$ time window, and the other pulse is discarded since it is less likely to be in coincidence with the spectrometer.

Finally, the clustering algorithm must associate the selected blocks to their respective clusters. In the ideal case where only one photon hits the calorimeter, then trivially, there exists only one cluster and every selected block belongs to it. However, several photons can hit the calorimeter simultaneously, whether they belong to the same event (for instance, a π^0 decaying into two photons) or different events happening at the same time.

The method used to separate several clusters is based on a cellular automaton [79]. To describe it, an analogy can be made with viruses propagation. Each block is associated with a value, initially equal to its energy. The algorithm then looks for local maxima: these blocks are the viruses. Then, at each step, each block takes the value of its highest-value neighbor, unless it has already been contaminated by a virus. A block taking the value of a virus is contaminated and becomes immune to further contamination. The algorithm stops when every block has been contaminated. The calorimeter blocks contaminated by the same virus then belong to the same cluster (see Fig. 4.8).

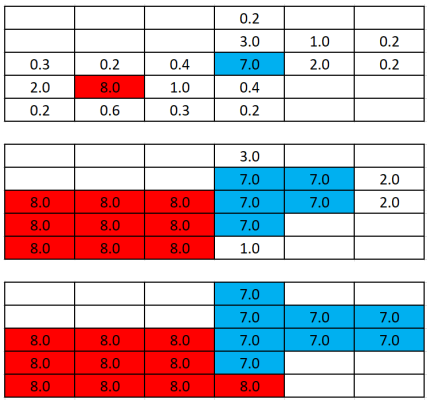

Figure 4.8: Illustration of the cellular automaton algorithm in a case with two clusters. Top: the starting value associated with each block is equal to their energy, the two local maxima (red and blue) are viruses. Middle: at the next step, every block except the ones already contaminated by viruses takes the value of their nearest highest neighbor. The blocks taking the values of the viruses become contaminated (red and blue). Bottom: the cellular automaton algorithm stops when every block has been contaminated.

4.4.2 Reconstructing cluster information

Once the relevant calorimeter blocks have been associated to their respective clusters, it is then possible to reconstruct the photon energy, time and position in the calorimeter.

The photon total energy E is computed as the sum of the energies E_i deposited in each block of a cluster:

$$E = \sum_i E_i \quad \text{with } E_i = C_i A_i, \tag{4.21}$$

where C_i are the calorimeter calibration coefficients and A_i are the amplitudes of the ARS pulses extracted during the waveform analysis.

The position x (y) of the photon in the calorimeter is computed as the sum of the cluster block positions x_i (y_i), weighted logarithmically by the relative energy deposited in each of them:

$$x = \frac{\sum_i w_i x_i}{\sum_i w_i} \quad \text{with } w_i = \max\left\{0, \left[W_0 + \ln\frac{E_i}{E}\right]\right\}, \tag{4.22}$$

$$y = \frac{\sum_i w_i y_i}{\sum_i w_i} \quad \text{with } w_i = \max\left\{0, \left[W_0 + \ln\frac{E_i}{E}\right]\right\}. \tag{4.23}$$

W_0 has two roles. First, it allows to tune the weight associated with each block: when $W_0 \to \infty$, the weights become independent from the relative energy deposit and each block is treated with the same importance. When $W_0 \to 0$, a larger weight is attributed to blocks with higher energy.

Second, W_0 acts as a threshold for blocks to participate in the position reconstruction: blocks in which the photon has deposited a relative energy smaller than e^{-W_0} are attributed a weight equal to 0, and are thus ignored in the computation.

The photon position x (y) in the calorimeter given by Eq. (4.22) ((4.23)) is not exact. First, it assumes that the energy is deposited at the surface of the calorimeter, which is not the case. The photon travels through a given distance inside the PbF_2 crystal before it starts to develop an electromagnetic shower. Let a be the shower depth, defined as the distance of the electromagnetic shower centroïd from the calorimeter surface along the propagation direction of the photon. Furthermore, the calorimeter is only a few meters away from the target and corrections must be applied to take into account the vertex position. In order to account for these two effects, the position x (y) of the photon at the surface of the calorimeter is corrected to become x_{corr} (y_{corr}):

$$x_{corr} = x\left(1 - \frac{a}{\sqrt{L_{vc}^2 + x^2}}\right), \tag{4.24}$$

$$y_{corr} = y\left(1 - \frac{a}{\sqrt{L_{vc}^2 + y^2}}\right), \tag{4.25}$$

with L_{vc} the distance of the calorimeter to the event vertex (see Fig. 4.9).

An optimization of the parameters a and W_0 performed first with a Monte-Carlo simulation and then with elastic scattering data yielded the results $a = 7$ cm and $W_0 = 4.3$. With the calorimeter 1.1 m away from the target, this allowed to achieve a spatial resolution of 3 mm at 3.0 GeV in the simulation, and 2 mm at 4.2 GeV with elastic scattering data [70]. However, the optimal values of the parameters a and W_0 depend on the photon energy. The study performed in [80] allowed to build parametrizations of a and W_0 with respect to the energy. The parametrization of a is given by:

$$a = 0.30E^{0.28} + 4.862, \tag{4.26}$$

with E the photon energy expressed in MeV, and a in cm. On the other hand, W_0 was found to depend weakly on the energy and the value $W_0 = 4.3$ was kept in this work. A spatial resolution of 3 mm was obtained in a Monte Carlo simulation for photons energy varying between 0.1 GeV and 5.0 GeV with the calorimeter 1.1 m away from the target [80].

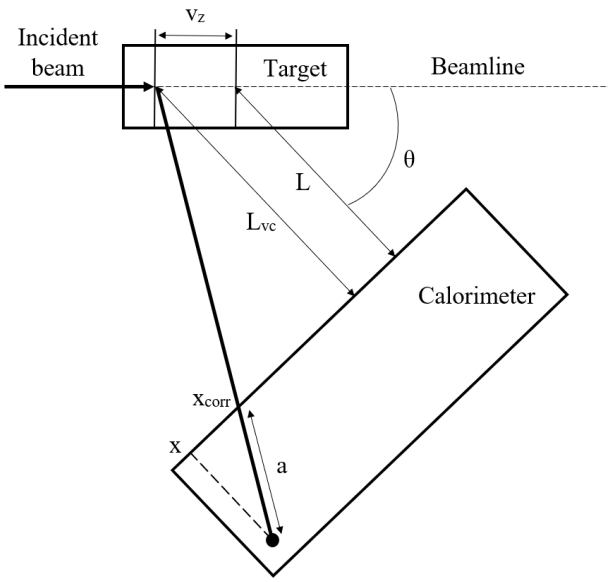

Figure 4.9: Schematic representation of the vertex and shower depth correction to the photon position in the calorimeter. For clarity, the vertex has been represented along the beam axis only (v_z), but transverse positions are taken into account as well. L is the distance of the calorimeter to the target center, while L_{vc} is the distance from the vertex to the calorimeter. θ is the calorimeter angle, and a is the shower depth, defined as the distance of the electromagnetic shower centroïd from the calorimeter surface, along its propagation direction.

Finally, the photon arrival time $t_{cluster}$ is computed as the sum of the corrected ARS times, weighted by the block relative energies:

$$t_{cluster} = \frac{\sum_i E_i (t_i - t_i^{corr})}{\sum_i E_i}, \tag{4.27}$$

where t_i are the ARS times and t_i^{corr} encompass all the corrections described in section 4.3.

4.5 Event selection and exclusivity

The next step of the data analysis is the event selection. There are two main goals:

- to select DVCS events, the exclusivity of the process must be ensured by identifying the scattered electron, the emitted photon and the recoil proton;
- to ensure the accuracy of the electron and the photon variables, DVCS events with unreliable reconstruction must be discarded. Corrections for the number of discarded events will be added afterward.

This section will now present the cuts applied to select DVCS events. However, the recoil proton identification will be explained in the next section, as the background subtraction is required beforehand.

4.5.1 Vertex cuts

As described previously, the target used for this DVCS experiment is a 15-cm-long cylindrical aluminum cell containing liquid hydrogen. Obviously, events with a vertex reconstructed outside of the target must be discarded. Furthermore, the electron beam might interact with the target aluminum walls instead of the liquid hydrogen, and such events must be removed as well.

Depending on the kinematic setting, using data taken with the optics target, the vertex resolution of the spectrometer has been measured between $\sim$ 2 mm and $\sim$ 5.5 mm. Taking into account these resolution effects, the cut consists of discarding events with a vertex less than 1 cm away from the target walls, as seen in Fig. 4.10. However, because of the Spring 2016 optics calibration difficulties (see section

3.2.2.3), kin48_2 suffers from a slightly worse vertex resolution than other kinematic settings. It was thus decided to use a larger cut of 1.3 cm instead of 1 cm for kin48_2.

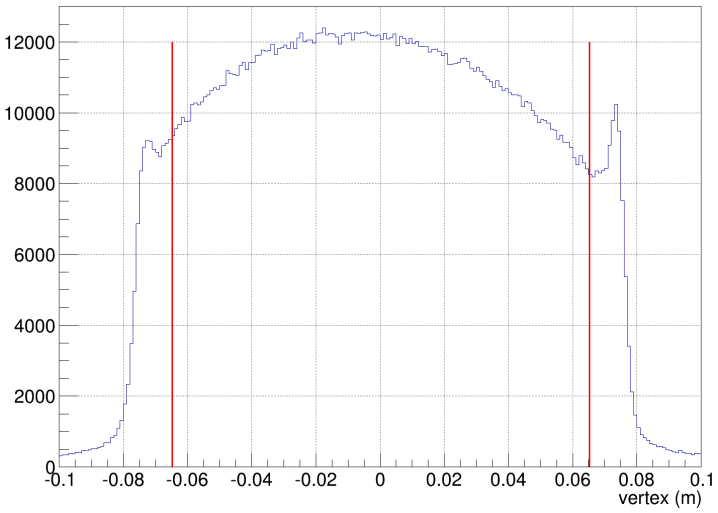

Figure 4.10: Vertex distribution of kin48_1. The target is a 15 cm long aluminum cell filled with liquid hydrogen. The distribution is not flat because of the spectrometer acceptance. The two peaks around -7.5 cm and 7.5 cm are the target aluminum walls. The vertex cuts (red lines) remove events with a vertex less than 1 cm away from the target edges to avoid contamination from the aluminum walls.

In an ideal case, the spectrometer should be pointing toward the center of the target. The origin for the reconstructed vertex is the intersection point between the spectrometer axis and the target axis. This way, the target center coïncides with 0 and its walls are located at -7.5 cm and 7.5 cm (see Fig. 4.10). Then, a 1 cm vertex cut consists simply in keeping events with a vertex between -6.5 cm and 6.5 cm. In reality, a small misalignment of the spectrometer direction with the target center can exist and will change from one kinematic setting to another as the detector is moved to different angles. This misalignment, combined with uncertainties on beam position and raster corrections, results in an apparent offset of the target position along the beam axis, as the reconstructed vertex origin no longer coïncides with the real target center. This apparent offset needs to be taken into account in the vertex cuts.

To measure the offset, data is taken on the optics target and the assumption is made that its central carbon foil is perfectly aligned with the center of the liquid hydrogen cell. The position of the reconstructed central foil then yields the offset (see Tab. 4.2). However, the alignment of the optics target and cryogenic cells is made at room temperature, and the cooling of the hydrogen target can move the cell because of material contraction. This factor leads to a small uncertainty on the targets positions.

Kinematic setting	Vertex offset (mm)
36_1	-4.7
36_2	+2.5
36_3	+4.6
48_1	+0.3
48_2	+1.7
48_3	+3.4
48_4	+3.9
60_1	+4.0
60_3	+3.3

Table 4.2: Summary of the vertex apparent offset for each kinematic setting.

Despite taking into account the vertex offset, the 1 cm cuts applied to kin36_1 were not satisfactory, as shown in Fig. 4.11: the offset seems to have been underestimated. Possible explanations are the uncertainty on the targets alignment, or the lack of calibration for one BPM (see section 2.2.1.2). For this kinematic setting, it was thus decided to increase the cut to 1.3 cm for the positive values of the vertex, to ensure complete elimination of the aluminum wall contamination.

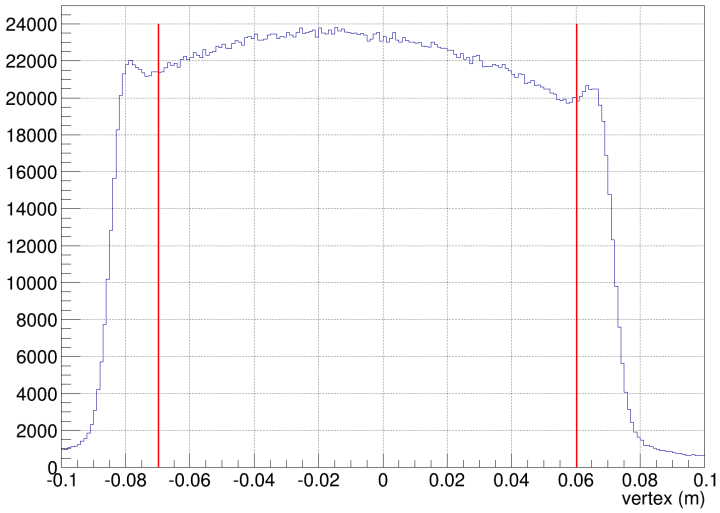

Figure 4.11: Vertex distribution of kin36_1. The red lines represent the 1 cm vertex cuts taking into account the reconstructed vertex offset. The cut on positive vertex values (right line) is too close to the target aluminum wall.

4.5.2 Spectrometer cuts

Cuts applied to the spectrometer aim at identifying the electrons and ensure the quality of their reconstructed variables. Cuts are also applied to ensure control over the spectrometer acceptance.

4.5.2.1 Electron identification

The identification of electrons from pions π^- is allowed by the Cherenkov and Pion Rejectors detectors: pions deposit almost no energy in them, contrary to the electrons. By discarding events with a low energy deposited in the Cherenkov and both layers of Pion Rejectors, one is able to eliminate π^- and keep only electrons. The cutting thresholds have been set to be 150 ADC channel for the total energy deposited in the Cherenkov, 200 ADC channels for the total normalized energy deposited in the first layer of Pion Rejectors, and 600 ADC channels for the total energy deposited in both layers [81] (see Fig. 4.12).

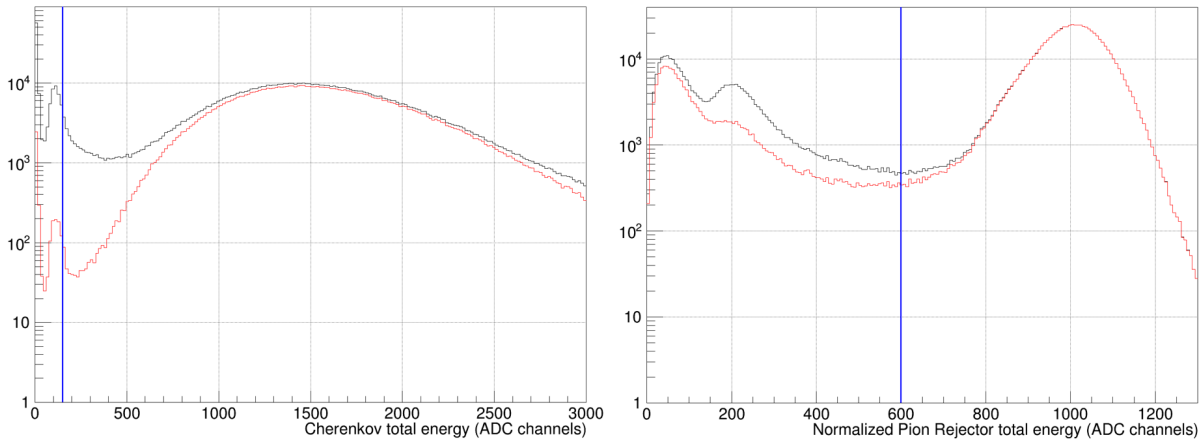

Figure 4.12: Left: distribution of the Cherenkov total energy with (red) and without (black) application of the 600 ADC cut on the Normalized Pion Rejectors total energy. Right: distribution of the Normalized Pion Rejectors total energy with (red) and without (black) application of the 150 ADC cut on the Cherenkov total energy. The blue lines represent the cuts. Both plots are from kin48_1 data. Electrons deposit a lot of energy in both detectors, while π^- do not.

4.5.2.2 Single track cuts

The particles tracking is performed by the two Vertical Drift Chambers. Each VDC is made of two wire planes, and at least one cluster in each wire plane is required to reconstruct a particle track. If several particles are detected at the same time, several tracks are reconstructed, and the event is discarded since it is difficult to know which track is associated to which particle, and thus which one should be considered for the DVCS event.

Furthermore, it is also possible for a single particle to create several clusters in the same wire plane. If this happens in more than one wire plane, then the current algorithm reconstructs several tracks or track candidates and is unable to find the correct one reliably [82]. Such events must be eliminated as well.

As a consequence, in order to ensure tracking quality, events where one wire plane at most has several clusters are the only ones kept. If more than one wire plane has several clusters, the event is discarded.

4.5.2.3 Acceptance cuts: the Hall A R-function

In order to ensure that the detected electrons are well within the spectrometer acceptance, cuts need to be applied. These cuts also ensure good control and computation of the non-trivial spectrometer acceptance.

The challenge of these cuts is that the spectrometer acceptance is 5-dimensional (x_{tg}, y_{tg}, θ_{tg}, ϕ_{tg}, δ_{tg}, see section 3.2.2), and the acceptance in the different variables are correlated. A naïve solution consisting in applying 1-dimensional cuts on each of the five variables would be extremely inefficient as parts of the spectrometer acceptance would be lost.

A better approach to the problem consists in applying a cut on the distance between the electron and the edges of the spectrometer acceptance. The determination of this cut is performed in two steps [83]:

- first, the different variables entering the spectrometer acceptance are plotted against one another to determine the limits of the spectrometer acceptance in different 2D planes (see Fig. 4.13). Then, a function called "R-function", developed in [84], computes for every electron their distance, in radians, to the closest boundary of the spectrometer acceptance in (θ_{tg}, ϕ_{tg}) which depends on the values of y_{tg} and δ_{tg}. This distance is called "R-value"; it is negative if the electron is outside of the defined spectrometer acceptance, positive if it is inside, and equal to 0 if it is exactly on the boundary. One will notice that the component x_{tg} is ignored in this cut: it is already constrained in [−2 mm, 2 mm] by the beam position, which is smaller than the spectrometer acceptance;

- for each kinematic setting, the data R-value distribution is compared to a Geant4 simulation of the experiment. As shown in Fig. 4.14, there is a positive threshold above which the data and Geant4 R-value distributions are matching. This threshold is called the R-cut, and by requiring the electrons R-values to be larger than the R-cut, this ensures that they are well inside the spectrometer acceptance. It will also allow to compute accurately the experiment acceptance.

The use of the R-function has been shown to be twice as efficient as applying 1-dimensional cuts on each variable [84]. The values of the R-cuts for each kinematic setting are shown in Tab. 4.3.

Kinematic setting	R-cut (rad)
36_1	0.003
36_2	0.005
36_3	0.005
48_1	0.003
48_2	0.003
48_3	0.006
48_4	0.0025
60_1	0.005
60_3	0.005

Table 4.3: Summary of the R-cuts values for each kinematic setting [86].

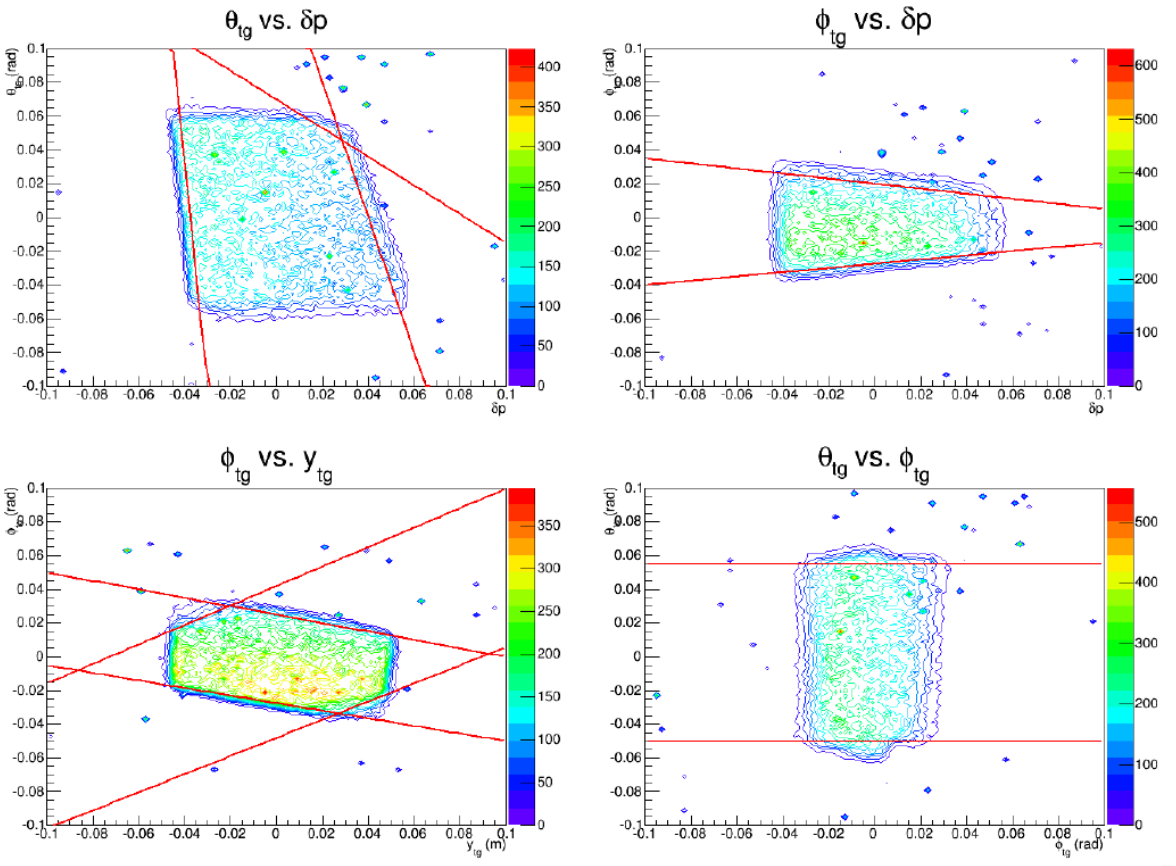

Figure 4.13: Top left: distribution of θ_{tg} against δ_{tg}. Top right: distribution of ϕ_{tg} against δ_{tg}. Bottom left: distribution of ϕ_{tg} against y_{tg}. Bottom right: distribution of θ_{tg} against ϕ_{tg}. All four plots are from kin48_1. The red lines define the edges of the spectrometer acceptance in these planes. Some planes boundaries are not present as they would be redundant with the limits set in other planes. (Figure extracted from [83]).

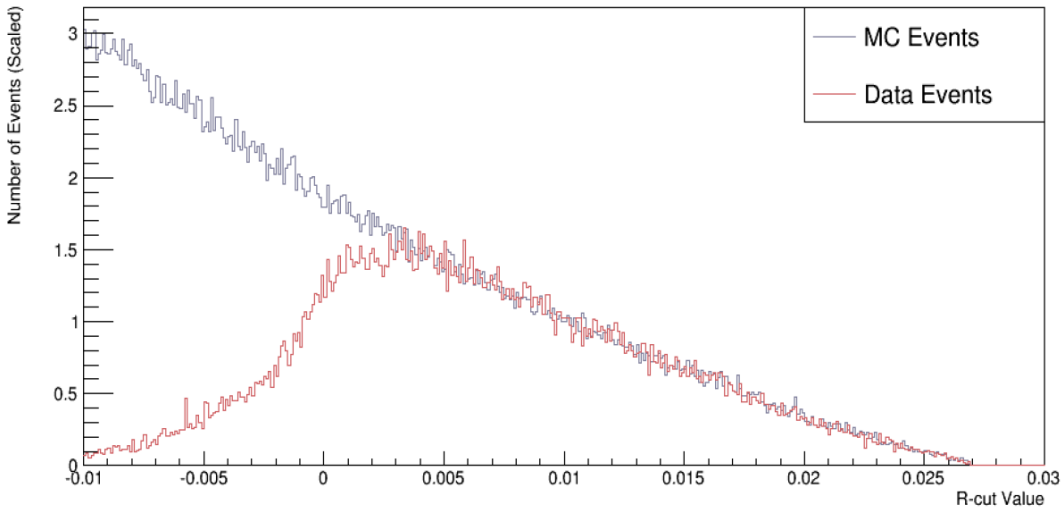

Figure 4.14: Normalized distributions of the electrons R-values for kin48_1 from the data (red) and a Geant4 simulation (blue). For R-values larger than 0.003, the distributions from the data and the Geant4 simulation are matching. (Figure extracted from [85]).

4.5.3 The calorimeter cuts

In order to ensure the quality of the photon reconstruction, cuts need to be applied on the calorimeter. First, as a single photon is expected in the final state, events with more than one reconstructed cluster are discarded for the DVCS analysis.

As explained in section 4.4, the clustering threshold is not enough to fully avoid the reconstruction of low energy photons. Applying a cut on the photon minimum energy is thus required. This cut is at least equal to the clustering threshold. Care has also been taken so that the energy cut is higher than the hardware threshold, which effectively changes with time as the PbF_2 crystals are damaged by radiations. Chosen cuts for every kinematic setting are displayed in Tab. 4.4.

Kinematic setting	Minimum photon energy required (GeV)
36_1	3.0
36_2	4.27
36_3	4.8
48_1	2.0
48_2	3.0
48_3	4.0
48_4	5.8
60_1	2.8
60_3	5.0

Table 4.4: Summary of the photon energy cuts for each kinematic setting.

Furthermore, even though the Molière radius of the PbF_2 crystals is small (2.2 cm), if a photon hits a block on the edges of the calorimeter, a non negligible part of its energy can still leak outside of the calorimeter through the sides of the crystal. In order to avoid an underestimation of the photon energy because of those leaks, events for which a cluster position is reconstructed in an edge block, less than 3 cm away from the sides of the calorimeter, are discarded. An additional cut on the cluster position superseding this one will be explained in section 4.6.2.

4.5.4 The beam helicity cut

In order to measure polarized DVCS cross sections, the beam helicity needs to be known. As described in section 2.1, the beam helicity is flipped at a frequency of 30 Hz by a Pockels cell, and around the moment when it is flipped, there is a 60 μs time window where the beam helicity is uncertain. As a consequence, the events occurring during that time must be discarded. One will notice that this cut is specific to the measurement of polarized cross sections, and is unnecessary for unpolarized ones.

4.6 Background subtraction

The next step of the analysis is the background subtraction. Indeed, the cuts described in the previous section are not enough to ensure that the selected events are all DVCS ones. Several sources of contamination compatible with the previous cuts need to be accounted for:

- accidental coincidences: requiring the photon to be detected in coincidence with the electron usually ensures that they are involved in the same event. However, it is also entirely possible for the photon to be produced in an event different from the electron and occurring accidentally at the same time;
- π^0 contamination: Deeply Virtual π^0 Production is a process where a π^0 is produced instead of a photon: $ep \to e'p'\pi^0$. The π^0 itself decays into two photons which are then detected in the calorimeter. However, if one of the two photons is missed, the π^0 event can be wrongly identified as a DVCS one;
- Semi-Inclusive DIS (SIDIS) associated with DVCS: these events have a final state similar to DVCS but with additional particles $ep \to e'p'\gamma X$. They can be wrongly identified as DVCS events if the additional particles of the final state are not detected. In principle, this contamination can be easily eliminated by cuts on the missing mass M_X^2. Indeed, the SIDIS process with the lowest missing mass is $ep \to e'p'\gamma\pi^0$, with $M_X^2 \approx 1.15$ GeV^2, which is larger than for DVCS. However, because of resolution effects, some residual contamination can still affect DVCS and a careful study of its systematic uncertainty is required. This study will be detailed in section 5.2.2.1.

- Associated DVCS through a resonance: these events have a final state where the recoiling proton is replaced by a resonance, like $ep \to e'\Delta\gamma$, for instance. Since the recoiling hadron is not detected, these events can be wrongfully identified as DVCS ones. However, the resonance yielding the lowest missing mass squared is the $\Delta(1232)$, which has a missing mass around 1.5 GeV^2, and a width of approximately 0.014 GeV^2. Moreover, its cross section is expected to be small at this experiment kinematic settings [87]. As a consequence, similarly to SIDIS, the contamination from resonances is expected to be very small for missing masses smaller than 1.15 GeV^2. Resonances will be treated jointly with SIDIS and in the following of this document, for convenience, only SIDIS contamination will be mentioned and the joint contribution of resonances will be implied.

This section will now provide details about the subtractions of the accidental events and π^0 contamination.

4.6.1 The accidental events subtraction

By selecting photons in the [−3 ns, 3 ns] time window when performing the clustering, two kind of coincidences are selected: true coincidences where the photon and the electron come from the same event, and accidental coincidences where they belong to different events which occurred close in time. In the latter case where electron and photon do not come from the same event, these detected coincidences are called accidental events.

In order to subtract this contamination, one relies on the fact that the probability for accidental events to be detected is independent from the clustering time window, as long as its width is unchanged. For instance, the number of accidental events in the window [−3 ns, 3 ns] is the same as in [−50 ns, −44 ns]. On the other hand, true coincidences will only be detected in the [−3 ns, 3 ns] time window.

In order to subtract the accidental events contamination, the clustering is also performed in a 6 ns wide time window taking care not to overlap [−3 ns, 3 ns]. The events reconstructed in this second time window and abiding by the selection cuts of section 4.5 are then subtracted from those identified in [−3 ns, 3 ns].

Care must be taken when choosing the time window for accidental events subtraction because of the beam structure. Indeed, as described in section 2.1, the beam has a frequency of 250 MHz and electron packages are sent every 4 ns. This gives the beam a time structure that needs to be taken into account: the window must be shifted by a multiple of 4 ns compared to [−3 ns, 3 ns]. For these reasons, the time window for accidental events subtraction has been chosen to be [−11 ns, −5 ns] (see Fig. 4.15).

In order to reduce the effect of statistical fluctuations, the clustering is also performed in [5 ns, 11 ns], and the number of events in both windows are averaged before being subtracted from the events in [−3 ns, 3 ns].

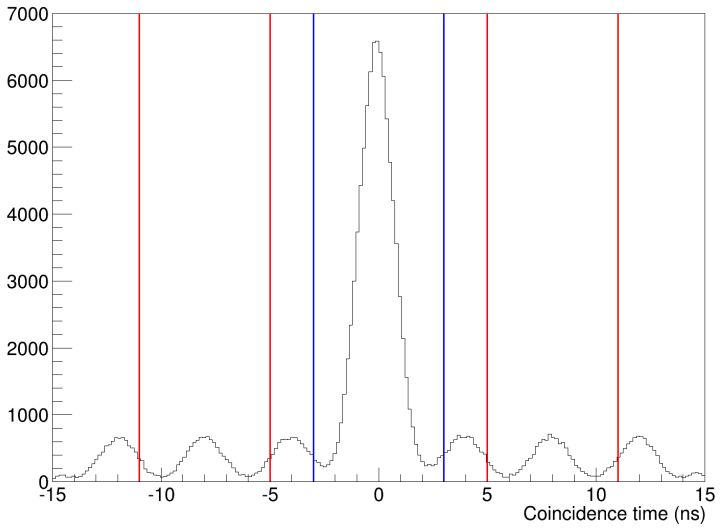

Figure 4.15: Coincidence time spectrum for kin48_4. The main coincidence time window [−3 ns, 3 ns] is delimited by the blue lines. The accidental events subtraction windows [−11 ns, −5 ns] and [5 ns, 11 ns] are located between the red lines. They are shifted by 8 ns with respect to the main coincidence time window to account for the 4 ns time structure of the beam.

4.6.2 The π^0 contamination subtraction

In $\sim 99\%$ of cases, π^0 decays into two photons which can then be detected in the calorimeter. In the π^0 rest frame, this decay is symmetric and the photons are emitted back to back. However, to switch to the laboratory frame, a Lorentz boost must be applied. If the decay is perpendicular to the π^0 momentum, then both photons have half of the π^0 initial energy (see top half of Fig. 4.16). However, in an asymmetric case, one of the two photons will get more energy than the other (see bottom half of Fig. 4.16). In extreme scenarios, a photon can acquire almost all of the π^0 energy while the other one has almost nothing. In this configuration, the photon with low energy can be missed by the calorimeter, while the one with high energy may yield a missing mass M_X^2 compatible with DVCS. This results in the wrongful identification of some π^0 events as DVCS ones.

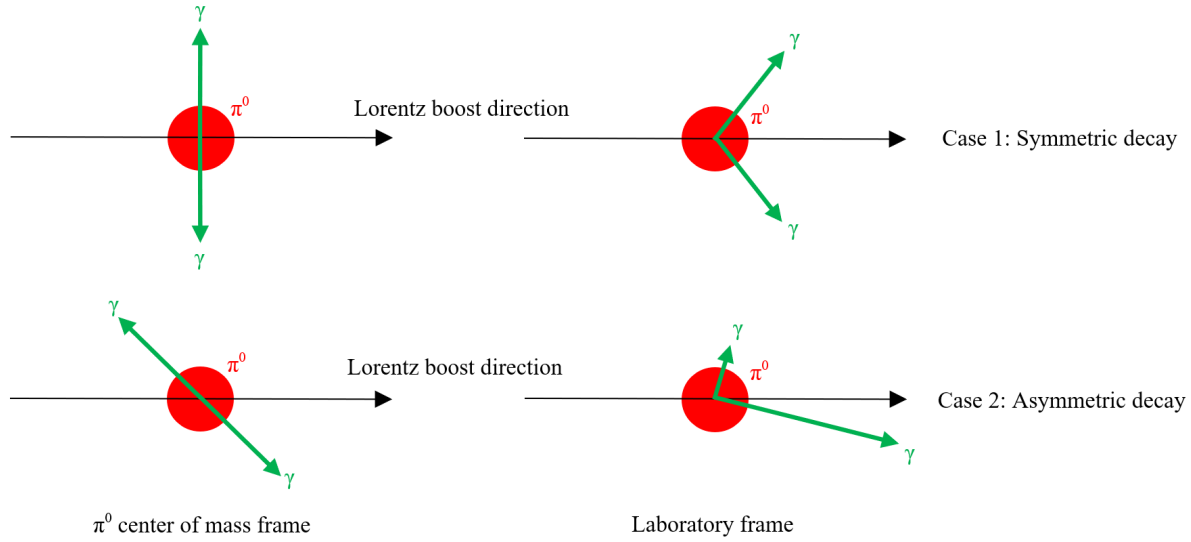

Figure 4.16: Representation of possible configurations of π^0 decays into two photons. Top: a symmetric decay with respect to the π^0 momentum results in the two emitted photons to have the same energy in the laboratory frame. Bottom: an asymmetric decay with respect to the π^0 propagation direction results in one photon having more energy than the other in the laboratory frame. In extreme cases, one photon can acquire almost all the energy of the initial π^0.

The π^0 contamination can be estimated from the data with the help of a Monte-Carlo simulation. First, π^0 are identified in the data by applying the following cuts:

- the photons from the decay must hit a calorimeter block that is not on the edge of the detector;
- the photon energies must be larger than the calorimeter trigger threshold;
- the invariant mass must be compatible with a π^0.

For each π^0 identified in the data, 5000 decays into two photons are simulated. The decays are generated isotropically in the π^0 rest frame and then a Lorentz boost corresponding to the π^0 momentum in the laboratory frame is applied. For each decay, either 0, 1 or 2 simulated photons will be considered detected, depending on whether they abide by the two first cuts used for π^0 identification, defined previously.

For each π^0, out of the 5000 simulated decays, one then counts the number n_0 (respectively n_1 and n_2) of cases where 0 (respectively 1 and 2) photons are detected. In the case where only one photon is detected, the simulation also computes every DVCS related variable necessary for the data analysis as if the photon was emitted by a DVCS event.

In order to eliminate the π^0 contamination, the simulated events where only one photon is detected are subtracted from the DVCS data with a weighting factor. The weighting factor is made of two parts. A first normalization factor

$$\frac{1}{5000}, \tag{4.28}$$

takes into account the number of simulated decays.

A second normalization factor

$$\frac{1}{\frac{n_2}{5000}} = \frac{5000}{n_2}, \tag{4.29}$$

takes into account the fact that the number of π^0 detected in the data is actually smaller than the total number of π^0 produced since some photons have been missed.

Finally, the weighting factor applied to the simulated events is:

$$\frac{1}{5000}\frac{5000}{n_2} = \frac{1}{n_2}. \tag{4.30}$$

This method presents the main advantage that it uses experimental π^0 data in order to subtract the π^0 contamination. The Monte Carlo simulation only intervenes in the isotropic decay of the detected π^0 into two photons, and the cross section of the π^0 production process is taken into account by using experimental π^0 data. An alternative method using a simulation to generate π^0 events would require a parametrization of the cross section of the π^0 production, which would make the subtraction model-dependent.

The efficiency of this subtraction technique was checked against a Geant4 simulation. In the simulation, π^0 events are generated and are then kept if 1 or 2 photons are detected in the calorimeter. From the generated π^0 data with two photons detected, the Monte Carlo method described previously is applied, and its results are compared to the simulated data with only one photon detected. As can be seen in Fig. 4.17, the π^0 contamination subtraction technique is efficient on all the surface of the calorimeter except its edges and corners.

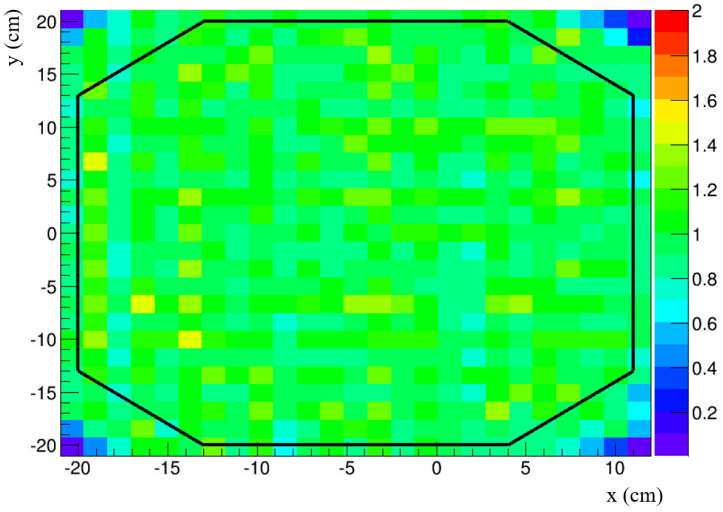

Figure 4.17: Efficiency map of the π^0 contamination subtraction technique depending on the position of the photon in the calorimeter for kin60_3. The efficiency is obtained by computing the ratio of the number of one-photon events obtained from the Monte-Carlo technique over the number of similar events generated by the Geant4 simulation. The Monte-Carlo technique works very well over all the surface of the calorimeter except its edges and corners. The black lines represent the octagonal cut that needs to be applied in order to ensure the efficiency of the π^0 contamination subtraction.

These inefficiency areas are the result of an acceptance effect: the calorimeter is unable to efficiently detect π^0's there because of the high probability for at least one photon to be outside of the detector acceptance. As a consequence, an additional geometrical cut must be added to the one described in section 4.5.3 to ensure the efficiency of the π^0 contamination subtraction. This octagonal cut is shown

in Fig. 4.17 and corresponds to the set of equations:

$$\begin{cases} x \leq 11\ cm \\ x \geq -20\ cm \\ y \leq 20\ cm \\ y \geq -20\ cm \\ y \leq x + 33\ cm \\ y \leq -x + 24\ cm \\ y \geq -x - 33\ cm \\ y \geq x - 24\ cm \end{cases} \tag{4.31}$$

As it is actually more restricting, the octagonal cut hereby supersedes the previous rectangular one. This cut is identical for every kinematic setting except kin48_4 for which the calorimeter is at an extremely small angle with respect to the beam line. The beam line shielding that was supposed to protect only the first column of blocks of the calorimeter turned out to mask a larger area of the detector than expected. This results in an inefficient detection of particles by the shielded area of the calorimeter as can be seen in Fig. 4.18 and a further restriction on the octagonal cut is required. For kin48_4, in Eq. (4.31), $x \leq 11$ cm is replaced by $x \leq 7.5$ cm.

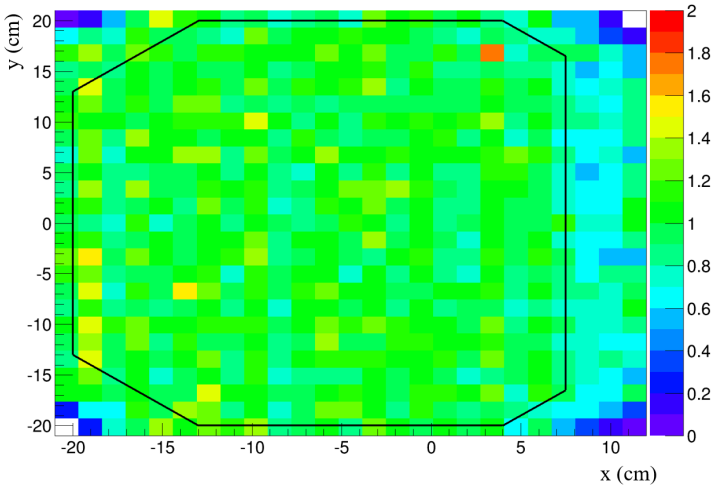

Figure 4.18: Efficiency map of the π^0 contamination subtraction technique depending on the position of the photons in the calorimeter for kin48_4. Because of the beam line shielding masking part of the calorimeter, a further restriction on the octagonal cut is required.

4.6.3 Identification of the recoil proton through the missing mass technique

As described in section 2.3, the recoil proton is not detected but can be identified by a cut on the missing mass. The squared DVCS missing mass is defined as $M_X^2 = (e + p - e' - \gamma)^2$, where e, p, e' and γ are notations for the four-vectors of the initial electron, initial proton, scattered electron and emitted photon, respectively. By conservation of energy and momentum, for DVCS, M_X^2 should be equal to the squared mass of the (recoil) proton, which is roughly equal to 0.88 GeV^2. In practice, because of resolution effects and energy calibration uncertainties, the squared missing mass resolution shows a peak close to the expected value (Fig. 4.19).

Selecting events which have a squared missing mass in the 0.88 GeV^2 peak allows to identify the recoil proton and ensures the exclusivity of the DVCS process. However, the choices of the missing mass cuts are one of the main source of systematic uncertainties of this experiment and will be discussed in section 5.2.2.1.

4.7 Corrections

Corrections are applied to take into account a number of events either discarded by the selection process, or simply missed during the experiment. This section will now describe these various corrections, except for the radiative ones which will be dealt with in section 5.1.2.

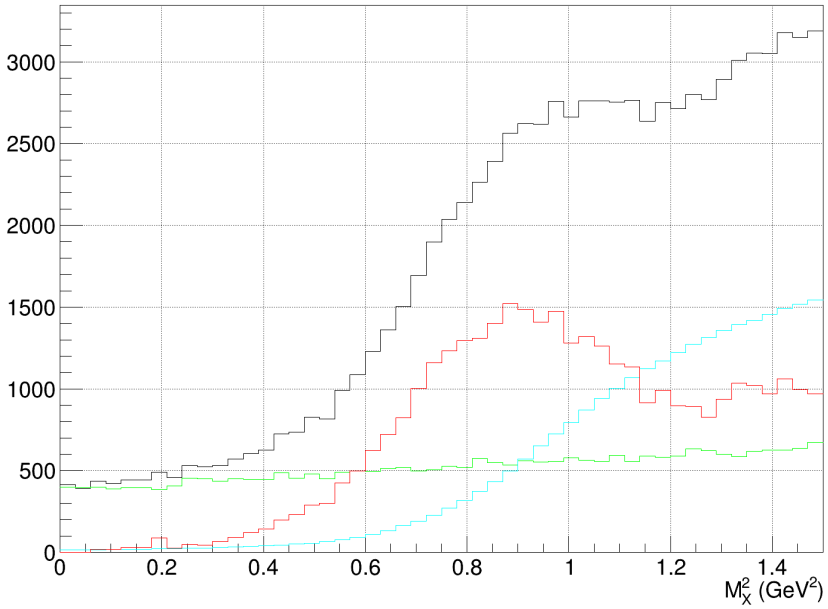

Figure 4.19: Distribution of the DVCS missing mass $M_X^2 = (e + p - e' - \gamma)^2$ for kin48_1 data. Black: DVCS missing mass before contamination subtraction. Red: DVCS missing mass after accidental and π^0 contamination subtractions. Green: Accidental events. Blue: π^0 contamination.

4.7.1 Trigger efficiency

The Cherenkov detector and scintillators S2 which form the spectrometer part of the DVCS trigger do not have a 100% efficiency. This implies that some DVCS events can be missed because the electron was not detected by the Cherenkov detector or S2. To avoid an underestimation of the number of DVCS events, their efficiency must be taken into account.

Efficiency measurements can be performed in dedicated runs. The trigger is set to be the coincidence of two detectors and the efficiency of a third detector can be computed as the ratio of the number of events it detected over the number of triggers. The efficiency of all three detector can be measured by cycling through which detectors are used as trigger. In this case, the scintillator S0 is used with S2 and the Cherenkov detector to measure their respective efficiencies.

Several efficiency measurements have been performed through the experiment and their results can be found in [88]. As the efficiencies did not change significantly from one measurement to another, it was decided to use averaged values for each kinematic setting (see Tab. 4.5).

Kinematic setting	S2 efficiency η_{S2}	Cherenkov efficiency η_{CER}
36_1	0.9974	0.9984
36_2	0.9969	0.9971
36_3	0.9961	0.9980
48_1	0.9964	0.9970
48_2	0.9964	0.9970
48_3	0.9964	0.9970
48_4	0.9964	0.9970
60_1	0.9968	0.9987
60_3	0.9960	0.9971

Table 4.5: Summary of the S2 scintillators and Cherenkov detector efficiencies for each kinematic setting.

The efficiency correction is applied by dividing the measured number of DVCS events by the values in Tab. 4.5 for each corresponding kinematic setting:

$$N_{DVCS}^{corrected} = N_{DVCS} \frac{1}{\eta_{S2}\eta_{CER}}. \tag{4.32}$$

4.7.2 Dead time correction and integrated luminosity

Some events may also be missed because the DAQ was busy recording an event and could not take in another one (see section 2.3.3). The effect of this dead time on the measured number of events must be corrected.

The dead time is computed using two scalers. For each run, a first "live" scaler counts the number of triggers with S2 and Cherenkov detectors in coincidence only when the DAQ is available, while a second "raw" scaler counts the number of triggers not withstanding whether the DAQ is available or busy recording an event[2]. The live time of each run is then computed as the ratio of the "live" scaler over the "raw" scaler counts, and the dead time is equal to 1− live time.

The dead time correction is taken into account in the experiment luminosity. The integrated luminosity $\mathcal{L}$ is computed as:

$$\mathcal{L} = \frac{Q_{corr}\rho l N_A}{eM_H}, \tag{4.33}$$

with Q_{corr} the accumulated beam charge corrected by the dead time, ρ the target density, l the target length, N_A the Avogadro number, e the positron charge and M_H the hydrogen molar mass. One will notice that the full target length is used to compute the luminosity despite the cuts applied to the vertex in section 4.5.1. However, the loss of DVCS events due to the vertex cuts is compensated by applying exactly the same cuts to the Geant4 simulation used to compute the experiment acceptance (see section 5.1), and further correction to the luminosity is not required.

The corrected charge Q_{corr} is computed by multiplying the accumulated beam charge Q_i by the live time T_i^{live} for every run i:

$$Q_{corr} = \sum_i Q_i T_i^{live}. \tag{4.34}$$

The average live time for each kinematic setting is summarized in Tab. 4.6.

Kinematic setting	Live time
36_1	0.981
36_2	0.980
36_3	0.966
48_1	0.985
48_2	0.962
48_3	0.985
48_4	0.978
60_1	0.979
60_3	0.974

Table 4.6: Summary of the live time for each kinematic setting.

A combined dead time and integrated luminosity systematic uncertainty of 1.6% was found in [89].

4.7.3 Multi-track correction

In section 4.5.2.2, events where more than one VDC wire plane had several clusters have been discarded because the electron track could not be reliably reconstructed. A correction must be applied to the number of remaining events to take into account the discarded ones.

Let N_1 be the number of events where multiple clusters were reconstructed in one wire plane at most and let N_{mc} be the number of events where multiple clusters were reconstructed in more than one wire plane. Furthermore, electrons were selected by applying cuts on the energy deposited in the Cherenkov detector and the Pion Rejectors. The correction coefficient $\eta_{tracking}$ is then computed as:

$$\eta_{tracking} = 1 + \frac{N_{mc}}{N_1}, \tag{4.35}$$

and its values for each kinematic are summarized in Tab. 4.7:

[2]The scalers themselves have a negligible dead time.

Kinematic setting	$\eta_{tracking}$
36_1	1.060
36_2	1.064
36_3	1.070
48_1	1.043
48_2	1.063
48_3	1.057
48_4	1.060
60_1	1.066
60_3	1.064

Table 4.7: Summary of the tracking correction coefficients for each kinematic setting [88].

The tracking correction is then applied by multiplying the measured number of DVCS events by $\eta_{tracking}$. Eq. (4.32) becomes:

$$N_{DVCS}^{corrected} = N_{DVCS}\eta_{tracking}\frac{1}{\eta_{S2}\eta_{CER}}. \tag{4.36}$$

4.7.4 Calorimeter multi-cluster correction

In section 4.5.3, events with more than one reconstructed cluster in the calorimeter have been rejected. However, a small number of DVCS events were present among them: while a single photon is expected, it is possible for accidental photons to be detected at the same time, leading to more than one cluster being reconstructed. Thus, selecting only single cluster events would result in the loss of a small quantity of DVCS events.

In order to recover them, events with two clusters in the calorimeter must be considered. Each of the two photon candidates is treated as if it was the only one reconstructed and is compared to the event selection cuts of section 4.5. If only one of the two photon candidates is compatible with a DVCS event, it is kept and the other one is discarded. In the extremely rare scenario where both photon candidates are compatible, the one which is kept is chosen randomly. If none of them is compatible with the selection cuts, the whole event is discarded. Depending on the kinematic setting, the two-clusters correction represents a contribution between $\sim$ 0.5% and $\sim$ 2% of the total number of DVCS event, except for kin48_1 where the correction reaches around $\sim$ 5%.

Events with more than two clusters are not considered: the probability for two accidental photons to be detected at the same time as the DVCS one is much lower than for a single accidental, and the two-clusters correction is already smaller than 2%. It is safe to assume that n-cluster corrections, with n $\geq$ 3, are negligible.

4.7.5 Polarization measurements

The beam polarization has been measured by both a Compton and a Møller polarimeter. However, only the Møller results are available, while the analysis of the Compton data is being finalized. Nevertheless, the preliminary Compton results are consistent with the Møller measurements [90].

The results of the Møller polarization measurements are summarized in Tab. 4.8. For kin48_4 and kin60_3, two Møller measurements have been performed instead of one. As the measured polarizations differed by only $\sim$1%, averages were used. Overall, the mean beam polarization was around $\sim$ 86%, with a statistical uncertainty between 0.1% and 0.2%, and a systematic uncertainty of 1%.

The polarization correction to the helicity-dependent cross section is then applied by dividing the measured number of DVCS events by η_{pol}. Eq. (4.36) then becomes:

$$N_{DVCS}^{corrected} = N_{DVCS}\eta_{tracking}\frac{1}{\eta_{S2}\eta_{CER}}\frac{1}{\eta_{pol}}. \tag{4.37}$$

This correction does not need to be applied for the unpolarized cross section.

4.7.6 Beam helicity correction

The last correction that needs to be applied must account for the events with an electron of unknown helicity which have been discarded in section 4.5.4. The proportion η_{hel} of electrons with unknown helicity

Kinematic setting	Beam polarization η_{pol}	Statistical uncertainty	Systematic uncertainty
36_1	0.846	±0.3%	±2.2%
36_2	0.868	±0.1%	±1.0%
36_3	0.854	±0.1%	±1.0%
48_1	0.867	±0.1%	±1.0%
48_2	0.870	±0.2%	±1.0%
48_3	0.870	±0.2%	±1.0%
48_4	0.875	±0.1%	±1.0%
60_1	0.862	±0.1%	±1.0%
60_3	0.848	±0.1%	±1.0%

Table 4.8: Summary of the beam polarization for each kinematic setting [91].

can be computed from the time required to flip and stabilize the Pockels cell. In principle, the transition time of the Pockels cell is 60 μs, but a conservative cut consisted in considering a 200 μs uncertainty window at first in 2014, which was then increased to 500 μs. As a consequence, 0.6% of the total number of electrons have an unknown helicity for kin36_1, and 1.5% for every other kinematic setting.

The beam helicity correction to the polarized cross section is then applied by multiplying the total charge by $1 - \eta_{hel}$. Eq. (4.38) then becomes:

$$Q_{corr} = \sum_i Q_i T_i^{live} (1 - \eta_{hel}), \tag{4.38}$$

with $1 - \eta_{hel} = 0.994$ for kin36_1, and $1 - \eta_{hel} = 0.985$ for every other kinematic setting.

Chapter 5

Geant4 simulation and cross sections extraction

The analysis from the previous chapter allowed to extract accurately the number of DVCS events and the integrated luminosity. However, in order to extract cross sections from the data, one also needs to know the phase space covered by the detectors. Because of the complexity of the experimental setup, correlations between the different variables, and radiative effects that modify the kinematic phase space, trying to compute the experiment acceptance analytically is impossible. As a consequence, the acceptance computation relies on a simulation. By implementing the experimental setup in a Geant4 simulation taking into account radiative corrections, the acceptance can be reproduced accurately.

After the DVCS cross sections have been properly extracted, it is necessary to evaluate the experiment systematic uncertainties. Several sources need to be accounted for. In particular, one of the main contributions that must be studied with care is the choice of the missing mass cuts which allows to identify the recoil proton.

This chapter will be divided into two parts. The first section will present the Geant4 simulation of the experiment. Radiative corrections will also be described as they are taken into account in the simulation. The second part of this chapter will deal with the cross section extraction method used for this experiment and will provide details about the study of the systematic uncertainties. Finally, preliminary results will be presented.

5.1 Geant4 simulation

5.1.1 Geometry

As Geant4 handles the interaction of particles with matter, a precise implementation of the experimental setup between the vertex and the detectors is necessary (see Fig. 5.1). The liquid hydrogen target cell, the scattering chamber and the beam pipe and shielding which have been implemented are exact copies of the real setup in Hall A [92]. Additionally, in order to avoid multiple scattering and reduce the quantity of matter that the scattered electron has to travel through, a section of the scattering chamber wall is replaced by a thin kapton window. This window covers a solid angle where the scattered electron can be detected by the spectrometer, taking into consideration the fact that the detector can be moved around the target. Similarly, a section of the scattering chamber wall is replaced by a thin aluminum window in front of the calorimeter. These thin kapton and aluminum windows have also been implemented in the simulation.

On the spectrometer side, only the kapton entrance window of the detector has been implemented. One of the main reasons why the spectrometer has not been fully implemented is because the simulation of magnetic fields in the detector, which is required for tracking, is very challenging and not reliable enough. Instead, a cut on the electron R-value allows to determine if it is within the spectrometer acceptance, in which case it is considered to be detected and its variables are recorded. Because this way of simulating the spectrometer without tracking does not allow to reproduce the fact that the detector is not perfectly pointing toward the target center, the apparent target offset described in section 4.5.1 is implemented instead.

On the calorimeter side, however, the detector and its shielding have been fully implemented. The position of each crystal has been surveyed with high precision during the experiment and copied in the

simulation. The electromagnetic showers developing in the PbF_2 crystals are handled by Geant4, and the energy deposited by the particles in each block are recorded as for real data. However, Cherenkov photons are not simulated.

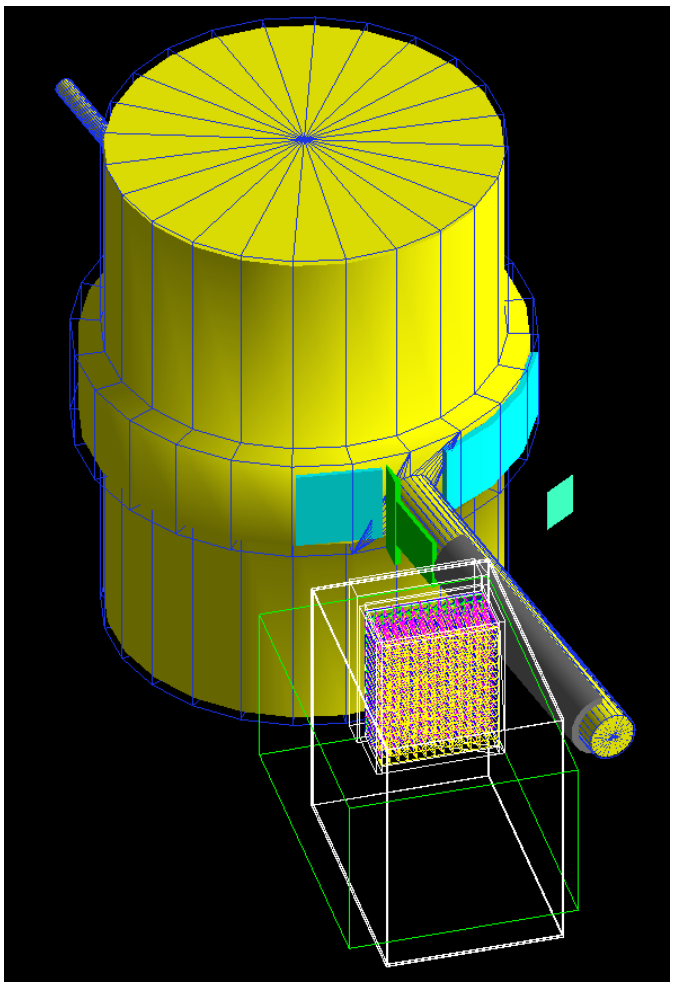

Figure 5.1: Geometry of the experimental setup implemented in the Geant4 simulation. The scattering chamber and beam pipes are represented in yellow, the beam line shielding in green and grey, and the kapton and aluminum windows in light blue. The kapton entrance window of the spectrometer is the light green square at the right of the beam line. The calorimeter has been fully implemented: the outlines of the box that encloses the detector and its shielding for low energy electromagnetic background are represented by the white lines. The blocks, their wrapping and supports are implemented inside the box.

5.1.2 Radiative corrections

Although Geant4 handles the interactions of the final states particle with matter, it does not take into account the ones of the electron in the initial state since it is not simulated, as will be seen later in the description of the simulation process. Radiative corrections need to be added in the event generator in order to take into account the energy loss of the initial electron due to Bremsstrahlung. These radiative effects are called “external” as they take place before or after the event vertex, unlike the “internal” ones which take place at the vertex.

It is convenient to add the real internal corrections in the event generator as well. Indeed, the radiation of an additional real photon generates a radiative tail in the missing mass spectrum, which needs to be taken into account in the acceptance computation. Therefore, it is beneficial to generate the radiative tail in the simulation in order to combine it with the detectors acceptance and resolution effects.

Although they can be added at a later stage, virtual internal corrections will be detailed in this section as well. Finally, the radiative corrections are considered for the leptonic part of the DVCS process only. Indeed, the radiative corrections for the electron are dominant, whereas the one for the proton are suppressed by its much larger mass.

5.1.2.1 External radiative corrections

An electron passing through matter radiates real photons due to Bremsstrahlung. The energy loss of the electron, ΔE, is equal to the sum of the energies of every radiated photon. To a good approximation, this energy loss follows the distribution [93]:

$$I(E_0, \Delta E, t_{mat}) = \frac{bt_{mat}}{\Delta E} \left[\frac{\Delta E}{E_0} \right]^{bt_{mat}}, \tag{5.1}$$

with E_0 the electron energy before Bremsstrahlung, t_{mat} the material thickness in units of radiation length, and $b \approx \frac{3}{4}$. This kind of radiation is called straggling effect.

The energy loss ΔE of the electron will follow the distribution $I(E_0, \Delta E, t_{mat})$ in a Monte Carlo simulation if it is computed event by event with the expression:

$$\Delta E = E_0 r^{1/bt_{mat}}, \tag{5.2}$$

with r generated uniformly in [0,1].

This energy loss is applied in the peaking approximation: the radiated photons are emitted in the same direction as the electron, so that its propagation direction is unchanged.

5.1.2.2 Internal radiative corrections

Additional photons, real or virtual, can be emitted at the event vertex: these radiations are called "internal". Because of internal radiative effects, the Born cross section (lowest order diagram) cannot be measured directly and corrections need to be taken into account. An extensive study of internal radiative corrections has been performed by M. Vanderhaeghen et al. in [94], and further considerations for the Hall A DVCS experiments are available in [95].

The internal radiative corrections presented here have been developed for elastic scattering [94]. However, they are identical for DVCS since they take place on the leptonic part of the diagrams, which are the same for elastic scattering and DVCS. At first order in QED, three internal radiative processes can be distinguished:

- the vertex correction (see Fig. 5.2 a): a virtual photon is emitted by the electron before scattering and reabsorbed after scattering;
- the vacuum polarization (see Fig. 5.2 b): the virtual photon emitted by the scattering electron fluctuates into an electron-positron pair;
- the internal Bremsstrahlung (see Fig. 5.2 c and d): a real photon is radiated by the electron before or after scattering.

One will notice that self-energy diagrams (see Fig. 5.2 e) do not participate to internal radiative corrections as their contribution was found to vanish for on-shell leptons [94].

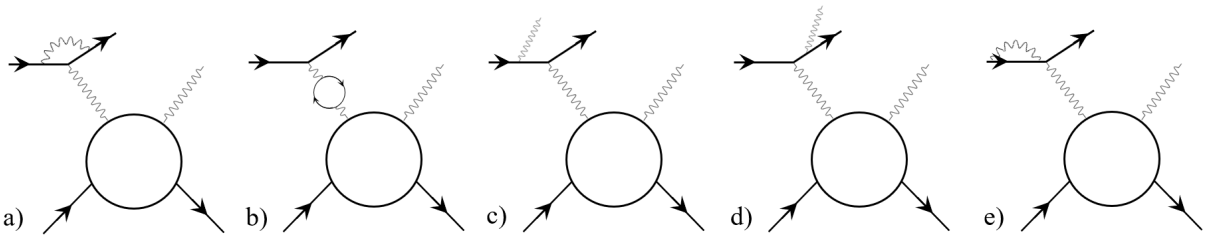

Figure 5.2: Illustration of the internal radiative effects for DVCS.

Corrections for the first two processes are referred to as virtual, whereas corrections for the third one are called real. Taking both virtual and real internal radiative corrections into account, the experimental and Born cross sections are related by the expression [95]:

$$\left(\frac{d\sigma}{d\Omega} \right)_{Exp} = \left(\frac{d\sigma}{d\Omega} \right)_{Born} \left[\frac{e^{\delta_{ver} + \delta_{brem}(\Delta E)}}{(1 - \delta_{vac})^2} \right], \tag{5.3}$$

where the subscript *ver* stands for the vertex correction, *vac* stands for the vacuum polarization, and *brem* stands for the internal Bremsstrahlung contributions, with:

$$\delta_{ver} = \frac{\alpha}{\pi}\left[\frac{3}{2}\ln\left(\frac{Q^2}{m_e^2}\right) - 2 - \frac{1}{2}\ln^2\left(\frac{Q^2}{m_e^2}\right) + \frac{\pi^2}{6}\right], \tag{5.4}$$

$$\delta_{vac} = \frac{\alpha}{3\pi}\left[\ln\left(\frac{Q^2}{m_e^2}\right) - \frac{5}{3}\right], \tag{5.5}$$

$$\delta_{brem}(\Delta E) = \frac{\alpha}{\pi}\left\{2\ln\left(\frac{\Delta E}{\sqrt{EE'}}\right)\left[\ln\left(\frac{Q^2}{m_e^2}\right) - 1\right] - \frac{1}{2}\ln^2\left(\frac{E}{E'}\right) + \frac{1}{2}\ln^2\left(\frac{Q^2}{m_e^2}\right) - \frac{\pi^2}{3} + \mathrm{Sp}\left(\cos^2\frac{\theta_e}{2}\right)\right\}, \tag{5.6}$$

with α the fine structure constant, m_e the electron mass, E (E') the electron energy before (after) scattering, θ_e the electron scattering angle and Sp the Spence function defined by:

$$\mathrm{Sp}(z) = -\int_0^z \frac{\ln(1-t)}{t}dt. \tag{5.7}$$

Neglecting the ΔE dependence of E' and Q^2, the term δ_{brem} can be split into a part $\delta_{brem,0}$ independent from ΔE, and a part $\delta_{brem,1}(\Delta E)$ which depends on ΔE:

$$\delta_{brem,0} = \frac{\alpha}{\pi}\left[\frac{1}{2}\ln^2\left(\frac{Q^2}{m_e^2}\right) - \frac{1}{2}\ln^2\left(\frac{E}{E'}\right) - \frac{\pi^2}{3} + Sp\left(\cos^2\frac{\theta_e}{2}\right)\right], \tag{5.8}$$

$$\delta_{brem,1}(\Delta E) = \frac{2\alpha}{\pi}\ln\left(\frac{\Delta E}{\sqrt{EE'}}\right)\left[\ln\left(\frac{Q^2}{m_e^2}\right) - 1\right]. \tag{5.9}$$

The term $\delta_{brem,0}$ can be interpreted as the emission of soft Bremsstrahlung photons which have an energy lower than the experiment resolution. Their contribution to the internal Bremsstrahlung radiative tail is negligible and $\delta_{brem,0}$ can be grouped with the virtual terms δ_{ver} and δ_{vac}. As a consequence, Eq. (5.3) can be rewritten as:

$$\left(\frac{d\sigma}{d\Omega}\right)_{Exp} = \left(\frac{d\sigma}{d\Omega}\right)_{Born}\left[\frac{e^{\delta_{ver}+\delta_{brem,0}}}{(1-\delta_{vac})^2}\right]\left(\frac{\Delta E}{\sqrt{EE'}}\right)^{\delta_S}, \tag{5.10}$$

with:

$$\delta_S = \frac{2\alpha}{\pi}\left[\ln\left(\frac{Q^2}{m_e^2}\right) - 1\right]. \tag{5.11}$$

Then, the radiative tail due to internal Bremsstrahlung is obtained by differentiating Eq. (5.10) with respect to ΔE:

$$\left(\frac{d^2\sigma}{d\Delta E d\Omega}\right)_{Exp} = \left(\frac{d\sigma}{d\Omega}\right)_{Born}\left[\frac{e^{\delta_{ver}+\delta_{brem,0}}}{(1-\delta_{vac})^2}\right]\frac{\delta_S}{\Delta E}\left(\frac{\Delta E}{E}\right)^{\delta_S}\left(\frac{E}{E'}\right)^{\delta_S/2}. \tag{5.12}$$

One will notice that the term $\frac{\delta_S}{\Delta E}\left(\frac{\Delta E}{E}\right)^{\delta_S}$ is similar to Eq. (5.1), with an equivalent radiator thickness δ_S. Thus, the internal Bremsstrahlung will be treated in the same way as the external radiative corrections. The correction will be applied twice: once for the incoming electron, and once for the outgoing electron, each time with the equivalent radiator thickness $\frac{\delta_S}{2}$. However, the additional term $\left(\frac{E}{E'}\right)^{\delta_S/2}$ needs to be taken into account. This term does not change the shape of the radiative tail and can be applied to the measured cross sections afterwards: it does not need to be present in the simulation [95].

For this experiment kinematic settings, $\delta_S \approx 0.07$, and $\left(\frac{E}{E'}\right)^{\delta_S/2}$ can be approximated by using the beam energy and spectrometer momentum. The values of $\left(\frac{E}{E'}\right)^{\delta_S/2}$ for every kinematic setting are summarized in Tab. 5.1.

Unlike internal Bremsstrahlung, the virtual corrections do not modify the kinematics of the reaction. Moreover, they are almost constant over the phase space of each kinematic settings. As a consequence, the virtual corrections can be applied to the measured cross sections afterwards and do not need to be implemented in the simulation.

However, the virtual correction $\left[\frac{e^{\delta_{ver}+\delta_{brem,0}}}{(1-\delta_{vac})^2}\right]$ computed for DVCS cannot be applied to Bethe-Heitler (BH). Indeed, because of the additional photon emitted by the leptonic part, virtual corrections to the

Kinematic setting	$\left(\frac{E}{E'}\right)^{\delta_S/2}$
36_1	1.04
36_2	1.04
36_3	1.03
48_1	1.04
48_2	1.03
48_3	1.04
48_4	1.04
60_1	1.03
60_3	1.04

Table 5.1: Summary of the $\left(\frac{E}{E'}\right)^{\delta_S/2}$ correction for each kinematic setting.

BH process are more complicated than for DVCS. In particular, self-energy diagrams now have to be taken into account (see Fig. 5.3). In principle, different virtual corrections should be applied to the DVCS, BH, and interference terms of the cross section, but applying a global correction can remain a good approximation as long as the different contributions are correctly taken into account.

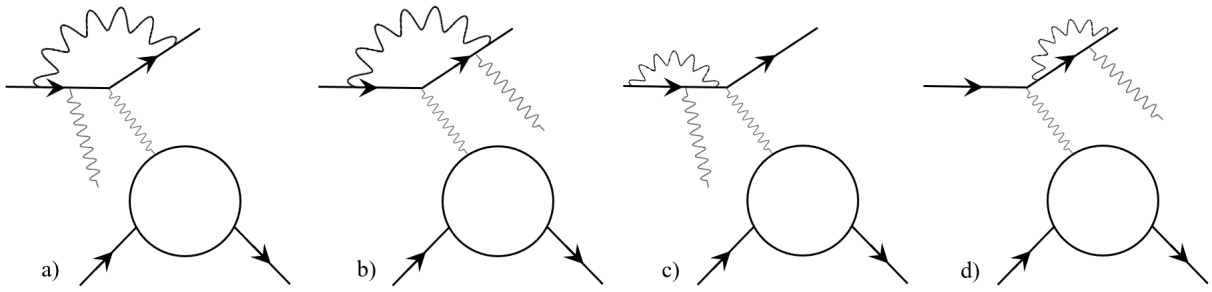

Figure 5.3: Illustration of vertex (a and b) and self-energy (c and d) virtual correction diagrams for Bethe-Heitler.

An additional difficulty is that unlike internal Bremsstrahlung, the virtual corrections to DVCS diagrams have the same final state as the DVCS reaction and thus they interfere with the DVCS amplitude. Virtual corrections must be summed coherently with DVCS, and as a consequence, a model of the DVCS amplitude is required to compute these corrections.

Virtual radiative corrections had been computed for a previous Hall A experiment (E00-110) for both unpolarized and polarized cross sections using a code developed by D. Lhuillier et al. relying on a factorized GPD ansatz [96]. They have not been computed yet for the current kinematic settings, but it is reasonable to assume that they will be similar to the previous ones. As a consequence, the virtual radiative corrections currently applied are $\eta_{virt} = 0.94$ for unpolarized cross sections and $\eta_{virt} = 0.97$ for polarized ones [97]. A systematic uncertainty of 2% had been reported for experiment E00-110.

5.1.3 The event generator and the simulation process

The DVCS reaction $ep \to e'p'\gamma$ can be split into two parts: a leptonic part $e \to e'\gamma^*$, and a hadronic part $\gamma^* p \to p'\gamma$. The event generator starts by generating the leptonic part.

The first variable generated is the event vertex v_z along the beam axis. The vertex is generated randomly following a uniform distribution within the boundaries of the hydrogen target. The vertex allows to compute the distance traveled by the initial electron through the target. Using this distance, the external radiative correction can be applied to the initial energy E according to the method described in section 5.1.2.1. The corrected energy is noted E_v^{ext}.

At first, the event will be generated in the horizontal plane. Because of the very small acceptance of the spectrometer, it is advantageous to not generate events in the complete DVCS phase space and to restrain oneself to reasonable ranges encompassing the detector acceptance in order to accelerate the simulation process. The ranges $[\phi_e^{min}, \phi_e^{max}]$ and $[p_e^{min}, p_e^{max}]$ of the scattered electron horizontal angle ϕ_e and momentum p_e are chosen wide enough to encompass the spectrometer acceptance even after radiative corrections.

Then, the event Q^2 and x_{Bj} can be generated. Their generation follows a uniform distribution in the intervals defined by:

$$Q^2_{min} = 2p_e^{min}E_v^{ext}(1-\cos\phi_e^{min}) < Q^2 < 2p_e^{max}E_v^{ext}(1-\cos\phi_e^{max}) = Q^2_{max}, \tag{5.13}$$

$$x_{Bj}^{min} = \max\left(\frac{p_e^{min}E_v^{ext}(1-\cos\phi_e^{min})}{M(E_v^{ext}-p_e^{min})}, 0.05\right) < x_{Bj} < \min\left(\frac{p_e^{max}E_v^{ext}(1-\cos\phi_e^{max})}{M(E_v^{ext}-p_e^{max})}, 0.95\right) = x_{Bj}^{max}, \tag{5.14}$$

with M the proton mass. The phase space factor $\Delta Q^2 \Delta x_{Bj} = [Q^2_{max} - Q^2_{min}][x_{Bj}^{max} - x_{Bj}^{min}]$ is associated to the event to account for the phase space region where it was generated.

In parallel of the generation of Q^2 and x_{Bj}, the energy E_v^{ext} is compared to the threshold p_e^{min}. If $E_v^{ext} < p_e^{min}$, then the amount of energy lost by external Bremsstrahlung is too large to generate a detectable event. In this case, the event is considered lost; however, it will still be accounted for in the total number of generated events used for the simulation normalization.

Then, the first correction for internal Bremsstrahlung, before the vertex, is applied as described in section 5.1.2.2, and the corrected energy is noted E_v. One will notice that this correction to the initial electron energy should have been performed before the generation of Q^2 and x_{Bj}. However, the knowledge of Q^2 is required to compute the correction.

Then, the scattered electron is generated. Its momentum and horizontal angle are computed as:

$$p_e = E_v - \frac{Q^2}{2Mx_{Bj}}, \tag{5.15}$$

$$\cos\phi_e = 1 - \frac{Q^2}{2p_eE_v}. \tag{5.16}$$

Because the first internal Bremsstrahlung correction was applied after the generation of Q^2 and x_{Bj}, if it is large, it is possible for the initial electron energy E_v to have become too low for the generation of a physical event. In the case where $p_e < 0$, the event is considered lost, but like previously it will still be accounted for in the total number of generated events. Once the scattered electron has been generated, the second part of the internal Bremsstrahlung correction can be applied as described in section 5.1.2.2.

Next, the event generator tackles the hadronic part $\gamma^* p \to p'\gamma$ of the DVCS reaction in the center-of-mass frame. The momentum of the virtual photon γ^* is computed from the initial electron after internal Bremsstrahlung, and the scattered electron before internal Bremsstrahlung. The squared momentum transfer t is generated in the interval $[t_{min}(Q^2, x_{Bj}) - 2\ \text{GeV}^2, t_{min}(Q^2, x_{Bj})]$ (see appendix B) following a uniform distribution. This interval is large enough to encompass the calorimeter acceptance: events with a squared momentum transfer t larger than t_{min} would be unphysical, and the detector acceptance in t varies between ~ 0.4 GeV^2 and ~ 1.2 GeV^2 depending on the kinematic setting. An additional phase space factor $\Delta t = 2$ GeV^2 is associated to the event. Then, the photon and proton momentum are computed and boosted to the laboratory frame.

Afterwards, the photon azimuthal angle ϕ is generated in the interval $[0, 2\pi]$ following a uniform distribution, an additional phase space factor $\Delta\phi = 2\pi$ is associated to the event, and the photon and proton momentum are rotated by ϕ around the virtual photon direction. Then, to take into account the vertical acceptance of the spectrometer, an angle φ is generated uniformly in an interval large enough to encompass the detector acceptance, and all three particle momenta are rotated by φ around the beam axis. An additional phase space factor $\Delta\varphi$ is associated to the event.

From this point on, Geant4 handles the transport of the electron to the spectrometer entrance. Further energy losses may happen due to interactions with the hydrogen target cell, the kapton window and the air between the scattering chamber and the spectrometer entrance. After the computation of these external radiative corrections by Geant4, the final electron energy is noted E'_r. If the electron hits the spectrometer entrance, a cut on its R-value identical to the data will determine whether it is detected or not. Geant4 also handles the transport of the photon to the calorimeter, as well as the electromagnetic shower developing in the PbF_2 crystals and the energy deposited in them.

Finally, the vertex position v_z is smeared by a Gaussian distribution to take into account the spectrometer resolution. The vertex resolution σ_{vertex} used for the smearing is given by the expression:

$$\sigma_{vertex} = \frac{\sigma_{90}}{\sin\theta_{HRS}}, \tag{5.17}$$

with θ_{HRS} the spectrometer angle and σ_{90} its vertex resolution if the detector was at $\theta_{HRS} = 90°$. In normal conditions, the nominal vertex resolution of the spectrometer at 90° is $\sigma_{90} = 1.2$ mm. However,

because of the challenges raised by the optics calibration, the achieved vertex resolution was slightly larger (see kinematic settings 48_2, 48_3 and 48_4 in Tab. 5.2). Nevertheless, as the experimental resolution is dominated by the calorimeter, the achieved vertex resolution is satisfactory.

Kinematic setting	σ_{90} (mm)
36_1	1.5
36_2	1.6
36_3	1.2
48_1	1.5
48_2	1.9
48_3	2.0
48_4	2.1
60_1	1.4
60_3	1.4

Table 5.2: Summary of the spectrometer vertex resolution at 90° for each kinematic setting.

The main steps of the event generation process are summarized in Fig. 5.4. The total phase space factor associated to a generated event is $\Delta\Omega_{MC} = \Delta Q^2(E_v^{ext})\Delta x_{Bj}(E_v^{ext})\Delta t\Delta\phi\Delta\varphi$. In particular, one will notice that $\Delta\Omega_{MC}$ is different from one event to another because of the external Bremsstrahlung.

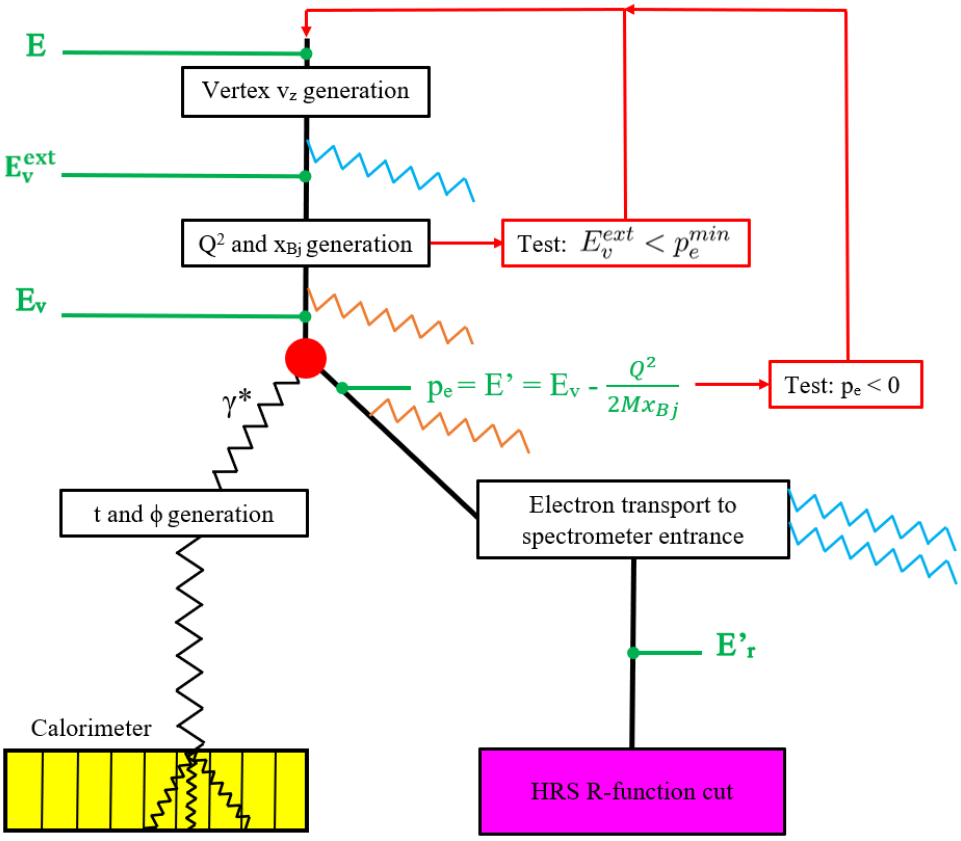

Figure 5.4: Schematic representation of the event generation in the simulation. External (internal) Bremsstrahlung is represented in blue (orange).

5.1.4 The simulation calibration and smearing

Because of resolution effects and the radiative tail due to Bremsstrahlung, the cuts applied on the DVCS missing mass will inevitably eliminate a non-negligible amount of DVCS events. This loss of events can be corrected by applying the same cuts to the Monte Carlo simulation as long as the simulation missing mass distribution matches perfectly the one from the data, in both position and shape. However, this is not the case at first:

- the simulation energy resolution is better than the data, resulting in a much narrower missing mass peak. This is because a bias is introduced by the fact that the simulation does not use Cherenkov photons to compute the energy deposited in the PbF_2 blocks, while a significant part of the experimental energy resolution is explained by fluctuations in the number of Cherenkov photons collected. Another small bias is due to the fact that the simulation does not reproduce the radiation damage suffered by the PbF_2 blocks;
- the position of the missing mass peak in the simulation is higher than the expected 0.88 GeV^2, implying that the photon energy is underestimated. This is because around $\sim 4\%$ of the photon energy leaks between and behind the calorimeter crystals. In the experimental data, these leaks are compensated by the energy calibration of the calorimeter, but that is not the case in the simulation.

As a consequence, both a calibration and a smearing of the simulation are required. They are performed simultaneously by multiplying event by event the photon momentum by a random variable following a Gaussian distribution $\text{Gaus}(\mu, \sigma)$, with μ and σ the calibration and smearing coefficient respectively:

$$\begin{pmatrix} q_x \\ q_y \\ q_z \\ E \end{pmatrix} \rightarrow Gauss(\mu, \sigma) \times \begin{pmatrix} q_x \\ q_y \\ q_z \\ E \end{pmatrix}. \tag{5.18}$$

The calorimeter gain and energy resolution evolve with time as the blocks darken because of radiation damage. As a consequence, the parameters μ and σ are computed for each kinematic setting.

Furthermore, the blocks of the calorimeter darken at different rates: radiation damage is stronger when close to the beam line, and the block quality and resistance to radiation may vary. For these reasons, the calorimeter gain and energy resolution may differ from one area to another. As a consequence, the parameters μ and σ must depend on the photon impact position in the calorimeter as well.

Reproducing the method applied in [98], the calorimeter surface is divided into $7 \times 7 = 49$ rectangular regions partially overlapping (see Fig. 5.5). Calibration and smearing coefficients μ_j and σ_j are computed independently for each region j. Then, parameters μ and σ are computed event by event depending on the photon impact position in the calorimeter by interpolating the coefficients μ_j and σ_j found previously. As can be seen in Fig. 5.5, the parameter μ varies by approximately 5% across the calorimeter surface, while σ fluctuates between ~ 0.2 GeV and ~ 0.4 GeV for photon energies of approximately 4.7 GeV. Small variations of μ and σ are naturally expected because of the precision of the calorimeter energy calibration and differences between each block. However, the larger fluctuations are imputable to a few calorimeter blocks with very low gain and whose energy calibration was challenging. For instance, the small (large) values of μ (σ) at the bottom left of the calorimeter are due to two blocks very sensitive to radiation damage that became very dark. The larger values of μ on the right side of the calorimeter are also explained by the existence of a block with low gain and high radiation damage sensitivity. Additional variations may also be explained by the influence of blocks on the calorimeter edges that could not be included in the π^0 energy calibration.

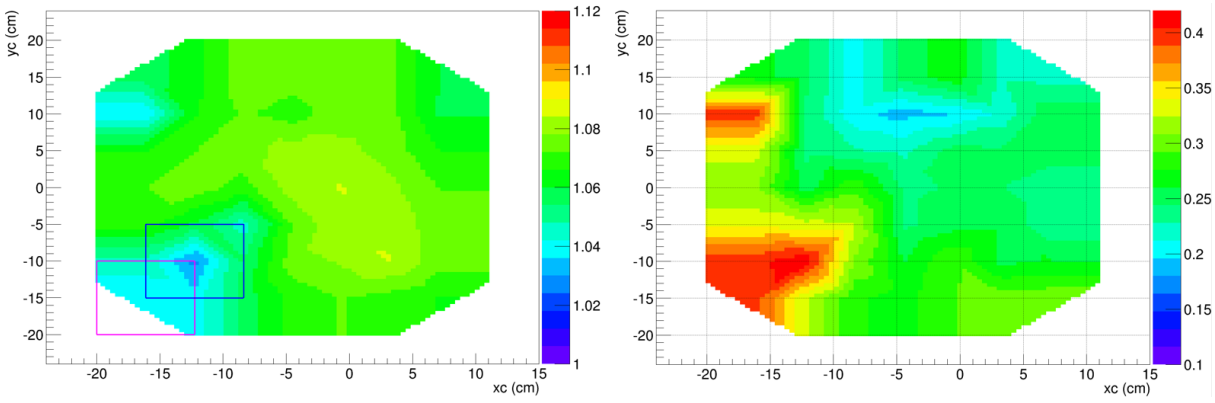

Figure 5.5: Left (Right): value of the interpolated parameter μ (σ) with respect to the impact position of the photon in the calorimeter for kin48_2. The parameter σ is expressed in GeV. The magenta and blue rectangles represent the boundaries of 2 out of the 49 rectangular regions where the coefficients μ_j and σ_j are computed.

The coefficients μ_j and σ_j are computed by fitting the simulation missing mass distribution to the data in the exclusivity peak region after subtracting accidental and π^0 events (see Fig. 5.6). The simulation missing mass distribution is normalized by the DVCS cross section which was extracted after a first iteration where it was not included in the normalization. The simulation missing mass distribution is also rescaled by a factor computed as the ratio of the integrals of the experimental and simulation missing mass between 0.5 GeV^2 and 0.95 GeV^2. The calibration and smearing coefficients found minimize the χ^2:

$$\chi^2_j(\mu_j, \sigma_j) = \frac{1}{N_{bin} - 2} \sum_{i=i_{min}}^{i_{max}} \left(\frac{N^{data}_{i,j} - N^{MC}_{i,j}}{\sigma^{data}_{i,j}} \right)^2 , \tag{5.19}$$

where the variable i runs over $N_{bin} = i_{max} - i_{min} + 1$ missing mass bins, N^{data}_i (N^{MC}_i) is the number of real (simulated) events in the bin i for the region j, and $\sigma^{data}_{i,j}$ is the associated statistical uncertainty. As shown in Fig. 5.6, the boundaries i_{min} and i_{max} are adjusted depending on the kinematic setting so that the exclusivity peak is included in the χ^2 minimization while avoiding SIDIS contamination as much as possible.

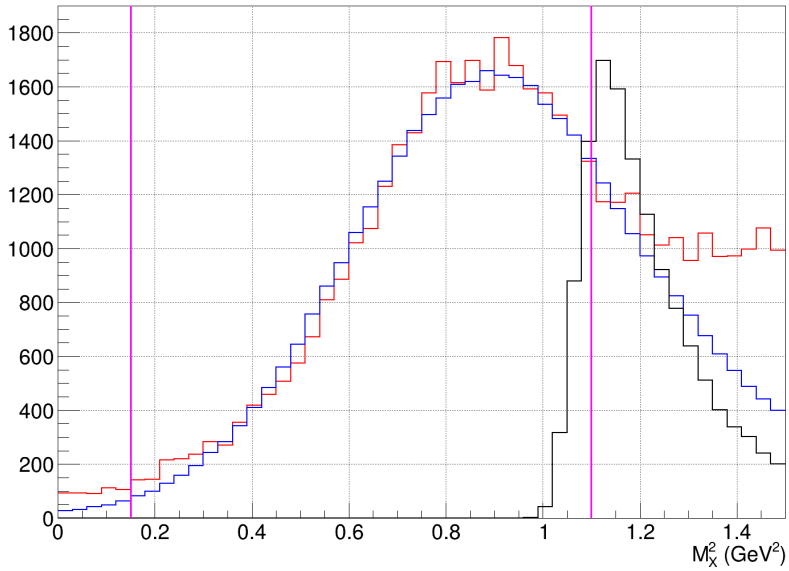

Figure 5.6: The missing mass distribution of kin48_2 for real data, after accidental and π^0 subtraction, is represented in red, while the one for the normalized, calibrated and smeared simulation is shown in blue. The magenta lines represent the boundaries i_{min} and i_{max} of the χ^2 minimization. The simulation missing mass distribution before calibration and smearing is represented in black and has been scaled to the same amplitude as the other histograms.

In Fig. 5.6 one will also notice that the tail at low missing mass is undershot by the simulation. Since no other source of contamination is expected at low missing mass, it is reasonable to assume that those are DVCS events and that a Gaussian smearing of the simulation is not able to completely describe the low missing mass tail of the data. Depending on the kinematic setting, the ratio of the number of DVCS events from the data not described by the simulation at low missing mass over the total number of events in the simulation (after rescaling) can vary between 2.8% and 5.6% (see Tab. 5.3). This ratio increases when the beam energy becomes larger. A non-Gaussian smearing of the simulation will be required in order to minimize this source of systematic uncertainty.

5.2 The cross section extraction

The number of events N_i in an experimental bin i and the DVCS cross section $\frac{d\sigma}{d\Omega}$ are related by the expression:

$$N_i = \mathcal{L} \int_{\Omega_i} \frac{d\sigma}{d\Omega} d\Omega = \mathcal{L} \frac{\int_{\Omega_i} \frac{d\sigma}{d\Omega} d\Omega}{\int_{\Omega_i} d\Omega} \int_{\Omega_i} d\Omega = \mathcal{L} \left\langle \frac{d\sigma}{d\Omega} \right\rangle_i \Delta\Omega_i, \tag{5.20}$$

Kinematic setting	$\frac{\int_{lowM_X^2}(N^{data}-N^{MC})}{\int N^{MC}}$
36_1	3.8%
36_2	4.4%
36_3	5.6%
48_1	2.8%
48_2	3.6%
48_3	4.2%
48_4	5.5%
60_1	4.5%
60_3	5.3%

Table 5.3: Summary of the ratio of the number of DVCS events from the data not described by the simulation at low missing mass over the total number of events in the simulation (after rescaling) for each kinematic setting.

where $\mathcal{L}$ is the integrated luminosity and $\Delta\Omega_i$ is the experimental acceptance for the bin i. The acceptance $\Delta\Omega_i$ can be computed using the Monte Carlo simulation described previously:

$$\Delta\Omega_i = \sum_{j=0}^{N_{MC}^i} \frac{\Delta\Omega_{MC}^j}{N_{MC}^{gene}}, \tag{5.21}$$

where the sum runs over the N_{MC}^i events reconstructed in the experimental bin i, $\Delta\Omega_{MC}^j$ is the phase space factor associated to the event j, and N_{MC}^{gene} is the number of events generated in the simulation. Then, by dividing N_i by $\mathcal{L}$ and $\Delta\Omega_i$, one can extract the average DVCS cross section over the bin i.

As described in section 1.3.4, the cross section is parametrized by linear and bi-linear combinations of CFFs $X(CFF)$ multiplied by kinematic factors $F(E, Q^2, x_{Bj}, t, \phi, \lambda)$ whose expressions are given in appendix B. If one makes the approximation that the combinations of CFFs are constant inside each experimental bin i, it is then possible to directly fit these combinations by integrating the kinematic factors into the Monte Carlo computation of the acceptance:

$$N_i = \mathcal{L}\int_{\Omega_i} F(E, Q^2, x_{Bj}, t, \phi, \lambda)X(CFF)d\Omega \approx \mathcal{L}\left\langle X(CFF)\right\rangle_i \int_{\Omega_i} F(E, Q^2, x_{Bj}, t, \phi, \lambda)d\Omega. \tag{5.22}$$

The first part of this section will explain in further detail this fitting method which was successfully used in previous Hall A experiments [70, 98]. This extraction procedure has the main advantage of taking into account the variations of the kinematic factors $F(E, Q^2, x_{Bj}, t, \phi, \lambda)$ within the experimental bins (see Eq. (5.22)). Furthermore, as will be described below, the method corrects the bin migration due to radiative effects and detectors resolution.

The second and third parts of this section will present the study of systematic uncertainties and discuss preliminary results.

5.2.1 The fitting method

The kinematic variables of an event are reconstructed from the detector information. However, the variables relevant to extract cross sections are the ones at the vertex. Let "reconstructed bins" be the name of the $\mathcal{R}$ bins constructed from kinematic variables measured by the detectors, and let "vertex bins" be the name of the $\mathcal{V}$ bins constructed from kinematic variables at the event vertex. Let N_r be the number of events in the reconstructed bin r, and N'_v be the number of events in the vertex bin v. Extracting cross sections requires the knowledge of N'_v:

$$N'_v = \mathcal{L}\int_v \frac{d\sigma}{d\Omega}d\Omega. \tag{5.23}$$

As only N_r is experimentally accessible, in an ideal case, one would like the kinematic variables measured by the detector to be identical to the ones at the vertex, so that $N_i = N'_i$ for any bin i. The cross section could then be indiscriminately extracted using the number of events in reconstructed or vertex bins. In reality, because of radiation effects and detector resolution, the kinematic variables measured by the detectors are different from the ones at the vertex. The immediate consequence is that

an event that belongs to a vertex bin i can migrate to a different reconstructed bin: $N_i \neq N'_i$. This effect is called bin migration.

Kinematic variables at the vertex are not accessible in real data, but they are in a simulation. From the Monte Carlo simulation, it is thus possible to access the probability K_{rv} for an event to migrate from the vertex bin v to the reconstructed bin r. The number of events N_r and N_v are then related by the equation:

$$N_r = \sum_{v=1}^{\mathcal{V}} K_{rv} N'_v, \tag{5.24}$$

and combining Eq. (5.23) and Eq. (5.24) one gets:

$$N_r = \mathcal{L} \sum_{v=1}^{\mathcal{V}} \int_v K_{rv} \frac{d\sigma}{d\Omega} d\Omega. \tag{5.25}$$

Let X_n be the $\mathcal{N}$ combinations of CFFs parametrizing the cross section, and $F_n(E, Q^2, x_{Bj}, t, \phi, \lambda)$ the associated kinematic factors so that:

$$\frac{d^5\sigma}{dQ^2 dx_{Bj} dt d\phi d\varphi} = \sum_{n=1}^{\mathcal{N}} F_n(E, Q^2, x_{Bj}, t, \phi, \lambda) X_n. \tag{5.26}$$

Combining Eq. (5.25) and Eq. (5.26) yields:

$$N_r = \mathcal{L} \sum_{v=1}^{\mathcal{V}} \sum_{n=1}^{\mathcal{N}} \langle X_n \rangle_v \int_v K_{rv} F_n(E, Q^2, x_{Bj}, t, \phi, \lambda) d\Omega. \tag{5.27}$$

Let K_{rvn} be the notation for $\int_v K_{rv} F_n(E, Q^2, x_{Bj}, t, \phi, \lambda) d\Omega$. Eq. (5.27) then becomes:

$$N_r = \mathcal{L} \sum_{v=1}^{\mathcal{V}} \sum_{n=1}^{\mathcal{N}} K_{rvn} \langle X_n \rangle_v , \tag{5.28}$$

and K_{rvn} can be computed with the Monte Carlo simulation as:

$$K_{rvn} = \sum_{i \in \{v \to r\}} F_n(E, Q^2, x_{Bj}, t, \phi, \lambda) \frac{\Delta\Omega^i_{MC}}{N^{gene}_{MC}}, \tag{5.29}$$

with i running over the events which migrated from the vertex bin v to the reconstructed bin r.

The quantity K_{rvn} encompasses both kinematic dependencies and bin migration effects. It is then possible to fit $\{\langle X_n \rangle_v\}$ to the data by minimizing the χ^2:

$$\chi^2(\{\langle X_n \rangle_v\}) = \sum_{r=1}^{\mathcal{R}} \left(\frac{N_r^{data} - N_r}{\sigma_r^{data}} \right)^2 , \tag{5.30}$$

with N_r^{data} the number of experimental events in the reconstructed bin r, σ_r^{data} the associated statistical uncertainty, and N_r is given by Eq. (5.28).

The minimization of Eq. (5.30) with respect to $\{\langle X_n \rangle_v\}$ leads to the resolution of the matrix equation $AX = B$ with A a $(\mathcal{N} \times \mathcal{V}) \times (\mathcal{N} \times \mathcal{V})$ square matrix and B a $\mathcal{N} \times \mathcal{V}$ column vector, whose coefficients are defined by:

$$A_{nv,n'v'} = \sum_{r=1}^{\mathcal{R}} \mathcal{L}^2 \frac{K_{rvn} K_{rv'n'}}{\left[\sigma_r^{data}\right]^2}, \tag{5.31}$$

$$B_{nv} = \sum_{r=1}^{\mathcal{R}} \mathcal{L} \frac{K_{rvn} N_r^{data}}{\left[\sigma_r^{data}\right]^2}, \tag{5.32}$$

and the solution X is obtained by inverting A:

$$\langle X_n \rangle_v = \sum_{n'=1}^{\mathcal{N}} \sum_{v'=1}^{\mathcal{V}} \left[A^{-1}\right]_{nv,n'v'} B_{n'v'}, \tag{5.33}$$

with A^{-1} the covariance matrix. The statistical uncertainty associated to $\langle X_n \rangle_v$ is given by $\sqrt{[A^{-1}]_{nv,nv}}$.

One will notice that for the χ^2 minimization to work, there must be more data bins than unknown variables. As there are $\mathcal{N} \times \mathcal{V}$ unknown variables $\langle X_n \rangle_v$, and $\mathcal{R}$ data bins (Eq. (5.30)), this implies that, at the very least, there must be more reconstructed bins than vertex bins. This is made possible by the variable ϕ. Indeed, as both N_r^{data} and $\langle X_n \rangle_v$ depend on Q^2, x_{Bj} and t, identical binning for these three variables are used for both reconstructed and vertex bins. However, $\langle X_n \rangle_v$ is independent of ϕ, while N_r^{data} does depend on it. As a consequence, an additional binning in ϕ is used for reconstructed bins only. It was chosen to use for each kinematic setting: only 1 bin in Q^2 and 1 bin in x_{Bj} because of the small acceptance of the spectrometer, 5 bins in t and 24 bins in ϕ, which results in 5 vertex bins, and 120 reconstructed bins.

It is usually advantageous to separate the values of t in $t - t_{min}(Q^2, x_{Bj})$ bins instead of t bins. Indeed, $t - t_{min}(Q^2, x_{Bj})$ is related to the distance of the real DVCS photon to the projection of the virtual one at the surface of the calorimeter. Furthermore, the virtual photon direction is heavily constrained toward the center of the calorimeter because of the tight acceptance of the spectrometer. As a consequence, the events distribution is flatter in $t - t_{min}(Q^2, x_{Bj})$ and thus the t-binning is actually performed in bins of $t - t_{min}(Q^2, x_{Bj})$.

Then, from the fitted combinations of CFFs $\langle X_n \rangle_v$ averaged over the vertex bins, it is possible to compute the fitted number of events N_r (Eq. (5.28)) and the fitted cross section averaged over each bin:

$$\frac{d^5\sigma_v^{fit}}{dQ^2 dx_{Bj} dt d\phi d\varphi} = \sum_{n=1}^{\mathcal{N}} F_n(E, \langle Q^2 \rangle, \langle x_{Bj} \rangle, \langle t \rangle, \phi, \lambda) \langle X_n \rangle_v . \tag{5.34}$$

Finally, the cross section corresponding to the measured data can be reconstructed as:

$$\frac{d^5\sigma_r^{data}}{dQ^2 dx_{Bj} dt d\phi d\varphi} = \frac{N_r^{data}}{N_r} \frac{d^5\sigma_r^{fit}}{dQ^2 dx_{Bj} dt d\phi d\varphi}. \tag{5.35}$$

As $d^5\sigma$ is independent of φ, integrating the cross section over φ yields a factor 2π, and the preliminary results presented in the following sections will be the four-fold cross sections $\frac{d^4\sigma}{dQ^2 dx_{Bj} dt d\phi} = \frac{1}{2\pi} \int \frac{d^5\sigma}{dQ^2 dx_{Bj} dt d\phi d\varphi} d\varphi$.

The harmonic expansion of the real part of the DVCS amplitude possesses $\cos(0\phi)$, $\cos(1\phi)$ and $\cos(2\phi)$ dependencies, while the imaginary part presents $\sin(1\phi)$ and $\sin(2\phi)$ dependencies. Thus, it was chosen to parametrize the unpolarized cross section with $\mathcal{N} = 3$ combinations of CFFs, and the helicity-dependent one with $\mathcal{N} = 2$.

The chosen parametrization aims at keeping dominant contributions with different $\phi-$dependencies in order to minimize correlations. As a consequence, the unpolarized cross section has been parametrized with $\mathcal{C}^{DVCS}(\mathcal{F}_{++}, \mathcal{F}_{++}^* \mid \mathcal{F}_{-+}, \mathcal{F}_{-+}^*)$, $\mathcal{R}e\mathcal{C}^I(\mathcal{F}_{++})$ and $\mathcal{R}e\mathcal{C}^I(\mathcal{F}_{0+})$, while the helicity-dependent cross section has been parametrized with $\mathcal{I}m\mathcal{C}^I(\mathcal{F}_{++})$ and $\mathcal{I}m\mathcal{C}^I(\mathcal{F}_{0+})$ (see appendix B). The χ^2 resulting from the fits (see Eq. (5.30)) and normalized by the number of degrees of freedom $dof = \mathcal{R} - \mathcal{N}\mathcal{V}$ are summarized in Tab. 5.4, and the fitted number of events for each reconstructed bin are displayed in appendix C. The specific case of the unpolarized cross section for kin36_2 is shown in Fig. 5.7.

Kinematic setting	χ^2_{unpol}/dof	χ^2_{pol}/dof
36_1	1.33	0.89
36_2	1.61	0.94
36_3	1.47	1.07
48_1	1.51	1.00
48_2	1.92	1.01
48_3	1.19	1.15
48_4	1.20	1.10
60_1	1.72	0.69
60_3	1.34	1.04

Table 5.4: Summary of the normalized χ^2 from the cross section fits (Eq. (5.30)) for each kinematic setting. The subscript *unpol* stands for the unpolarized cross section, while *pol* designates the helicity-dependent one. The number of degrees of freedom is $dof = \mathcal{R} - \mathcal{N}\mathcal{V}$.

As shown in Tab. 5.4, the normalized χ^2 are reasonably close to 1 for both unpolarized and polarized cross sections for every kinematic setting, although it is slightly larger than 2 for the unpolarized cross

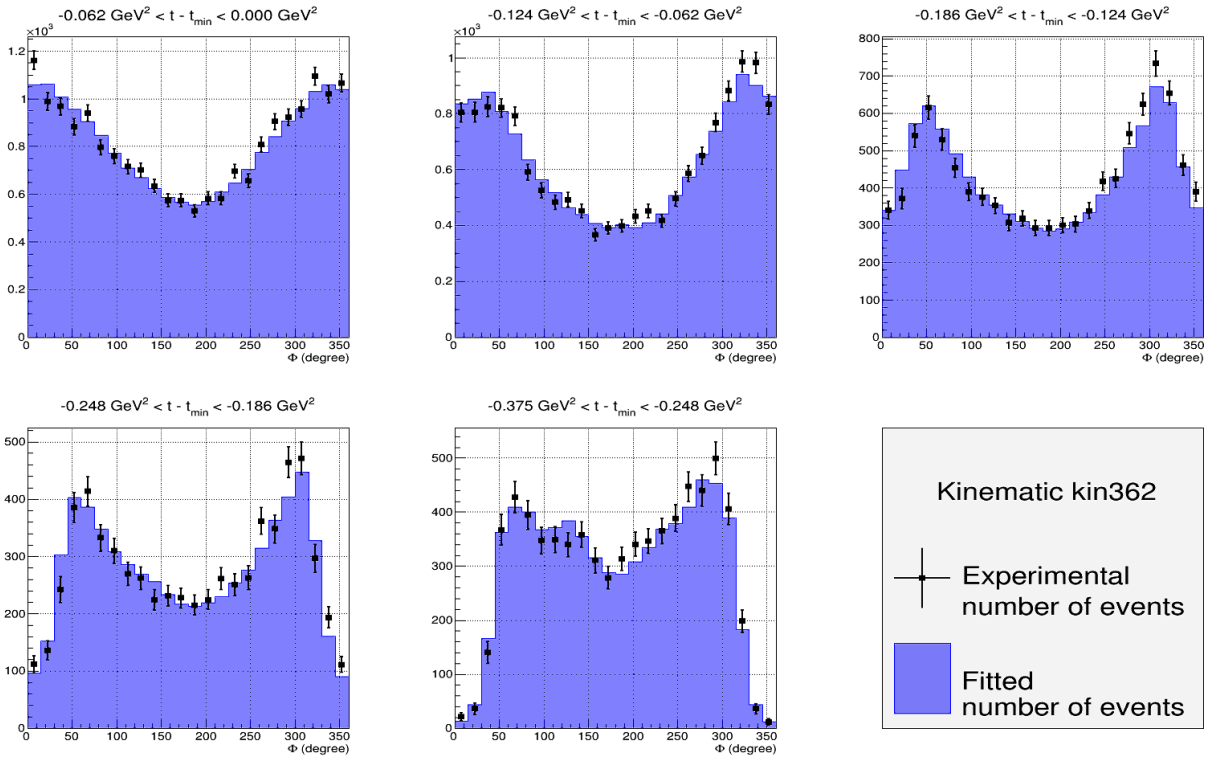

Figure 5.7: Unpolarized number of DVCS events for kin36_2, with $\langle Q^2 \rangle = 3.67$ GeV^2, $\langle x_{Bj} \rangle = 0.37$ and and $\chi^2/dof = 1.61$. The black squares (blue histograms) are the experimental (fitted) number of DVCS events for each bin. The uncertainty bars are statistical only.

section of kin36_1. One will also notice that the fits show better results for polarized cross sections than unpolarized ones.

In Fig. 5.7, the experimental number of DVCS events are displayed in black with the statistical uncertainties represented by the error bars, while the fitted number of events are shown in blue. The number of events generated in the Monte Carlo simulation was chosen sufficiently large so that its statistical uncertainties are negligible with respect to the experimental ones. As can be seen, the experimental number of events in every bin is well fitted by the simulation, which is reflected by the normalized χ^2 whose value (1.69) is close to 1. However, because of the calorimeter acceptance, there are relatively few events with ϕ close to 0° or 360° for the two t-bins where $t - t_{min}$ is the largest (bottom of Fig. 5.7). As a consequence, large statistical uncertainties are expected for the cross sections associated to these few bins.

5.2.2 Systematic uncertainties

Systematic uncertainties can be divided into two categories: uncorrelated uncertainties which are associated to individual experimental bins, and correlated uncertainties which affect all bins equally. In this work, the systematic uncertainty associated with the missing mass cuts falls into the first category, while every other uncertainty are treated as the second one.

5.2.2.1 Missing mass cuts

One of the largest contributions to systematic uncertainties for this experiment comes from the choice of the missing mass cuts. It can be split into two effects:

- as stated in section 4.6, in theory, the SIDIS missing mass should reach no lower than 1.15 GeV^2, and applying a cut at a lower value should remove all SIDIS contamination. In practice, this is not exactly the case. Because of energy calibration uncertainties, the theoretical limit of 1.15 GeV^2 can actually be shifted to lower values. Moreover, because of detectors resolution, the SIDIS missing mass will extend to values below this limit. On the other hand, one does not want to apply a cut on the missing mass which is too severe otherwise statistical uncertainties would become large. As a consequence, some SIDIS contamination may remain after the event selection;

- the simulation calibration and smearing procedure do not allow to perfectly reproduce the calorimeter gain and resolution.

As shown by the magenta lines in Fig. 5.8 (left), two missing mass cuts are applied for each kinematic setting, on each side of the exclusivity peak. The choice of the cut values is made by studying the ratio of the integrals of the experimental and simulation missing mass spectra. The simulation missing mass distribution has been preemptively rescaled by a factor computed as the ratio of the integrals of the experimental and simulation missing mass between 0.6 GeV^2 and 0.9 GeV^2, so that the amplitude of the exclusivity peaks are identical. As shown in Fig. 5.8 (right), on the right side of the exclusivity peak, the ratio is constant around 1 until SIDIS contamination becomes significant, at which point the ratio increases quickly as the experimental and simulation distributions are no longer matching. In order to minimize the SIDIS contamination, the cutting value is chosen on the plateau far enough from the point where the ratio starts to increase, while compromising with the amount of events that has to be kept to limit statistical uncertainties. As a further constraint, the value of the cut on the right of the exclusivity peak should not be larger than 1.1 GeV^2 in order to minimize contamination from SIDIS whose theoretical limit is approximately 1.15 GeV^2.

The discrepancy between real data and simulation on the left side of the exclusivity peak (see Fig. 5.8 left) is not due to SIDIS, but to the fact that a Gaussian smearing of the simulation is not enough to accurately describe the low missing mass tail of the data, as explained in section 5.1.4. As a consequence, an additional uncertainty between 2.8% and 5.6% must be taken into account, depending on the kinematic setting, until the simulation smearing is improved. Nevertheless, studying the ratio of the integrals of the experimental and simulation missing mass spectra also allows to select a cut value above which both spectra are matching. The missing mass cuts are summarized in Tab. 5.5 for every kinematic setting.

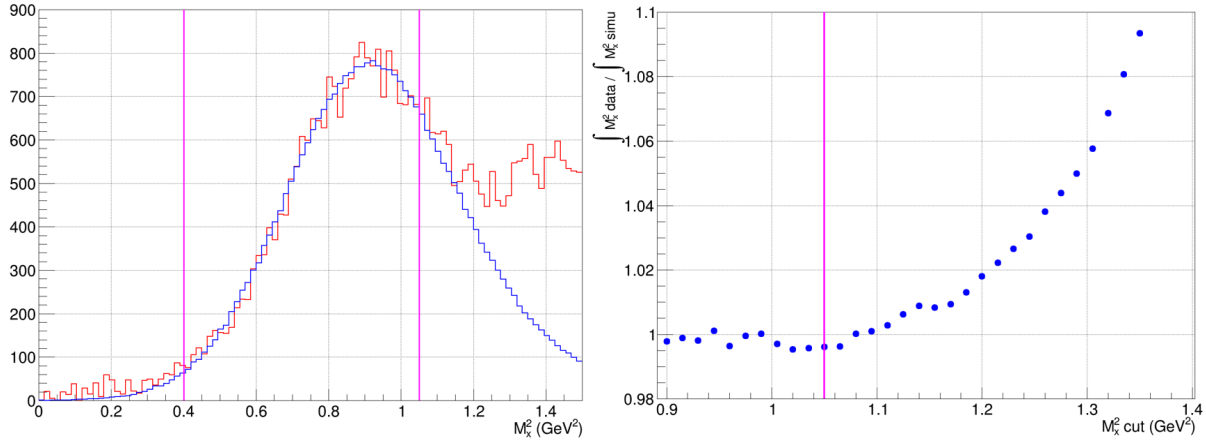

Figure 5.8: Left: the experimental (simulation) missing mass distribution of kin48_1 is represented in red (blue). Right: evolution of the ratio of the integrals of the experimental and simulation missing mass spectra with respect to the cut at the right of the exclusivity peak. The magenta lines represent the chosen cuts on the missing mass.

Kinematic setting	Left side M_X^2 cut (GeV^2)	Right side M_X^2 cut (GeV^2)
36_1	0.35	1.10
36_2	0.35	1.10
36_3	0.30	1.10
48_1	0.40	1.05
48_2	0.35	1.10
48_3	0.30	1.10
48_4	0.30	1.10
60_1	0.50	1.00
60_3	0.30	1.10

Table 5.5: Summary of the missing mass cuts for each kinematic setting.

In order to evaluate the systematic uncertainties introduced by these choices, the variations of the experimental cross section (see Eq. (5.35)) with respect to the values of the missing mass cuts are

studied. It is possible to visually locate in Fig. 5.8 the missing mass values beyond which the simulation and experimental spectra are mismatched with a precision of roughly 0.05 GeV^2. As a consequence, the missing mass cuts values are conservatively allowed to vary in a slightly larger ± 0.06 GeV^2 interval around the nominal cuts reported in Tab. 5.5. The largest variations of the cross section around its nominal value are then taken as systematic uncertainties (see Fig. 5.9). As the uncertainty introduced by the cut on the left side of the exclusivity peak is independent from the one introduced by the cut on the right, they are added quadratically. The total systematic uncertainty is evaluated individually for each reconstructed bin.

On average, an uncertainty between 2% and 5% has been measured. Additional work on the Monte Carlo smearing process may allow to further reduce this uncertainty by improving the matching of the simulation and experimental missing mass spectra. Indeed, the calibration and smearing of the simulation was challenging for a few regions of the calorimeter where the missing mass exclusivity peak is difficult to distinguish from the background. This was usually the case in regions with few events and affected by blocks with low gain, on the left side of the calorimeter. Adjusting for each region the boundaries i_{min} and i_{max} of the simulation calibration-smearing process could improve slightly the matching of the simulation and experimental missing mass spectra. Using a non-Gaussian smearing may also improve the agreement between the data and the simulation.

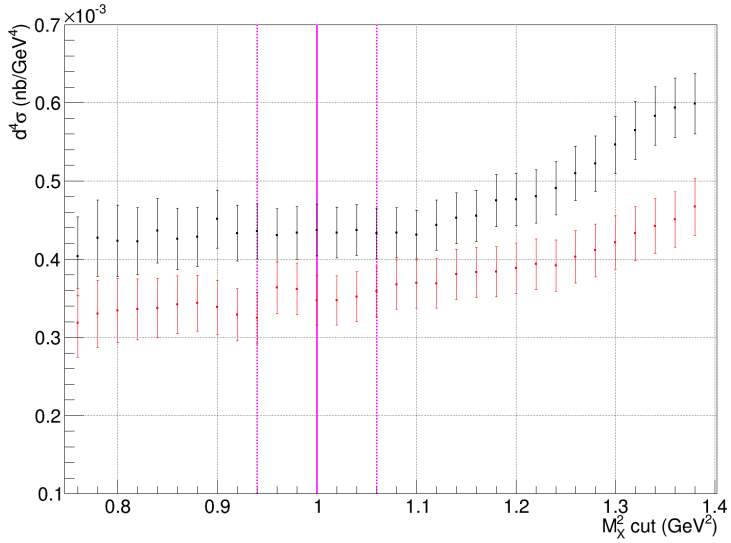

Figure 5.9: Variation of the experimental unpolarized cross section of kin_601 with respect to the missing mass cut at the right of the exclusivity peak, for -0.268 GeV$^2 < t - t_{min} < -0.134$ GeV^2, $\phi \approx 97°$ (black) and $\phi \approx 172°$ (red). The plain magenta line represents the value of the nominal missing mass cut (see Tab. 5.5). The dotted magenta lines represent the ± 0.06 GeV^2 interval where the largest variations of the cross section around its nominal value are taken as systematic uncertainties.

5.2.2.2 Choice of CFFs combinations for the cross-section parametrization

Another contribution to systematic uncertainties comes from the choice of the CFFs combinations used to parametrize and extract the cross section. Indeed, by choosing to rely on some specific CFFS combinations instead of others, the dependencies of the cross section on some terms is hereby assumed.

Different parametrizations have been tested for the unpolarized cross section. Using $\mathcal{R}e\mathcal{C}^{I,V}(\mathcal{F}_{++})$ instead of $\mathcal{C}^{DVCS}(\mathcal{F}_{++}, \mathcal{F}^*_{++} \mid \mathcal{F}_{-+}, \mathcal{F}^*_{-+})$ yields similarly good fit results, while the utilization of $\mathcal{R}e\mathcal{C}^{I}(\mathcal{F}_{-+})$ worsen the fit quality. Using the parametrization $\mathcal{R}e\mathcal{C}^{I}(\mathcal{F}_{++})$, $\mathcal{R}e\mathcal{C}^{I,V}(\mathcal{F}_{++})$, $\mathcal{R}e\mathcal{C}^{I,A}(\mathcal{F}_{++})$ does not yield good fit results either.

The systematic uncertainty is evaluated by comparing the cross sections obtained using parametrizations that yielded similarly good fit results. Let the *reference* parametrization be the one chosen in the previous section ($\mathcal{C}^{DVCS}(\mathcal{F}_{++}, \mathcal{F}^*_{++} \mid \mathcal{F}_{-+}, \mathcal{F}^*_{-+})$, $\mathcal{R}e\mathcal{C}^{I}(\mathcal{F}_{++})$ and $\mathcal{R}e\mathcal{C}^{I}(\mathcal{F}_{0+})$), and the *alternative* parametrization the one where $\mathcal{C}^{DVCS}(\mathcal{F}_{++}, \mathcal{F}^*_{++} \mid \mathcal{F}_{-+}, \mathcal{F}^*_{-+})$ is replaced by $\mathcal{R}e\mathcal{C}^{I,V}(\mathcal{F}_{++})$.

As can be seen in Fig. 5.10, depending on the parametrization choice, the cross section can vary up to $\sim 1.0\%$. The value of 1.0% is thus chosen as the systematic uncertainty associated to the choice of the CFFs combinations used to parametrize the cross section. However, since this uncertainty has a shape

because of the ϕ-modulation, an in-depth study of its effects on specific harmonic dependencies might be necessary.

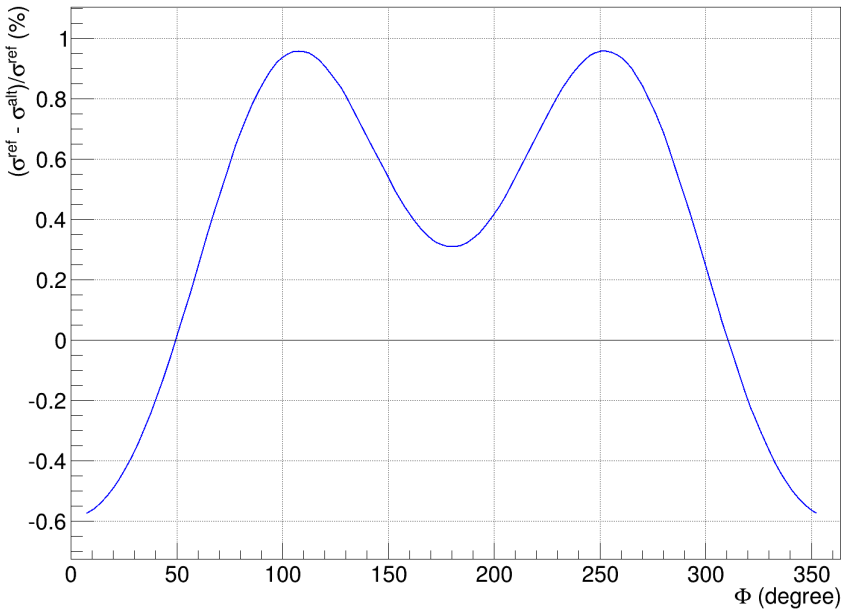

Figure 5.10: Relative difference between the unpolarized cross section parametrized with the $\mathcal{C}^{DVCS}$ term and the one parametrized with the $\mathcal{R}e\mathcal{C}^{I,V}$ term, for kin36_2, with $\langle Q^2 \rangle = 3.6$ GeV^2, $\langle x_{Bj} \rangle = 0.36$ and -0.248 GeV$^2 < t - t_{min} < -0.186$ GeV^2. The ϕ-dependence of the relative difference is due to the $\cos\phi$ and $\cos 2\phi$ dependence of $\mathcal{R}e\mathcal{C}^{I,V}$ whereas $\mathcal{C}^{DVCS}$ does not depend on ϕ. Both parametrization yielded a fit of similar quality: $\chi^2_{ref}/dof = 1.61$ and $\chi^2_{alt}/dof = 1.56$.

5.2.2.3 Correlated systematic uncertainties summary

The systematic uncertainties regarding the spectrometer cuts and virtual radiative corrections have not been evaluated yet. However, it is reasonable to assume that they should be very close to those reported for the E00-110 experiment. The correlated systematic uncertainties are summarized in Tab. 5.6. As a reminder, one needs to quadratically add to the values reported in Tab. 5.6:

- The uncorrelated uncertainties from the missing mass cuts, evaluated between 2% and 5% depending on the kinematic setting and the experimental bin.
- The correlated uncertainties, depending on the kinematic setting, arising from the fact that a Gaussian smearing of the simulation does not allow to accurately describe the low missing mass tail from the data (see Tab. 5.3). This uncertainty is quite large, between 2.8% and 5.6%, but can be greatly reduced by a non-Gaussian smearing of the simulation.

5.2.3 Preliminary results

5.2.3.1 Unpolarized and polarized DVCS cross sections

The figures 5.11 and 5.12 display respectively the unpolarized and helicity-dependent cross section with respect to ϕ for a $t-$bin of kin36_2. The experimental cross section and the associated statistical uncertainty is represented by the black dots, while the fit is shown by the black curve. The contribution from the pure Bethe-Heitler is the red curve, while the contributions of the combinations of CFFs $\langle X_n \rangle_v$ parametrizing the cross section, multiplied by the corresponding kinematic factors $F_n(E, \langle Q^2 \rangle_v, \langle x_{Bj} \rangle_v, \langle t \rangle_v, \phi_r, \lambda)$ (see appendix B) are represented in green, magenta and cyan. The statistical uncertainties associated to the cross section fit and the combinations of CFFs are computed from the covariance matrix A^{-1} and are represented by their respective colored areas. The blue error band at the bottom of the figures represents the total systematic uncertainty introduced by the missing mass cuts.

The experiment preliminary results are summarized for every kinematic setting in Fig. 5.13 to 5.30. The values of the experimental cross sections, the associated statistical uncertainties, and the systematic

Correlated systematic uncertainty	Value (%)
HRS electron identification *	0.5
HRS multi-track correction *	0.5
HRS acceptance (R-function) *	1.0
Luminosity and dead time	1.6
Virtual radiative corrections *	2.0
Beam polarization	1.0 (2.2)
CFFs parametrization	1.0
Total (unpolarized)	**3.0**
Total (helicity-dependent)	**3.2 (3.7)**

Table 5.6: Summary of the correlated systematic uncertainties. Uncertainties with a * have yet to be evaluated and are assumed to be close to the ones reported in [98]. The values between parenthesis correspond to kin36_1.

uncertainties due to the missing mass cuts are summarized for every experimental bin and for every kinematic setting in tables available in appendix D.

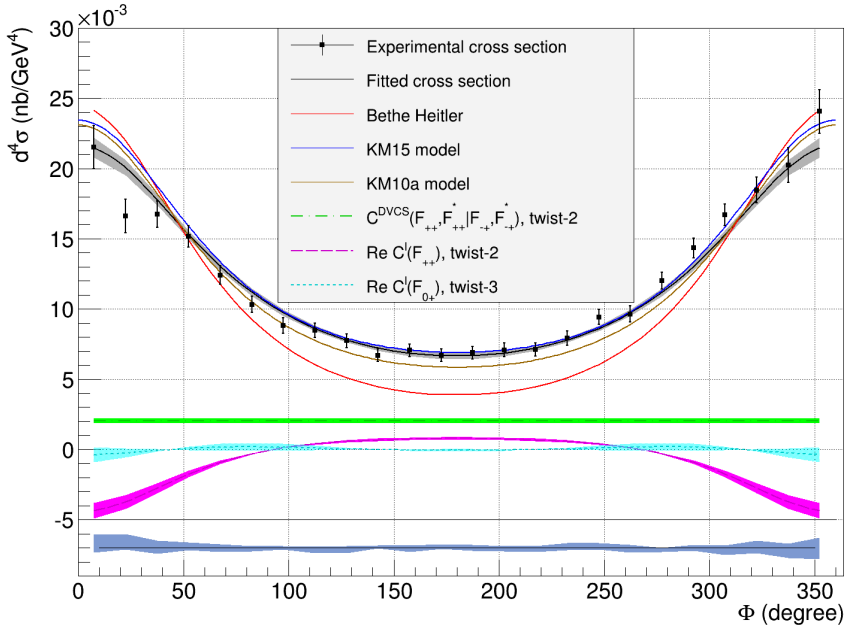

Figure 5.11: Unpolarized cross section for kin36_2, with a beam energy $E_{beam} = 8.5$ GeV, $\langle Q^2 \rangle = 3.6$ GeV^2, $\langle x_{Bj} \rangle = 0.36$ and -0.186 GeV$^2 < t - t_{min} < -0.124$ GeV^2. The black dots represent the experimental cross section with statistical uncertainty bars while the black curve with statistical uncertainty band is the cross section fit. The Bethe-Heitler is represented in red, while the models KM10a and KM15 are respectively in brown and blue. The contributions of the combinations of CFFs $\langle X_n \rangle_v$ parametrizing the unpolarized cross section, multiplied by the corresponding kinematic factors $F_n(E, \langle Q^2 \rangle_v, \langle x_{Bj} \rangle_v, \langle t \rangle_v, \phi_r, \lambda)$ are represented in green, magenta and cyan, with their respective statistical uncertainty bands. The blue uncertainty band at the bottom represents the total systematic uncertainty introduced by the missing mass cuts.

In the unpolarized case (see Fig. 5.11), the cross section can be clearly distinguished from the pure Bethe-Heitler contribution and sizeable DVCS and interference terms can be measured. In particular, with the CFFs combinations chosen in section 5.2.1, for values of ϕ close to 180°, the DVCS term is dominant. On the other hand, for values of ϕ close to 0° and 360°, the absolute value of the interference becomes comparable or larger than the DVCS term.

The statistical and systematic uncertainties are of comparable size, although for the helicity-dependent cross section, the statistical ones tends to be slightly larger than the systematic ones. Furthermore, in the helicity-dependent case, because the quantity which is measured is a difference of cross sections, the relative statistical and systematic uncertainties are larger than in the unpolarized case (see Fig. 5.12).

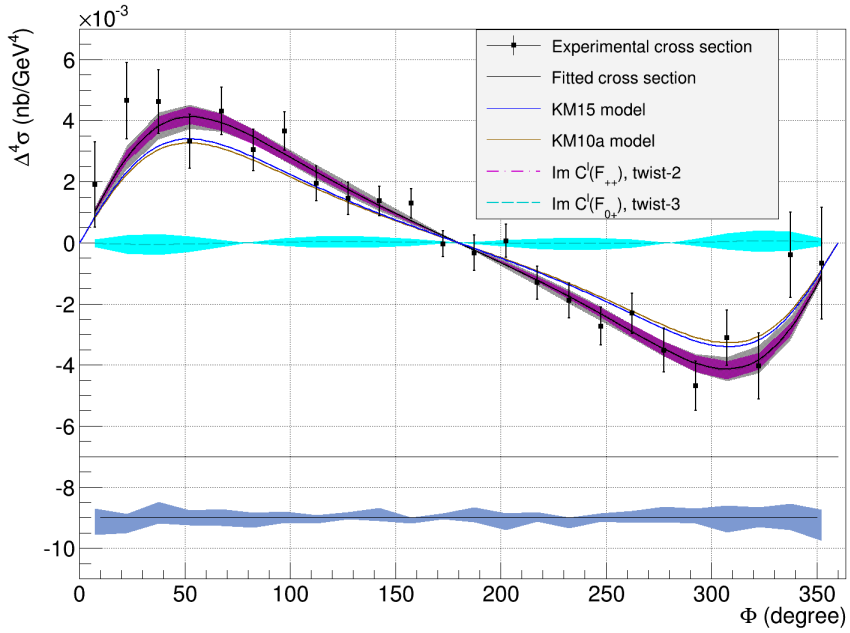

Figure 5.12: Helicity-dependent cross section for kin36_2, with a beam energy $E_{beam} = 8.5$ GeV, $\langle Q^2 \rangle = 3.6$ GeV^2, $\langle x_{Bj} \rangle = 0.36$ and -0.186 GeV$^2 < t - t_{min} < -0.124$ GeV^2. The black dots represent the experimental cross section with statistical uncertainty bars while the black curve with statistical uncertainty band is the cross section fit. The models KM10a and KM15 are respectively in brown and blue. The contributions of the combinations of CFFs $\langle X_n \rangle_v$ parametrizing the helicity-dependent cross section, multiplied by the corresponding kinematic factors $F_n(E, \langle Q^2 \rangle_v, \langle x_{Bj} \rangle_v, \langle t \rangle_v, \phi_r, \lambda)$ are represented in magenta, and cyan, with their respective statistical uncertainty bands. The blue uncertainty band at the bottom represents the total systematic uncertainty introduced by the missing mass cuts.

As predicted, statistical uncertainties can become very large for values of ϕ close to 0° or 360° for the two t-bins where $t - t_{min}$ is the largest because of a lack of events due to the calorimeter acceptance (see Fig. 5.13 and 5.14).

For both unpolarized and helicity-dependent cross sections, the twist-2 CFF contributions tend to be dominant while the twist-3 ones are close to 0 (see Fig. 5.11 and 5.12). In a few cases, some twist-3 contributions seem to rise to non negligible values. However, the associated uncertainty bands are often large and compatible with 0 when taking systematic uncertainties into account: it is unclear whether this is a genuine effect, or simply a consequence of statistic and systematic uncertainties (see Fig. 5.13 to 5.30).

For every kinematic setting, the obtained cross sections have been compared to two global fits to DVCS data: KM10a and KM15. The model KM10a did not use Hall A data, while the model KM15 includes Hall A and CLAS data up to their latest results of 2015. In particular the Hall A data of 2015 supersede the previous ones of 2006. Further details concerning these models can be found in [20] and [99]. An executable developed by K. Kumerički and D. Müller in order to compute cross sections for each model is available at http://calculon.phy.hr/gpd/.

In the case of the unpolarized cross sections (see Fig. 5.11), the model KM15 (blue curve) is in a very good agreement with the data for every kinematic setting. On the other hand, the model KM10a (brown) tends to undershoot the experimental cross sections. When x_{Bj} becomes larger, the discrepancy between the experimental cross section and the models tends to increase (see Fig. 5.13 to 5.30), which is expected since the models were designed for smaller values of x_{Bj}.

Regarding the helicity-dependent cross sections (see Fig. 5.12), the data tend to be fairly well described by both fits KM10a and KM15 for every value of Q^2 or x_{Bj} (see Fig. 5.13 to 5.30). The global fits seem to show a better agreement with the unpolarized cross sections than the helicity-dependent ones, but one also has to keep in mind that uncertainties are larger in the latter case.

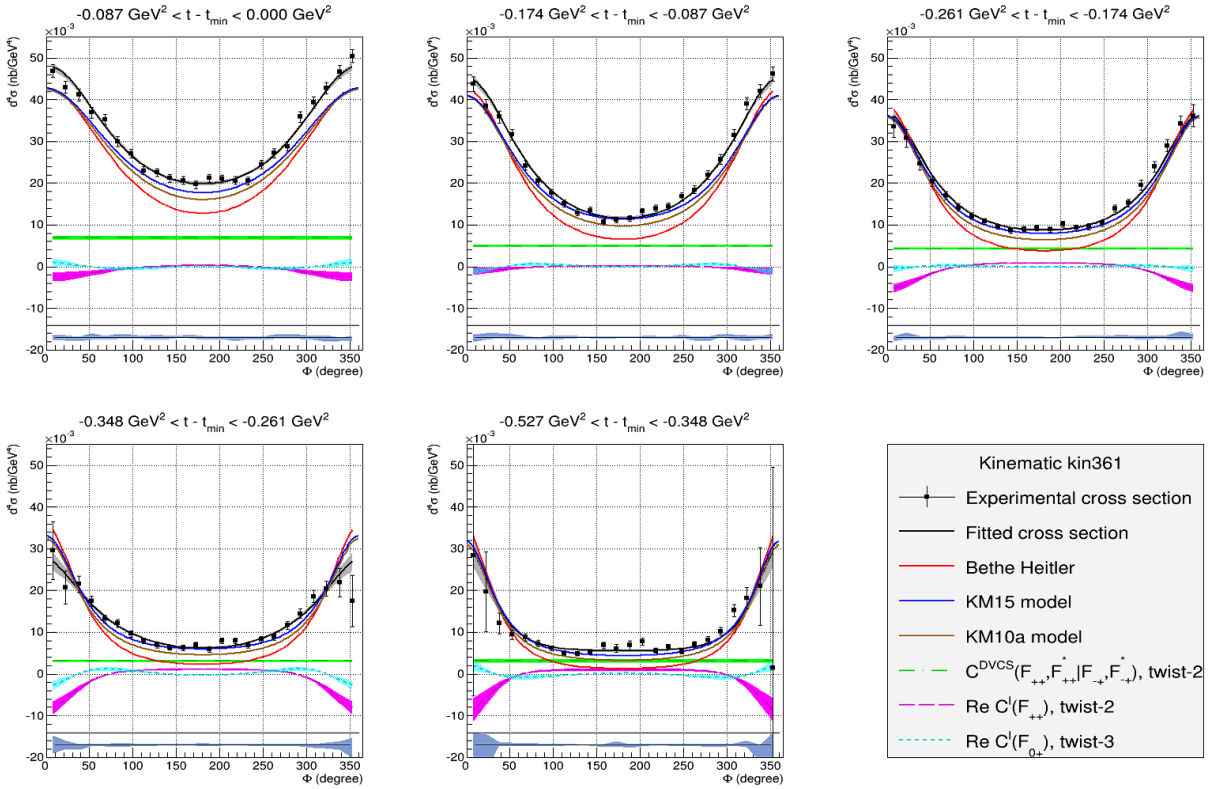

Figure 5.13: Unpolarized cross sections for kin36_1, with $E_{beam} = 7.38$ GeV, $\langle Q^2 \rangle = 3.17$ GeV^2, $\langle x_{Bj} \rangle = 0.36$ and $\chi^2/dof = 1.33$. The uncertainty bars are statistical only. The blue error band at the bottom represents the systematic uncertainty associated with the missing mass cuts.

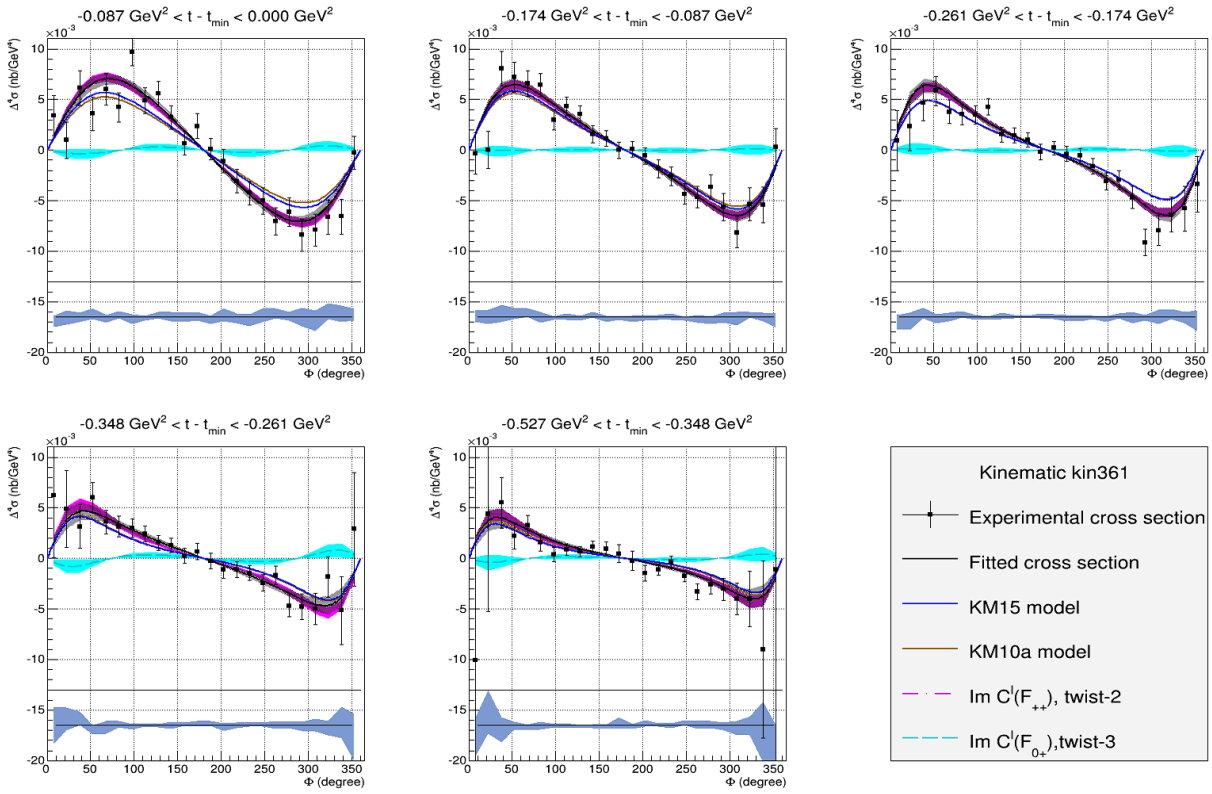

Figure 5.14: Helicity-dependent cross sections for kin36_1, with $E_{beam} = 7.38$ GeV, $\langle Q^2 \rangle = 3.17$ GeV^2, $\langle x_{Bj} \rangle = 0.36$ and $\chi^2/dof = 0.89$. The uncertainty bars are statistical only. The blue error band at the bottom represents the systematic uncertainty associated with the missing mass cuts.

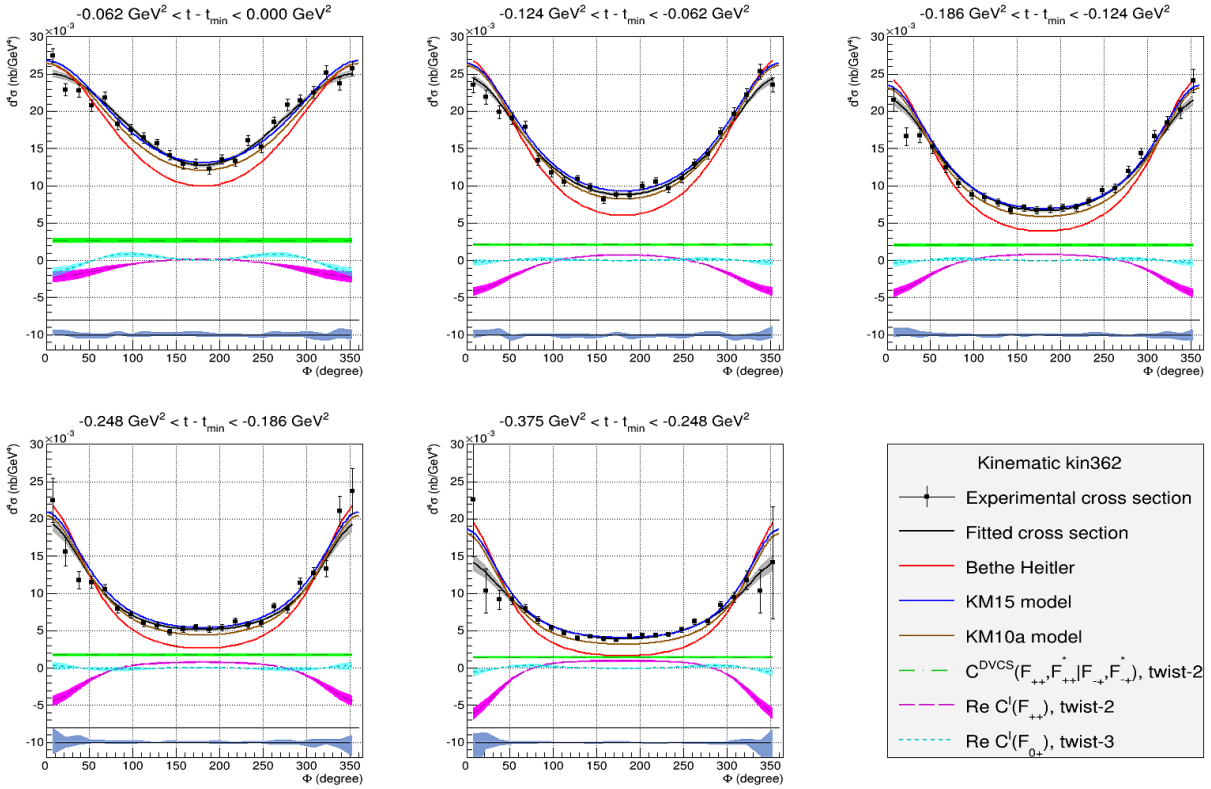

Figure 5.15: Unpolarized cross sections for kin36_2, with $E_{beam} = 8.52$ GeV, $\langle Q^2 \rangle = 3.67$ GeV^2, $\langle x_{Bj} \rangle = 0.37$ and and $\chi^2/dof = 1.61$. The uncertainty bars are statistical only. The blue error band at the bottom represents the systematic uncertainty associated with the missing mass cuts.

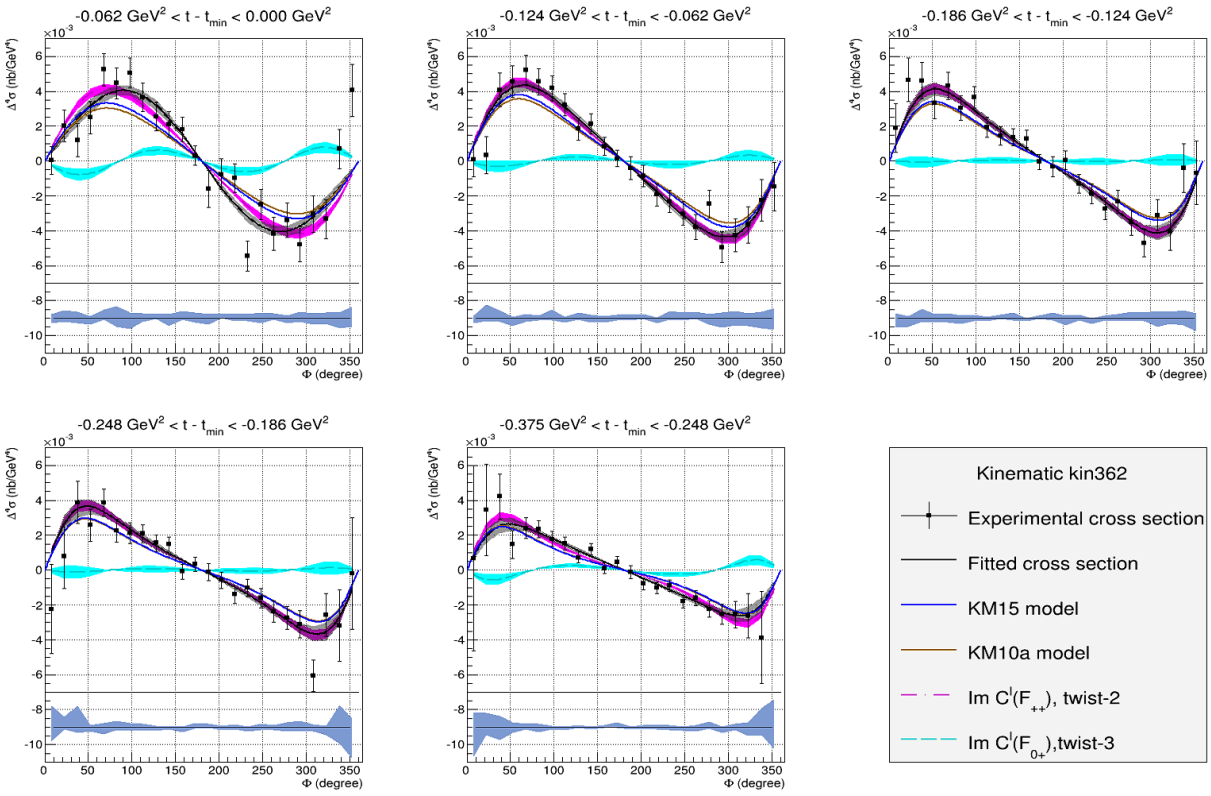

Figure 5.16: Helicity-dependent cross sections for kin36_2, with $E_{beam} = 8.52$ GeV, $\langle Q^2 \rangle = 3.67$ GeV^2, $\langle x_{Bj} \rangle = 0.37$ and $\chi^2/dof = 0.94$. The uncertainty bars are statistical only. The blue error band at the bottom represents the systematic uncertainty associated with the missing mass cuts.

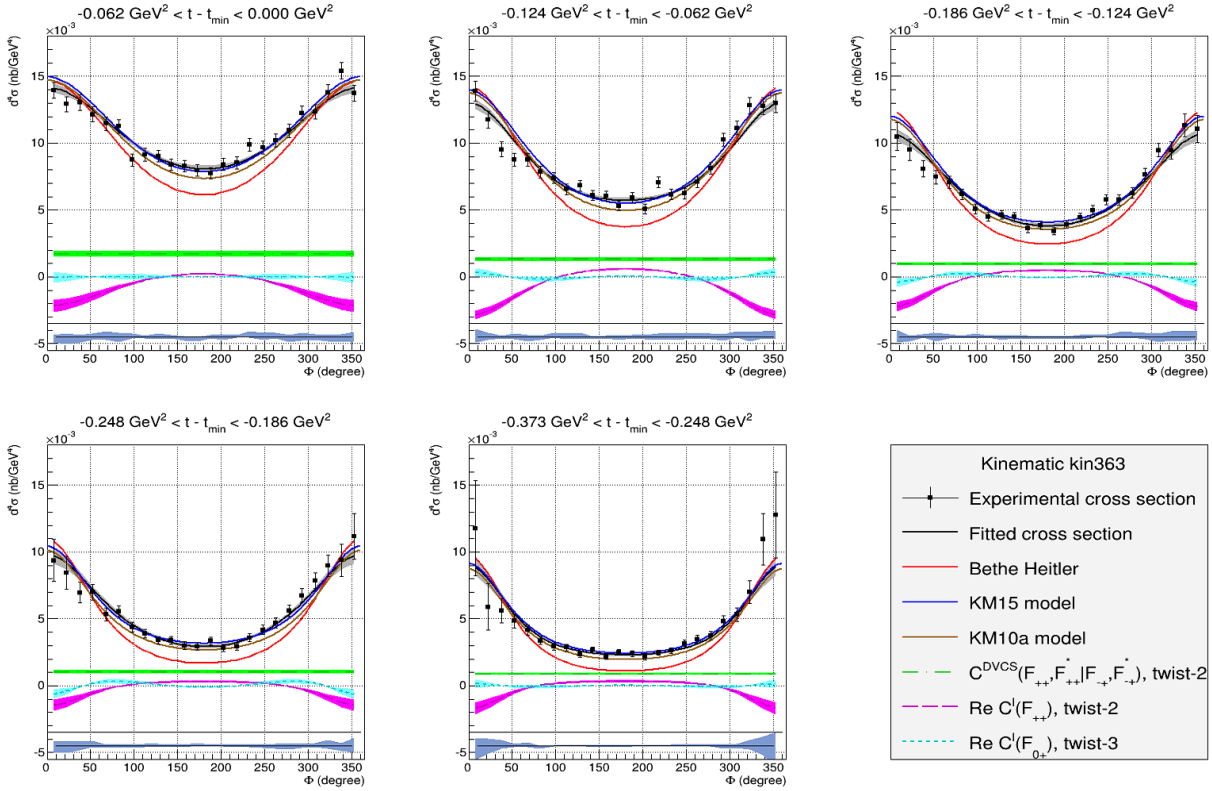

Figure 5.17: Unpolarized cross sections for kin36_3, with $E_{beam} = 10.59$ GeV, $\langle Q^2 \rangle = 4.57$ GeV^2, $\langle x_{Bj} \rangle = 0.37$ and $\chi^2/dof = 1.47$. The uncertainty bars are statistical only. The blue error band at the bottom represents the systematic uncertainty associated with the missing mass cuts.

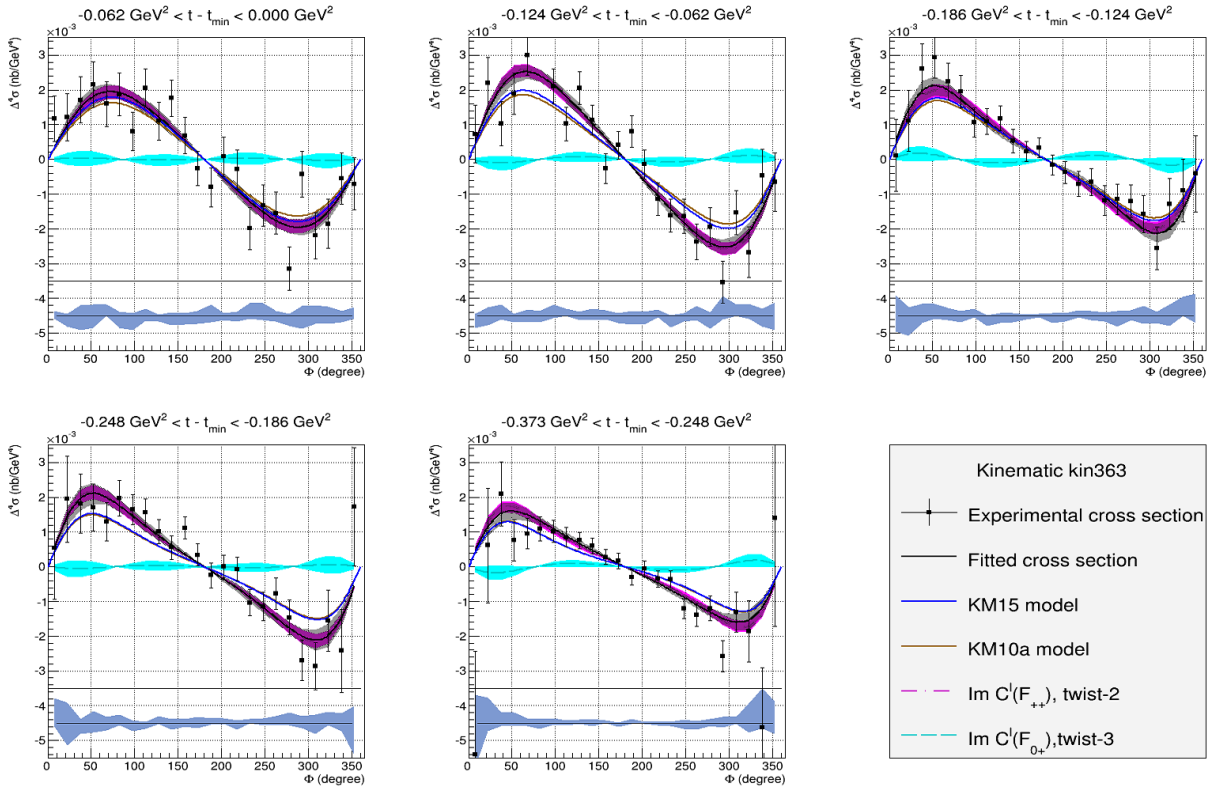

Figure 5.18: Helicity-dependent cross sections for kin36_3, with $E_{beam} = 10.59$ GeV, $\langle Q^2 \rangle = 4.57$ GeV^2, $\langle x_{Bj} \rangle = 0.37$ and $\chi^2/dof = 1.07$. The uncertainty bars are statistical only. The blue error band at the bottom represents the systematic uncertainty associated with the missing mass cuts.

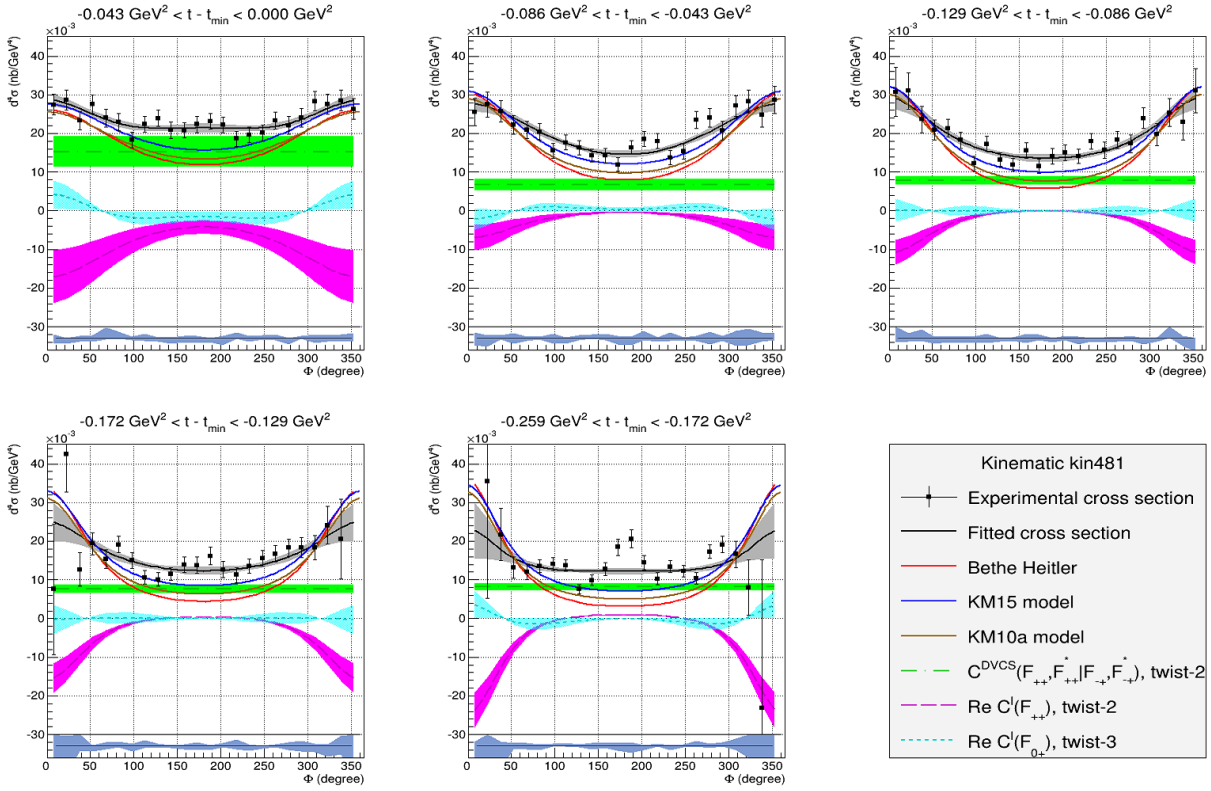

Figure 5.19: Unpolarized cross sections for kin48_1, with $E_{beam} = 4.49$ GeV, $\langle Q^2 \rangle = 2.71$ GeV^2, $\langle x_{Bj} \rangle = 0.48$ and $\chi^2/dof = 1.51$. The uncertainty bars are statistical only. The blue error band at the bottom represents the systematic uncertainty associated with the missing mass cuts.

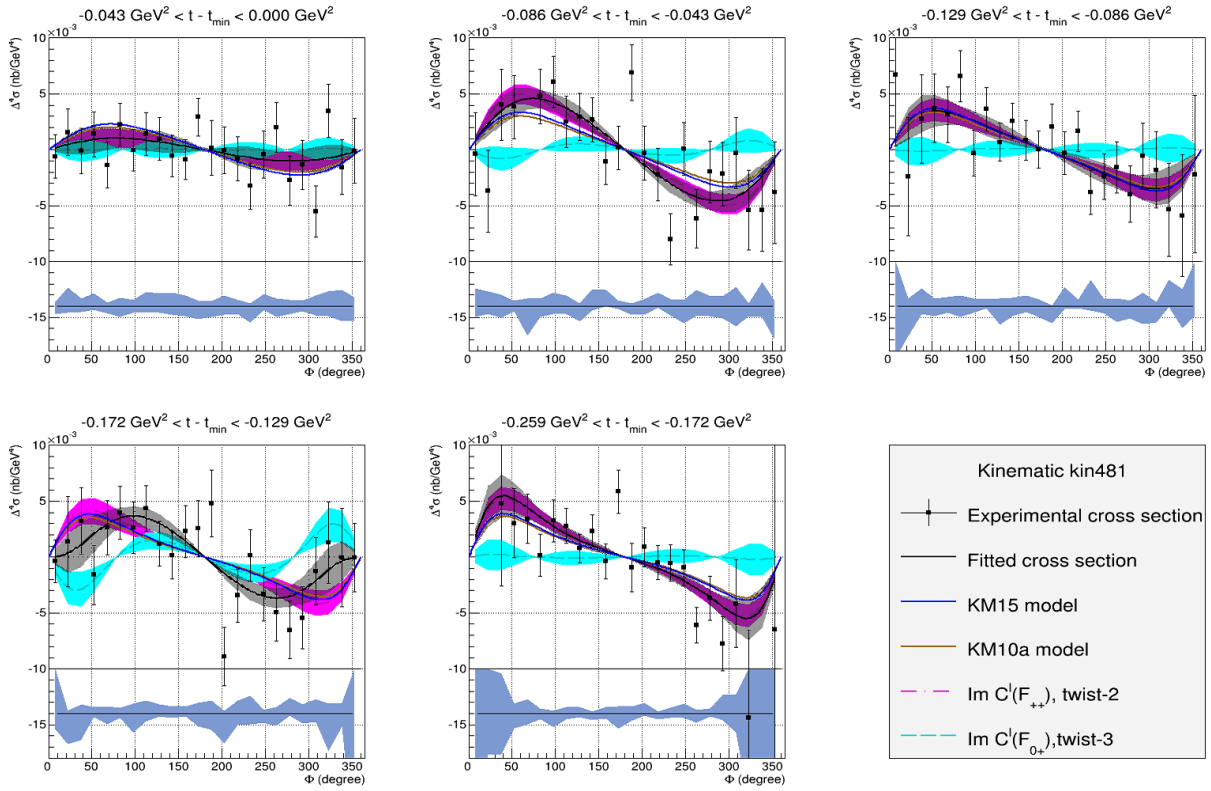

Figure 5.20: Helicity-dependent cross sections for kin48_1, with $E_{beam} = 4.49$ GeV, $\langle Q^2 \rangle = 2.71$ GeV^2, $\langle x_{Bj} \rangle = 0.48$ and $\chi^2/dof = 1.00$. The uncertainty bars are statistical only. The blue error band at the bottom represents the systematic uncertainty associated with the missing mass cuts.

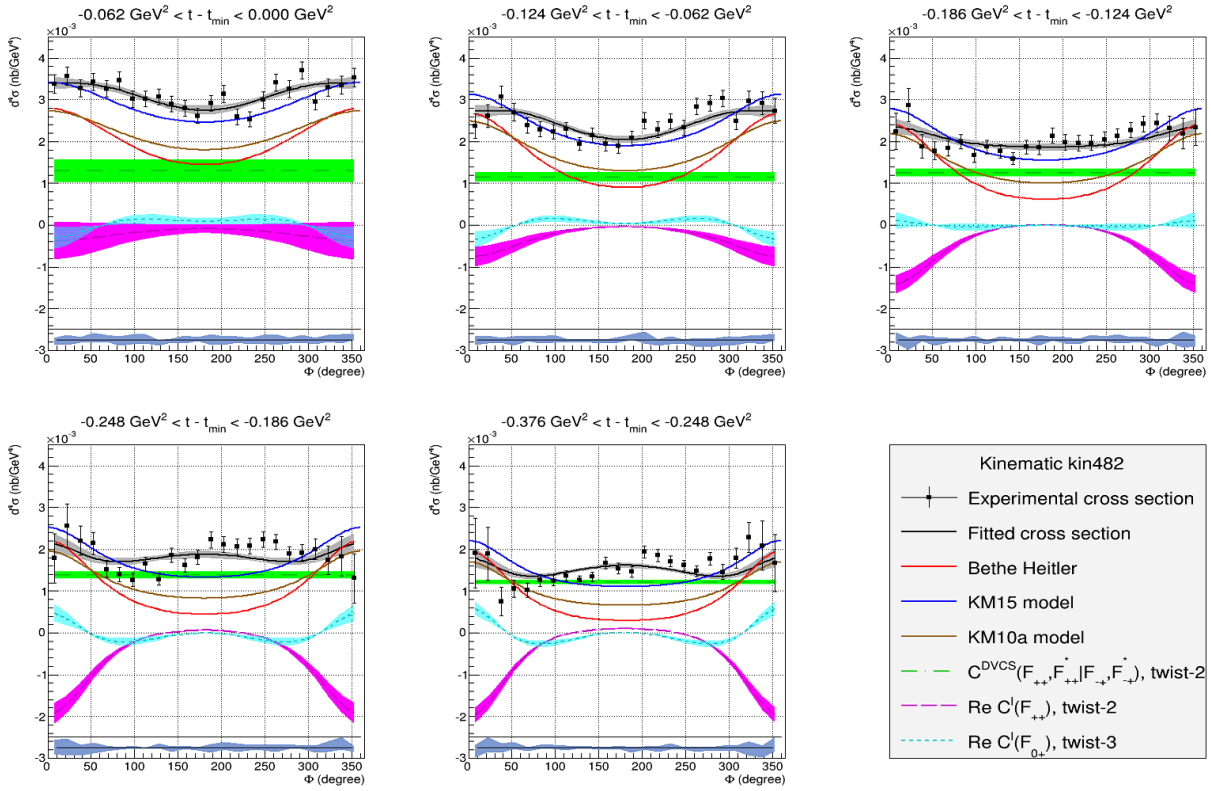

Figure 5.21: Unpolarized cross sections for kin48_2, with $E_{beam} = 8.85$ GeV, $\langle Q^2 \rangle = 4.55$ GeV^2, $\langle x_{Bj} \rangle = 0.50$ and $\chi^2/dof = 1.92$. The uncertainty bars are statistical only. The blue error band at the bottom represents the systematic uncertainty associated with the missing mass cuts.

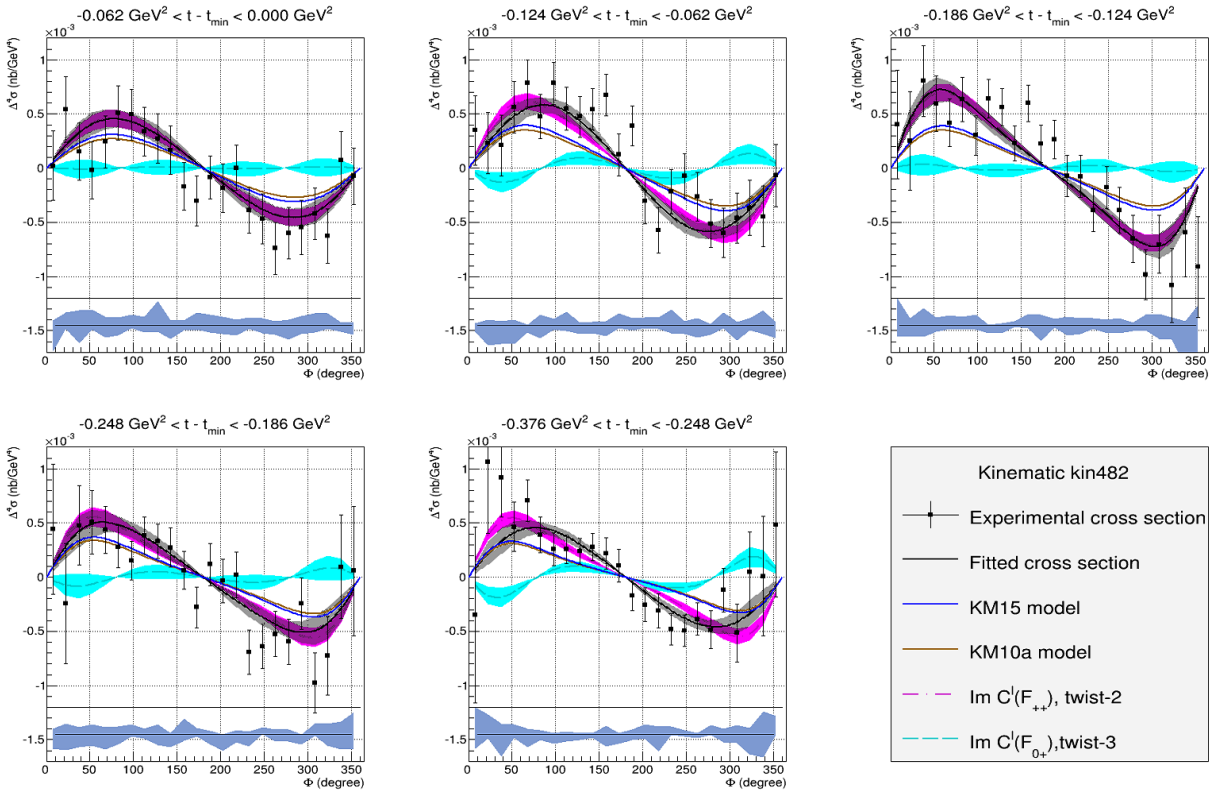

Figure 5.22: Helicity-dependent cross sections for kin48_2, with $E_{beam} = 8.85$ GeV, $\langle Q^2 \rangle = 4.55$ GeV^2, $\langle x_{Bj} \rangle = 0.50$ and $\chi^2/dof = 1.01$. The uncertainty bars are statistical only. The blue error band at the bottom represents the systematic uncertainty associated with the missing mass cuts.

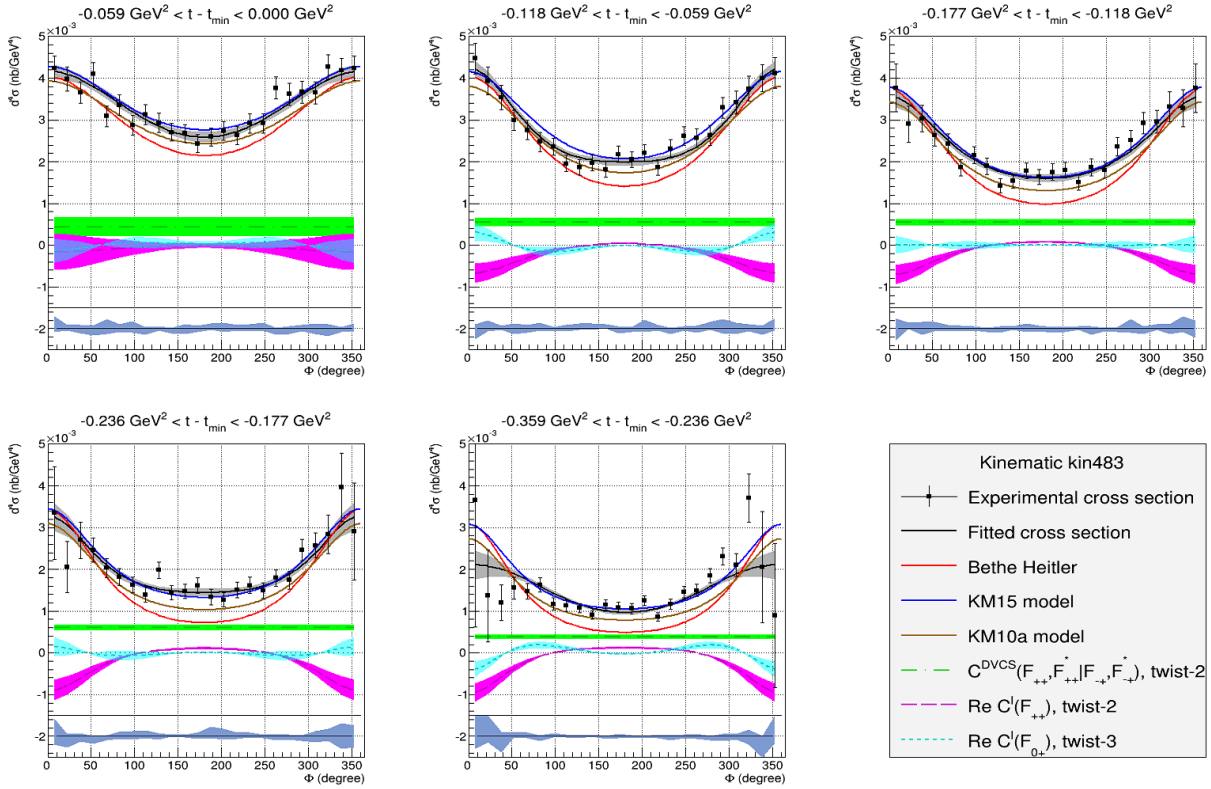

Figure 5.23: Unpolarized cross sections for kin48_3, with $E_{beam} = 8.85$ GeV, $\langle Q^2 \rangle = 5.35$ GeV^2, $\langle x_{Bj} \rangle = 0.48$ and $\chi^2/dof = 1.19$. The uncertainty bars are statistical only. The blue error band at the bottom represents the systematic uncertainty associated with the missing mass cuts.

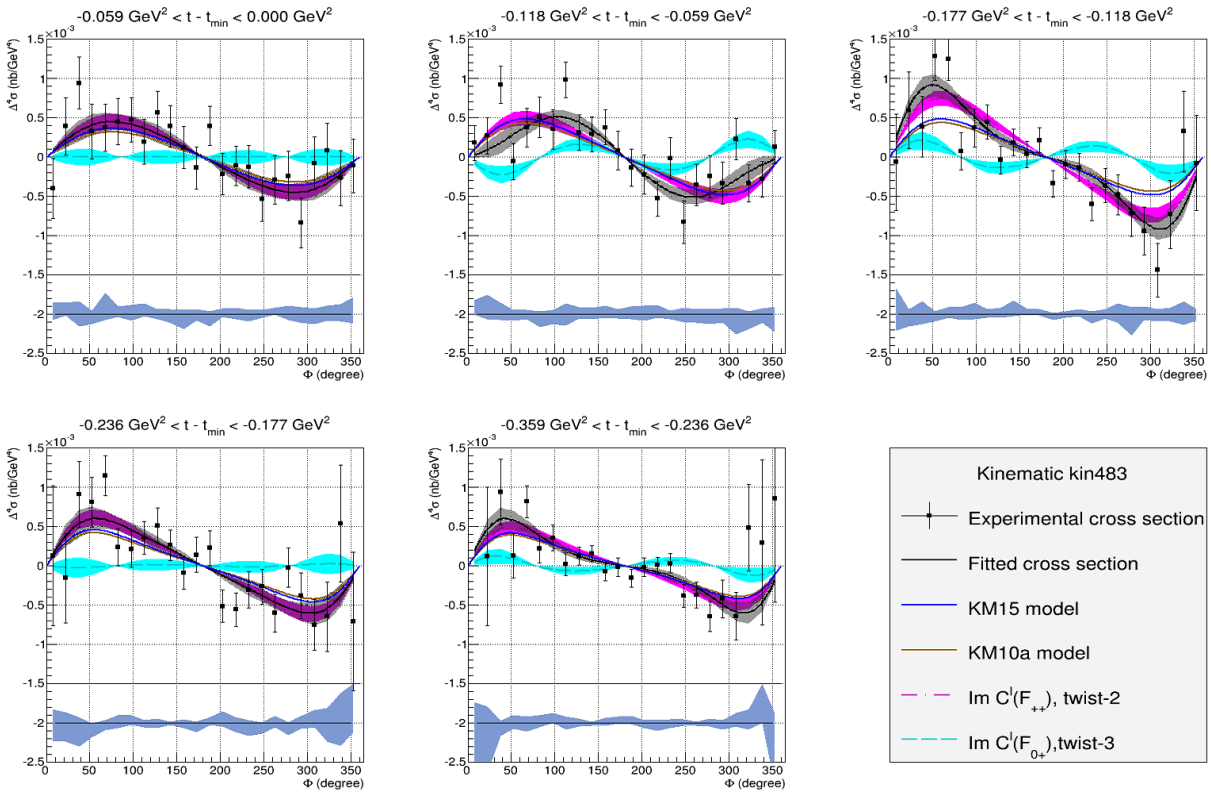

Figure 5.24: Helicity-dependent cross sections for kin48_3, with $E_{beam} = 8.85$ GeV, $\langle Q^2 \rangle = 5.35$ GeV^2, $\langle x_{Bj} \rangle = 0.48$ and $\chi^2/dof = 1.15$. The uncertainty bars are statistical only. The blue error band at the bottom represents the systematic uncertainty associated with the missing mass cuts.

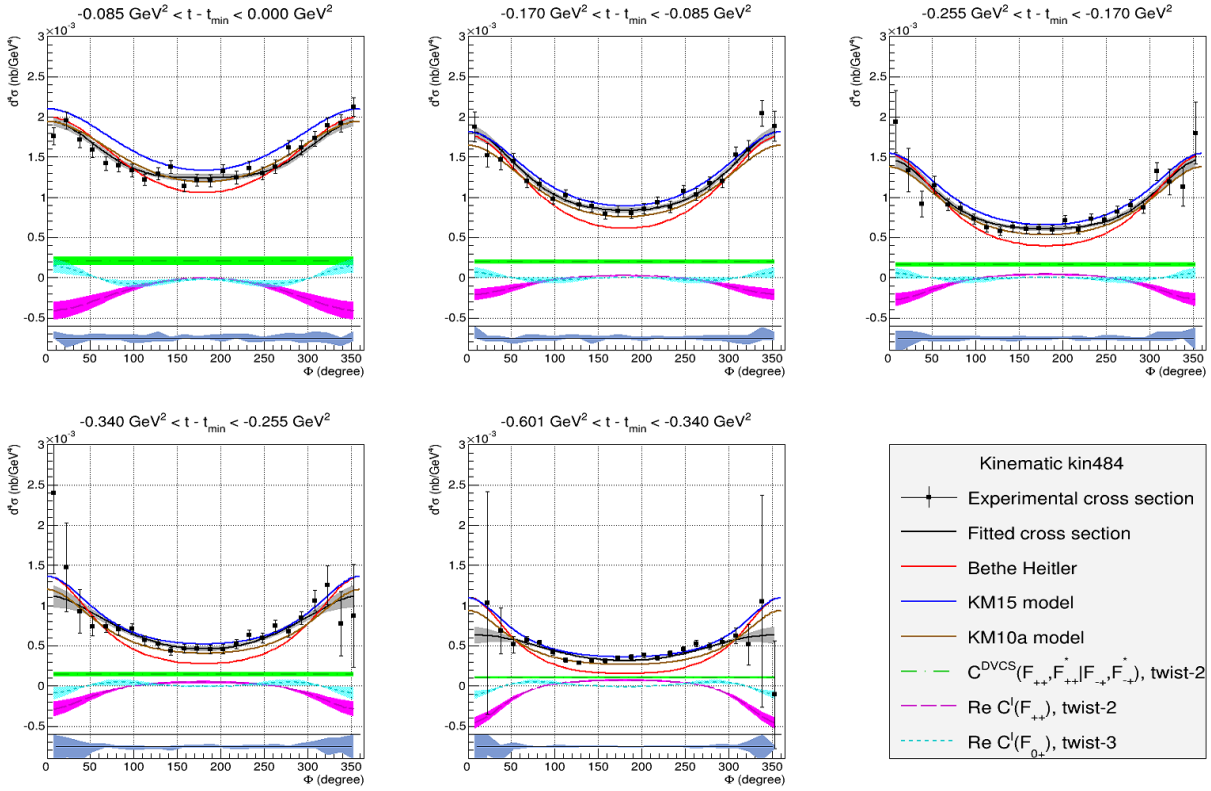

Figure 5.25: Unpolarized cross sections for kin48_4, with $E_{beam} = 10.99$ GeV, $\langle Q^2 \rangle = 7.10$ GeV^2, $\langle x_{Bj} \rangle = 0.50$ and $\chi^2/dof = 1.20$. The uncertainty bars are statistical only. The blue error band at the bottom represents the systematic uncertainty associated with the missing mass cuts.

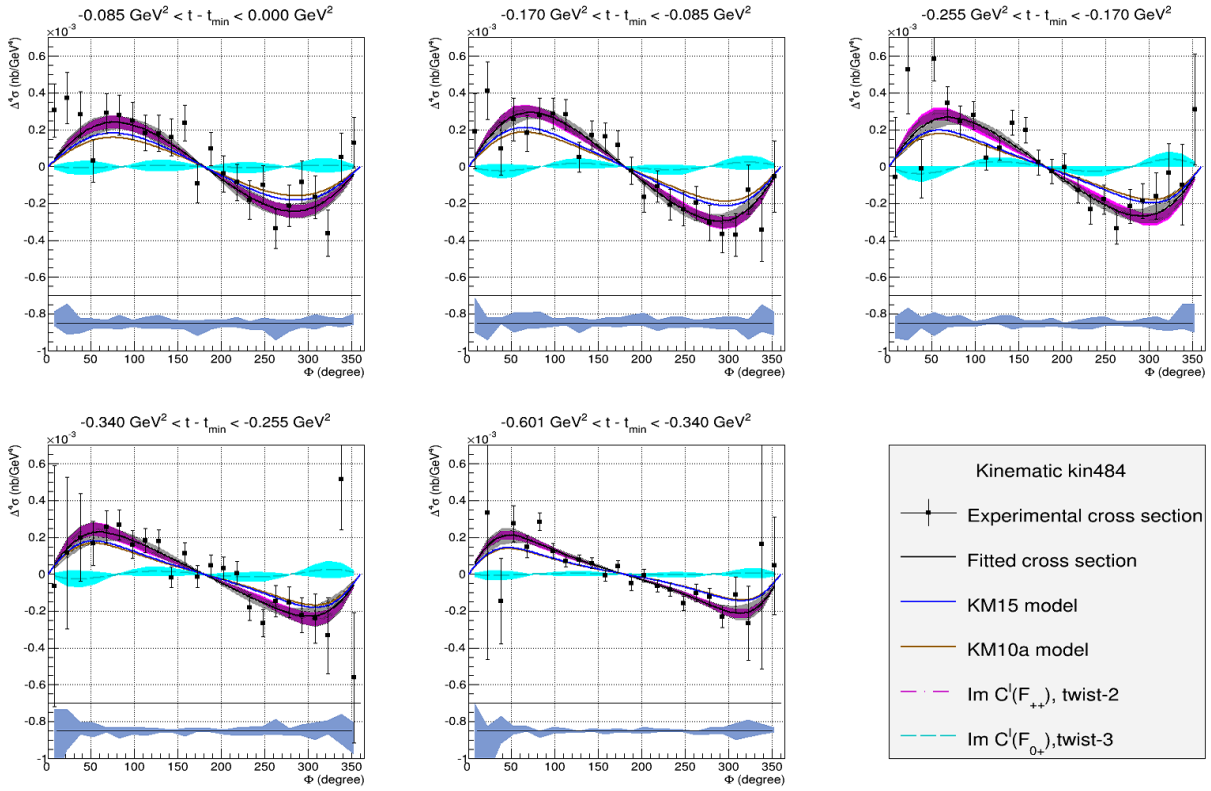

Figure 5.26: Helicity-dependent cross sections for kin48_4, with $E_{beam} = 10.99$ GeV, $\langle Q^2 \rangle = 7.10$ GeV^2, $\langle x_{Bj} \rangle = 0.50$ and $\chi^2/dof = 1.10$. The uncertainty bars are statistical only. The blue error band at the bottom represents the systematic uncertainty associated with the missing mass cuts.

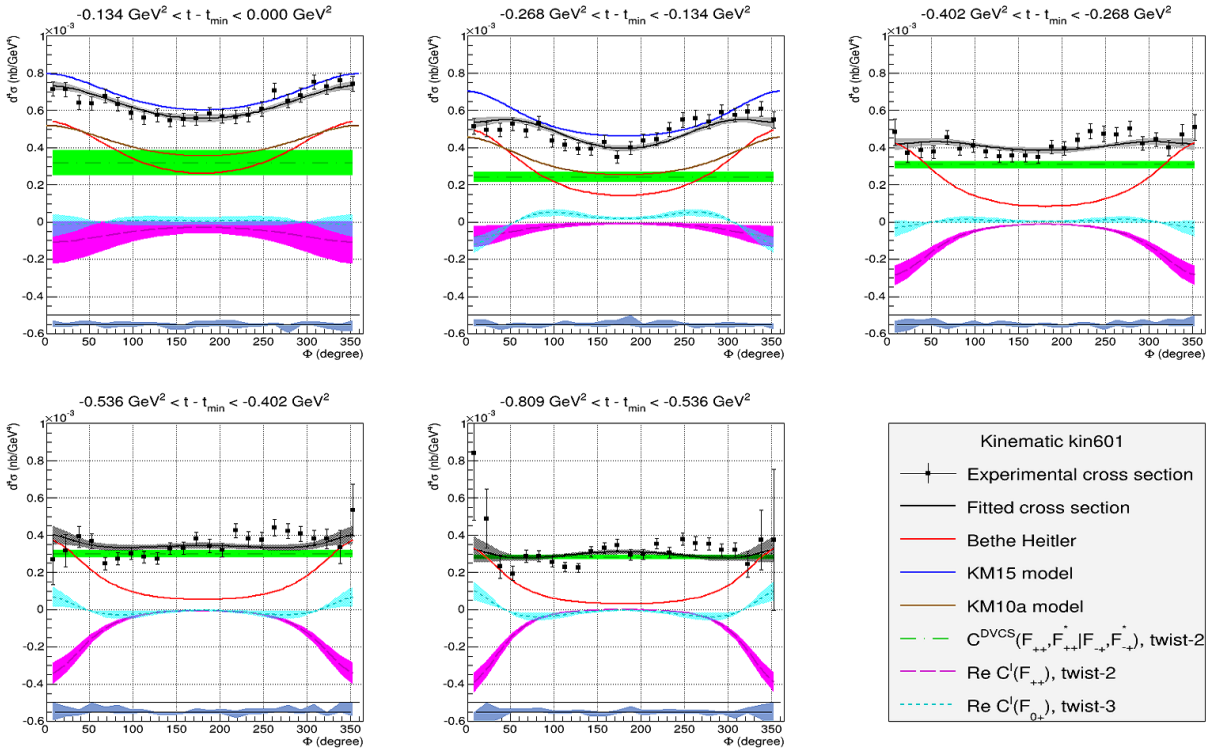

Figure 5.27: Unpolarized cross sections for kin60_1, with $E_{beam} = 8.52$ GeV, $\langle Q^2 \rangle = 5.63$ GeV^2, $\langle x_{Bj} \rangle = 0.61$ and $\chi^2/dof = 1.72$. The uncertainty bars are statistical only. The blue error band at the bottom represents the systematic uncertainty associated with the missing mass cuts. The executable available at http://calculon.phy.hr/gpd/ does not allow to evaluate the models at large t for this kinematic setting.

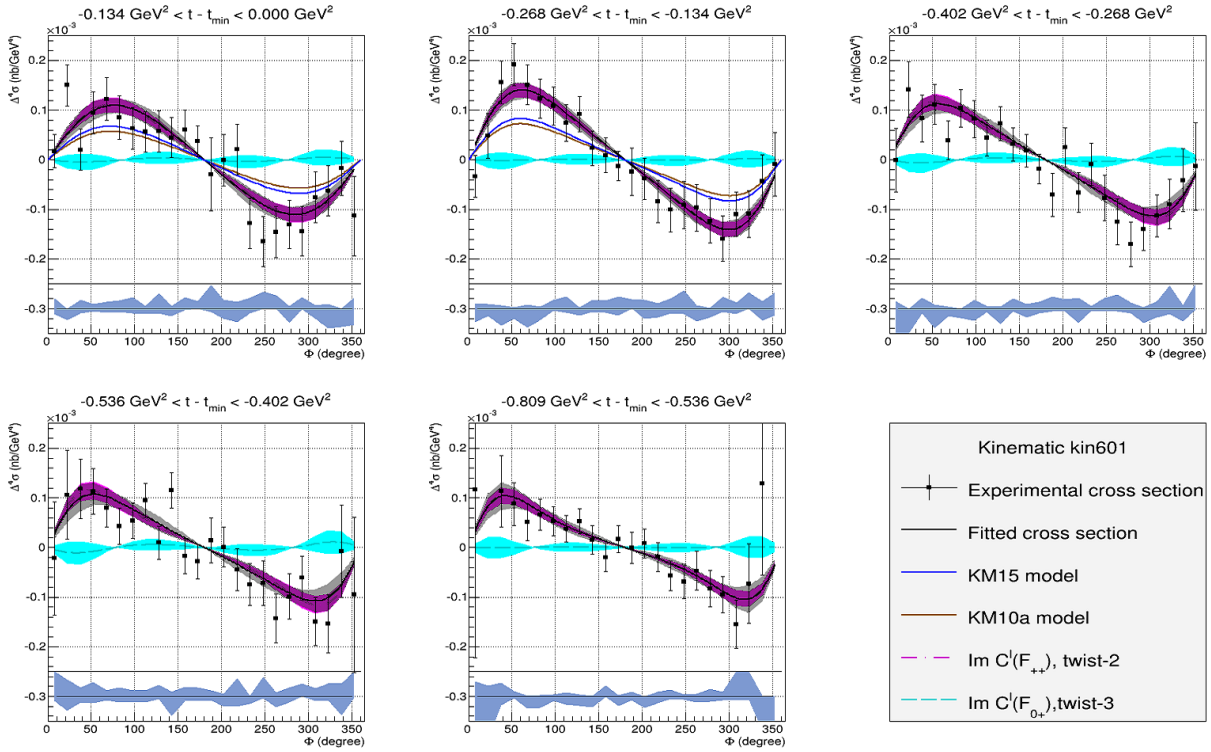

Figure 5.28: Helicity-dependent cross sections for kin60_1, with $E_{beam} = 8.52$ GeV, $\langle Q^2 \rangle = 5.63$ GeV^2, $\langle x_{Bj} \rangle = 0.61$ and $\chi^2/dof = 0.69$. The uncertainty bars are statistical only. The blue error band at the bottom represents the systematic uncertainty associated with the missing mass cuts. The executable available at http://calculon.phy.hr/gpd/ does not allow to evaluate the models at large t for this kinematic setting.

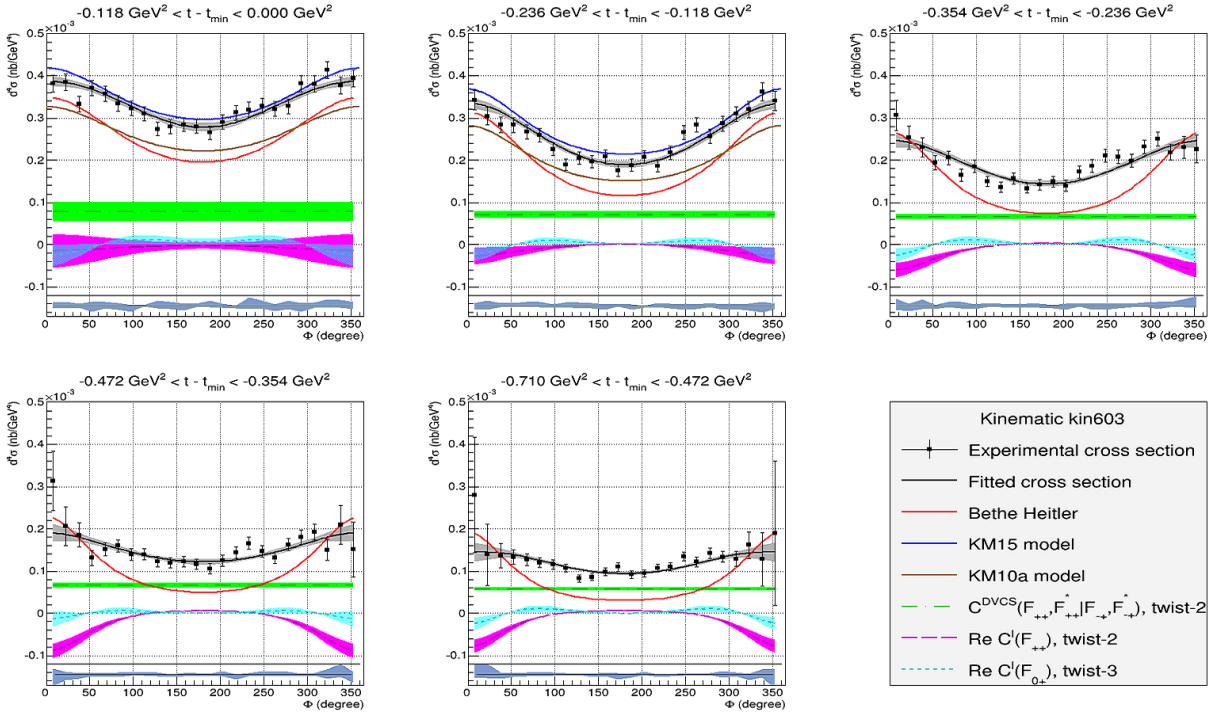

Figure 5.29: Unpolarized cross sections for kin60_3, with $E_{beam} = 10.59$ GeV, $\langle Q^2 \rangle = 8.48$ GeV^2, $\langle x_{Bj} \rangle = 0.61$ and $\chi^2/dof = 1.34$. The uncertainty bars are statistical only. The blue error band at the bottom represents the systematic uncertainty associated with the missing mass cuts. The executable available at http://calculon.phy.hr/gpd/ does not allow to evaluate the models at large t for this kinematic setting.

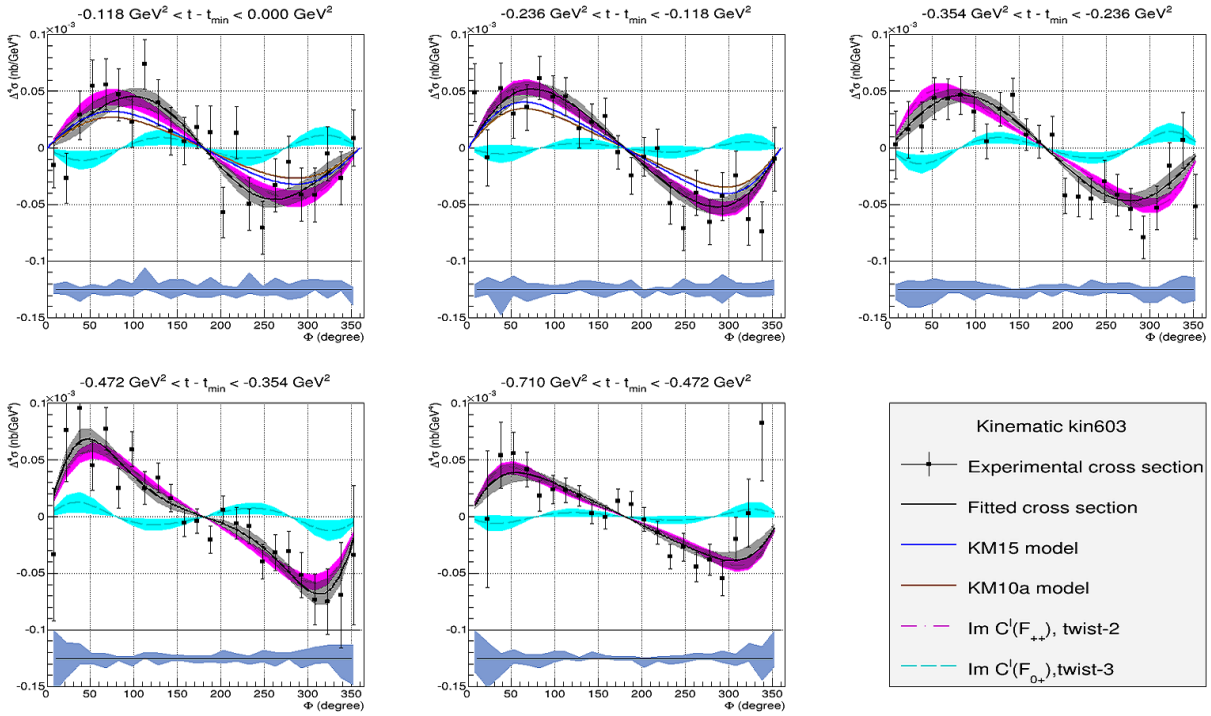

Figure 5.30: Helicity-dependent cross sections for kin60_3, with $E_{beam} = 10.59$ GeV, $\langle Q^2 \rangle = 8.48$ GeV^2, $\langle x_{Bj} \rangle = 0.61$ and $\chi^2/dof = 1.04$. The uncertainty bars are statistical only. The blue error band at the bottom represents the systematic uncertainty associated with the missing mass cuts. The executable available at http://calculon.phy.hr/gpd/ does not allow to evaluate the models at large t for this kinematic setting.

5.2.3.2 Scaling test: Q^2 dependence of the CFFs combinations

The Q^2 dependence of the CFFs combinations used in the parametrization of the cross sections (scaling test), for each value of x_{Bj} and integrated over t, has also been studied.

The DVCS cross section has mainly a $sin(\phi)$ dependence on the twist-2 term $\mathcal{I}m\mathcal{C}^I(\mathcal{F}_{++})$. As one can see in Fig. 5.31, this term was found to be independent from Q^2, which is an indication towards the twist-2 dominance. This result is consistent with the ones from the previous Hall A experiment [48], although the values of $\mathcal{I}m\mathcal{C}^I(\mathcal{F}_{++})$ which were found cannot be compared directly since the ranges in t are different. One will also notice that the lever arms in Q^2 and x_{Bj} are much larger than for the previous Hall A experiment. For instance, for $x_{Bj} = 0.48$, there is a factor 3 in Q^2.

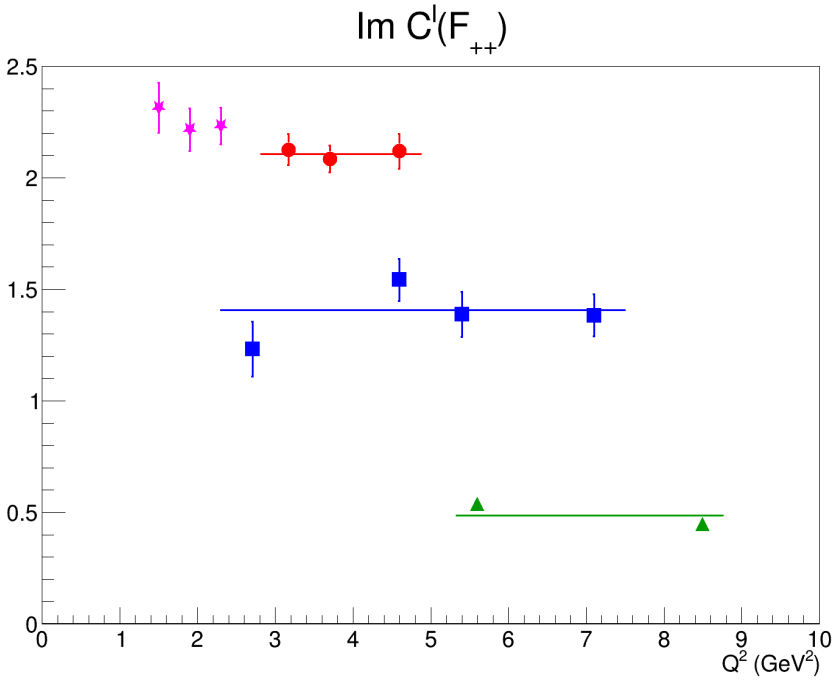

Figure 5.31: Q^2 dependence of the imaginary part of the twist-2 CFFs combination used in the cross section parametrization ($\mathcal{I}m\mathcal{C}^I(\mathcal{F}_{++})$), integrated over t, for $x_{Bj} = 0.36$ and $\langle t \rangle = -0.35$ GeV^2 (red), $x_{Bj} = 0.48$ and $\langle t \rangle = -0.47$ GeV^2 (blue) and $x_{Bj} = 0.60$ and $\langle t \rangle = -1.06$ GeV^2 (green), with statistical uncertainties. The magenta stars correspond to the results of the previous Hall A experiment at $x_{Bj} = 0.36$ and $\langle t \rangle = -0.27$ GeV^2 [48].

The DVCS cross section has a dependence on the twist-2 term $\mathcal{C}^{DVCS}(\mathcal{F}_{++}, \mathcal{F}^*_{++} \mid \mathcal{F}_{-+}, \mathcal{F}^*_{-+})$ which is constant in ϕ, and a dependence on the twist-2 term $\mathcal{R}e\mathcal{C}^I(\mathcal{F}_{++})$ which is mainly of the form $constant + cos(\phi)$. As one can see in Fig. 5.32, surprisingly, these two terms have a dependence in Q^2, which could indicate the existence of higher twist effects. However, one has to keep in mind that the DVCS term also includes contributions from gluons, and most importantly, the two terms are correlated. Indeed, in the formalism of [24], the dependence of the DVCS cross section in the azimuthal angle ϕ is not sufficient to separate completely the DVCS and interference terms. For these reasons, the interpretation of this result might not be straightforward.

The future DVCS experiment scheduled in the Hall C of Jefferson Lab may help with the interpretation of this result. Indeed, part of the program of this next experiment will be to take DVCS data at the same kinematic settings as for this Hall A experiment, but with different beam energies [56]. Since the DVCS and interference terms do not have the same dependence in the beam energy, it may help to separate these two correlated terms.

Finally, the DVCS cross section has mainly a $cos(2\phi)$ and $sin(2\phi)$ dependence on the terms $\mathcal{R}e\mathcal{C}^I(\mathcal{F}_{0+})$ and $\mathcal{I}m\mathcal{C}^I(\mathcal{F}_{0+})$, respectively. As can be seen in Fig. 5.33, these twist-3 terms were found to be very small, but not necessarily equal to 0 which may highlight the existence of twist-3 contributions.

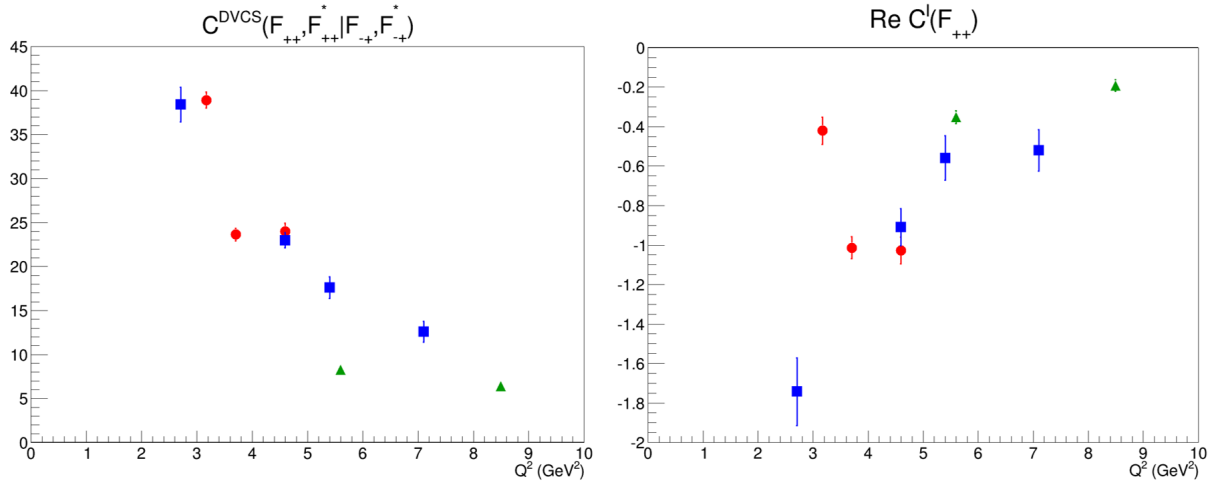

Figure 5.32: Q^2 dependence of the real part of the twist-2 CFFs combinations used in the cross section parametrization ($\mathcal{C}^{DVCS}(\mathcal{F}_{++}, \mathcal{F}^*_{++} \mid \mathcal{F}_{-+}, \mathcal{F}^*_{-+})$ and $\mathcal{R}e\mathcal{C}^I(\mathcal{F}_{++})$), integrated over t, for $x_{Bj} = 0.36$ and $\langle t \rangle = -0.35$ GeV^2 (red), $x_{Bj} = 0.48$ and $\langle t \rangle = -0.47$ GeV^2 (blue) and $x_{Bj} = 0.60$ and $\langle t \rangle = -1.06$ GeV^2 (green), with statistical uncertainties.

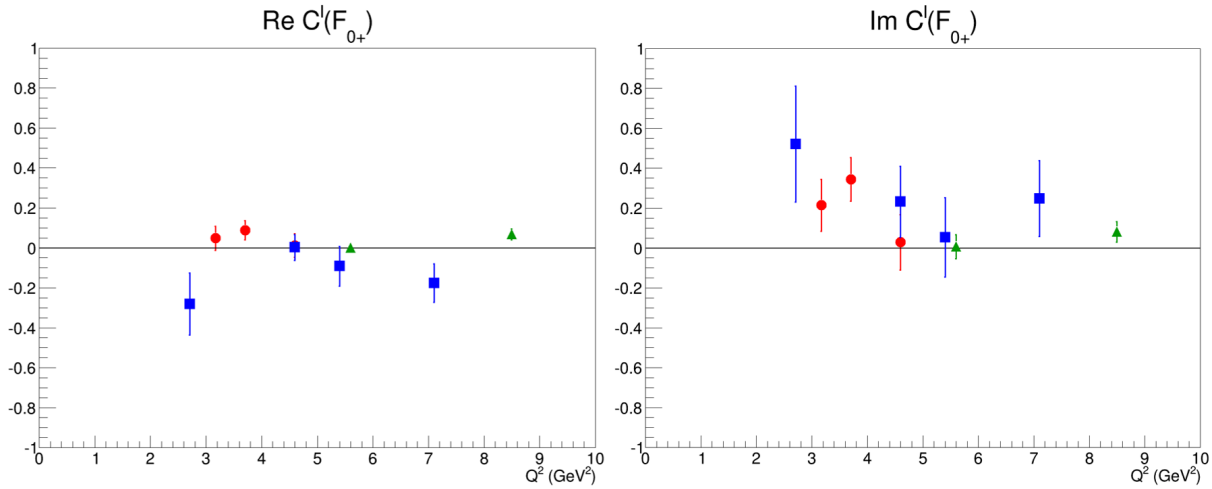

Figure 5.33: Q^2 dependence of the twist-3 CFFs combinations used in the cross section parametrization ($\mathcal{R}e\mathcal{C}^I(\mathcal{F}_{0+})$ and $\mathcal{I}m\mathcal{C}^I(\mathcal{F}_{0+})$), integrated over t, for $x_{Bj} = 0.36$ and $\langle t \rangle = -0.35$ GeV^2 (red), $x_{Bj} = 0.48$ and $\langle t \rangle = -0.47$ GeV^2 (blue) and $x_{Bj} = 0.60$ and $\langle t \rangle = -1.06$ GeV^2 (green), with statistical uncertainties.

Conclusion

Generalized Parton Distributions contain a wealth of information and have become an invaluable tool to study hadron structure. A recent outstanding success was the ability to perform for the first time a three dimensional tomography of the nucleon, and one of the most awaited results will be the measurement of the total orbital angular momentum of quarks in the nucleon.

Deeply Virtual Compton Scattering is widely considered as the golden channel to access GPDs. Out of all the deeply exclusive electro-production processes from which GPDs can be extracted, DVCS final state is the simplest, and thus its cross section offers the least difficult interpretation in terms of GPDs. Nevertheless, extracting DVCS cross sections is no easy task. The precise identification of all the final state particles and their separation from background, combined with a very small cross section, makes the measurement extremely challenging.

The development of high luminosity accelerator facilities allowed to overcome the difficulty raised by the very low cross section of DVCS and made it possible to perform dedicated DVCS experiment with high statistical precision. The experiment E00-110 that took place in the Hall A of Jefferson Lab in 2004 was the first of this kind. Then, in 2014, the CEBAF upgrade to 12 GeV opened the possibility to explore yet uncharted kinematic regions of GPDs. The experiment E12-06-114, which is the subject of this document, is the natural extension of the experiment E00-110 program in these new regions.

In order to ensure that the variables of the final state particles are accurately reconstructed, great care has been taken with the beam line and detectors calibration. Regarding the spectrometer, a challenge arose during Spring 2016 because of the aging and degradation of the supraconducting properties of one of its magnets, thus requiring separate calibrations for each kinematic setting. In order to accelerate the optics calibration process, the spectrometer was set at a small angle to increase counting rates, at the price of worsening the optics reconstruction on the edges of the target for DVCS data which were taken with the spectrometer at a larger angle. Then during Fall 2016, the replacement magnet unexpectedly suffered from a saturation effect. These difficulties prevented the standard calibration algorithm to be applied directly. Nevertheless, corrections either empirical or supported by a simulation and modifications to the calibration procedure have been successfully devised in order to overcome these difficulties. Although the achieved resolution was slightly degraded compared to the spectrometer nominal values, the experimental resolution is dominated by the calorimeter and the optics calibration was thus deemed satisfactory.

Regarding the calorimeter energy calibration, a challenge arose because of the large radiation damage due to a combination of high luminosity, increased energy compared to previous experiments, and the aging of the blocks. In addition to the usual elastic calibration, which allowed to reach an energy resolution of 3% at 7.0 GeV, a new calibration based on the reconstruction of the π^0 invariant mass has been used. Applied daily, this new method allowed to calibrate the calorimeter gain with a precision of 1% to 2% and correct the continuous loss of gain due to radiation damage. However, after long down-time periods, radiation damage could have sizable effects on time scales as short as a few hours. An additional empirical correction has then been successfully devised to compensate the fast darkening of the calorimeter blocks. Radiation was also responsible for the damage of several raster power supplies, but the system was successfully re-calibrated after every replacement.

A careful analysis of the data quality has been performed and allowed to filter out every run with unreliable data. Additionally, a method has been developed to recover data which would have otherwise been compromised because of a loss of synchronization between the calorimeter and the spectrometer. The accidental loss of one third of the total statistics of one kinematic setting has thus been avoided. Furthermore, scripts have been created to monitor the calorimeter and spectrometer synchronization as well as the raster power supplies possible failures in order to prevent further losses of data.

Combined with a smart trigger system to limit the dead time, the ARS electronics have been essential in order to achieve the aforementioned energy resolution, as well as a time resolution below the nanosecond. In order to exploit the ARS electronics abilities to the fullest, the main parameters of the waveform analysis have been optimized to ensure the proper extraction of the time and energy information con-

tained in the ARS signals. The proper treatment of pile-up in the waveform analysis algorithm has also been verified. Results show that the amount of pile-up events is actually very small and that arguably they do not contribute significantly to the calorimeter energy resolution. One can discuss whether using $PbWO_4$ crystals, which have an energy resolution twice better than PbF_2, might be a better choice for future experiments [56].

The methods used with great effectiveness in previous Hall A experiments [98] to subtract accidental and π^0 contamination from DVCS data have been adapted and successfully applied to this experiment. Regarding accidental events subtraction, care has been taken to select events in time windows of the same width as the coincidence one and respecting the new 4 ns time structure of the beam. Concerning the π^0 contamination subtraction, the efficiency of the method used has been checked against a Geant4 simulation for every kinematic setting. The method has been validated for the whole calorimeter surface except its corners and edges where π^0 reconstruction is inefficient because of acceptance effects. For the specific case of kin48_4, the efficiency check with Geant4 allowed to discover that the calorimeter region protected by the beam line shielding was wider than expected and a larger inefficiency zone was taken into account.

DVCS events were carefully selected by applying a collection of cuts enforcing good detection efficiency, accurate variable reconstruction, and ensuring the process exclusivity through particle identification. In particular, new cuts were defined in [83] for the spectrometer acceptance because of its new optics calibration and tight fiducial cuts were enforced on the calorimeter acceptance to certify the good efficiency of the π^0 contamination subtraction. Moreover, strict cuts on the missing mass $M_X^2 = (e + p - e' - \gamma)^2$ allowed to ensure the DVCS process exclusivity despite not detecting directly the recoil proton, while simultaneously filtering out almost all SIDIS and resonances contamination. In addition, correction coefficients have been applied in order to take into account trigger and tracking efficiencies, polarization and dead time. Furthermore, a method used in [98] to correct for events with several clusters in the calorimeter has been adapted for this experiment.

The use of a Monte Carlo simulation allows to extract with great accuracy the complicated experimental acceptance. The geometry of the experimental setup implemented in Geant4 has been updated to be an exact replica of the real apparatus installed in Hall A [92]. In addition, real radiative corrections are implemented in the simulation in order to include in the acceptance computation the combined effects of the subsequent radiative tail with the detector acceptance and resolutions. On the other hand, virtual radiative corrections still need to be computed for every kinematic setting of this experiment: the approximation currently used assumes that these corrections should be similar to the ones used for experiment E00-110. Furthermore, because the simulation is not able to reproduce perfectly the energy gain and resolution of the real calorimeter, the calibration and smearing method developed in [98] has been adapted to this experiment and successfully used in order to match the simulation missing mass spectra to the real data. Even though DVCS events are lost by the strict missing mass cuts applied to the data, they can then be compensated by applying identical cuts to the simulation. However, the Gaussian smearing of the simulation is not able to perfectly reproduce the low missing mass tail of the data. Depending on the kinematic setting, an uncertainty between 2.8% and 5.6% was found. It is expected that a non-Gaussian smearing could greatly minimize this uncertainty.

Preliminary cross sections have been extracted over a total of 9 kinematic settings divided into 120 experimental bins each. Helicity-dependent and independent cross sections allowed to separate the real and imaginary parts of the DVCS amplitude. The extraction procedure was based on a parametrization of the cross sections by linear and bi-linear combinations of CFFs. Different combinations were tested, and two of them yielded good fitting results. In the unpolarized case, the cross sections could be clearly distinguished from the pure Bethe-Heitler and sizeable DVCS and interference terms could be measured. In particular, with the cross-section parametrization used, for values of ϕ close to 180°, the DVCS term was found to be dominant compared to the interference terms, while for values of ϕ close to 0° and 360°, the absolute value of the interference became comparable or larger than the DVCS term. For both helicity-dependent and independent cross sections, overall, twist-2 DVCS and interference terms were found to be dominant, while twist-3 terms were found small. For a few kinematic settings, twist-3 contributions were found to be non negligible, but it is unclear if it is genuine or a consequence of uncertainties.

The preliminary cross sections have been compared to the models KM10a and KM15 resulting from global fits to previous DVCS data. Regarding the unpolarized cross sections, the model KM15 was found to be in a very good agreement with the data for every kinematic setting. On the other hand, the model KM10a was found to undershoot the experimental cross sections. The agreement between the models and the data was found to worsen for growing values of x_{Bj}, which was expected since both models were designed for lower values of x_{Bj}. Concerning the helicity-dependent cross sections, both models KM10a

and KM15 were found to describe the data fairly well. The agreement between the data and the model KM15 is not as good as in the unpolarized case, but one has to keep in mind that uncertainties are larger for polarized cross sections.

The Q^2 dependence (scaling test) of the CFF combinations used in the parametrization of the cross section has been studied for each value of x_{Bj} and integrated over t. The twist-2 term $\mathcal{I}m\mathcal{C}^I(\mathcal{F}_{++})$ was found to be independent from Q^2, which is consistent with the results of the previous Hall A experiment [48] and is an indication towards the twist-2 dominance. Quite surprisingly, the twist-2 terms $\mathcal{C}^{DVCS}(\mathcal{F}_{++}, \mathcal{F}^*_{++} \mid \mathcal{F}_{-+}, \mathcal{F}^*_{-+})$ and $\mathcal{R}e\mathcal{C}^I(\mathcal{F}_{++})$ were found to depend on Q^2. However, it is most probable that both terms are correlated and that the ϕ-dependence of the cross section is not sufficient to separate them completely. As a consequence, the interpretation of this result is not straightforward. Finally, the twist-3 terms $\mathcal{R}e\mathcal{C}^I(\mathcal{F}_{0+})$ and $\mathcal{I}m\mathcal{C}^I(\mathcal{F}_{0+})$ were found to be very small, but not necessarily equal to 0, which may highlight the existence of some twist-3 contributions.

The point-to-point systematic uncertainty associated with the missing mass cuts has been evaluated to be between 2% and 5%. Additional work on the simulation smearing will be required if one wants to reduce this uncertainty further: a non-Gaussian smearing and adjustments to the missing mass window used to compute the smearing parameters could yield a non negligible improvement. The systematic uncertainty associated with the choice of the CFFs parametrization has been evaluated at 1.0%, the one related to the luminosity and the dead time was evaluated at 1.6%, and the one associated with the polarization measurement was evaluated at 1.0% for every kinematic setting except kin36_1 [91]. The remaining systematic uncertainties have yet to be assessed but are expected to be very close to those of the E00-110 experiment.

These results are not completely finalized yet. The t-dependence of the CFF combinations used to parametrize the cross sections has yet to be studied, and the non-Gaussian smearing of the simulation is a main concern to minimize systematic uncertainties as much as possible.

Extracting information about the GPDs is an extremely challenging task. However, a lot of progress has been made since the first results measured at HERA. Dedicated experiments have recently started to yield high precision results that should allow to progressively pin down the elusive GPDs. With the growing number of experiments planned for the near future, and the culminating point embodied by the EIC project, this is indeed a very exciting era for the hadronic physics community and the quest for GPDs.

Appendix A

Addendum about elastic cross sections

In the laboratory frame, if the nucleon is considered to be point like, spin-less and of infinite mass (it has no recoil), and the electron is spin-less and not relativistic, one can derive the Rutherford cross section:

$$\left(\frac{d\sigma}{d\Omega}\right)_{Rutherford} = \frac{\alpha^2}{16E^2\sin^4\left(\frac{\theta}{2}\right)}. \tag{A.1}$$

If the no recoil approximation is removed (finite nucleon mass), Eq. (A.1) has an additional factor as shown in Eq. (A.2):

$$\left(\frac{d\sigma}{d\Omega}\right) = \frac{\alpha^2}{16E^2\sin^4\left(\frac{\theta}{2}\right)}\frac{E'}{E}. \tag{A.2}$$

Then, if one considers the electron to be a spin $\frac{1}{2}$, relativistic particle, the Mott cross section can be derived [6]:

$$\left(\frac{d\sigma}{d\Omega}\right)_{Mott} = \frac{\alpha^2}{4E^2\sin^4\left(\frac{\theta}{2}\right)}\frac{E'}{E}\cos^2\left(\frac{\theta}{2}\right). \tag{A.3}$$

If in addition, the nucleon has now spin $\frac{1}{2}$, with a normal (Dirac) magnetic moment, Eq. (A.3) gets an additional term which conveys that the cross section increases at backward angles and becomes Eq. (A.4):

$$\left(\frac{d\sigma}{d\Omega}\right) = \left(\frac{d\sigma}{d\Omega}\right)_{Mott}\left(1 + \frac{Q^2}{4M^2}2\tan^2\left(\frac{\theta}{2}\right)\right). \tag{A.4}$$

On another hand, if the extended structure of the nucleon is considered instead, Eq. (A.3) gets an additional factor and becomes Eq. (A.5):

$$\left(\frac{d\sigma}{d\Omega}\right) = \left(\frac{d\sigma}{d\Omega}\right)_{Mott}|F(\Delta)|^2, \tag{A.5}$$

with $\Delta = p - p'$. In the case of elastic scattering, one further has $\Delta = -q$. $F(\Delta)$ is a Form Factor, and is the Fourier transform of the transverse spatial distribution of charge $\rho(r)$ as shown in Eq. (A.6):

$$F(\Delta) = \int \rho(r)e^{i\Delta r}dr^3. \tag{A.6}$$

Finally, if one considers a spin $\frac{1}{2}$ nucleon, with an anomalous magnetic moment and an extended structure, the Mott cross section (Eq. (A.3)) becomes the Rosenbluth cross section [7]:

$$\left(\frac{d\sigma}{d\Omega}\right)_{Rosenbluth} = \left(\frac{d\sigma}{d\Omega}\right)_{Mott}\left\{F_1^2(Q^2) + \frac{Q^2}{4M^2}\left[F_2^2(Q^2) + 2\left(F_1(Q^2) + F_2(Q^2)\right)^2\tan^2\left(\frac{\theta}{2}\right)\right]\right\}. \tag{A.7}$$

with $F_1(Q^2)$ and $F_2(Q^2)$ the Dirac and Pauli Form Factors, respectively.

Appendix B

The cross-section DVCS and Interference terms

The parametrization of the DVCS and interference terms of the cross section presented in this appendix were developed by Belitsky, Müller and Ji in [24].

B.1 The cross-section DVCS term

The term $|T_{DVCS}|^2$ is given by the expression:

$$|T_{DVCS}|^2 = \frac{e^6}{y^2 Q^2}\left\{c_0^{DVCS} + \sum_{n=1}^{2}\left[c_n^{DVCS}\cos(n\phi) + s_n^{DVCS}\sin(n\phi)\right]\right\}. \tag{B.1}$$

Let the quantities t_{min}, t_{max} and $\widetilde{K}$ be defined by:

$$t_{min} = -Q^2\frac{2(1-x_{Bj})(1-\sqrt{1+\epsilon^2})+\epsilon^2}{4x_{Bj}(1-x_{Bj})+\epsilon^2}, \tag{B.2}$$

$$t_{max} = -Q^2\frac{2(1-x_{Bj})(1+\sqrt{1+\epsilon^2})+\epsilon^2}{4x_{Bj}(1-x_{Bj})+\epsilon^2}, \tag{B.3}$$

$$\widetilde{K} = \sqrt{(1-x_{Bj})x_{Bj}+\frac{\epsilon^2}{4}}\sqrt{\frac{(t_{min}-t)(t-t_{max})}{Q^2}}. \tag{B.4}$$

Let $\mathcal{F}$ be a general notation for the twist-2 CFFs $\mathcal{H}$, $\mathcal{E}$, $\widetilde{\mathcal{H}}$, $\widetilde{\mathcal{E}}$ (the subscript q is dropped for notation simplicity). The quantities $\mathcal{F}_{ab}$, where a and b label the helicity state of the initial and final photon respectively, are defined as:

$$\mathcal{F}_{++} = \mathcal{F} + \mathcal{O}(\frac{1}{Q^2}), \tag{B.5}$$

$$\mathcal{F}_{0+} = \frac{\sqrt{2}\widetilde{K}}{\sqrt{1+\epsilon^2}Q\left(2-x_{Bj}+\frac{x_{Bj}t}{Q^2}\right)}\mathcal{F}^{eff} + \mathcal{O}(\frac{1}{Q^2}) + \mathcal{O}(\alpha_s), \tag{B.6}$$

$$\mathcal{F}_{-+} = \frac{\widetilde{K}^2}{2M^2\left(2-x_{Bj}+\frac{x_{Bj}t}{Q^2}\right)^2}\mathcal{F}_T + \mathcal{O}(\frac{1}{Q^2}), \tag{B.7}$$

with $\mathcal{F}_T$ the twist-2 gluon transversity CFFs and $\mathcal{F}^{eff}$ the effective twist-3 CFFs defined as:

$$\mathcal{F}^{eff} = -2\xi\left(\frac{1}{1+\xi}\mathcal{F} + \mathcal{F}_+^{twist-3} - \mathcal{F}_+^{twist-3}\right) + \mathcal{O}(\frac{1}{Q^2}) + \mathcal{O}(\frac{\alpha_s}{Q^2}), \tag{B.8}$$

with $\mathcal{F}_+^{twist-3}$ and $\mathcal{F}_-^{twist-3}$ twist-3 CFFs.

Then, the harmonic coefficients c_n^{DVCS} and s_n^{DVCS} are defined by:

$$c_0^{DVCS} = 2\frac{2-2y+y^2+\frac{\epsilon^2}{2}y^2}{1+\epsilon^2}\mathcal{C}^{DVCS}(\mathcal{F}_{++},\mathcal{F}^*_{++} \mid \mathcal{F}_{-+},\mathcal{F}^*_{-+}) + 8\frac{1-y-\frac{\epsilon^2}{4}y^2}{1+\epsilon^2}\mathcal{C}^{DVCS}(\mathcal{F}_{0+},\mathcal{F}^*_{0+}), \quad \text{(B.9)}$$

$$\left\{ \begin{array}{c} c_1^{DVCS} \\ s_1^{DVCS} \end{array} \right\} = \frac{4\sqrt{2}\sqrt{1-y-\frac{\epsilon^2}{4}y^2}}{1+\epsilon^2} \left\{ \begin{array}{c} 2-y \\ -\lambda y\sqrt{1+\epsilon^2} \end{array} \right\} \left\{ \begin{array}{c} \mathcal{R}e \\ \mathcal{I}m \end{array} \right\} \mathcal{C}^{DVCS}(\mathcal{F}_{0+} \mid \mathcal{F}^*_{++},\mathcal{F}^*_{-+}), \quad \text{(B.10)}$$

$$c_2^{DVCS} = 8\frac{1-y-\frac{\epsilon^2}{4}y^2}{1+\epsilon^2}\mathcal{R}e\mathcal{C}^{DVCS}(\mathcal{F}_{-+},\mathcal{F}^*_{++}), \quad \text{(B.11)}$$

$$s_2^{DVCS} = 0, \quad \text{(B.12)}$$

where $\lambda = \pm 1$ corresponds to the beam helicity and $\mathcal{C}^{DVCS}(\mathcal{F}_{++},\mathcal{F}^*_{++} \mid \mathcal{F}_{-+},\mathcal{F}^*_{-+})$ and $\mathcal{C}^{DVCS}(\mathcal{F}_{0+} \mid \mathcal{F}^*_{++},\mathcal{F}^*_{-+})$ are notations for incoherent sums of transverse helicity-flip and non-flip CFFs:

$$\mathcal{C}^{DVCS}(\mathcal{F}_{++},\mathcal{F}^*_{++} \mid \mathcal{F}_{-+},\mathcal{F}^*_{-+}) = \mathcal{C}^{DVCS}(\mathcal{F}_{++},\mathcal{F}^*_{++}) + \mathcal{C}^{DVCS}(\mathcal{F}_{-+},\mathcal{F}^*_{-+}), \quad \text{(B.13)}$$

$$\mathcal{C}^{DVCS}(\mathcal{F}_{0+} \mid \mathcal{F}^*_{++},\mathcal{F}^*_{-+}) = \mathcal{C}^{DVCS}(\mathcal{F}_{0+},\mathcal{F}^*_{++}) + \mathcal{C}^{DVCS}(\mathcal{F}_{0+},\mathcal{F}^*_{-+}), \quad \text{(B.14)}$$

and the bi-linear combination of CFFs $\mathcal{C}^{DVCS}(\mathcal{F},\mathcal{F})$ are defined by:

$$\begin{aligned}\mathcal{C}^{DVCS}(\mathcal{F},\mathcal{F}^*) =& \frac{4(1-x_{Bj})(1+\frac{x_{Bj}t}{Q^2})}{\left(2-x_{Bj}+\frac{x_{Bj}t}{Q^2}\right)^2}\left[\mathcal{H}\mathcal{H}^* + \widetilde{\mathcal{H}}\widetilde{\mathcal{H}}^*\right] + \frac{\left(2+\frac{t}{Q^2}\right)\epsilon^2}{\left(2-x_{Bj}+\frac{x_{Bj}t}{Q^2}\right)^2}\widetilde{\mathcal{H}}\widetilde{\mathcal{H}}^* - \frac{t}{4M^2}\mathcal{E}\mathcal{E}^* \\ & - \frac{x_{Bj}^2}{\left(2-x_{Bj}+\frac{x_{Bj}t}{Q^2}\right)^2}\left\{\left(1+\frac{t}{Q^2}\right)^2\left[\mathcal{H}\mathcal{E}^* + \mathcal{E}\mathcal{H}^* + \mathcal{E}\mathcal{E}^*\right] + \widetilde{\mathcal{H}}\widetilde{\mathcal{E}}^* + \widetilde{\mathcal{E}}\widetilde{\mathcal{H}}^* + \frac{t}{4M^2}\widetilde{\mathcal{E}}\widetilde{\mathcal{E}}^*\right\}.\end{aligned} \quad \text{(B.15)}$$

B.2 The cross-section Interference term

The term I is given by the expression:

$$I = \frac{e^6}{x_{Bj}y^3t\mathcal{P}_1(\phi)\mathcal{P}_2(\phi)}\left\{c_0^I + \sum_{n=1}^{3}\left[c_n^I\cos(n\phi) + s_n^I\sin(n\phi)\right]\right\}. \quad \text{(B.16)}$$

The harmonic coefficients are defined by:

$$c_0^I = C_{++}(0)\mathcal{R}e\mathcal{C}^I_{++}(0 \mid \mathcal{F}_{++}) + \{_{++} \rightarrow {}_{0+}\} + \{_{++} \rightarrow {}_{-+}\}, \quad \text{(B.17)}$$

$$\left\{ \begin{array}{c} c_1^I \\ s_1^I \end{array} \right\} = \left\{ \begin{array}{c} C_{++}(1) \\ \lambda S_{++}(1) \end{array} \right\} \left\{ \begin{array}{c} \mathcal{R}e \\ \mathcal{I}m \end{array} \right\} \left\{ \begin{array}{c} \mathcal{C}^I_{++}(1 \mid \mathcal{F}_{++}) \\ \mathcal{S}^I_{++}(1 \mid \mathcal{F}_{++}) \end{array} \right\} + \{_{++} \rightarrow {}_{0+}\} + \{_{++} \rightarrow {}_{-+}\}, \quad \text{(B.18)}$$

$$\left\{ \begin{array}{c} c_2^I \\ s_2^I \end{array} \right\} = \left\{ \begin{array}{c} C_{0+}(2) \\ \lambda S_{0+}(2) \end{array} \right\} \left\{ \begin{array}{c} \mathcal{R}e \\ \mathcal{I}m \end{array} \right\} \left\{ \begin{array}{c} \mathcal{C}^I_{0+}(2 \mid \mathcal{F}_{0+}) \\ \mathcal{S}^I_{0+}(2 \mid \mathcal{F}_{0+}) \end{array} \right\} + \{_{0+} \rightarrow {}_{++}\} + \{_{0+} \rightarrow {}_{-+}\}, \quad \text{(B.19)}$$

$$c_3^I = C_{-+}(3)\mathcal{R}e\mathcal{C}^I_{-+}(3 \mid \mathcal{F}_{-+}) + \{_{-+} \rightarrow {}_{++}\} + \{_{-+} \rightarrow {}_{0+}\}, \quad \text{(B.20)}$$

$$s_3^I = 0, \quad \text{(B.21)}$$

where the terms are ordered by decreasing importance and $\mathcal{C}^I_{ab}(n \mid \mathcal{F}_{ab})$ and $\mathcal{S}^I_{ab}(n \mid \mathcal{F}_{ab})$ are notations for:

$$\mathcal{C}^I_{ab}(n \mid \mathcal{F}_{ab}) = \mathcal{C}^I(\mathcal{F}_{ab}) + \frac{C^V_{ab}(n)}{C_{ab}(n)}\mathcal{C}^{I,V}(\mathcal{F}_{ab}) + \frac{C^A_{ab}(n)}{C_{ab}(n)}\mathcal{C}^{I,A}(\mathcal{F}_{ab}), \tag{B.22}$$

$$\mathcal{S}^I_{ab}(n \mid \mathcal{F}_{ab}) = \mathcal{C}^I(\mathcal{F}_{ab}) + \frac{S^V_{ab}(n)}{S_{ab}(n)}\mathcal{C}^{I,V}(\mathcal{F}_{ab}) + \frac{S^A_{ab}(n)}{S_{ab}(n)}\mathcal{C}^{I,A}(\mathcal{F}_{ab}). \tag{B.23}$$

The coefficients $C_{ab}(n)$, $C^V_{ab}(n)$, $C^A_{ab}(n)$, $S_{ab}(n)$, $S^V_{ab}(n)$ and $S^A_{ab}(n)$ are kinematic factors which can be computed and whose expressions are given in [24]. The coefficients with a V or A superscript are suppressed by a factor $\frac{t}{Q^2}$ with respect to the related coefficients without superscript. Finally, $\mathcal{C}^I(\mathcal{F})$, $\mathcal{C}^{I,V}(\mathcal{F})$ and $\mathcal{C}^{I,A}(\mathcal{F})$ are linear combinations of CFFs defined by:

$$\mathcal{C}^I(\mathcal{F}) = F_1\mathcal{H} - \frac{t}{4M^2}F_2\mathcal{E} + \frac{x_{Bj}}{2 - x_{Bj} + \frac{x_{Bj}t}{Q^2}}(F_1 + F_2)\widetilde{\mathcal{H}}, \tag{B.24}$$

$$\mathcal{C}^{I,V}(\mathcal{F}) = \frac{x_{Bj}}{2 - x_{Bj} + \frac{x_{Bj}t}{Q^2}}(F_1 + F_2)(\mathcal{H} + \mathcal{E}), \tag{B.25}$$

$$\mathcal{C}^{I,A}(\mathcal{F}) = \frac{x_{Bj}}{2 - x_{Bj} + \frac{x_{Bj}t}{Q^2}}(F_1 + F_2)\widetilde{\mathcal{H}}. \tag{B.26}$$

One will notice that the Dirac and Pauli Form Factors F_1 and F_2 are present in Eq. (B.24), (B.25) and (B.26) because of the Bethe-Heitler contribution.

Appendix C

The fitted number of DVCS events

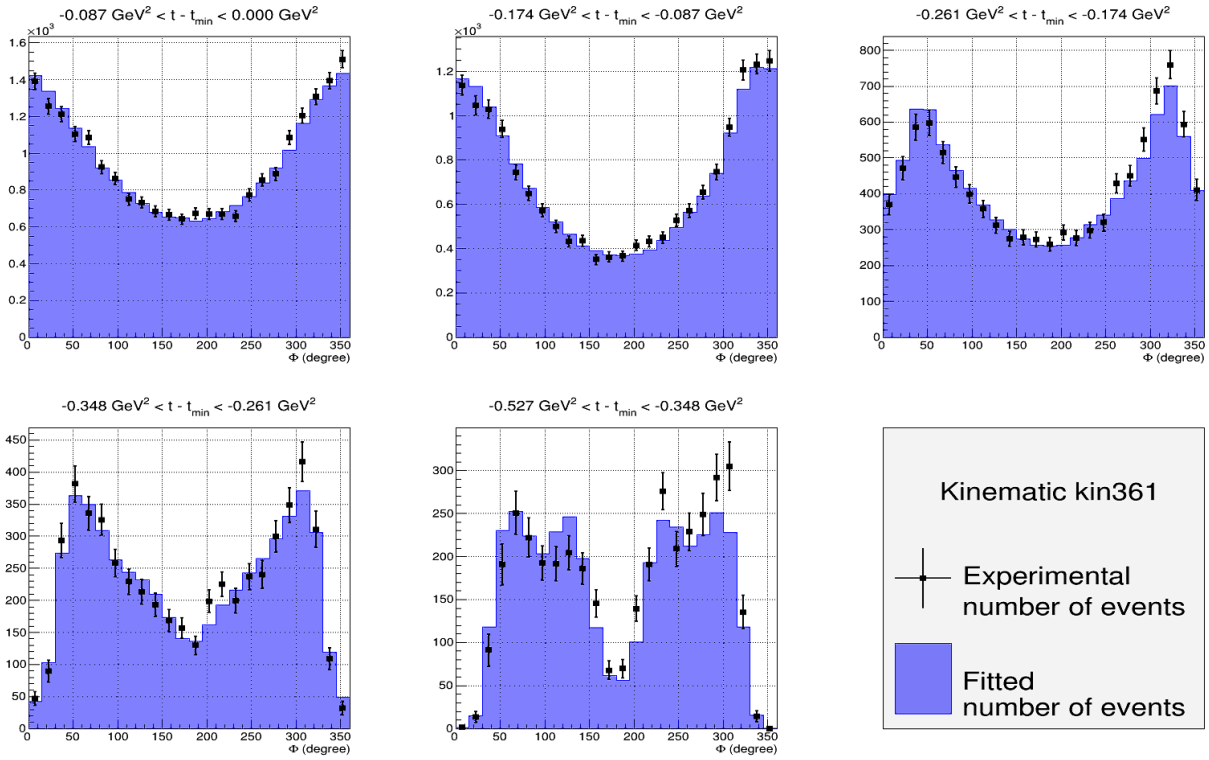

Figure C.1: Unpolarized number of DVCS events for kin36_1, with $\langle Q^2 \rangle = 3.17$ GeV^2, $\langle x_{Bj} \rangle = 0.36$ and $\chi^2/dof = 1.33$. The black squares (blue histograms) are the experimental (fitted) number of DVCS events for each bin. The uncertainty bars are statistical only. The simulation statistical uncertainty is negligible with respect to the experimental one.

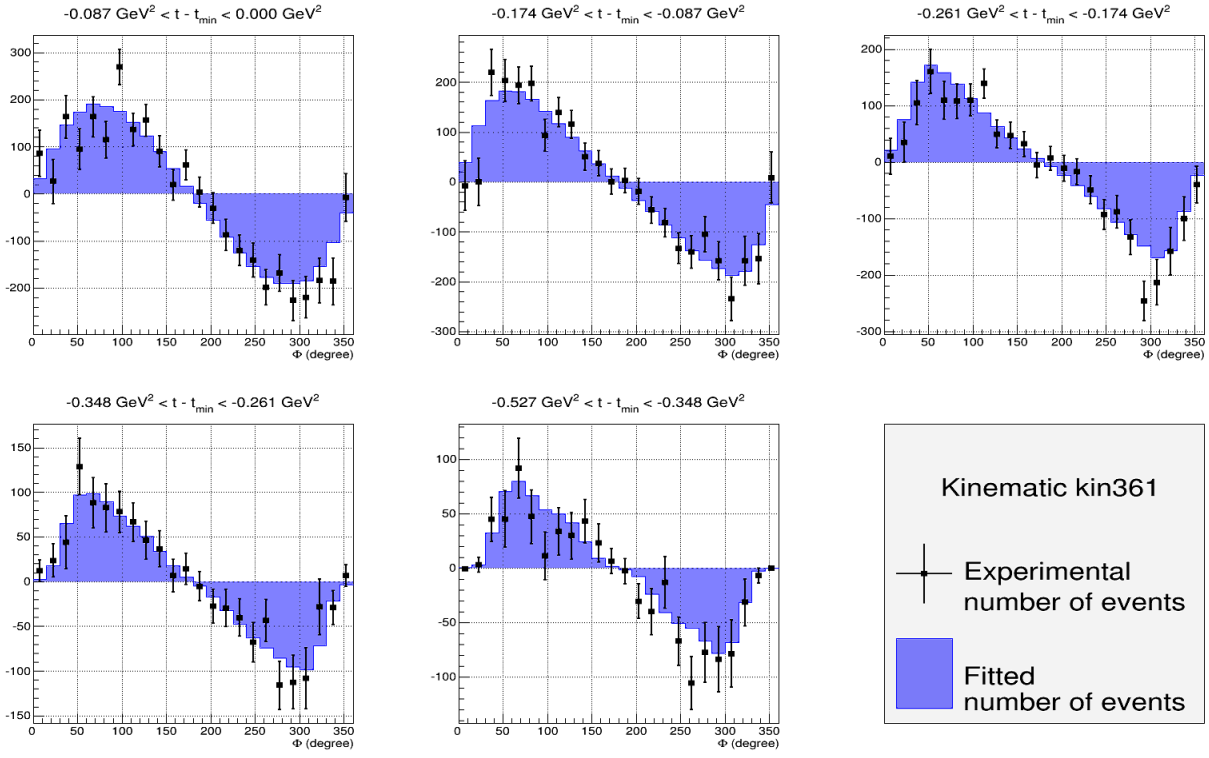

Figure C.2: Helicity-dependent number of DVCS events for kin36_1, with $\langle Q^2 \rangle = 3.17$ GeV^2, $\langle x_{Bj} \rangle = 0.36$ and $\chi^2/dof = 0.89$. The black squares (blue histograms) are the experimental (fitted) number of DVCS events for each bin. The uncertainty bars are statistical only. The simulation statistical uncertainty is negligible with respect to the experimental one.

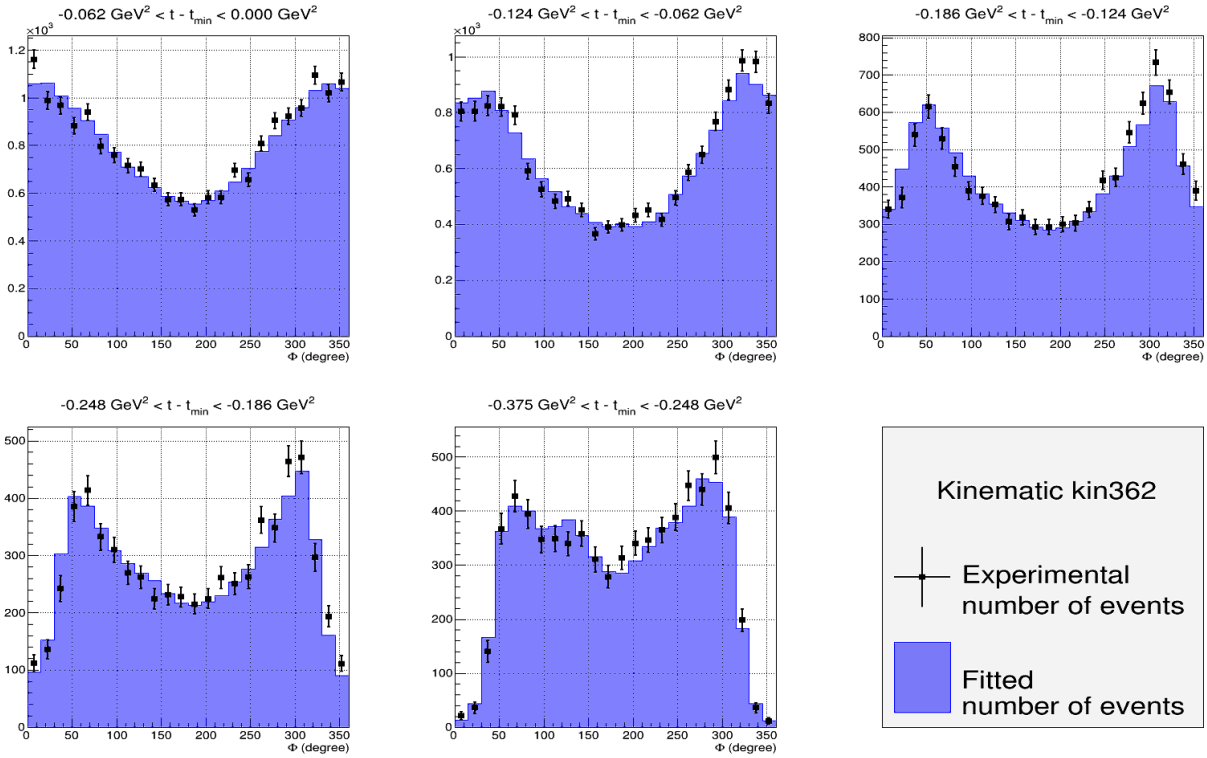

Figure C.3: Unpolarized number of DVCS events for kin36_2, with $\langle Q^2 \rangle = 3.67$ GeV^2, $\langle x_{Bj} \rangle = 0.37$ and and $\chi^2/dof = 1.61$. The black squares (blue histograms) are the experimental (fitted) number of DVCS events for each bin. The uncertainty bars are statistical only. The simulation statistical uncertainty is negligible with respect to the experimental one.

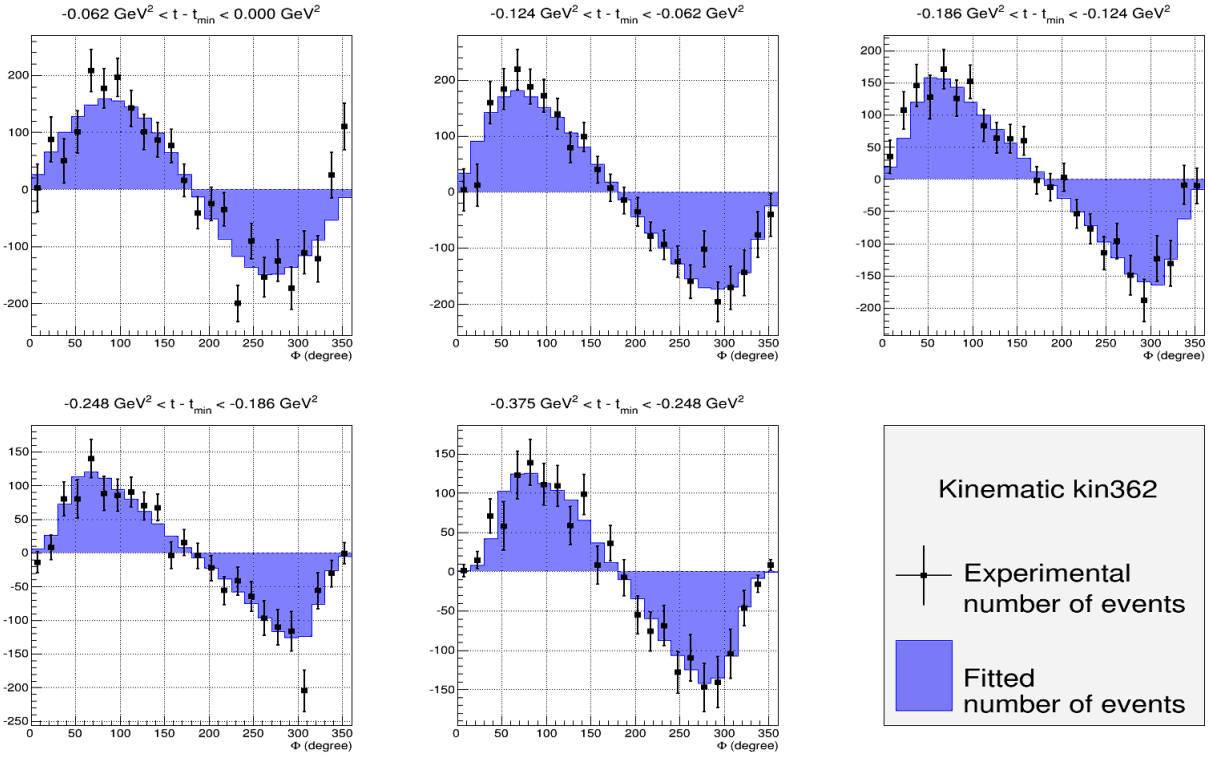

Figure C.4: Helicity-dependent number of DVCS events for kin36_2, with $\langle Q^2 \rangle = 3.67$ GeV^2, $\langle x_{Bj} \rangle = 0.37$ and $\chi^2/dof = 0.94$. The black squares (blue histograms) are the experimental (fitted) number of DVCS events for each bin. The uncertainty bars are statistical only. The simulation statistical uncertainty is negligible with respect to the experimental one.

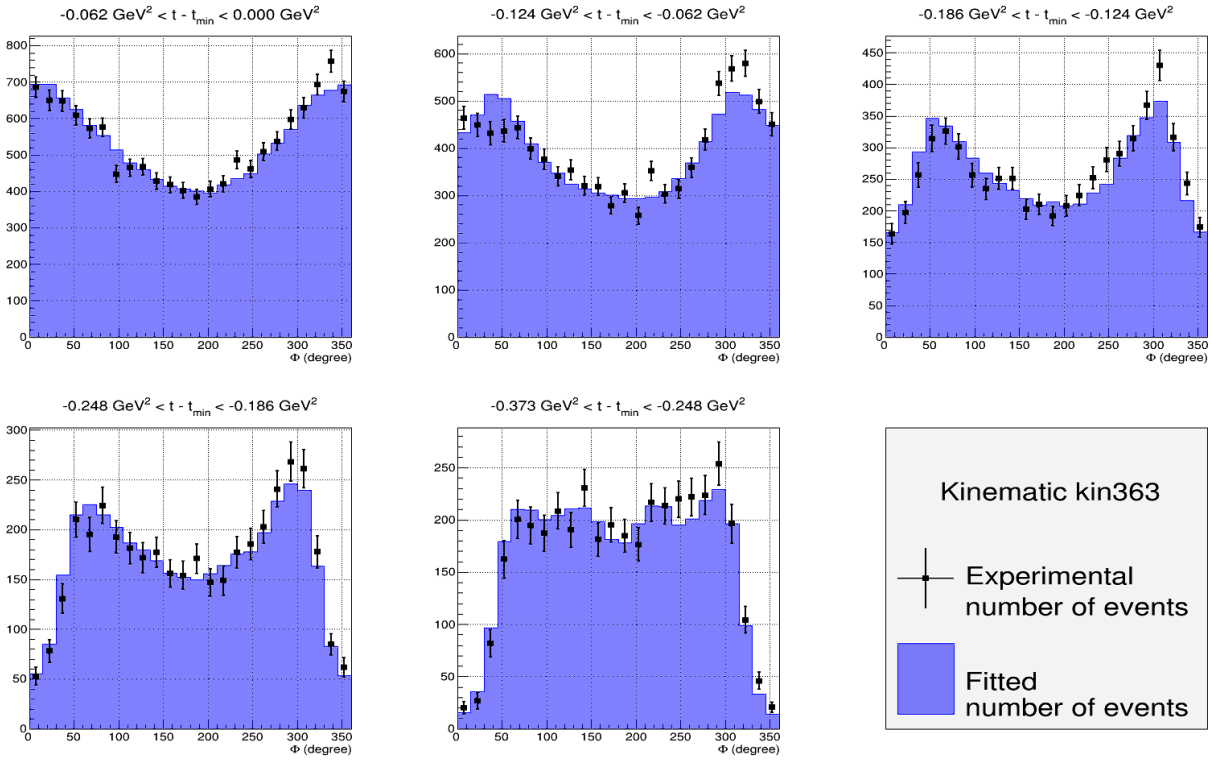

Figure C.5: Unpolarized number of DVCS events for kin36_3, with $\langle Q^2 \rangle = 4.57$ GeV^2, $\langle x_{Bj} \rangle = 0.37$ and $\chi^2/dof = 1.47$. The black squares (blue histograms) are the experimental (fitted) number of DVCS events for each bin. The uncertainty bars are statistical only. The simulation statistical uncertainty is negligible with respect to the experimental one.

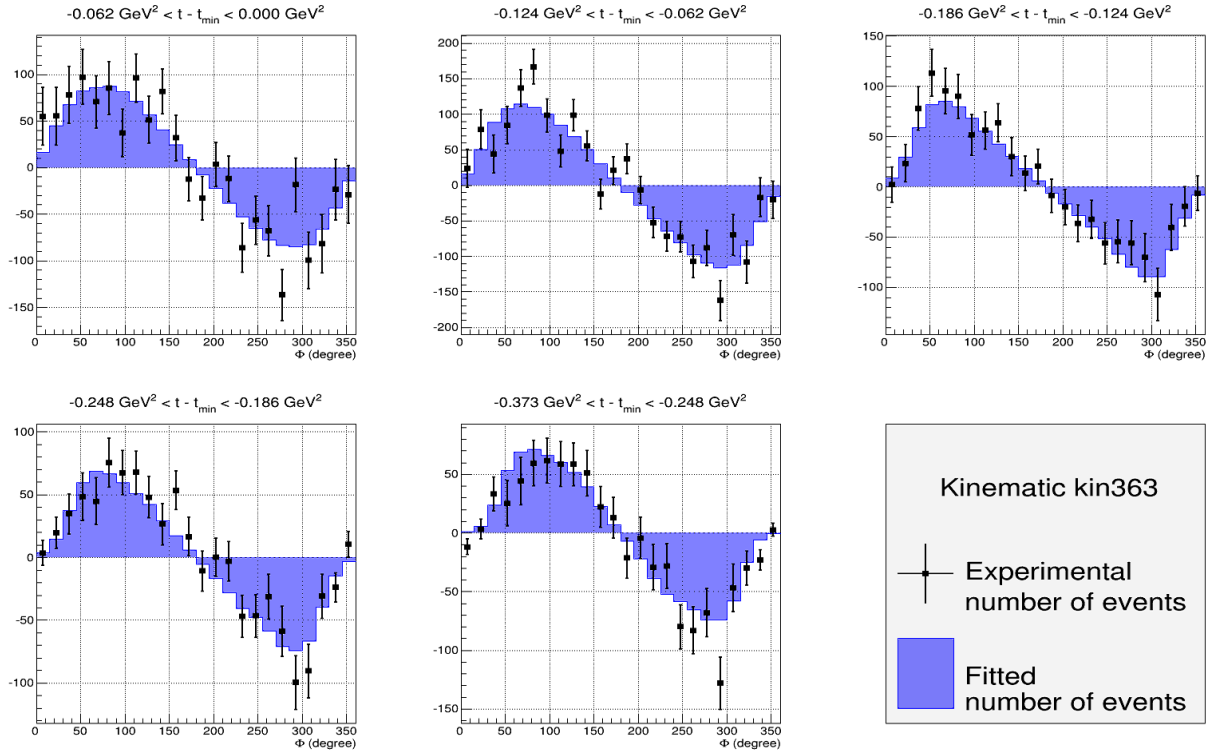

Figure C.6: Helicity-dependent number of DVCS events for kin36_3, with $\langle Q^2 \rangle = 4.57$ GeV^2, $\langle x_{Bj} \rangle = 0.37$ and $\chi^2/dof = 1.07$. The black squares (blue histograms) are the experimental (fitted) number of DVCS events for each bin. The uncertainty bars are statistical only. The simulation statistical uncertainty is negligible with respect to the experimental one.

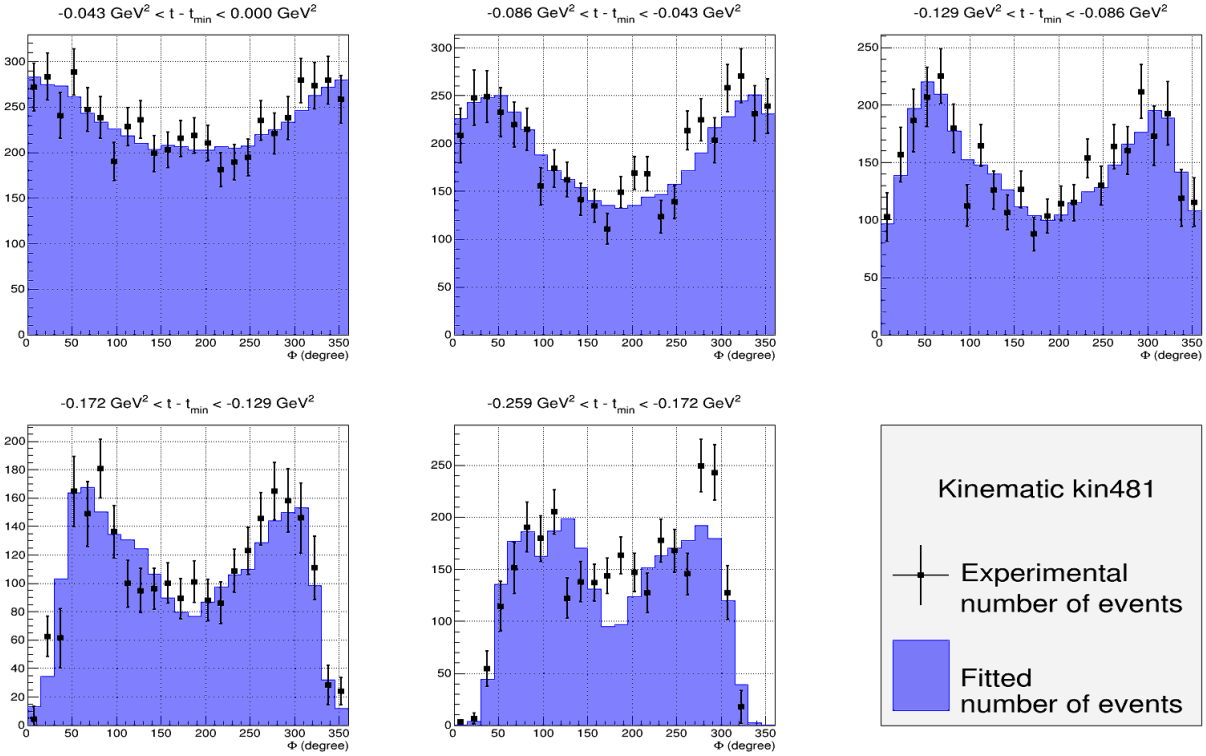

Figure C.7: Unpolarized number of DVCS events for kin48_1, with $\langle Q^2 \rangle = 2.71$ GeV^2, $\langle x_{Bj} \rangle = 0.48$ and $\chi^2/dof = 1.51$. The black squares (blue histograms) are the experimental (fitted) number of DVCS events for each bin. The uncertainty bars are statistical only. The simulation statistical uncertainty is negligible with respect to the experimental one.

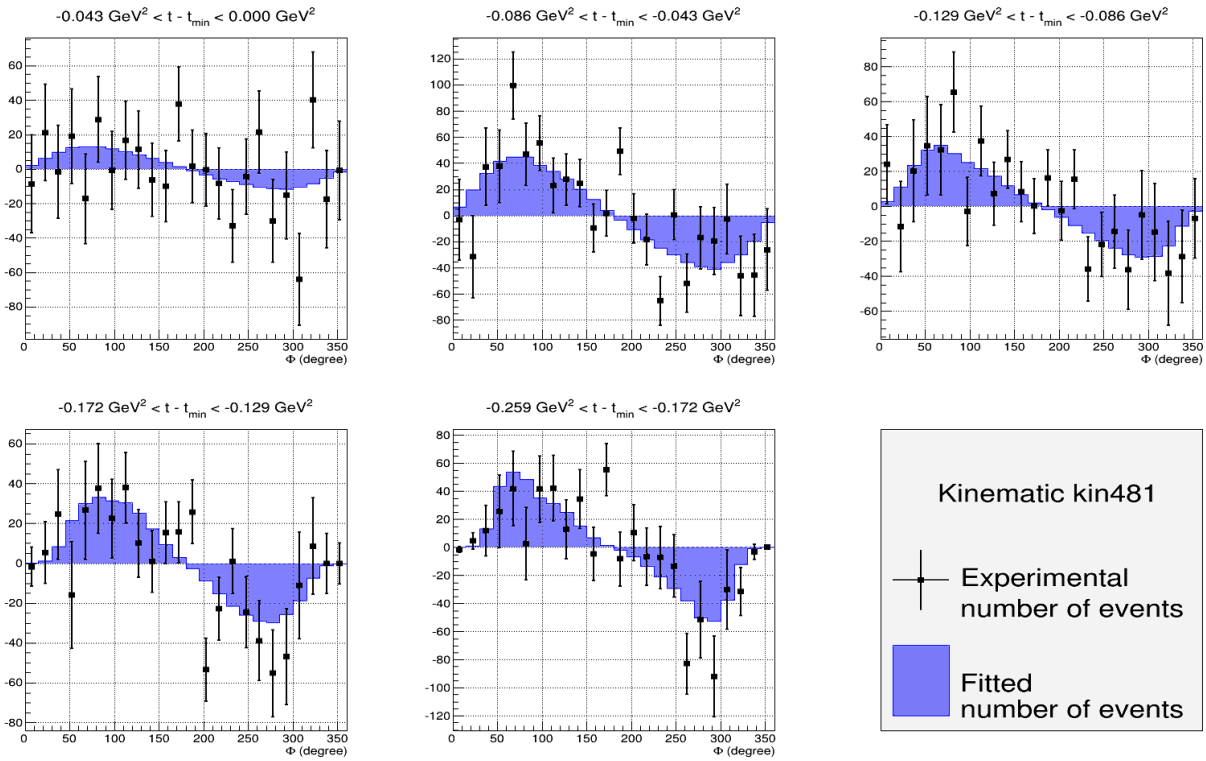

Figure C.8: Helicity-dependent number of DVCS events for kin48_1, with $\langle Q^2 \rangle = 2.71$ GeV^2, $\langle x_{Bj} \rangle = 0.48$ and $\chi^2/dof = 1.00$. The black squares (blue histograms) are the experimental (fitted) number of DVCS events for each bin. The uncertainty bars are statistical only. The simulation statistical uncertainty is negligible with respect to the experimental one.

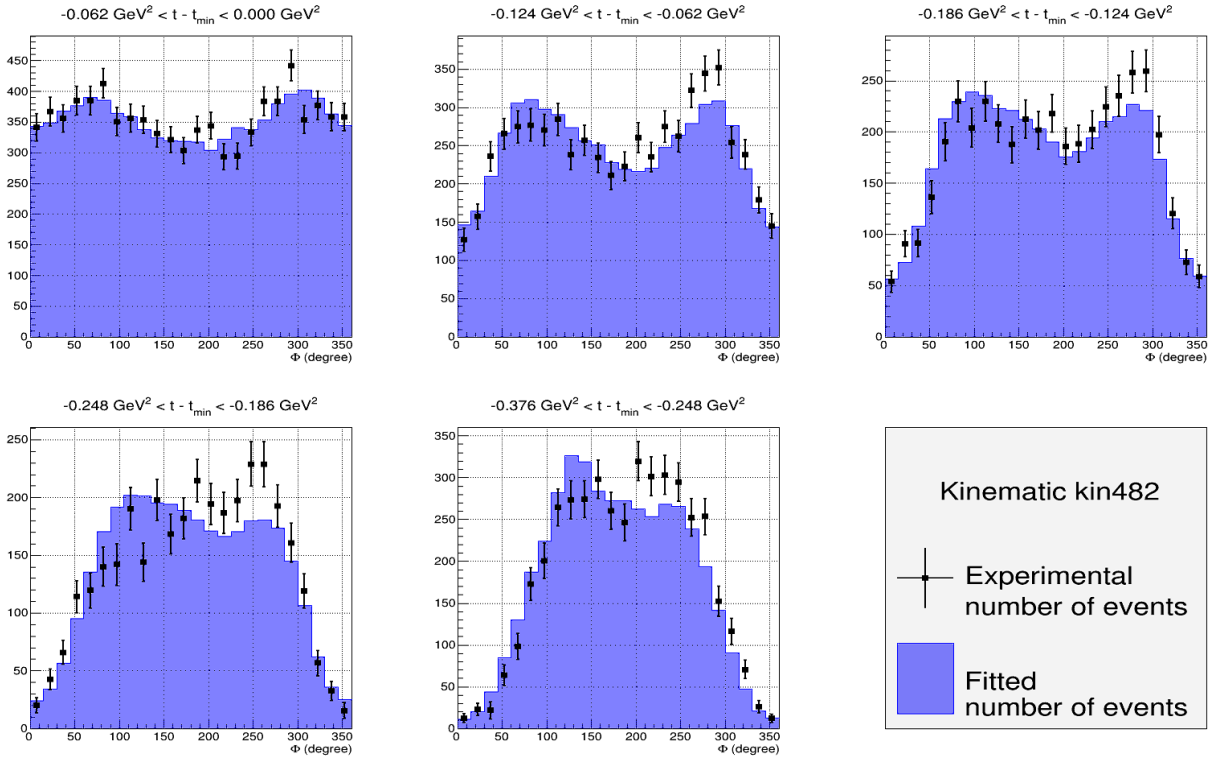

Figure C.9: Unpolarized number of DVCS events for kin48_2, with $\langle Q^2 \rangle = 4.55$ GeV^2, $\langle x_{Bj} \rangle = 0.50$ and $\chi^2/dof = 1.92$. The black squares (blue histograms) are the experimental (fitted) number of DVCS events for each bin. The uncertainty bars are statistical only. The simulation statistical uncertainty is negligible with respect to the experimental one.

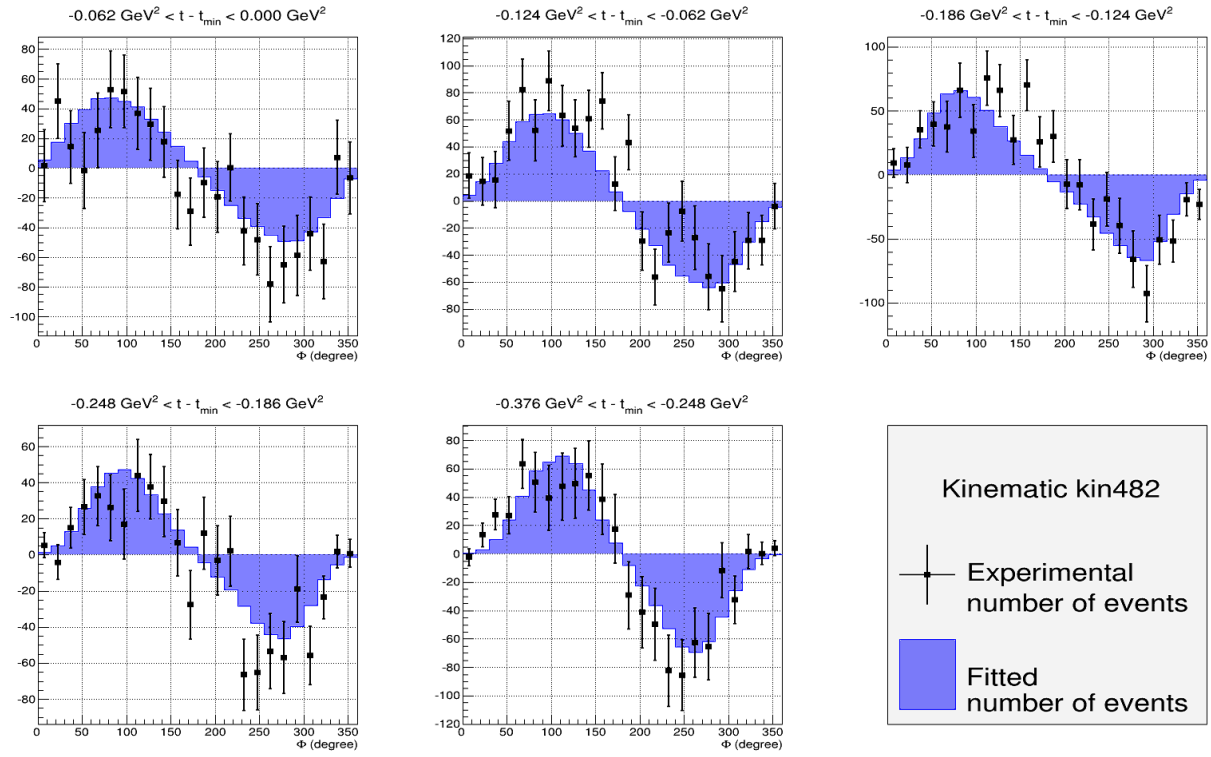

Figure C.10: Helicity-dependent number of DVCS events for kin48_2, with $\langle Q^2 \rangle = 4.55$ GeV^2, $\langle x_{Bj} \rangle = 0.50$ and $\chi^2/dof = 1.01$. The black squares (blue histograms) are the experimental (fitted) number of DVCS events for each bin. The uncertainty bars are statistical only. The simulation statistical uncertainty is negligible with respect to the experimental one.

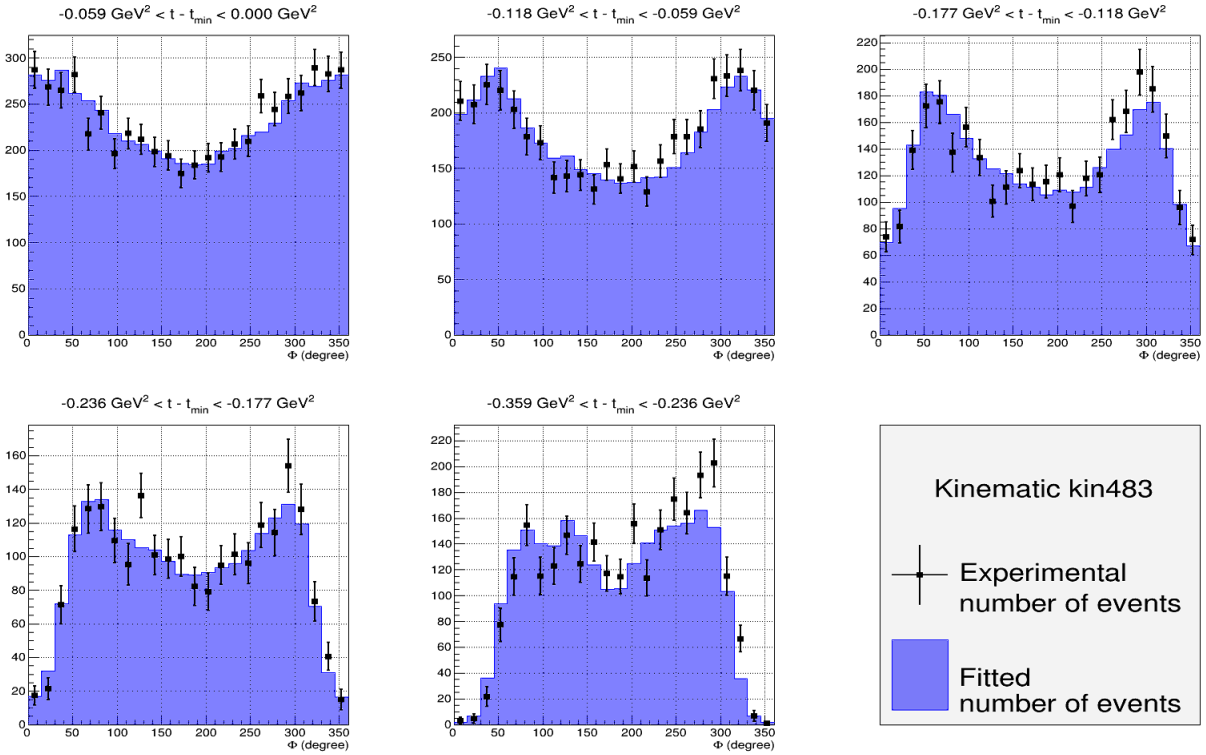

Figure C.11: Unpolarized number of DVCS events for kin48_3, with $\langle Q^2 \rangle = 5.35$ GeV^2, $\langle x_{Bj} \rangle = 0.48$ and $\chi^2/dof = 1.19$. The black squares (blue histograms) are the experimental (fitted) number of DVCS events for each bin. The uncertainty bars are statistical only. The simulation statistical uncertainty is negligible with respect to the experimental one.

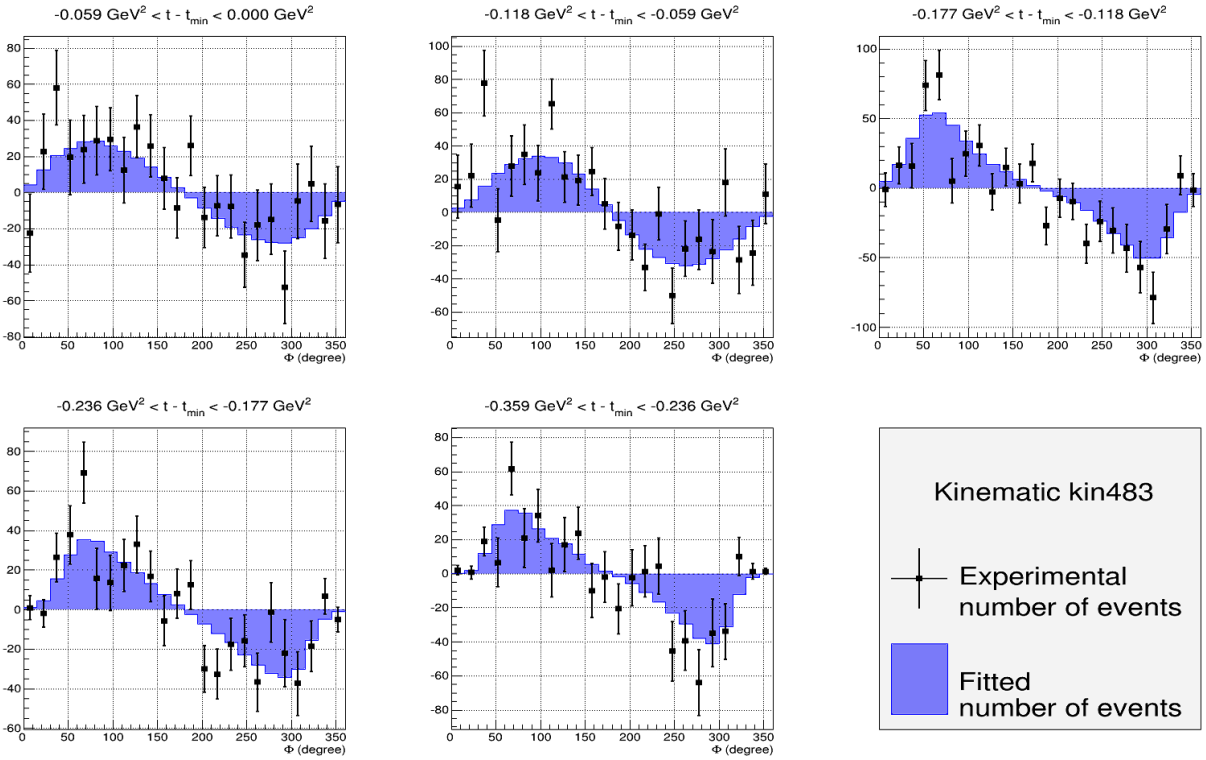

Figure C.12: Helicity-dependent number of DVCS events for kin48_3, with $\langle Q^2 \rangle = 5.35$ GeV^2, $\langle x_{Bj} \rangle = 0.48$ and $\chi^2/dof = 1.15$. The black squares (blue histograms) are the experimental (fitted) number of DVCS events for each bin. The uncertainty bars are statistical only. The simulation statistical uncertainty is negligible with respect to the experimental one.

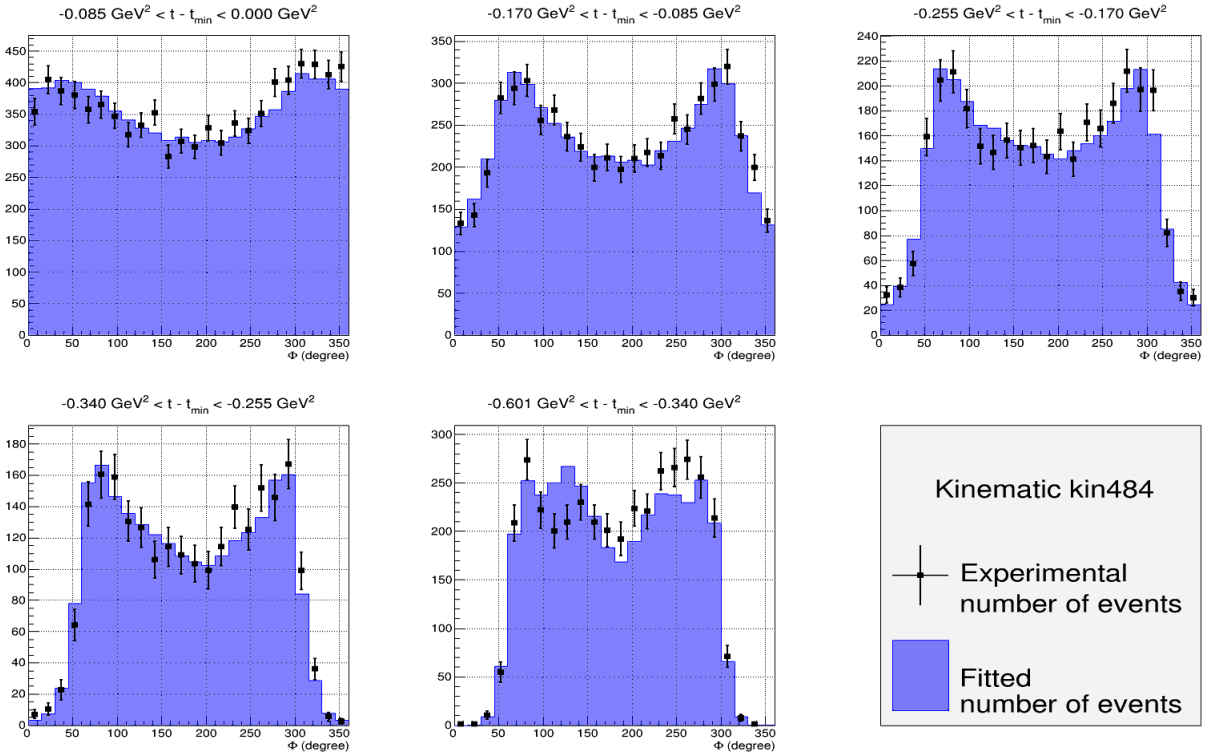

Figure C.13: Unpolarized number of DVCS events for kin48_4, with $\langle Q^2 \rangle = 7.10$ GeV^2, $\langle x_{Bj} \rangle = 0.50$ and $\chi^2/dof = 1.20$. The black squares (blue histograms) are the experimental (fitted) number of DVCS events for each bin. The uncertainty bars are statistical only. The simulation statistical uncertainty is negligible with respect to the experimental one.

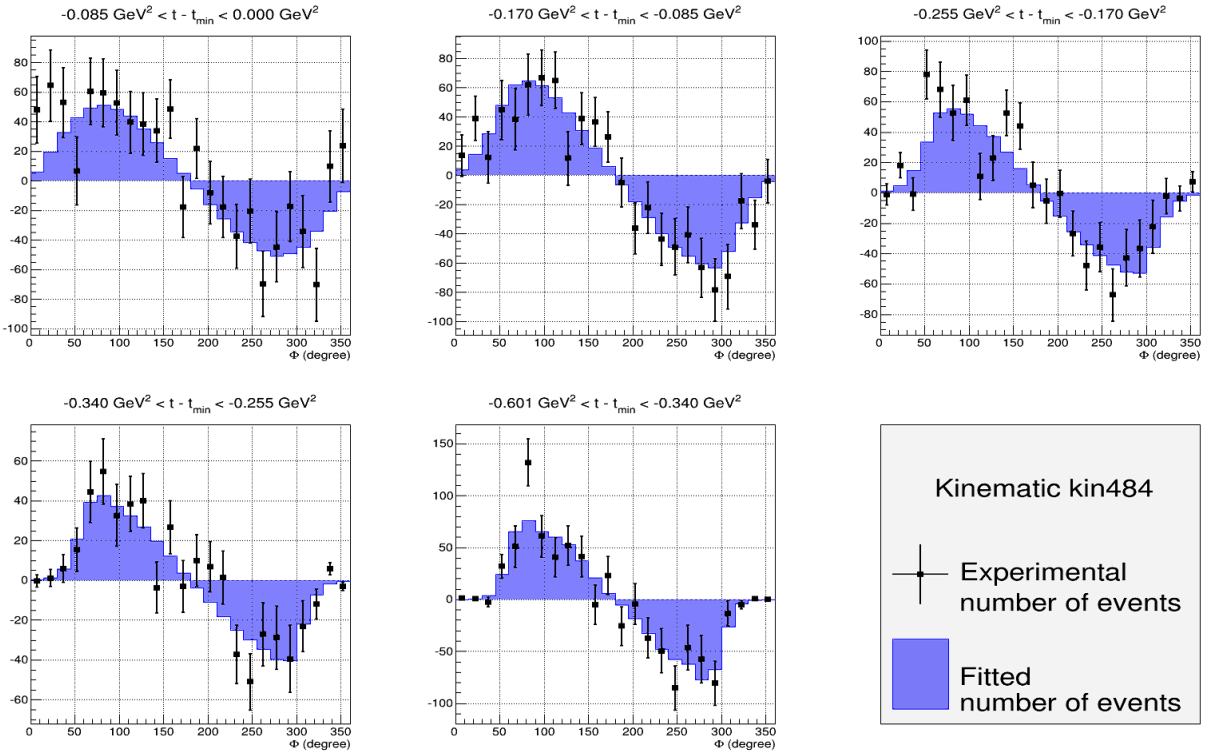

Figure C.14: Helicity-dependent number of DVCS events for kin48_4, with $\langle Q^2 \rangle = 7.10$ GeV^2, $\langle x_{Bj} \rangle = 0.50$ and $\chi^2/dof = 1.10$. The black squares (blue histograms) are the experimental (fitted) number of DVCS events for each bin. The uncertainty bars are statistical only. The simulation statistical uncertainty is negligible with respect to the experimental one.

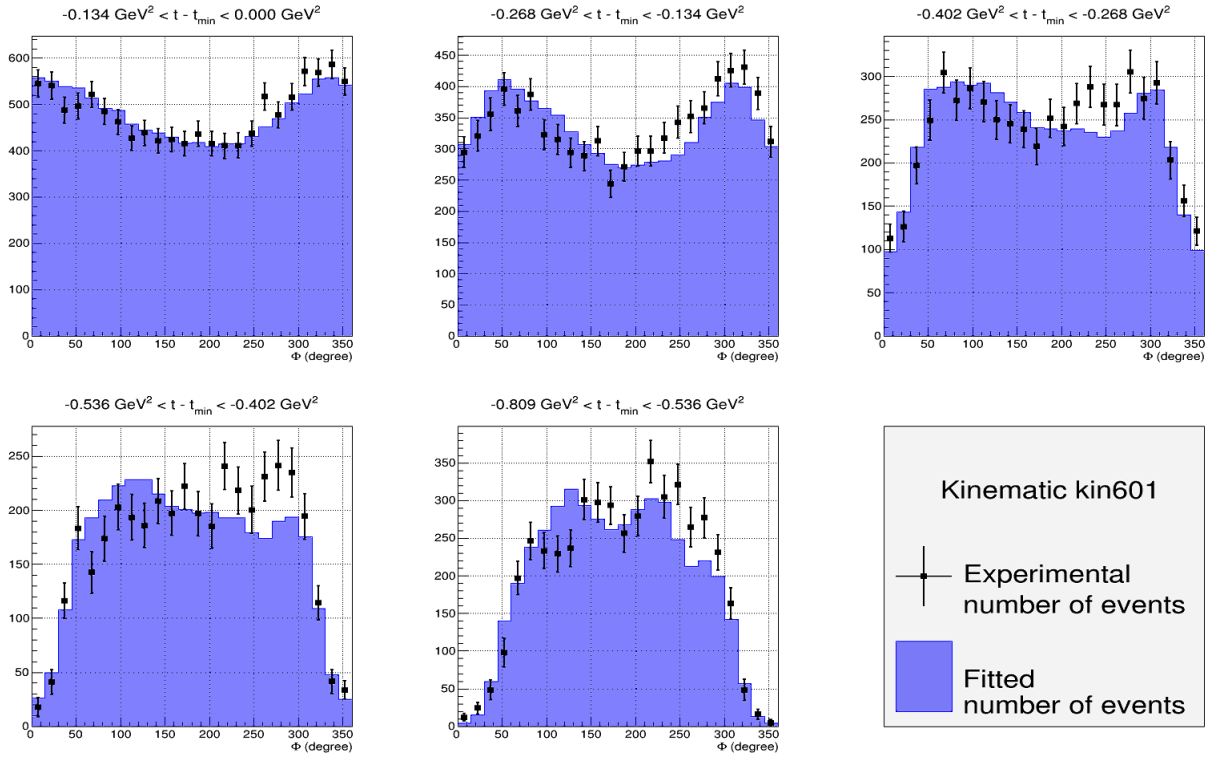

Figure C.15: Unpolarized number of DVCS events for kin60_1, with $\langle Q^2 \rangle = 5.63$ GeV^2, $\langle x_{Bj} \rangle = 0.61$ and $\chi^2/dof = 1.72$. The black squares (blue histograms) are the experimental (fitted) number of DVCS events for each bin. The uncertainty bars are statistical only. The simulation statistical uncertainty is negligible with respect to the experimental one.

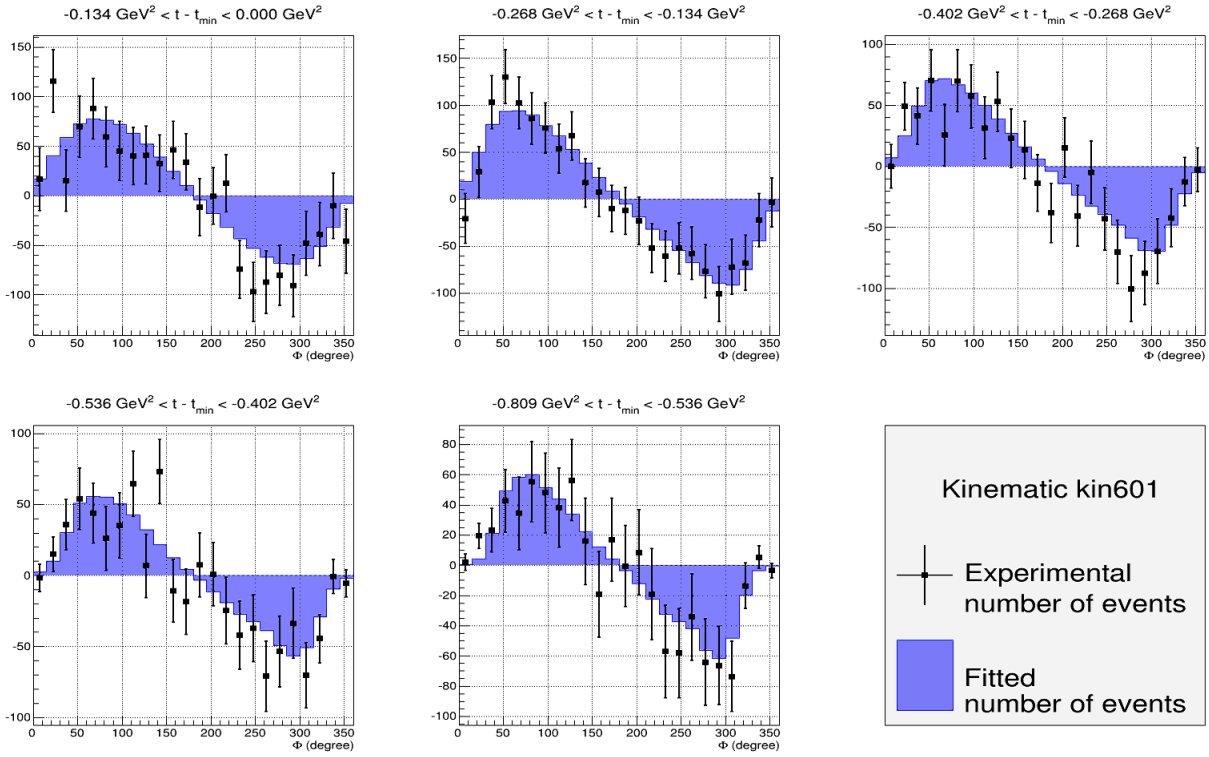

Figure C.16: Helicity-dependent number of DVCS events for kin60_1, with $\langle Q^2 \rangle = 5.63$ GeV^2, $\langle x_{Bj} \rangle = 0.61$ and $\chi^2/dof = 0.69$. The black squares (blue histograms) are the experimental (fitted) number of DVCS events for each bin. The uncertainty bars are statistical only. The simulation statistical uncertainty is negligible with respect to the experimental one.

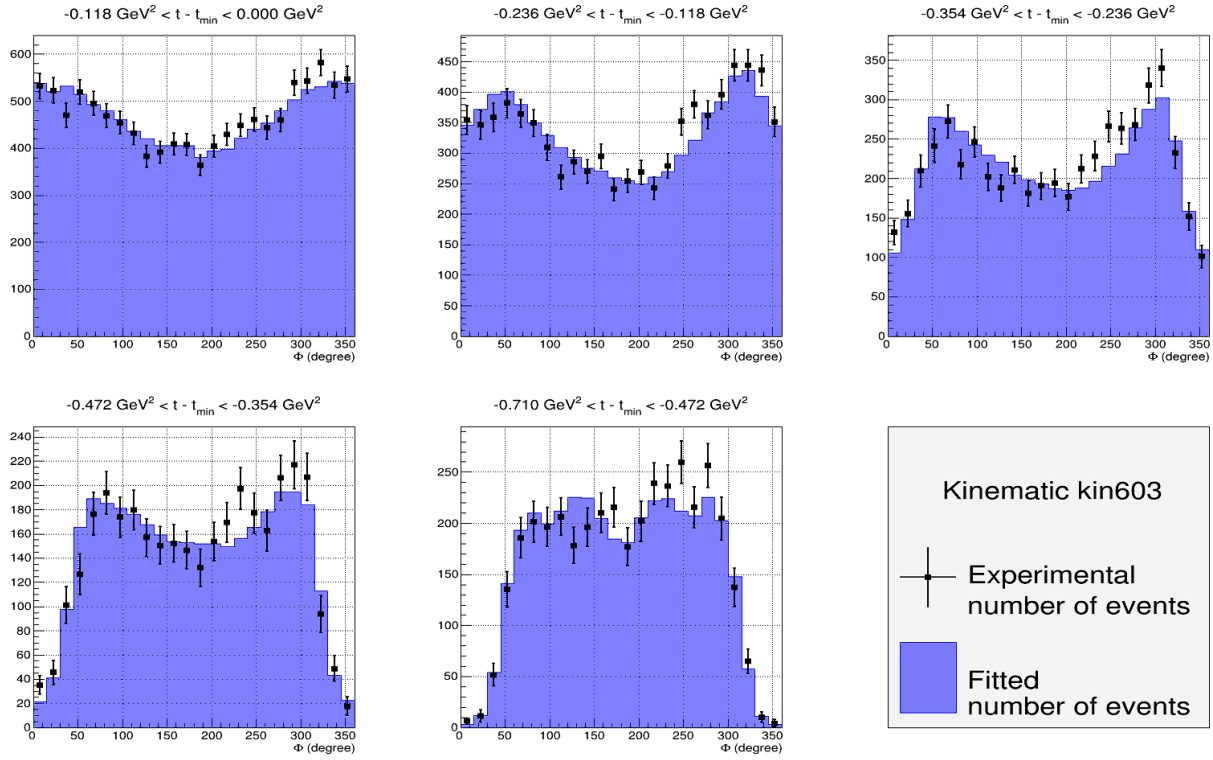

Figure C.17: Unpolarized number of DVCS events for kin60_3, with $\langle Q^2 \rangle = 8.48$ GeV^2, $\langle x_{Bj} \rangle = 0.61$ and $\chi^2/dof = 1.34$. The black squares (blue histograms) are the experimental (fitted) number of DVCS events for each bin. The uncertainty bars are statistical only. The simulation statistical uncertainty is negligible with respect to the experimental one.

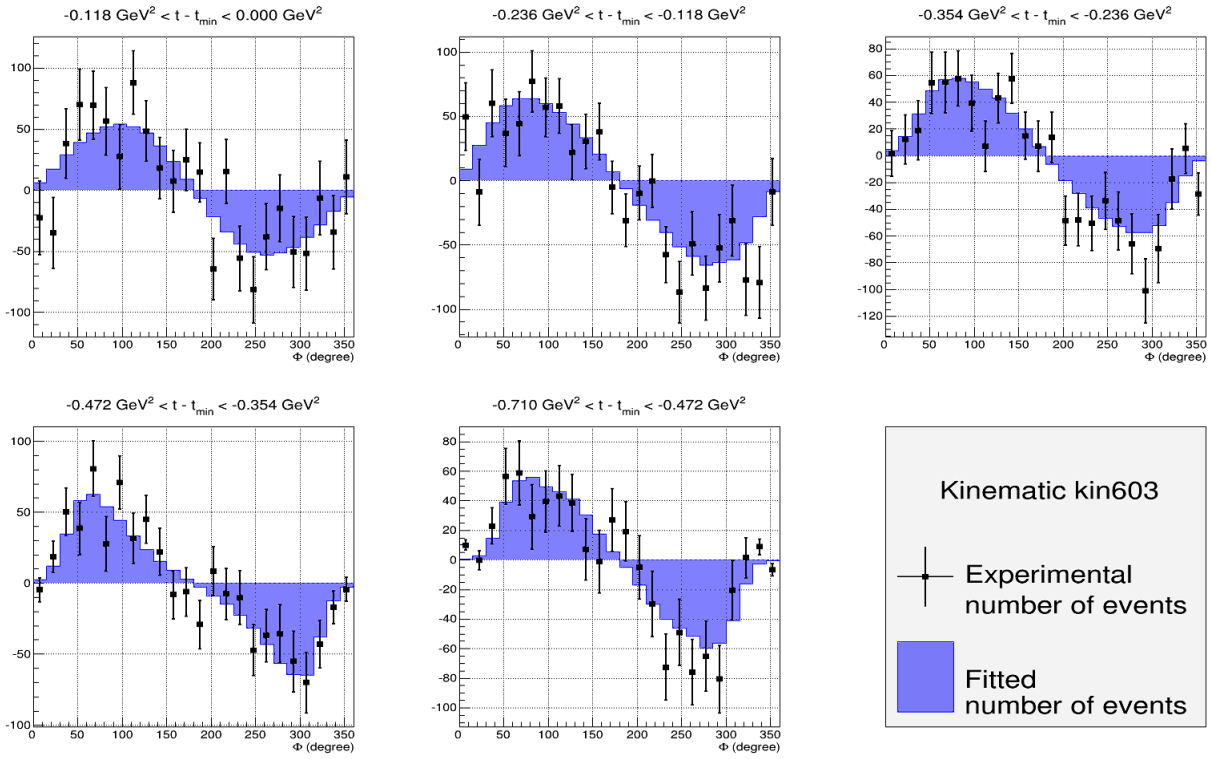

Figure C.18: Helicity-dependent number of DVCS events for kin60_3, with $\langle Q^2 \rangle = 8.48$ GeV^2, $\langle x_{Bj} \rangle = 0.61$ and $\chi^2/dof = 1.04$. The black squares (blue histograms) are the experimental (fitted) number of DVCS events for each bin. The uncertainty bars are statistical only. The simulation statistical uncertainty is negligible with respect to the experimental one.

Appendix D

Tables of unpolarized and polarized DVCS cross sections

In this appendix, t' is the notation for $t - t_{min}$.

ϕ (deg)	$\langle x_{Bj}\rangle = 0.363$ $\langle Q^2\rangle = 3.167$ GeV^2 $\langle t'\rangle = -0.044$ GeV^2	$\langle x_{Bj}\rangle = 0.363$ $\langle Q^2\rangle = 3.169$ GeV^2 $\langle t'\rangle = -0.130$ GeV^2	$\langle x_{Bj}\rangle = 0.365$ $\langle Q^2\rangle = 3.180$ GeV^2 $\langle t'\rangle = -0.216$ GeV^2	$\langle x_{Bj}\rangle = 0.365$ $\langle Q^2\rangle = 3.184$ GeV^2 $\langle t'\rangle = -0.302$ GeV^2	$\langle x_{Bj}\rangle = 0.364$ $\langle Q^2\rangle = 3.180$ GeV^2 $\langle t'\rangle = -0.418$ GeV^2
7.5	$46.85 \pm 1.52\ ^{+0.69}_{-0.56}$	$43.74 \pm 1.73\ ^{+0.77}_{-1.04}$	$33.54 \pm 2.60\ ^{+0.34}_{-0.79}$	$29.55 \pm 6.95\ ^{+2.32}_{-1.99}$	$28.43 \pm 33.69\ ^{+6.62}_{-2.78}$
22.5	$43.00 \pm 1.45\ ^{+0.54}_{-0.68}$	$38.45 \pm 1.59\ ^{+1.06}_{-0.41}$	$30.77 \pm 2.14\ ^{+1.19}_{-0.26}$	$20.71 \pm 3.90\ ^{+1.06}_{-1.02}$	$19.70 \pm 9.61\ ^{+2.66}_{-5.75}$
37.5	$41.20 \pm 1.41\ ^{+0.24}_{-0.79}$	$35.87 \pm 1.47\ ^{+0.98}_{-0.08}$	$24.66 \pm 1.51\ ^{+0.35}_{-0.43}$	$21.58 \pm 1.99\ ^{+0.15}_{-1.10}$	$12.16 \pm 2.46\ ^{+0.63}_{-0.08}$
52.5	$36.92 \pm 1.33\ ^{+1.08}_{-0.46}$	$31.62 \pm 1.30\ ^{+0.86}_{-0.55}$	$20.45 \pm 1.22\ ^{+0.18}_{-0.54}$	$17.44 \pm 1.30\ ^{+0.13}_{-0.39}$	$9.41 \pm 1.17\ ^{+0.57}_{-0.30}$
67.5	$35.29 \pm 1.25\ ^{+0.37}_{-0.43}$	$24.25 \pm 1.10\ ^{+0.35}_{-0.35}$	$16.93 \pm 1.00\ ^{+0.37}_{-0.25}$	$13.17 \pm 1.01\ ^{+0.23}_{-0.27}$	$8.74 \pm 0.87\ ^{+0.29}_{-0.25}$
82.5	$29.95 \pm 1.15\ ^{+0.85}_{-0.29}$	$20.62 \pm 1.00\ ^{+0.10}_{-0.50}$	$14.14 \pm 0.90\ ^{+0.54}_{-0.18}$	$12.15 \pm 0.91\ ^{+0.50}_{-0.54}$	$7.30 \pm 0.74\ ^{+0.43}_{-0.20}$
97.5	$27.03 \pm 1.07\ ^{+0.74}_{-0.37}$	$17.69 \pm 0.90\ ^{+0.58}_{-0.42}$	$12.12 \pm 0.78\ ^{+0.22}_{-0.33}$	$9.61 \pm 0.80\ ^{+0.43}_{-0.38}$	$6.19 \pm 0.64\ ^{+0.11}_{-0.30}$
112.5	$23.04 \pm 0.97\ ^{+0.28}_{-0.38}$	$15.11 \pm 0.81\ ^{+0.34}_{-0.23}$	$10.77 \pm 0.72\ ^{+0.28}_{-0.10}$	$8.00 \pm 0.69\ ^{+0.14}_{-0.33}$	$5.09 \pm 0.53\ ^{+0.14}_{-0.21}$
127.5	$22.58 \pm 0.96\ ^{+0.79}_{-0.49}$	$12.95 \pm 0.76\ ^{+0.36}_{-0.08}$	$9.57 \pm 0.68\ ^{+0.28}_{-0.35}$	$6.94 \pm 0.63\ ^{+0.30}_{-0.11}$	$4.83 \pm 0.46\ ^{+0.20}_{-0.10}$
142.5	$21.19 \pm 0.94\ ^{+0.43}_{-0.33}$	$13.45 \pm 0.77\ ^{+0.27}_{-0.18}$	$8.59 \pm 0.66\ ^{+0.23}_{-0.18}$	$6.32 \pm 0.60\ ^{+0.13}_{-0.20}$	$5.33 \pm 0.52\ ^{+0.10}_{-0.15}$
157.5	$20.63 \pm 0.92\ ^{+0.52}_{-0.04}$	$10.70 \pm 0.69\ ^{+0.24}_{-0.27}$	$9.05 \pm 0.67\ ^{+0.18}_{-0.31}$	$6.26 \pm 0.63\ ^{+0.23}_{-0.09}$	$6.89 \pm 0.76\ ^{+0.25}_{-0.41}$
172.5	$19.66 \pm 0.88\ ^{+0.45}_{-0.27}$	$11.24 \pm 0.71\ ^{+0.43}_{-0.07}$	$9.28 \pm 0.69\ ^{+0.36}_{-0.10}$	$6.96 \pm 0.71\ ^{+0.45}_{-0.11}$	$6.12 \pm 0.95\ ^{+0.85}_{-0.26}$
187.5	$21.20 \pm 0.93\ ^{+0.14}_{-0.50}$	$11.52 \pm 0.72\ ^{+0.23}_{-0.12}$	$8.90 \pm 0.66\ ^{+0.05}_{-0.31}$	$5.95 \pm 0.67\ ^{+0.33}_{-0.29}$	$6.86 \pm 1.05\ ^{+0.14}_{-0.74}$
202.5	$21.04 \pm 0.93\ ^{+0.23}_{-0.34}$	$13.20 \pm 0.76\ ^{+0.39}_{-0.17}$	$10.15 \pm 0.73\ ^{+0.26}_{-0.14}$	$7.89 \pm 0.69\ ^{+0.26}_{-0.06}$	$7.75 \pm 0.80\ ^{+0.22}_{-0.39}$
217.5	$20.64 \pm 0.93\ ^{+0.14}_{-0.79}$	$13.97 \pm 0.79\ ^{+0.44}_{-0.35}$	$9.31 \pm 0.69\ ^{+0.30}_{-0.06}$	$8.03 \pm 0.68\ ^{+0.16}_{-0.03}$	$5.61 \pm 0.57\ ^{+0.28}_{-0.00}$
232.5	$20.57 \pm 0.94\ ^{+0.28}_{-0.34}$	$14.39 \pm 0.84\ ^{+0.23}_{-0.39}$	$9.57 \pm 0.71\ ^{+0.34}_{-0.11}$	$6.96 \pm 0.66\ ^{+0.44}_{-0.15}$	$6.62 \pm 0.52\ ^{+0.14}_{-0.10}$
247.5	$24.56 \pm 1.04\ ^{+0.27}_{-0.48}$	$16.75 \pm 0.89\ ^{+0.79}_{-0.12}$	$10.43 \pm 0.77\ ^{+0.37}_{-0.11}$	$8.30 \pm 0.71\ ^{+0.23}_{-0.30}$	$5.41 \pm 0.52\ ^{+0.27}_{-0.27}$
262.5	$27.19 \pm 1.08\ ^{+0.66}_{-0.32}$	$18.42 \pm 0.96\ ^{+0.19}_{-0.63}$	$14.00 \pm 0.86\ ^{+0.48}_{-0.32}$	$8.90 \pm 0.80\ ^{+0.15}_{-0.29}$	$7.06 \pm 0.69\ ^{+0.24}_{-0.17}$
277.5	$28.85 \pm 1.14\ ^{+0.69}_{-0.07}$	$21.97 \pm 1.07\ ^{+0.14}_{-0.77}$	$15.22 \pm 0.95\ ^{+0.54}_{-0.18}$	$11.66 \pm 0.95\ ^{+0.30}_{-0.33}$	$8.13 \pm 0.81\ ^{+0.38}_{-0.42}$
292.5	$35.94 \pm 1.29\ ^{+0.67}_{-0.34}$	$25.67 \pm 1.19\ ^{+0.96}_{-0.00}$	$19.55 \pm 1.13\ ^{+0.34}_{-0.56}$	$14.47 \pm 1.13\ ^{+0.17}_{-0.32}$	$10.23 \pm 0.95\ ^{+0.26}_{-0.52}$
307.5	$39.33 \pm 1.32\ ^{+0.32}_{-0.57}$	$31.49 \pm 1.31\ ^{+0.65}_{-0.48}$	$23.95 \pm 1.28\ ^{+0.30}_{-0.38}$	$18.60 \pm 1.39\ ^{+0.18}_{-0.65}$	$15.22 \pm 1.40\ ^{+0.42}_{-0.22}$
322.5	$42.77 \pm 1.41\ ^{+0.57}_{-0.95}$	$39.10 \pm 1.44\ ^{+0.54}_{-0.85}$	$29.02 \pm 1.47\ ^{+0.46}_{-0.25}$	$20.48 \pm 1.85\ ^{+0.60}_{-0.82}$	$18.18 \pm 2.62\ ^{+1.01}_{-0.55}$
337.5	$46.69 \pm 1.50\ ^{+0.01}_{-0.83}$	$42.04 \pm 1.55\ ^{+0.39}_{-0.33}$	$34.18 \pm 2.00\ ^{+1.55}_{-0.57}$	$21.93 \pm 3.47\ ^{+0.84}_{-1.16}$	$21.04 \pm 9.25\ ^{+0.00}_{-3.85}$
352.5	$50.42 \pm 1.54\ ^{+0.43}_{-0.74}$	$46.14 \pm 1.72\ ^{+0.88}_{-0.45}$	$36.16 \pm 2.63\ ^{+0.81}_{-0.34}$	$17.50 \pm 6.10\ ^{+1.65}_{-3.01}$	$1.39 \pm 48.29\ ^{+22.50}_{-3.33}$

Table D.1: Unpolarized experimental cross section (pb) for kin361.

ϕ (deg)	$\langle x_{Bj}\rangle = 0.363$ $\langle Q^2\rangle = 3.167$ GeV^2 $\langle t'\rangle = -0.044$ GeV^2	$\langle x_{Bj}\rangle = 0.363$ $\langle Q^2\rangle = 3.169$ GeV^2 $\langle t'\rangle = -0.130$ GeV^2	$\langle x_{Bj}\rangle = 0.365$ $\langle Q^2\rangle = 3.180$ GeV^2 $\langle t'\rangle = -0.216$ GeV^2	$\langle x_{Bj}\rangle = 0.365$ $\langle Q^2\rangle = 3.184$ GeV^2 $\langle t'\rangle = -0.302$ GeV^2	$\langle x_{Bj}\rangle = 0.364$ $\langle Q^2\rangle = 3.180$ GeV^2 $\langle t'\rangle = -0.418$ GeV^2
7.5	$3.42 \pm 1.97\ ^{+0.18}_{-0.99}$	$-0.32 \pm 2.04\ ^{+0.63}_{-0.45}$	$0.95 \pm 2.95\ ^{+0.21}_{-1.26}$	$6.22 \pm 6.15\ ^{+1.79}_{-1.83}$	$-10.09 \pm 26.50\ ^{+0.80}_{-3.09}$
22.5	$0.99 \pm 1.78\ ^{+0.61}_{-0.74}$	$0.01 \pm 1.85\ ^{+0.71}_{-0.72}$	$2.35 \pm 2.40\ ^{+0.43}_{-1.28}$	$4.90 \pm 3.83\ ^{+1.77}_{-0.49}$	$4.38 \pm 9.67\ ^{+3.44}_{-0.84}$
37.5	$6.15 \pm 1.73\ ^{+0.42}_{-0.46}$	$8.04 \pm 1.70\ ^{+1.19}_{-0.51}$	$4.69 \pm 1.75\ ^{+0.91}_{-0.15}$	$3.15 \pm 2.13\ ^{+1.38}_{-0.00}$	$5.51 \pm 2.49\ ^{+0.80}_{-1.71}$
52.5	$3.60 \pm 1.67\ ^{+0.83}_{-0.21}$	$7.22 \pm 1.50\ ^{+0.93}_{-0.20}$	$5.86 \pm 1.43\ ^{+0.27}_{-0.60}$	$6.03 \pm 1.47\ ^{+0.02}_{-0.93}$	$2.22 \pm 1.29\ ^{+0.38}_{-0.40}$
67.5	$6.04 \pm 1.57\ ^{+0.18}_{-0.57}$	$6.57 \pm 1.27\ ^{+0.86}_{-0.00}$	$3.79 \pm 1.16\ ^{+0.46}_{-0.41}$	$3.60 \pm 1.15\ ^{+0.44}_{-0.87}$	$3.25 \pm 0.97\ ^{+0.05}_{-0.46}$
82.5	$4.23 \pm 1.45\ ^{+0.60}_{-0.17}$	$6.44 \pm 1.13\ ^{+0.47}_{-0.52}$	$3.52 \pm 1.02\ ^{+0.57}_{-0.03}$	$3.16 \pm 1.02\ ^{+0.40}_{-0.17}$	$1.58 \pm 0.84\ ^{+0.39}_{-0.43}$
97.5	$9.71 \pm 1.35\ ^{+0.29}_{-0.73}$	$3.00 \pm 1.03\ ^{+0.09}_{-0.29}$	$3.47 \pm 0.89\ ^{+0.21}_{-0.25}$	$2.98 \pm 0.90\ ^{+0.18}_{-0.42}$	$0.36 \pm 0.71\ ^{+0.18}_{-0.18}$
112.5	$4.90 \pm 1.25\ ^{+0.12}_{-0.31}$	$4.32 \pm 0.92\ ^{+0.35}_{-0.24}$	$4.27 \pm 0.80\ ^{+0.09}_{-0.27}$	$2.39 \pm 0.78\ ^{+0.22}_{-0.15}$	$0.88 \pm 0.58\ ^{+0.21}_{-0.29}$
127.5	$5.59 \pm 1.23\ ^{+0.52}_{-0.11}$	$3.52 \pm 0.85\ ^{+0.16}_{-0.36}$	$1.54 \pm 0.76\ ^{+0.40}_{-0.18}$	$1.54 \pm 0.71\ ^{+0.13}_{-0.19}$	$0.68 \pm 0.49\ ^{+0.01}_{-0.30}$
142.5	$3.24 \pm 1.19\ ^{+0.52}_{-0.44}$	$1.55 \pm 0.84\ ^{+0.50}_{-0.10}$	$1.47 \pm 0.72\ ^{+0.20}_{-0.16}$	$1.27 \pm 0.70\ ^{+0.36}_{-0.36}$	$1.16 \pm 0.54\ ^{+0.09}_{-0.27}$
157.5	$0.69 \pm 1.19\ ^{+0.40}_{-0.46}$	$1.15 \pm 0.76\ ^{+0.13}_{-0.47}$	$1.02 \pm 0.72\ ^{+0.17}_{-0.15}$	$0.26 \pm 0.72\ ^{+0.27}_{-0.08}$	$0.95 \pm 0.73\ ^{+0.04}_{-0.33}$
172.5	$2.36 \pm 1.23\ ^{+0.51}_{-0.33}$	$0.00 \pm 0.81\ ^{+0.05}_{-0.28}$	$-0.19 \pm 0.75\ ^{+0.36}_{-0.16}$	$0.69 \pm 0.83\ ^{+0.41}_{-0.16}$	$0.47 \pm 0.87\ ^{+0.79}_{-0.34}$
187.5	$0.11 \pm 1.06\ ^{+0.16}_{-0.71}$	$0.08 \pm 0.76\ ^{+0.12}_{-0.49}$	$0.21 \pm 0.68\ ^{+0.28}_{-0.19}$	$-0.25 \pm 0.77\ ^{+0.46}_{-0.06}$	$-0.23 \pm 0.93\ ^{+0.18}_{-0.33}$
202.5	$-1.08 \pm 1.14\ ^{+0.85}_{-0.38}$	$-0.57 \pm 0.80\ ^{+0.16}_{-0.37}$	$-0.38 \pm 0.77\ ^{+0.21}_{-0.44}$	$-1.14 \pm 0.80\ ^{+0.22}_{-0.55}$	$-1.47 \pm 0.77\ ^{+0.53}_{-0.17}$
217.5	$-3.05 \pm 1.15\ ^{+0.37}_{-0.62}$	$-1.84 \pm 0.88\ ^{+0.19}_{-0.28}$	$-0.56 \pm 0.74\ ^{+0.16}_{-0.38}$	$-1.10 \pm 0.77\ ^{+0.27}_{-0.29}$	$-1.11 \pm 0.59\ ^{+0.23}_{-0.11}$
232.5	$-4.23 \pm 1.16\ ^{+0.27}_{-0.88}$	$-2.61 \pm 0.92\ ^{+0.34}_{-0.24}$	$-1.59 \pm 0.79\ ^{+0.15}_{-0.23}$	$-1.43 \pm 0.74\ ^{+0.28}_{-0.14}$	$-0.32 \pm 0.56\ ^{+0.21}_{-0.26}$
247.5	$-5.02 \pm 1.28\ ^{+0.84}_{-0.45}$	$-4.33 \pm 1.00\ ^{+0.00}_{-0.33}$	$-3.10 \pm 0.87\ ^{+0.10}_{-0.47}$	$-2.43 \pm 0.80\ ^{+0.29}_{-0.11}$	$-1.75 \pm 0.58\ ^{+0.47}_{-0.00}$
262.5	$-7.07 \pm 1.34\ ^{+0.88}_{-0.12}$	$-4.63 \pm 1.08\ ^{+0.25}_{-0.54}$	$-2.97 \pm 0.97\ ^{+0.36}_{-0.16}$	$-1.66 \pm 0.90\ ^{+0.41}_{-0.36}$	$-3.30 \pm 0.76\ ^{+0.40}_{-0.37}$
277.5	$-6.10 \pm 1.40\ ^{+0.47}_{-0.38}$	$-3.64 \pm 1.21\ ^{+0.07}_{-0.69}$	$-4.70 \pm 1.09\ ^{+0.52}_{-0.61}$	$-4.68 \pm 1.09\ ^{+0.35}_{-0.28}$	$-2.59 \pm 0.91\ ^{+0.40}_{-0.29}$
292.5	$-8.39 \pm 1.58\ ^{+0.92}_{-0.94}$	$-5.64 \pm 1.35\ ^{+0.40}_{-0.53}$	$-9.12 \pm 1.30\ ^{+0.21}_{-0.31}$	$-4.77 \pm 1.27\ ^{+0.33}_{-0.55}$	$-3.04 \pm 1.09\ ^{+0.26}_{-0.48}$
307.5	$-7.90 \pm 1.60\ ^{+0.67}_{-1.44}$	$-8.14 \pm 1.50\ ^{+0.47}_{-0.81}$	$-7.93 \pm 1.50\ ^{+0.71}_{-0.66}$	$-5.00 \pm 1.57\ ^{+0.68}_{-0.66}$	$-4.00 \pm 1.58\ ^{+0.40}_{-1.00}$
322.5	$-6.59 \pm 1.69\ ^{+1.32}_{-0.19}$	$-5.35 \pm 1.65\ ^{+0.50}_{-0.08}$	$-6.38 \pm 1.71\ ^{+0.75}_{-0.22}$	$-1.84 \pm 2.00\ ^{+0.44}_{-0.97}$	$-4.00 \pm 2.73\ ^{+0.87}_{-1.01}$
337.5	$-6.56 \pm 1.74\ ^{+1.13}_{-0.48}$	$-5.40 \pm 1.76\ ^{+0.40}_{-0.41}$	$-5.79 \pm 2.21\ ^{+0.50}_{-0.66}$	$-5.14 \pm 3.36\ ^{+1.86}_{-1.25}$	$-9.00 \pm 8.76\ ^{+2.31}_{-3.55}$
352.5	$-0.25 \pm 1.64\ ^{+0.86}_{-0.36}$	$0.31 \pm 1.86\ ^{+0.33}_{-1.02}$	$-3.37 \pm 2.73\ ^{+0.66}_{-1.37}$	$2.91 \pm 5.60\ ^{+1.12}_{-3.57}$	$-1.09 \pm 32.42\ ^{+0.08}_{-14.35}$

Table D.2: Helicity-dependent experimental cross section (pb) for kin361.

ϕ (deg)	$\langle x_{Bj}\rangle = 0.367$ $\langle Q^2\rangle = 3.650$ GeV^2 $\langle t'\rangle = -0.032$ GeV^2	$\langle x_{Bj}\rangle = 0.367$ $\langle Q^2\rangle = 3.653$ GeV^2 $\langle t'\rangle = -0.093$ GeV^2	$\langle x_{Bj}\rangle = 0.369$ $\langle Q^2\rangle = 3.669$ GeV^2 $\langle t'\rangle = -0.155$ GeV^2	$\langle x_{Bj}\rangle = 0.370$ $\langle Q^2\rangle = 3.678$ GeV^2 $\langle t'\rangle = -0.216$ GeV^2	$\langle x_{Bj}\rangle = 0.370$ $\langle Q^2\rangle = 3.679$ GeV^2 $\langle t'\rangle = -0.304$ GeV^2
7.5	$27.45 \pm 0.92\ ^{+0.69}_{-0.00}$	$23.51 \pm 1.02\ ^{+0.69}_{-0.37}$	$21.52 \pm 1.52\ ^{+0.94}_{-0.33}$	$22.49 \pm 2.93\ ^{+3.07}_{-1.59}$	$22.55 \pm 7.59\ ^{+1.20}_{-4.68}$
22.5	$22.91 \pm 0.84\ ^{+0.70}_{-0.13}$	$21.88 \pm 0.96\ ^{+0.66}_{-0.16}$	$16.62 \pm 1.19\ ^{+1.00}_{-0.14}$	$15.57 \pm 1.91\ ^{+0.75}_{-0.70}$	$10.37 \pm 2.98\ ^{+1.41}_{-0.89}$
37.5	$22.77 \pm 0.84\ ^{+0.38}_{-0.50}$	$19.89 \pm 0.84\ ^{+0.89}_{-0.02}$	$16.76 \pm 0.94\ ^{+0.51}_{-0.43}$	$11.78 \pm 1.12\ ^{+1.00}_{-0.35}$	$9.18 \pm 1.31\ ^{+0.47}_{-0.43}$
52.5	$20.77 \pm 0.81\ ^{+0.23}_{-0.45}$	$19.05 \pm 0.78\ ^{+0.00}_{-0.83}$	$15.18 \pm 0.77\ ^{+0.39}_{-0.16}$	$11.53 \pm 0.79\ ^{+0.39}_{-0.13}$	$9.20 \pm 0.72\ ^{+0.21}_{-0.23}$
67.5	$21.82 \pm 0.79\ ^{+0.16}_{-0.52}$	$17.92 \pm 0.74\ ^{+0.26}_{-0.23}$	$12.40 \pm 0.67\ ^{+0.27}_{-0.27}$	$10.58 \pm 0.67\ ^{+0.33}_{-0.09}$	$7.97 \pm 0.53\ ^{+0.22}_{-0.19}$
82.5	$18.31 \pm 0.74\ ^{+0.55}_{-0.01}$	$13.38 \pm 0.65\ ^{+0.15}_{-0.12}$	$10.33 \pm 0.59\ ^{+0.16}_{-0.24}$	$7.92 \pm 0.55\ ^{+0.30}_{-0.20}$	$6.43 \pm 0.44\ ^{+0.18}_{-0.14}$
97.5	$17.53 \pm 0.72\ ^{+0.16}_{-0.27}$	$11.81 \pm 0.61\ ^{+0.19}_{-0.23}$	$8.83 \pm 0.54\ ^{+0.13}_{-0.13}$	$7.19 \pm 0.51\ ^{+0.27}_{-0.24}$	$5.35 \pm 0.38\ ^{+0.18}_{-0.09}$
112.5	$16.42 \pm 0.68\ ^{+0.53}_{-0.33}$	$10.52 \pm 0.55\ ^{+0.18}_{-0.47}$	$8.48 \pm 0.52\ ^{+0.11}_{-0.39}$	$6.00 \pm 0.45\ ^{+0.27}_{-0.03}$	$4.73 \pm 0.33\ ^{+0.09}_{-0.07}$
127.5	$15.65 \pm 0.65\ ^{+0.35}_{-0.13}$	$10.87 \pm 0.56\ ^{+0.29}_{-0.31}$	$7.74 \pm 0.48\ ^{+0.15}_{-0.36}$	$5.68 \pm 0.42\ ^{+0.11}_{-0.16}$	$4.04 \pm 0.27\ ^{+0.09}_{-0.04}$
142.5	$14.12 \pm 0.62\ ^{+0.41}_{-0.20}$	$9.84 \pm 0.52\ ^{+0.14}_{-0.51}$	$6.69 \pm 0.45\ ^{+0.20}_{-0.04}$	$4.82 \pm 0.39\ ^{+0.33}_{-0.09}$	$4.27 \pm 0.28\ ^{+0.04}_{-0.17}$
157.5	$12.91 \pm 0.60\ ^{+0.43}_{-0.23}$	$8.12 \pm 0.49\ ^{+0.07}_{-0.31}$	$7.06 \pm 0.45\ ^{+0.17}_{-0.27}$	$5.22 \pm 0.41\ ^{+0.18}_{-0.12}$	$3.97 \pm 0.29\ ^{+0.14}_{-0.08}$
172.5	$12.95 \pm 0.60\ ^{+0.51}_{-0.22}$	$8.82 \pm 0.50\ ^{+0.48}_{-0.06}$	$6.70 \pm 0.45\ ^{+0.27}_{-0.07}$	$5.43 \pm 0.43\ ^{+0.13}_{-0.15}$	$3.79 \pm 0.28\ ^{+0.23}_{-0.02}$
187.5	$12.21 \pm 0.60\ ^{+0.37}_{-0.34}$	$8.74 \pm 0.49\ ^{+0.16}_{-0.57}$	$6.88 \pm 0.46\ ^{+0.21}_{-0.19}$	$5.22 \pm 0.42\ ^{+0.23}_{-0.15}$	$4.32 \pm 0.30\ ^{+0.13}_{-0.02}$
202.5	$13.52 \pm 0.63\ ^{+0.16}_{-0.31}$	$9.99 \pm 0.54\ ^{+0.07}_{-0.39}$	$7.09 \pm 0.47\ ^{+0.13}_{-0.26}$	$5.40 \pm 0.42\ ^{+0.31}_{-0.17}$	$4.44 \pm 0.29\ ^{+0.10}_{-0.12}$
217.5	$13.28 \pm 0.62\ ^{+0.28}_{-0.24}$	$10.52 \pm 0.56\ ^{+0.16}_{-0.34}$	$7.11 \pm 0.48\ ^{+0.14}_{-0.29}$	$6.24 \pm 0.46\ ^{+0.04}_{-0.20}$	$4.37 \pm 0.29\ ^{+0.02}_{-0.18}$
232.5	$16.09 \pm 0.68\ ^{+0.09}_{-0.31}$	$9.70 \pm 0.56\ ^{+0.28}_{-0.31}$	$7.91 \pm 0.50\ ^{+0.35}_{-0.18}$	$5.77 \pm 0.44\ ^{+0.30}_{-0.12}$	$4.51 \pm 0.29\ ^{+0.05}_{-0.15}$
247.5	$15.18 \pm 0.67\ ^{+0.21}_{-0.39}$	$11.04 \pm 0.58\ ^{+0.18}_{-0.49}$	$9.43 \pm 0.54\ ^{+0.33}_{-0.13}$	$6.06 \pm 0.48\ ^{+0.17}_{-0.10}$	$5.15 \pm 0.33\ ^{+0.10}_{-0.14}$
262.5	$18.53 \pm 0.73\ ^{+0.51}_{-0.20}$	$12.97 \pm 0.62\ ^{+0.27}_{-0.22}$	$9.64 \pm 0.57\ ^{+0.22}_{-0.33}$	$8.23 \pm 0.53\ ^{+0.38}_{-0.26}$	$6.19 \pm 0.38\ ^{+0.06}_{-0.23}$
277.5	$20.88 \pm 0.78\ ^{+0.41}_{-0.34}$	$14.26 \pm 0.66\ ^{+0.52}_{-0.14}$	$12.01 \pm 0.62\ ^{+0.00}_{-0.30}$	$7.93 \pm 0.55\ ^{+0.44}_{-0.18}$	$6.23 \pm 0.40\ ^{+0.18}_{-0.24}$
292.5	$21.43 \pm 0.79\ ^{+0.48}_{-0.21}$	$17.11 \pm 0.72\ ^{+0.43}_{-0.24}$	$14.34 \pm 0.69\ ^{+0.24}_{-0.22}$	$11.38 \pm 0.67\ ^{+0.22}_{-0.32}$	$8.41 \pm 0.51\ ^{+0.12}_{-0.31}$
307.5	$22.50 \pm 0.82\ ^{+0.48}_{-0.58}$	$19.66 \pm 0.78\ ^{+0.00}_{-0.77}$	$16.70 \pm 0.75\ ^{+0.18}_{-0.49}$	$12.69 \pm 0.76\ ^{+0.52}_{-0.66}$	$9.46 \pm 0.67\ ^{+0.32}_{-0.21}$
322.5	$25.21 \pm 0.87\ ^{+0.21}_{-0.81}$	$22.17 \pm 0.85\ ^{+0.14}_{-0.51}$	$18.46 \pm 0.91\ ^{+0.52}_{-0.39}$	$13.36 \pm 1.10\ ^{+0.41}_{-0.25}$	$11.76 \pm 1.24\ ^{+0.55}_{-0.35}$
337.5	$23.70 \pm 0.86\ ^{+0.97}_{-0.42}$	$25.31 \pm 0.97\ ^{+0.41}_{-0.80}$	$20.24 \pm 1.23\ ^{+0.31}_{-0.70}$	$21.03 \pm 2.00\ ^{+0.48}_{-0.77}$	$10.31 \pm 2.91\ ^{+0.35}_{-1.71}$
352.5	$25.70 \pm 0.90\ ^{+0.63}_{-0.59}$	$23.54 \pm 1.00\ ^{+1.18}_{-0.38}$	$24.07 \pm 1.56\ ^{+0.73}_{-0.81}$	$23.72 \pm 3.05\ ^{+1.01}_{-1.86}$	$14.12 \pm 7.54\ ^{+1.81}_{-2.94}$

Table D.3: Unpolarized experimental cross section (pb) for kin362.

ϕ (deg)	$\langle x_{Bj}\rangle = 0.367$ $\langle Q^2\rangle = 3.650$ GeV^2 $\langle t'\rangle = -0.032$ GeV^2	$\langle x_{Bj}\rangle = 0.367$ $\langle Q^2\rangle = 3.653$ GeV^2 $\langle t'\rangle = -0.093$ GeV^2	$\langle x_{Bj}\rangle = 0.369$ $\langle Q^2\rangle = 3.669$ GeV^2 $\langle t'\rangle = -0.155$ GeV^2	$\langle x_{Bj}\rangle = 0.370$ $\langle Q^2\rangle = 3.678$ GeV^2 $\langle t'\rangle = -0.216$ GeV^2	$\langle x_{Bj}\rangle = 0.370$ $\langle Q^2\rangle = 3.679$ GeV^2 $\langle t'\rangle = -0.304$ GeV^2
7.5	$0.05 \pm 0.80\ ^{+0.25}_{-0.28}$	$0.11 \pm 1.00\ ^{+0.16}_{-0.29}$	$1.90 \pm 1.40\ ^{+0.29}_{-0.56}$	$-2.23 \pm 2.55\ ^{+1.25}_{-0.84}$	$0.68 \pm 5.30\ ^{+0.81}_{-1.68}$
22.5	$2.00 \pm 0.90\ ^{+0.45}_{-0.20}$	$0.34 \pm 1.05\ ^{+0.77}_{-0.18}$	$4.65 \pm 1.25\ ^{+0.12}_{-0.51}$	$0.81 \pm 1.86\ ^{+0.60}_{-0.13}$	$3.45 \pm 2.61\ ^{+0.81}_{-0.44}$
37.5	$1.21 \pm 0.94\ ^{+0.35}_{-0.28}$	$4.07 \pm 0.96\ ^{+0.47}_{-0.21}$	$4.62 \pm 1.04\ ^{+0.51}_{-0.19}$	$3.88 \pm 1.21\ ^{+1.21}_{-0.33}$	$4.22 \pm 1.29\ ^{+0.67}_{-0.76}$
52.5	$2.51 \pm 0.93\ ^{+0.11}_{-0.37}$	$4.55 \pm 0.90\ ^{+0.09}_{-0.45}$	$3.33 \pm 0.89\ ^{+0.25}_{-0.25}$	$2.57 \pm 0.92\ ^{+0.12}_{-0.24}$	$1.47 \pm 0.78\ ^{+0.30}_{-0.32}$
67.5	$5.24 \pm 0.93\ ^{+0.49}_{-0.09}$	$5.22 \pm 0.85\ ^{+0.23}_{-0.20}$	$4.31 \pm 0.78\ ^{+0.29}_{-0.27}$	$3.87 \pm 0.78\ ^{+0.22}_{-0.43}$	$2.39 \pm 0.60\ ^{+0.20}_{-0.11}$
82.5	$4.47 \pm 0.88\ ^{+0.69}_{-0.50}$	$4.54 \pm 0.75\ ^{+0.14}_{-0.12}$	$3.04 \pm 0.68\ ^{+0.17}_{-0.32}$	$2.27 \pm 0.65\ ^{+0.35}_{-0.18}$	$2.36 \pm 0.49\ ^{+0.20}_{-0.29}$
97.5	$5.04 \pm 0.87\ ^{+0.34}_{-0.61}$	$4.18 \pm 0.71\ ^{+0.47}_{-0.12}$	$3.65 \pm 0.63\ ^{+0.21}_{-0.17}$	$2.12 \pm 0.59\ ^{+0.23}_{-0.20}$	$1.79 \pm 0.43\ ^{+0.07}_{-0.11}$
112.5	$3.66 \pm 0.83\ ^{+0.28}_{-0.21}$	$3.22 \pm 0.63\ ^{+0.07}_{-0.25}$	$1.95 \pm 0.58\ ^{+0.08}_{-0.18}$	$2.09 \pm 0.51\ ^{+0.19}_{-0.16}$	$1.54 \pm 0.36\ ^{+0.04}_{-0.15}$
127.5	$2.55 \pm 0.80\ ^{+0.24}_{-0.03}$	$1.83 \pm 0.63\ ^{+0.32}_{-0.08}$	$1.45 \pm 0.53\ ^{+0.19}_{-0.06}$	$1.56 \pm 0.47\ ^{+0.09}_{-0.20}$	$0.73 \pm 0.30\ ^{+0.14}_{-0.06}$
142.5	$2.11 \pm 0.74\ ^{+0.26}_{-0.45}$	$2.16 \pm 0.57\ ^{+0.21}_{-0.27}$	$1.36 \pm 0.48\ ^{+0.32}_{-0.11}$	$1.47 \pm 0.43\ ^{+0.02}_{-0.11}$	$1.20 \pm 0.31\ ^{+0.03}_{-0.15}$
157.5	$1.80 \pm 0.69\ ^{+0.42}_{-0.10}$	$0.84 \pm 0.51\ ^{+0.11}_{-0.27}$	$1.29 \pm 0.48\ ^{+0.00}_{-0.19}$	$-0.08 \pm 0.44\ ^{+0.04}_{-0.31}$	$0.11 \pm 0.32\ ^{+0.10}_{-0.05}$
172.5	$0.32 \pm 0.57\ ^{+0.32}_{-0.25}$	$0.14 \pm 0.46\ ^{+0.19}_{-0.12}$	$-0.04 \pm 0.42\ ^{+0.15}_{-0.05}$	$0.33 \pm 0.42\ ^{+0.24}_{-0.10}$	$0.48 \pm 0.29\ ^{+0.26}_{-0.04}$
187.5	$-1.59 \pm 1.08\ ^{+0.26}_{-0.36}$	$-0.40 \pm 0.65\ ^{+0.19}_{-0.12}$	$-0.33 \pm 0.57\ ^{+0.33}_{-0.14}$	$-0.12 \pm 0.51\ ^{+0.19}_{-0.06}$	$-0.12 \pm 0.37\ ^{+0.04}_{-0.13}$
202.5	$-0.77 \pm 0.88\ ^{+0.29}_{-0.02}$	$-0.87 \pm 0.62\ ^{+0.25}_{-0.05}$	$0.06 \pm 0.53\ ^{+0.14}_{-0.41}$	$-0.58 \pm 0.48\ ^{+0.08}_{-0.17}$	$-0.78 \pm 0.34\ ^{+0.13}_{-0.11}$
217.5	$-0.98 \pm 0.82\ ^{+0.23}_{-0.15}$	$-1.93 \pm 0.63\ ^{+0.05}_{-0.30}$	$-1.30 \pm 0.54\ ^{+0.19}_{-0.14}$	$-1.39 \pm 0.52\ ^{+0.16}_{-0.14}$	$-1.02 \pm 0.33\ ^{+0.16}_{-0.11}$
232.5	$-5.46 \pm 0.86\ ^{+0.25}_{-0.16}$	$-2.31 \pm 0.64\ ^{+0.42}_{-0.07}$	$-1.88 \pm 0.57\ ^{+0.01}_{-0.34}$	$-1.00 \pm 0.49\ ^{+0.03}_{-0.23}$	$-0.89 \pm 0.33\ ^{+0.13}_{-0.19}$
247.5	$-2.48 \pm 0.86\ ^{+0.31}_{-0.30}$	$-3.00 \pm 0.68\ ^{+0.32}_{-0.14}$	$-2.73 \pm 0.61\ ^{+0.14}_{-0.12}$	$-1.60 \pm 0.55\ ^{+0.20}_{-0.18}$	$-1.78 \pm 0.37\ ^{+0.04}_{-0.19}$
262.5	$-4.17 \pm 0.94\ ^{+0.28}_{-0.08}$	$-3.79 \pm 0.72\ ^{+0.38}_{-0.03}$	$-2.31 \pm 0.66\ ^{+0.23}_{-0.18}$	$-2.37 \pm 0.62\ ^{+0.10}_{-0.16}$	$-1.60 \pm 0.43\ ^{+0.11}_{-0.26}$
277.5	$-3.37 \pm 0.99\ ^{+0.18}_{-0.29}$	$-2.47 \pm 0.78\ ^{+0.24}_{-0.36}$	$-3.52 \pm 0.72\ ^{+0.36}_{-0.15}$	$-2.73 \pm 0.65\ ^{+0.28}_{-0.26}$	$-2.22 \pm 0.46\ ^{+0.34}_{-0.09}$
292.5	$-4.76 \pm 1.01\ ^{+0.36}_{-0.23}$	$-4.93 \pm 0.88\ ^{+0.32}_{-0.52}$	$-4.69 \pm 0.81\ ^{+0.31}_{-0.19}$	$-3.11 \pm 0.78\ ^{+0.35}_{-0.23}$	$-2.53 \pm 0.58\ ^{+0.05}_{-0.31}$
307.5	$-3.03 \pm 1.04\ ^{+0.29}_{-0.37}$	$-4.25 \pm 0.94\ ^{+0.41}_{-0.42}$	$-3.11 \pm 0.90\ ^{+0.41}_{-0.48}$	$-6.05 \pm 0.90\ ^{+0.14}_{-0.26}$	$-2.54 \pm 0.76\ ^{+0.19}_{-0.16}$
322.5	$-3.33 \pm 1.12\ ^{+0.31}_{-0.32}$	$-3.65 \pm 1.03\ ^{+0.27}_{-0.44}$	$-4.03 \pm 1.08\ ^{+0.35}_{-0.31}$	$-2.58 \pm 1.22\ ^{+0.09}_{-0.47}$	$-2.61 \pm 1.28\ ^{+0.26}_{-0.51}$
337.5	$0.69 \pm 1.12\ ^{+0.33}_{-0.59}$	$-2.25 \pm 1.20\ ^{+0.35}_{-0.58}$	$-0.40 \pm 1.40\ ^{+0.46}_{-0.41}$	$-3.17 \pm 2.04\ ^{+1.26}_{-0.96}$	$-3.87 \pm 2.65\ ^{+1.10}_{-0.46}$
352.5	$4.06 \pm 1.49\ ^{+0.67}_{-0.48}$	$-1.46 \pm 1.37\ ^{+0.56}_{-0.65}$	$-0.67 \pm 1.82\ ^{+0.27}_{-0.75}$	$-0.19 \pm 3.21\ ^{+0.49}_{-1.81}$	$8.18 \pm 6.58\ ^{+1.58}_{-1.27}$

Table D.4: Helicity-dependent experimental cross section (pb) for kin362.

ϕ (deg)	$\langle x_{Bj}\rangle = 0.369$ $\langle Q^2\rangle = 4.532$ GeV^2 $\langle t'\rangle = -0.031$ GeV^2	$\langle x_{Bj}\rangle = 0.370$ $\langle Q^2\rangle = 4.550$ GeV^2 $\langle t'\rangle = -0.093$ GeV^2	$\langle x_{Bj}\rangle = 0.372$ $\langle Q^2\rangle = 4.574$ GeV^2 $\langle t'\rangle = -0.154$ GeV^2	$\langle x_{Bj}\rangle = 0.373$ $\langle Q^2\rangle = 4.585$ GeV^2 $\langle t'\rangle = -0.216$ GeV^2	$\langle x_{Bj}\rangle = 0.371$ $\langle Q^2\rangle = 4.568$ GeV^2 $\langle t'\rangle = -0.303$ GeV^2
7.5	$13.94 \pm 0.58\ ^{+0.16}_{-0.43}$	$13.89 \pm 0.73\ ^{+0.56}_{-0.41}$	$10.50 \pm 1.03\ ^{+0.56}_{-0.40}$	$9.37 \pm 1.59\ ^{+0.37}_{-0.50}$	$11.78 \pm 3.54\ ^{+0.54}_{-1.05}$
22.5	$12.92 \pm 0.56\ ^{+0.29}_{-0.51}$	$11.77 \pm 0.65\ ^{+0.33}_{-0.23}$	$9.51 \pm 0.82\ ^{+0.12}_{-0.31}$	$8.44 \pm 1.22\ ^{+0.30}_{-0.53}$	$5.90 \pm 1.74\ ^{+0.53}_{-0.61}$
37.5	$13.05 \pm 0.56\ ^{+0.14}_{-0.45}$	$9.54 \pm 0.54\ ^{+0.12}_{-0.09}$	$8.08 \pm 0.62\ ^{+0.23}_{-0.08}$	$6.98 \pm 0.79\ ^{+0.31}_{-0.30}$	$5.60 \pm 0.91\ ^{+0.41}_{-0.23}$
52.5	$12.16 \pm 0.54\ ^{+0.25}_{-0.21}$	$8.79 \pm 0.48\ ^{+0.26}_{-0.18}$	$7.48 \pm 0.51\ ^{+0.31}_{-0.32}$	$7.01 \pm 0.58\ ^{+0.39}_{-0.11}$	$4.85 \pm 0.54\ ^{+0.19}_{-0.11}$
67.5	$11.47 \pm 0.52\ ^{+0.44}_{-0.19}$	$8.77 \pm 0.47\ ^{+0.18}_{-0.30}$	$7.08 \pm 0.45\ ^{+0.19}_{-0.10}$	$5.36 \pm 0.47\ ^{+0.12}_{-0.19}$	$4.16 \pm 0.39\ ^{+0.27}_{-0.09}$
82.5	$11.28 \pm 0.51\ ^{+0.31}_{-0.37}$	$7.84 \pm 0.44\ ^{+0.08}_{-0.22}$	$6.18 \pm 0.41\ ^{+0.11}_{-0.12}$	$5.55 \pm 0.44\ ^{+0.10}_{-0.09}$	$3.39 \pm 0.31\ ^{+0.01}_{-0.19}$
97.5	$8.75 \pm 0.46\ ^{+0.29}_{-0.13}$	$7.40 \pm 0.43\ ^{+0.31}_{-0.04}$	$5.07 \pm 0.37\ ^{+0.29}_{-0.09}$	$4.38 \pm 0.37\ ^{+0.13}_{-0.14}$	$2.94 \pm 0.28\ ^{+0.07}_{-0.08}$
112.5	$9.14 \pm 0.46\ ^{+0.11}_{-0.13}$	$6.55 \pm 0.40\ ^{+0.27}_{-0.16}$	$4.50 \pm 0.33\ ^{+0.10}_{-0.06}$	$3.90 \pm 0.34\ ^{+0.16}_{-0.11}$	$2.87 \pm 0.24\ ^{+0.07}_{-0.05}$
127.5	$9.04 \pm 0.45\ ^{+0.29}_{-0.16}$	$6.83 \pm 0.40\ ^{+0.31}_{-0.11}$	$4.65 \pm 0.32\ ^{+0.13}_{-0.19}$	$3.41 \pm 0.30\ ^{+0.18}_{-0.05}$	$2.34 \pm 0.20\ ^{+0.10}_{-0.00}$
142.5	$8.38 \pm 0.44\ ^{+0.17}_{-0.10}$	$6.09 \pm 0.37\ ^{+0.07}_{-0.14}$	$4.49 \pm 0.31\ ^{+0.12}_{-0.12}$	$3.40 \pm 0.29\ ^{+0.08}_{-0.10}$	$2.67 \pm 0.20\ ^{+0.04}_{-0.09}$
157.5	$8.28 \pm 0.44\ ^{+0.05}_{-0.26}$	$6.04 \pm 0.37\ ^{+0.10}_{-0.10}$	$3.62 \pm 0.29\ ^{+0.09}_{-0.17}$	$3.02 \pm 0.27\ ^{+0.09}_{-0.11}$	$2.15 \pm 0.19\ ^{+0.10}_{-0.12}$
172.5	$7.98 \pm 0.43\ ^{+0.00}_{-0.31}$	$5.30 \pm 0.34\ ^{+0.10}_{-0.20}$	$3.86 \pm 0.29\ ^{+0.05}_{-0.13}$	$2.96 \pm 0.27\ ^{+0.20}_{-0.02}$	$2.49 \pm 0.21\ ^{+0.08}_{-0.09}$
187.5	$7.74 \pm 0.43\ ^{+0.17}_{-0.13}$	$5.95 \pm 0.37\ ^{+0.16}_{-0.10}$	$3.42 \pm 0.27\ ^{+0.11}_{-0.14}$	$3.35 \pm 0.29\ ^{+0.10}_{-0.06}$	$2.40 \pm 0.20\ ^{+0.07}_{-0.06}$
202.5	$8.41 \pm 0.45\ ^{+0.16}_{-0.20}$	$5.08 \pm 0.35\ ^{+0.15}_{-0.14}$	$3.92 \pm 0.31\ ^{+0.03}_{-0.10}$	$2.85 \pm 0.27\ ^{+0.13}_{-0.05}$	$2.11 \pm 0.19\ ^{+0.07}_{-0.00}$
217.5	$8.53 \pm 0.45\ ^{+0.17}_{-0.03}$	$7.08 \pm 0.41\ ^{+0.25}_{-0.22}$	$4.43 \pm 0.33\ ^{+0.15}_{-0.18}$	$2.94 \pm 0.29\ ^{+0.13}_{-0.10}$	$2.48 \pm 0.20\ ^{+0.03}_{-0.07}$
232.5	$9.91 \pm 0.49\ ^{+0.43}_{-0.05}$	$6.15 \pm 0.40\ ^{+0.29}_{-0.21}$	$4.98 \pm 0.34\ ^{+0.21}_{-0.07}$	$3.60 \pm 0.32\ ^{+0.16}_{-0.11}$	$2.60 \pm 0.21\ ^{+0.13}_{-0.07}$
247.5	$9.69 \pm 0.49\ ^{+0.32}_{-0.22}$	$6.24 \pm 0.40\ ^{+0.25}_{-0.17}$	$5.78 \pm 0.38\ ^{+0.14}_{-0.08}$	$4.18 \pm 0.35\ ^{+0.09}_{-0.16}$	$3.18 \pm 0.25\ ^{+0.09}_{-0.07}$
262.5	$10.21 \pm 0.49\ ^{+0.32}_{-0.10}$	$7.09 \pm 0.42\ ^{+0.24}_{-0.13}$	$5.75 \pm 0.38\ ^{+0.35}_{-0.11}$	$4.72 \pm 0.38\ ^{+0.16}_{-0.20}$	$3.48 \pm 0.28\ ^{+0.10}_{-0.07}$
277.5	$10.93 \pm 0.51\ ^{+0.16}_{-0.37}$	$8.13 \pm 0.45\ ^{+0.28}_{-0.14}$	$6.26 \pm 0.40\ ^{+0.36}_{-0.06}$	$5.60 \pm 0.43\ ^{+0.21}_{-0.29}$	$3.73 \pm 0.32\ ^{+0.15}_{-0.06}$
292.5	$12.23 \pm 0.54\ ^{+0.30}_{-0.28}$	$10.28 \pm 0.49\ ^{+0.20}_{-0.26}$	$7.65 \pm 0.46\ ^{+0.32}_{-0.17}$	$6.75 \pm 0.49\ ^{+0.14}_{-0.15}$	$4.83 \pm 0.39\ ^{+0.11}_{-0.19}$
307.5	$12.36 \pm 0.54\ ^{+0.24}_{-0.21}$	$11.14 \pm 0.52\ ^{+0.44}_{-0.08}$	$9.48 \pm 0.52\ ^{+0.28}_{-0.36}$	$7.84 \pm 0.58\ ^{+0.19}_{-0.12}$	$5.34 \pm 0.51\ ^{+0.18}_{-0.18}$
322.5	$13.82 \pm 0.57\ ^{+0.15}_{-0.30}$	$12.81 \pm 0.60\ ^{+0.35}_{-0.34}$	$9.47 \pm 0.64\ ^{+0.41}_{-0.24}$	$8.97 \pm 0.81\ ^{+0.43}_{-0.23}$	$7.01 \pm 0.87\ ^{+0.41}_{-0.24}$
337.5	$15.43 \pm 0.61\ ^{+0.21}_{-0.37}$	$12.76 \pm 0.64\ ^{+0.45}_{-0.12}$	$11.34 \pm 0.84\ ^{+0.45}_{-0.32}$	$9.39 \pm 1.21\ ^{+0.24}_{-0.37}$	$10.96 \pm 1.91\ ^{+0.72}_{-0.71}$
352.5	$13.76 \pm 0.58\ ^{+0.39}_{-0.31}$	$12.99 \pm 0.70\ ^{+0.49}_{-0.17}$	$11.09 \pm 1.01\ ^{+0.41}_{-0.21}$	$11.18 \pm 1.70\ ^{+0.57}_{-0.51}$	$12.76 \pm 3.21\ ^{+1.39}_{-1.70}$

Table D.5: Unpolarized experimental cross section (pb) for kin363.

ϕ (deg)	$\langle x_{Bj}\rangle = 0.369$ $\langle Q^2\rangle = 4.532$ GeV^2 $\langle t'\rangle = -0.031$ GeV^2	$\langle x_{Bj}\rangle = 0.370$ $\langle Q^2\rangle = 4.550$ GeV^2 $\langle t'\rangle = -0.093$ GeV^2	$\langle x_{Bj}\rangle = 0.372$ $\langle Q^2\rangle = 4.574$ GeV^2 $\langle t'\rangle = -0.154$ GeV^2	$\langle x_{Bj}\rangle = 0.373$ $\langle Q^2\rangle = 4.585$ GeV^2 $\langle t'\rangle = -0.216$ GeV^2	$\langle x_{Bj}\rangle = 0.371$ $\langle Q^2\rangle = 4.568$ GeV^2 $\langle t'\rangle = -0.303$ GeV^2
7.5	1.17 ± 0.66 $^{+0.14}_{-0.08}$	0.73 ± 0.82 $^{+0.05}_{-0.35}$	0.12 ± 1.03 $^{+0.60}_{-0.46}$	0.53 ± 1.46 $^{+0.72}_{-0.10}$	-5.40 ± 2.97 $^{+0.81}_{-1.23}$
22.5	1.21 ± 0.68 $^{+0.07}_{-0.31}$	2.19 ± 0.75 $^{+0.24}_{-0.26}$	1.11 ± 0.88 $^{+0.25}_{-0.58}$	1.95 ± 1.24 $^{+0.59}_{-0.64}$	0.61 ± 1.65 $^{+0.74}_{-0.24}$
37.5	1.72 ± 0.67 $^{+0.30}_{-0.40}$	1.03 ± 0.63 $^{+0.32}_{-0.11}$	2.60 ± 0.72 $^{+0.35}_{-0.20}$	1.81 ± 0.85 $^{+0.13}_{-0.32}$	2.09 ± 0.92 $^{+0.31}_{-0.08}$
52.5	2.15 ± 0.65 $^{+0.32}_{-0.35}$	1.90 ± 0.59 $^{+0.06}_{-0.18}$	2.94 ± 0.60 $^{+0.35}_{-0.08}$	1.71 ± 0.67 $^{+0.35}_{-0.27}$	0.76 ± 0.59 $^{+0.31}_{-0.09}$
67.5	1.59 ± 0.64 $^{+0.33}_{-0.00}$	3.00 ± 0.57 $^{+0.18}_{-0.17}$	2.23 ± 0.53 $^{+0.23}_{-0.13}$	1.30 ± 0.55 $^{+0.18}_{-0.20}$	0.96 ± 0.44 $^{+0.14}_{-0.09}$
82.5	1.87 ± 0.62 $^{+0.11}_{-0.35}$	3.64 ± 0.53 $^{+0.13}_{-0.18}$	1.95 ± 0.47 $^{+0.14}_{-0.19}$	1.97 ± 0.51 $^{+0.24}_{-0.07}$	1.09 ± 0.36 $^{+0.13}_{-0.16}$
97.5	0.80 ± 0.55 $^{+0.07}_{-0.41}$	2.10 ± 0.51 $^{+0.33}_{-0.06}$	1.06 ± 0.42 $^{+0.19}_{-0.05}$	1.65 ± 0.43 $^{+0.09}_{-0.24}$	1.01 ± 0.31 $^{+0.13}_{-0.03}$
112.5	2.05 ± 0.55 $^{+0.21}_{-0.15}$	1.02 ± 0.48 $^{+0.20}_{-0.01}$	1.10 ± 0.37 $^{+0.03}_{-0.28}$	1.56 ± 0.39 $^{+0.04}_{-0.17}$	0.85 ± 0.28 $^{+0.09}_{-0.07}$
127.5	1.10 ± 0.55 $^{+0.04}_{-0.17}$	2.05 ± 0.47 $^{+0.12}_{-0.12}$	1.18 ± 0.35 $^{+0.08}_{-0.21}$	1.01 ± 0.34 $^{+0.20}_{-0.02}$	0.76 ± 0.24 $^{+0.10}_{-0.01}$
142.5	1.76 ± 0.52 $^{+0.09}_{-0.27}$	1.13 ± 0.44 $^{+0.21}_{-0.12}$	0.53 ± 0.34 $^{+0.07}_{-0.19}$	0.55 ± 0.35 $^{+0.12}_{-0.20}$	0.60 ± 0.23 $^{+0.11}_{-0.08}$
157.5	0.69 ± 0.53 $^{+0.08}_{-0.25}$	-0.27 ± 0.43 $^{+0.16}_{-0.11}$	0.23 ± 0.29 $^{+0.04}_{-0.11}$	1.12 ± 0.32 $^{+0.11}_{-0.11}$	0.27 ± 0.22 $^{+0.07}_{-0.01}$
172.5	-0.27 ± 0.49 $^{+0.14}_{-0.22}$	0.41 ± 0.39 $^{+0.08}_{-0.20}$	0.34 ± 0.29 $^{+0.06}_{-0.03}$	0.34 ± 0.32 $^{+0.19}_{-0.14}$	0.17 ± 0.23 $^{+0.01}_{-0.11}$
187.5	-0.80 ± 0.56 $^{+0.32}_{-0.18}$	0.79 ± 0.45 $^{+0.15}_{-0.24}$	-0.16 ± 0.29 $^{+0.08}_{-0.21}$	-0.24 ± 0.36 $^{+0.14}_{-0.05}$	-0.30 ± 0.23 $^{+0.12}_{-0.02}$
202.5	0.08 ± 0.57 $^{+0.08}_{-0.13}$	-0.14 ± 0.42 $^{+0.12}_{-0.25}$	-0.37 ± 0.32 $^{+0.09}_{-0.16}$	-0.00 ± 0.33 $^{+0.15}_{-0.02}$	-0.05 ± 0.22 $^{+0.05}_{-0.02}$
217.5	-0.29 ± 0.56 $^{+0.13}_{-0.17}$	-1.14 ± 0.48 $^{+0.18}_{-0.05}$	-0.71 ± 0.35 $^{+0.16}_{-0.05}$	-0.07 ± 0.35 $^{+0.07}_{-0.19}$	-0.35 ± 0.23 $^{+0.07}_{-0.06}$
232.5	-1.99 ± 0.60 $^{+0.37}_{-0.08}$	-1.61 ± 0.48 $^{+0.01}_{-0.34}$	-0.65 ± 0.38 $^{+0.15}_{-0.13}$	-1.03 ± 0.37 $^{+0.13}_{-0.01}$	-0.37 ± 0.25 $^{+0.04}_{-0.09}$
247.5	-1.33 ± 0.60 $^{+0.36}_{-0.13}$	-1.63 ± 0.49 $^{+0.07}_{-0.18}$	-1.19 ± 0.43 $^{+0.10}_{-0.16}$	-1.14 ± 0.42 $^{+0.15}_{-0.07}$	-1.21 ± 0.29 $^{+0.11}_{-0.18}$
262.5	-1.54 ± 0.61 $^{+0.14}_{-0.16}$	-2.36 ± 0.51 $^{+0.28}_{-0.12}$	-1.15 ± 0.45 $^{+0.14}_{-0.31}$	-0.78 ± 0.45 $^{+0.21}_{-0.05}$	-1.39 ± 0.33 $^{+0.06}_{-0.19}$
277.5	-3.14 ± 0.63 $^{+0.07}_{-0.30}$	-1.94 ± 0.55 $^{+0.10}_{-0.38}$	-1.21 ± 0.47 $^{+0.16}_{-0.12}$	-1.46 ± 0.50 $^{+0.31}_{-0.06}$	-1.20 ± 0.36 $^{+0.13}_{-0.09}$
292.5	-0.43 ± 0.66 $^{+0.29}_{-0.37}$	-3.53 ± 0.61 $^{+0.58}_{-0.11}$	-1.58 ± 0.54 $^{+0.28}_{-0.22}$	-2.69 ± 0.57 $^{+0.21}_{-0.15}$	-2.58 ± 0.45 $^{+0.19}_{-0.12}$
307.5	-2.19 ± 0.67 $^{+0.31}_{-0.23}$	-1.53 ± 0.63 $^{+0.33}_{-0.00}$	-2.56 ± 0.62 $^{+0.11}_{-0.20}$	-2.87 ± 0.67 $^{+0.25}_{-0.31}$	-1.31 ± 0.57 $^{+0.18}_{-0.02}$
322.5	-1.85 ± 0.70 $^{+0.27}_{-0.24}$	-2.67 ± 0.73 $^{+0.34}_{-0.08}$	-1.29 ± 0.73 $^{+0.32}_{-0.28}$	-1.55 ± 0.88 $^{+0.33}_{-0.06}$	-1.87 ± 0.88 $^{+0.57}_{-0.27}$
337.5	-0.54 ± 0.74 $^{+0.15}_{-0.18}$	-0.47 ± 0.76 $^{+0.21}_{-0.31}$	-0.90 ± 0.90 $^{+0.56}_{-0.00}$	-2.42 ± 1.20 $^{+0.28}_{-0.22}$	-4.63 ± 1.72 $^{+1.38}_{-0.15}$
352.5	-0.71 ± 0.75 $^{+0.25}_{-0.08}$	-0.65 ± 0.84 $^{+0.38}_{-0.42}$	-0.41 ± 1.10 $^{+0.63}_{-0.20}$	1.72 ± 1.70 $^{+0.50}_{-0.93}$	1.39 ± 3.10 $^{+0.61}_{-0.31}$

Table D.6: Helicity-dependent experimental cross section (pb) for kin363.

ϕ (deg)	$\langle x_{Bj}\rangle = 0.483$ $\langle Q^2\rangle = 2.707$ GeV^2 $\langle t'\rangle = -0.022$ GeV^2	$\langle x_{Bj}\rangle = 0.483$ $\langle Q^2\rangle = 2.708$ GeV^2 $\langle t'\rangle = -0.064$ GeV^2	$\langle x_{Bj}\rangle = 0.484$ $\langle Q^2\rangle = 2.713$ GeV^2 $\langle t'\rangle = -0.107$ GeV^2	$\langle x_{Bj}\rangle = 0.485$ $\langle Q^2\rangle = 2.715$ GeV^2 $\langle t'\rangle = -0.150$ GeV^2	$\langle x_{Bj}\rangle = 0.485$ $\langle Q^2\rangle = 2.717$ GeV^2 $\langle t'\rangle = -0.210$ GeV^2
7.5	$27.39 \pm 2.66\ ^{+1.00}_{-1.20}$	$25.49 \pm 3.49\ ^{+1.64}_{-1.85}$	$30.79 \pm 6.32\ ^{+3.67}_{-1.00}$	$7.58 \pm 16.82\ ^{+11.25}_{-4.90}$	$203.10 \pm 126.41\ ^{+1.17}_{-120.99}$
22.5	$28.69 \pm 2.62\ ^{+0.00}_{-1.37}$	$27.50 \pm 3.21\ ^{+0.80}_{-2.12}$	$31.01 \pm 4.71\ ^{+1.36}_{-0.91}$	$42.46 \pm 9.70\ ^{+2.65}_{-7.31}$	$35.41 \pm 30.14\ ^{+17.32}_{-12.14}$
37.5	$23.29 \pm 2.42\ ^{+0.70}_{-0.92}$	$25.70 \pm 2.81\ ^{+0.91}_{-0.24}$	$23.60 \pm 3.43\ ^{+2.21}_{-0.67}$	$12.71 \pm 4.34\ ^{+3.05}_{-1.38}$	$21.75 \pm 6.75\ ^{+1.25}_{-5.42}$
52.5	$27.60 \pm 2.43\ ^{+0.88}_{-0.76}$	$22.24 \pm 2.46\ ^{+1.30}_{-1.32}$	$20.93 \pm 2.63\ ^{+0.47}_{-1.34}$	$19.36 \pm 2.91\ ^{+0.26}_{-1.44}$	$13.15 \pm 2.74\ ^{+0.89}_{-0.86}$
67.5	$24.00 \pm 2.33\ ^{+2.82}_{-0.22}$	$20.92 \pm 2.24\ ^{+0.52}_{-0.64}$	$21.38 \pm 2.26\ ^{+0.61}_{-1.10}$	$15.45 \pm 2.37\ ^{+1.00}_{-0.81}$	$12.07 \pm 1.95\ ^{+0.76}_{-0.79}$
82.5	$23.03 \pm 2.21\ ^{+1.74}_{-0.15}$	$20.43 \pm 2.10\ ^{+0.51}_{-0.30}$	$18.27 \pm 2.14\ ^{+0.40}_{-1.26}$	$19.16 \pm 2.19\ ^{+1.19}_{-0.35}$	$13.59 \pm 1.70\ ^{+0.40}_{-1.07}$
97.5	$18.40 \pm 2.02\ ^{+0.41}_{-0.39}$	$15.53 \pm 1.96\ ^{+1.22}_{-1.35}$	$12.20 \pm 1.98\ ^{+0.41}_{-1.12}$	$15.01 \pm 2.03\ ^{+0.69}_{-1.48}$	$14.08 \pm 1.72\ ^{+0.67}_{-0.13}$
112.5	$22.38 \pm 2.06\ ^{+1.18}_{-0.57}$	$17.64 \pm 1.97\ ^{+0.21}_{-1.31}$	$17.26 \pm 1.93\ ^{+1.21}_{-1.23}$	$10.60 \pm 1.75\ ^{+1.51}_{-0.54}$	$13.68 \pm 1.44\ ^{+0.81}_{-0.13}$
127.5	$23.93 \pm 2.11\ ^{+0.26}_{-0.75}$	$16.29 \pm 1.84\ ^{+0.74}_{-0.56}$	$13.21 \pm 1.74\ ^{+0.17}_{-0.85}$	$10.12 \pm 1.67\ ^{+0.61}_{-0.36}$	$7.57 \pm 1.20\ ^{+0.54}_{-0.31}$
142.5	$20.85 \pm 2.06\ ^{+0.31}_{-1.32}$	$14.23 \pm 1.67\ ^{+1.00}_{-0.11}$	$11.90 \pm 1.69\ ^{+0.35}_{-0.70}$	$11.50 \pm 1.73\ ^{+0.27}_{-0.49}$	$9.90 \pm 1.39\ ^{+0.78}_{-0.81}$
157.5	$20.82 \pm 1.97\ ^{+0.67}_{-0.97}$	$14.30 \pm 1.81\ ^{+1.21}_{-0.50}$	$15.58 \pm 1.97\ ^{+1.26}_{-1.26}$	$13.94 \pm 1.99\ ^{+0.46}_{-0.77}$	$12.79 \pm 1.64\ ^{+1.02}_{-0.46}$
172.5	$22.31 \pm 2.07\ ^{+0.56}_{-1.21}$	$11.94 \pm 1.72\ ^{+0.64}_{-1.56}$	$11.49 \pm 1.89\ ^{+0.93}_{-0.54}$	$13.79 \pm 2.18\ ^{+0.96}_{-1.06}$	$18.44 \pm 2.18\ ^{+0.87}_{-1.17}$
187.5	$23.13 \pm 2.06\ ^{+0.06}_{-1.04}$	$16.39 \pm 1.82\ ^{+0.50}_{-1.80}$	$14.07 \pm 2.03\ ^{+0.11}_{-0.96}$	$16.21 \pm 2.37\ ^{+0.23}_{-1.07}$	$20.63 \pm 2.23\ ^{+1.06}_{-1.71}$
202.5	$22.21 \pm 2.05\ ^{+0.64}_{-1.80}$	$18.62 \pm 1.90\ ^{+1.94}_{-0.55}$	$15.06 \pm 2.03\ ^{+0.58}_{-0.41}$	$12.69 \pm 2.09\ ^{+0.87}_{-0.32}$	$14.47 \pm 1.82\ ^{+0.26}_{-1.07}$
217.5	$18.68 \pm 1.96\ ^{+1.63}_{-0.17}$	$18.04 \pm 1.92\ ^{+0.32}_{-0.86}$	$14.09 \pm 1.93\ ^{+0.39}_{-1.66}$	$11.30 \pm 1.92\ ^{+1.74}_{-0.76}$	$10.27 \pm 1.53\ ^{+0.68}_{-0.07}$
232.5	$19.66 \pm 2.04\ ^{+0.69}_{-0.80}$	$13.75 \pm 1.90\ ^{+1.46}_{-0.66}$	$18.05 \pm 2.01\ ^{+0.10}_{-0.84}$	$13.57 \pm 1.90\ ^{+0.43}_{-1.26}$	$13.40 \pm 1.57\ ^{+0.23}_{-1.04}$
247.5	$20.16 \pm 2.10\ ^{+0.73}_{-0.24}$	$15.40 \pm 1.97\ ^{+0.28}_{-0.40}$	$15.67 \pm 2.05\ ^{+0.18}_{-1.06}$	$15.55 \pm 2.09\ ^{+0.17}_{-0.62}$	$12.27 \pm 1.50\ ^{+0.42}_{-0.31}$
262.5	$23.35 \pm 2.19\ ^{+1.08}_{-0.49}$	$23.47 \pm 2.25\ ^{+0.65}_{-0.71}$	$18.38 \pm 2.17\ ^{+0.21}_{-0.92}$	$16.72 \pm 2.13\ ^{+0.53}_{-0.36}$	$10.45 \pm 1.44\ ^{+1.45}_{-0.17}$
277.5	$22.11 \pm 2.24\ ^{+0.07}_{-1.59}$	$24.09 \pm 2.36\ ^{+1.69}_{-1.54}$	$17.34 \pm 2.27\ ^{+0.67}_{-0.69}$	$18.27 \pm 2.24\ ^{+0.91}_{-1.06}$	$17.24 \pm 1.74\ ^{+0.62}_{-0.42}$
292.5	$24.01 \pm 2.35\ ^{+0.61}_{-0.15}$	$20.80 \pm 2.42\ ^{+0.61}_{-0.66}$	$23.90 \pm 2.65\ ^{+0.00}_{-1.53}$	$18.41 \pm 2.58\ ^{+1.39}_{-1.33}$	$19.14 \pm 2.10\ ^{+1.07}_{-0.09}$
307.5	$28.35 \pm 2.50\ ^{+0.94}_{-1.15}$	$27.11 \pm 2.61\ ^{+1.85}_{-1.91}$	$19.72 \pm 2.94\ ^{+0.33}_{-0.91}$	$18.35 \pm 3.11\ ^{+0.67}_{-1.55}$	$16.61 \pm 3.40\ ^{+1.85}_{-1.00}$
322.5	$27.54 \pm 2.57\ ^{+0.73}_{-0.91}$	$28.34 \pm 2.94\ ^{+2.54}_{-1.76}$	$25.42 \pm 3.64\ ^{+3.21}_{-0.00}$	$24.08 \pm 4.88\ ^{+0.50}_{-2.77}$	$8.06 \pm 7.15\ ^{+6.25}_{-3.04}$
337.5	$28.54 \pm 2.67\ ^{+0.95}_{-0.62}$	$24.80 \pm 3.11\ ^{+1.54}_{-0.79}$	$23.01 \pm 4.73\ ^{+0.73}_{-1.95}$	$20.57 \pm 10.26\ ^{+2.65}_{-2.21}$	$-23.18 \pm 38.43\ ^{+38.16}_{-2.89}$
352.5	$26.29 \pm 2.69\ ^{+1.29}_{-0.83}$	$28.69 \pm 3.45\ ^{+1.42}_{-0.56}$	$31.08 \pm 5.65\ ^{+0.07}_{-3.50}$	$50.82 \pm 20.27\ ^{+6.06}_{-9.00}$	$-90.57 \pm 90.60\ ^{+87.73}_{-69.39}$

Table D.7: Unpolarized experimental cross section (pb) for kin481.

ϕ (deg)	$\langle x_{Bj}\rangle = 0.483$ $\langle Q^2\rangle = 2.707$ GeV^2 $\langle t'\rangle = -0.022$ GeV^2	$\langle x_{Bj}\rangle = 0.483$ $\langle Q^2\rangle = 2.708$ GeV^2 $\langle t'\rangle = -0.064$ GeV^2	$\langle x_{Bj}\rangle = 0.484$ $\langle Q^2\rangle = 2.713$ GeV^2 $\langle t'\rangle = -0.107$ GeV^2	$\langle x_{Bj}\rangle = 0.485$ $\langle Q^2\rangle = 2.715$ GeV^2 $\langle t'\rangle = -0.150$ GeV^2	$\langle x_{Bj}\rangle = 0.485$ $\langle Q^2\rangle = 2.717$ GeV^2 $\langle t'\rangle = -0.210$ GeV^2
7.5	-0.59 ± 1.94 $^{+0.36}_{-0.67}$	-0.39 ± 3.70 $^{+1.56}_{-0.97}$	6.68 ± 6.33 $^{+4.15}_{-4.54}$	-0.34 ± 1.91 $^{+9.56}_{-1.40}$	-107.46 ± 143.08 $^{+77.98}_{-36.25}$
22.5	1.55 ± 2.07 $^{+1.67}_{-0.60}$	-3.69 ± 3.66 $^{+1.35}_{-0.67}$	-2.41 ± 5.30 $^{+0.71}_{-2.67}$	1.38 ± 4.03 $^{+0.28}_{-2.76}$	21.54 ± 28.58 $^{+22.46}_{-3.72}$
37.5	-0.12 ± 2.05 $^{+0.70}_{-0.54}$	4.04 ± 3.20 $^{+1.02}_{-1.05}$	2.74 ± 3.97 $^{+1.58}_{-0.68}$	3.21 ± 2.96 $^{+0.80}_{-2.36}$	4.83 ± 7.39 $^{+3.60}_{-3.61}$
52.5	1.40 ± 2.01 $^{+1.17}_{-0.34}$	3.83 ± 2.83 $^{+0.48}_{-0.42}$	3.71 ± 3.03 $^{+0.73}_{-0.87}$	-1.58 ± 2.64 $^{+0.56}_{-0.35}$	3.03 ± 3.09 $^{+0.86}_{-1.33}$
67.5	-1.35 ± 2.04 $^{+0.34}_{-0.61}$	10.15 ± 2.61 $^{+0.73}_{-2.59}$	3.13 ± 2.49 $^{+0.81}_{-0.61}$	2.61 ± 2.42 $^{+0.66}_{-0.97}$	3.43 ± 2.18 $^{+1.26}_{-0.93}$
82.5	2.25 ± 1.94 $^{+0.73}_{-0.99}$	4.78 ± 2.43 $^{+0.72}_{-0.95}$	6.58 ± 2.31 $^{+0.94}_{-0.96}$	3.97 ± 2.37 $^{+0.48}_{-0.37}$	0.18 ± 1.90 $^{+0.47}_{-0.51}$
97.5	-0.06 ± 1.85 $^{+0.54}_{-0.57}$	6.06 ± 2.29 $^{+1.22}_{-0.68}$	-0.31 ± 2.05 $^{+0.70}_{-0.56}$	2.62 ± 2.31 $^{+0.91}_{-1.71}$	3.26 ± 1.87 $^{+0.26}_{-1.24}$
112.5	1.40 ± 1.91 $^{+1.28}_{-0.58}$	2.48 ± 2.29 $^{+0.94}_{-0.71}$	3.63 ± 1.94 $^{+0.66}_{-0.18}$	4.35 ± 2.03 $^{+1.17}_{-0.69}$	2.78 ± 1.54 $^{+0.58}_{-0.53}$
127.5	0.97 ± 1.93 $^{+1.13}_{-0.57}$	2.93 ± 2.11 $^{+0.26}_{-1.32}$	0.68 ± 1.70 $^{+0.72}_{-1.67}$	1.19 ± 2.01 $^{+0.85}_{-0.24}$	0.78 ± 1.26 $^{+0.60}_{-0.32}$
142.5	-0.54 ± 1.83 $^{+1.24}_{-0.78}$	2.71 ± 1.97 $^{+1.56}_{-0.38}$	2.58 ± 1.58 $^{+0.74}_{-0.92}$	0.12 ± 2.07 $^{+0.61}_{-0.40}$	2.33 ± 1.42 $^{+0.20}_{-0.56}$
157.5	-0.87 ± 1.80 $^{+0.94}_{-0.90}$	-1.05 ± 2.05 $^{+1.47}_{-0.00}$	0.85 ± 1.78 $^{+0.93}_{-0.53}$	2.31 ± 2.33 $^{+0.64}_{-0.26}$	-0.39 ± 1.57 $^{+0.54}_{-0.44}$
172.5	2.92 ± 1.68 $^{+0.52}_{-1.12}$	0.19 ± 1.96 $^{+0.48}_{-0.26}$	0.02 ± 1.67 $^{+0.66}_{-0.93}$	2.54 ± 2.51 $^{+0.94}_{-1.17}$	5.87 ± 1.96 $^{+0.65}_{-1.37}$
187.5	0.16 ± 2.45 $^{+0.43}_{-0.95}$	6.91 ± 2.49 $^{+0.27}_{-0.75}$	2.05 ± 2.02 $^{+0.08}_{-1.51}$	4.81 ± 2.99 $^{+1.13}_{-1.48}$	-0.92 ± 2.16 $^{+0.64}_{-0.63}$
202.5	-0.06 ± 2.10 $^{+0.95}_{-0.79}$	-0.29 ± 2.41 $^{+0.63}_{-0.78}$	-0.30 ± 1.93 $^{+1.73}_{-0.26}$	-8.90 ± 2.62 $^{+0.24}_{-2.65}$	0.88 ± 1.73 $^{+0.92}_{-0.21}$
217.5	-0.82 ± 2.00 $^{+0.56}_{-0.67}$	-2.24 ± 2.36 $^{+1.23}_{-0.11}$	1.65 ± 1.81 $^{+0.56}_{-0.21}$	-3.44 ± 2.39 $^{+1.15}_{-1.00}$	-0.51 ± 1.52 $^{+0.17}_{-0.50}$
232.5	-3.25 ± 2.08 $^{+0.24}_{-1.45}$	-8.01 ± 2.27 $^{+0.62}_{-0.83}$	-3.82 ± 1.97 $^{+2.33}_{-0.39}$	0.13 ± 2.30 $^{+1.61}_{-0.97}$	-0.53 ± 1.61 $^{+0.48}_{-0.41}$
247.5	-0.42 ± 2.09 $^{+1.10}_{-0.35}$	0.08 ± 2.38 $^{+0.60}_{-1.54}$	-2.39 ± 2.03 $^{+0.65}_{-0.64}$	-3.31 ± 2.40 $^{+0.30}_{-0.82}$	-0.97 ± 1.60 $^{+0.88}_{-0.37}$
262.5	2.00 ± 2.23 $^{+0.71}_{-0.95}$	-6.16 ± 2.64 $^{+1.43}_{-0.84}$	-1.58 ± 2.28 $^{+0.69}_{-1.41}$	-4.92 ± 2.55 $^{+0.58}_{-1.10}$	-6.10 ± 1.60 $^{+0.35}_{-0.81}$
277.5	-2.74 ± 2.19 $^{+0.60}_{-0.69}$	-1.98 ± 2.77 $^{+0.90}_{-0.89}$	-3.99 ± 2.51 $^{+0.54}_{-1.08}$	-6.52 ± 2.58 $^{+1.41}_{-0.20}$	-3.67 ± 1.95 $^{+0.44}_{-0.28}$
292.5	-1.35 ± 2.21 $^{+0.48}_{-0.48}$	-2.18 ± 2.86 $^{+0.90}_{-1.10}$	-0.57 ± 2.97 $^{+1.18}_{-1.61}$	-5.43 ± 2.79 $^{+0.81}_{-0.89}$	-7.73 ± 2.42 $^{+1.63}_{-0.55}$
307.5	-5.54 ± 2.30 $^{+0.97}_{-0.85}$	-0.30 ± 3.18 $^{+1.71}_{-1.76}$	-1.80 ± 3.42 $^{+0.38}_{-1.45}$	-1.26 ± 3.02 $^{+1.27}_{-0.74}$	-4.17 ± 3.91 $^{+1.73}_{-1.71}$
322.5	3.48 ± 2.41 $^{+1.33}_{-0.92}$	-5.40 ± 3.54 $^{+0.27}_{-0.88}$	-5.35 ± 4.19 $^{+2.33}_{-0.05}$	1.28 ± 3.63 $^{+0.88}_{-3.37}$	-14.40 ± 7.87 $^{+4.60}_{-7.37}$
337.5	-1.55 ± 2.48 $^{+1.45}_{-1.35}$	-5.40 ± 3.72 $^{+2.16}_{-0.99}$	-5.88 ± 5.44 $^{+1.53}_{-1.96}$	-0.07 ± 4.40 $^{+0.93}_{-1.18}$	-23.18 ± 37.66 $^{+15.79}_{-27.43}$
352.5	-0.09 ± 2.88 $^{+0.78}_{-1.29}$	-3.83 ± 4.56 $^{+0.46}_{-3.01}$	-2.20 ± 7.04 $^{+4.15}_{-0.81}$	-0.05 ± 3.05 $^{+4.02}_{-12.31}$	-6.48 ± 117.70 $^{+52.85}_{-234.01}$

Table D.8: Helicity-dependent experimental cross section (pb) for kin481.

ϕ (deg)	$\langle x_{Bj}\rangle = 0.497$ $\langle Q^2\rangle = 4.497$ GeV^2 $\langle t'\rangle = -0.031$ GeV^2	$\langle x_{Bj}\rangle = 0.501$ $\langle Q^2\rangle = 4.528$ GeV^2 $\langle t'\rangle = -0.093$ GeV^2	$\langle x_{Bj}\rangle = 0.504$ $\langle Q^2\rangle = 4.558$ GeV^2 $\langle t'\rangle = -0.154$ GeV^2	$\langle x_{Bj}\rangle = 0.506$ $\langle Q^2\rangle = 4.573$ GeV^2 $\langle t'\rangle = -0.216$ GeV^2	$\langle x_{Bj}\rangle = 0.508$ $\langle Q^2\rangle = 4.593$ GeV^2 $\langle t'\rangle = -0.305$ GeV^2
7.5	$3.39 \pm 0.22\ ^{+0.05}_{-0.10}$	$2.37 \pm 0.29\ ^{+0.08}_{-0.13}$	$2.24 \pm 0.43\ ^{+0.18}_{-0.08}$	$1.79 \pm 0.59\ ^{+0.19}_{-0.15}$	$1.92 \pm 0.84\ ^{+0.07}_{-0.25}$
22.5	$3.57 \pm 0.23\ ^{+0.13}_{-0.11}$	$2.61 \pm 0.27\ ^{+0.11}_{-0.08}$	$2.87 \pm 0.40\ ^{+0.05}_{-0.24}$	$2.56 \pm 0.53\ ^{+0.22}_{-0.18}$	$1.89 \pm 0.63\ ^{+0.34}_{-0.11}$
37.5	$3.28 \pm 0.21\ ^{+0.08}_{-0.07}$	$3.07 \pm 0.25\ ^{+0.05}_{-0.07}$	$1.88 \pm 0.28\ ^{+0.12}_{-0.03}$	$2.21 \pm 0.35\ ^{+0.07}_{-0.19}$	$0.75 \pm 0.35\ ^{+0.10}_{-0.11}$
52.5	$3.43 \pm 0.21\ ^{+0.17}_{-0.06}$	$2.71 \pm 0.21\ ^{+0.08}_{-0.14}$	$1.78 \pm 0.21\ ^{+0.06}_{-0.14}$	$2.15 \pm 0.27\ ^{+0.12}_{-0.14}$	$1.06 \pm 0.21\ ^{+0.15}_{-0.03}$
67.5	$3.26 \pm 0.20\ ^{+0.12}_{-0.06}$	$2.39 \pm 0.18\ ^{+0.10}_{-0.04}$	$1.84 \pm 0.18\ ^{+0.05}_{-0.06}$	$1.52 \pm 0.19\ ^{+0.05}_{-0.09}$	$1.02 \pm 0.16\ ^{+0.02}_{-0.09}$
82.5	$3.46 \pm 0.20\ ^{+0.08}_{-0.14}$	$2.30 \pm 0.17\ ^{+0.08}_{-0.08}$	$2.00 \pm 0.17\ ^{+0.04}_{-0.05}$	$1.40 \pm 0.17\ ^{+0.02}_{-0.05}$	$1.26 \pm 0.14\ ^{+0.07}_{-0.04}$
97.5	$3.02 \pm 0.20\ ^{+0.14}_{-0.11}$	$2.24 \pm 0.17\ ^{+0.12}_{-0.07}$	$1.66 \pm 0.16\ ^{+0.10}_{-0.04}$	$1.27 \pm 0.16\ ^{+0.06}_{-0.01}$	$1.25 \pm 0.13\ ^{+0.07}_{-0.04}$
112.5	$3.02 \pm 0.19\ ^{+0.14}_{-0.09}$	$2.30 \pm 0.17\ ^{+0.03}_{-0.06}$	$1.87 \pm 0.16\ ^{+0.00}_{-0.11}$	$1.65 \pm 0.16\ ^{+0.01}_{-0.04}$	$1.36 \pm 0.11\ ^{+0.05}_{-0.06}$
127.5	$3.07 \pm 0.19\ ^{+0.00}_{-0.14}$	$1.94 \pm 0.16\ ^{+0.02}_{-0.06}$	$1.77 \pm 0.16\ ^{+0.08}_{-0.02}$	$1.29 \pm 0.15\ ^{+0.11}_{-0.02}$	$1.27 \pm 0.11\ ^{+0.03}_{-0.01}$
142.5	$2.90 \pm 0.19\ ^{+0.03}_{-0.06}$	$2.15 \pm 0.16\ ^{+0.04}_{-0.06}$	$1.59 \pm 0.15\ ^{+0.05}_{-0.04}$	$1.86 \pm 0.17\ ^{+0.04}_{-0.10}$	$1.34 \pm 0.11\ ^{+0.04}_{-0.03}$
157.5	$2.79 \pm 0.19\ ^{+0.11}_{-0.09}$	$1.94 \pm 0.16\ ^{+0.01}_{-0.09}$	$1.87 \pm 0.16\ ^{+0.04}_{-0.05}$	$1.61 \pm 0.16\ ^{+0.04}_{-0.03}$	$1.67 \pm 0.13\ ^{+0.02}_{-0.04}$
172.5	$2.62 \pm 0.18\ ^{+0.07}_{-0.04}$	$1.90 \pm 0.16\ ^{+0.07}_{-0.08}$	$1.85 \pm 0.17\ ^{+0.11}_{-0.14}$	$1.81 \pm 0.17\ ^{+0.02}_{-0.07}$	$1.54 \pm 0.13\ ^{+0.06}_{-0.03}$
187.5	$2.92 \pm 0.19\ ^{+0.14}_{-0.11}$	$2.08 \pm 0.18\ ^{+0.14}_{-0.00}$	$2.14 \pm 0.18\ ^{+0.06}_{-0.01}$	$2.23 \pm 0.19\ ^{+0.08}_{-0.11}$	$1.46 \pm 0.13\ ^{+0.02}_{-0.12}$
202.5	$3.15 \pm 0.20\ ^{+0.09}_{-0.11}$	$2.50 \pm 0.19\ ^{+0.20}_{-0.08}$	$1.98 \pm 0.19\ ^{+0.08}_{-0.08}$	$2.12 \pm 0.19\ ^{+0.14}_{-0.04}$	$1.94 \pm 0.14\ ^{+0.03}_{-0.05}$
217.5	$2.59 \pm 0.19\ ^{+0.09}_{-0.06}$	$2.29 \pm 0.19\ ^{+0.02}_{-0.14}$	$1.96 \pm 0.19\ ^{+0.04}_{-0.09}$	$2.06 \pm 0.20\ ^{+0.11}_{-0.10}$	$1.86 \pm 0.14\ ^{+0.03}_{-0.11}$
232.5	$2.53 \pm 0.18\ ^{+0.05}_{-0.11}$	$2.48 \pm 0.18\ ^{+0.09}_{-0.10}$	$1.97 \pm 0.18\ ^{+0.12}_{-0.02}$	$2.08 \pm 0.19\ ^{+0.07}_{-0.07}$	$1.71 \pm 0.13\ ^{+0.10}_{-0.06}$
247.5	$3.00 \pm 0.20\ ^{+0.12}_{-0.08}$	$2.33 \pm 0.18\ ^{+0.01}_{-0.09}$	$2.05 \pm 0.18\ ^{+0.09}_{-0.04}$	$2.23 \pm 0.19\ ^{+0.08}_{-0.07}$	$1.61 \pm 0.13\ ^{+0.02}_{-0.05}$
262.5	$3.41 \pm 0.21\ ^{+0.13}_{-0.12}$	$2.84 \pm 0.19\ ^{+0.05}_{-0.16}$	$2.13 \pm 0.18\ ^{+0.13}_{-0.08}$	$2.18 \pm 0.19\ ^{+0.06}_{-0.10}$	$1.48 \pm 0.13\ ^{+0.04}_{-0.10}$
277.5	$3.27 \pm 0.20\ ^{+0.06}_{-0.09}$	$2.92 \pm 0.19\ ^{+0.03}_{-0.16}$	$2.28 \pm 0.18\ ^{+0.08}_{-0.06}$	$1.89 \pm 0.18\ ^{+0.09}_{-0.03}$	$1.78 \pm 0.15\ ^{+0.01}_{-0.07}$
292.5	$3.70 \pm 0.21\ ^{+0.11}_{-0.08}$	$3.03 \pm 0.20\ ^{+0.07}_{-0.13}$	$2.42 \pm 0.19\ ^{+0.08}_{-0.07}$	$1.91 \pm 0.20\ ^{+0.05}_{-0.04}$	$1.46 \pm 0.17\ ^{+0.06}_{-0.08}$
307.5	$2.96 \pm 0.19\ ^{+0.05}_{-0.10}$	$2.50 \pm 0.20\ ^{+0.07}_{-0.12}$	$2.44 \pm 0.22\ ^{+0.02}_{-0.18}$	$2.00 \pm 0.25\ ^{+0.06}_{-0.12}$	$1.79 \pm 0.24\ ^{+0.05}_{-0.09}$
322.5	$3.29 \pm 0.20\ ^{+0.13}_{-0.05}$	$2.96 \pm 0.24\ ^{+0.10}_{-0.06}$	$2.32 \pm 0.29\ ^{+0.04}_{-0.07}$	$1.74 \pm 0.34\ ^{+0.15}_{-0.10}$	$2.28 \pm 0.36\ ^{+0.15}_{-0.18}$
337.5	$3.35 \pm 0.22\ ^{+0.13}_{-0.08}$	$2.92 \pm 0.28\ ^{+0.11}_{-0.10}$	$2.19 \pm 0.37\ ^{+0.21}_{-0.19}$	$1.83 \pm 0.47\ ^{+0.26}_{-0.05}$	$2.09 \pm 0.59\ ^{+0.06}_{-0.25}$
352.5	$3.54 \pm 0.22\ ^{+0.15}_{-0.01}$	$2.74 \pm 0.30\ ^{+0.15}_{-0.02}$	$2.34 \pm 0.44\ ^{+0.10}_{-0.16}$	$1.31 \pm 0.59\ ^{+0.03}_{-0.10}$	$1.67 \pm 0.69\ ^{+0.27}_{-0.08}$

Table D.9: Unpolarized experimental cross section (pb) for kin482.

ϕ (deg)	$\langle x_{Bj}\rangle = 0.497$ $\langle Q^2\rangle = 4.497$ GeV^2 $\langle t'\rangle = -0.031$ GeV^2	$\langle x_{Bj}\rangle = 0.501$ $\langle Q^2\rangle = 4.528$ GeV^2 $\langle t'\rangle = -0.093$ GeV^2	$\langle x_{Bj}\rangle = 0.504$ $\langle Q^2\rangle = 4.558$ GeV^2 $\langle t'\rangle = -0.154$ GeV^2	$\langle x_{Bj}\rangle = 0.506$ $\langle Q^2\rangle = 4.573$ GeV^2 $\langle t'\rangle = -0.216$ GeV^2	$\langle x_{Bj}\rangle = 0.508$ $\langle Q^2\rangle = 4.593$ GeV^2 $\langle t'\rangle = -0.305$ GeV^2
7.5	0.02 ± 0.32 $^{+0.04}_{-0.24}$	0.35 ± 0.32 $^{+0.02}_{-0.06}$	0.41 ± 0.50 $^{+0.36}_{-0.11}$	0.44 ± 0.60 $^{+0.05}_{-0.13}$	-0.35 ± 0.81 $^{+0.27}_{-0.13}$
22.5	0.54 ± 0.31 $^{+0.12}_{-0.03}$	0.23 ± 0.28 $^{+0.05}_{-0.18}$	0.25 ± 0.45 $^{+0.07}_{-0.11}$	-0.24 ± 0.55 $^{+0.10}_{-0.15}$	1.06 ± 0.65 $^{+0.18}_{-0.04}$
37.5	0.15 ± 0.27 $^{+0.14}_{-0.17}$	0.21 ± 0.28 $^{+0.04}_{-0.17}$	0.80 ± 0.33 $^{+0.15}_{-0.11}$	0.48 ± 0.37 $^{+0.07}_{-0.12}$	0.92 ± 0.36 $^{+0.10}_{-0.21}$
52.5	-0.02 ± 0.26 $^{+0.15}_{-0.04}$	0.56 ± 0.24 $^{+0.05}_{-0.18}$	0.59 ± 0.26 $^{+0.07}_{-0.06}$	0.51 ± 0.29 $^{+0.09}_{-0.10}$	0.46 ± 0.23 $^{+0.09}_{-0.03}$
67.5	0.24 ± 0.24 $^{+0.08}_{-0.11}$	0.78 ± 0.22 $^{+0.01}_{-0.07}$	0.42 ± 0.22 $^{+0.09}_{-0.03}$	0.44 ± 0.22 $^{+0.07}_{-0.14}$	0.71 ± 0.19 $^{+0.05}_{-0.12}$
82.5	0.51 ± 0.25 $^{+0.07}_{-0.09}$	0.47 ± 0.21 $^{+0.10}_{-0.12}$	0.64 ± 0.21 $^{+0.08}_{-0.04}$	0.28 ± 0.20 $^{+0.07}_{-0.09}$	0.39 ± 0.16 $^{+0.04}_{-0.06}$
97.5	0.49 ± 0.24 $^{+0.10}_{-0.03}$	0.78 ± 0.19 $^{+0.06}_{-0.04}$	0.30 ± 0.18 $^{+0.10}_{-0.04}$	0.15 ± 0.18 $^{+0.09}_{-0.02}$	0.26 ± 0.15 $^{+0.01}_{-0.09}$
112.5	0.34 ± 0.22 $^{+0.08}_{-0.06}$	0.55 ± 0.20 $^{+0.12}_{-0.05}$	0.64 ± 0.18 $^{+0.01}_{-0.07}$	0.38 ± 0.17 $^{+0.05}_{-0.04}$	0.26 ± 0.13 $^{+0.02}_{-0.07}$
127.5	0.27 ± 0.23 $^{+0.22}_{-0.06}$	0.47 ± 0.19 $^{+0.02}_{-0.08}$	0.56 ± 0.17 $^{+0.02}_{-0.07}$	0.33 ± 0.16 $^{+0.09}_{-0.10}$	0.24 ± 0.12 $^{+0.01}_{-0.06}$
142.5	0.17 ± 0.22 $^{+0.05}_{-0.13}$	0.54 ± 0.19 $^{+0.03}_{-0.07}$	0.23 ± 0.16 $^{+0.04}_{-0.01}$	0.27 ± 0.18 $^{+0.01}_{-0.12}$	0.28 ± 0.12 $^{+0.01}_{-0.03}$
157.5	-0.17 ± 0.22 $^{+0.05}_{-0.05}$	0.67 ± 0.19 $^{+0.04}_{-0.10}$	0.60 ± 0.17 $^{+0.11}_{-0.03}$	0.06 ± 0.17 $^{+0.14}_{-0.06}$	0.22 ± 0.14 $^{+0.08}_{-0.12}$
172.5	-0.30 ± 0.23 $^{+0.12}_{-0.04}$	0.12 ± 0.20 $^{+0.11}_{-0.03}$	0.23 ± 0.17 $^{+0.10}_{-0.15}$	-0.28 ± 0.19 $^{+0.06}_{-0.02}$	0.11 ± 0.15 $^{+0.01}_{-0.09}$
187.5	-0.08 ± 0.20 $^{+0.10}_{-0.07}$	0.39 ± 0.18 $^{+0.06}_{-0.05}$	0.27 ± 0.18 $^{+0.06}_{-0.02}$	0.12 ± 0.20 $^{+0.03}_{-0.10}$	-0.17 ± 0.14 $^{+0.04}_{-0.05}$
202.5	-0.18 ± 0.22 $^{+0.08}_{-0.08}$	-0.30 ± 0.21 $^{+0.07}_{-0.03}$	-0.07 ± 0.19 $^{+0.08}_{-0.10}$	-0.03 ± 0.20 $^{+0.00}_{-0.15}$	-0.25 ± 0.15 $^{+0.09}_{-0.04}$
217.5	0.00 ± 0.21 $^{+0.05}_{-0.09}$	-0.57 ± 0.21 $^{+0.07}_{-0.03}$	-0.08 ± 0.20 $^{+0.06}_{-0.08}$	0.02 ± 0.21 $^{+0.04}_{-0.07}$	-0.31 ± 0.16 $^{+0.07}_{-0.16}$
232.5	-0.39 ± 0.21 $^{+0.07}_{-0.03}$	-0.22 ± 0.20 $^{+0.14}_{-0.07}$	-0.39 ± 0.20 $^{+0.07}_{-0.04}$	-0.69 ± 0.21 $^{+0.03}_{-0.11}$	-0.48 ± 0.15 $^{+0.07}_{-0.01}$
247.5	-0.47 ± 0.23 $^{+0.07}_{-0.08}$	-0.07 ± 0.21 $^{+0.04}_{-0.08}$	-0.18 ± 0.20 $^{+0.05}_{-0.08}$	-0.64 ± 0.20 $^{+0.06}_{-0.00}$	-0.49 ± 0.14 $^{+0.04}_{-0.02}$
262.5	-0.74 ± 0.24 $^{+0.04}_{-0.09}$	-0.26 ± 0.22 $^{+0.06}_{-0.11}$	-0.39 ± 0.21 $^{+0.07}_{-0.07}$	-0.52 ± 0.21 $^{+0.04}_{-0.07}$	-0.39 ± 0.15 $^{+0.01}_{-0.03}$
277.5	-0.60 ± 0.24 $^{+0.05}_{-0.13}$	-0.51 ± 0.22 $^{+0.01}_{-0.09}$	-0.65 ± 0.22 $^{+0.03}_{-0.05}$	-0.60 ± 0.21 $^{+0.04}_{-0.07}$	-0.48 ± 0.17 $^{+0.09}_{-0.01}$
292.5	-0.55 ± 0.25 $^{+0.08}_{-0.08}$	-0.60 ± 0.23 $^{+0.12}_{-0.02}$	-0.98 ± 0.23 $^{+0.09}_{-0.05}$	-0.24 ± 0.23 $^{+0.00}_{-0.09}$	-0.12 ± 0.20 $^{+0.05}_{-0.07}$
307.5	-0.42 ± 0.24 $^{+0.11}_{-0.06}$	-0.46 ± 0.23 $^{+0.03}_{-0.14}$	-0.70 ± 0.27 $^{+0.10}_{-0.12}$	-0.98 ± 0.28 $^{+0.10}_{-0.01}$	-0.52 ± 0.27 $^{+0.09}_{-0.08}$
322.5	-0.63 ± 0.25 $^{+0.11}_{-0.03}$	-0.37 ± 0.26 $^{+0.06}_{-0.05}$	-1.08 ± 0.34 $^{+0.07}_{-0.13}$	-0.73 ± 0.36 $^{+0.10}_{-0.11}$	0.05 ± 0.37 $^{+0.06}_{-0.19}$
337.5	0.08 ± 0.26 $^{+0.03}_{-0.06}$	-0.45 ± 0.28 $^{+0.14}_{-0.08}$	-0.59 ± 0.41 $^{+0.04}_{-0.38}$	0.10 ± 0.48 $^{+0.12}_{-0.14}$	0.01 ± 0.55 $^{+0.21}_{-0.21}$
352.5	-0.07 ± 0.26 $^{+0.02}_{-0.09}$	-0.07 ± 0.29 $^{+0.03}_{-0.12}$	-0.91 ± 0.46 $^{+0.18}_{-0.27}$	0.06 ± 0.60 $^{+0.20}_{-0.14}$	0.49 ± 0.67 $^{+0.17}_{-0.01}$

Table D.10: Helicity-dependent experimental cross section (pb) for kin482.

ϕ (deg)	$\langle x_{Bj}\rangle = 0.482$ $\langle Q^2\rangle = 5.331$ GeV^2 $\langle t'\rangle = -0.030$ GeV^2	$\langle x_{Bj}\rangle = 0.483$ $\langle Q^2\rangle = 5.339$ GeV^2 $\langle t'\rangle = -0.088$ GeV^2	$\langle x_{Bj}\rangle = 0.485$ $\langle Q^2\rangle = 5.360$ GeV^2 $\langle t'\rangle = -0.147$ GeV^2	$\langle x_{Bj}\rangle = 0.486$ $\langle Q^2\rangle = 5.371$ GeV^2 $\langle t'\rangle = -0.206$ GeV^2	$\langle x_{Bj}\rangle = 0.486$ $\langle Q^2\rangle = 5.379$ GeV^2 $\langle t'\rangle = -0.291$ GeV^2
7.5	$4.23 \pm 0.29\ ^{+0.29}_{-0.07}$	$4.47 \pm 0.37\ ^{+0.11}_{-0.25}$	$3.76 \pm 0.57\ ^{+0.24}_{-0.28}$	$3.35 \pm 1.11\ ^{+0.41}_{-0.20}$	$3.65 \pm 3.04\ ^{+0.49}_{-0.29}$
22.5	$3.98 \pm 0.29\ ^{+0.10}_{-0.04}$	$3.94 \pm 0.33\ ^{+0.19}_{-0.06}$	$2.90 \pm 0.44\ ^{+0.15}_{-0.02}$	$2.05 \pm 0.62\ ^{+0.06}_{-0.26}$	$1.37 \pm 1.10\ ^{+0.51}_{-0.15}$
37.5	$3.66 \pm 0.26\ ^{+0.09}_{-0.11}$	$3.54 \pm 0.29\ ^{+0.08}_{-0.02}$	$3.03 \pm 0.32\ ^{+0.15}_{-0.15}$	$2.70 \pm 0.43\ ^{+0.08}_{-0.13}$	$1.20 \pm 0.43\ ^{+0.12}_{-0.38}$
52.5	$4.10 \pm 0.28\ ^{+0.07}_{-0.17}$	$3.00 \pm 0.24\ ^{+0.13}_{-0.13}$	$2.64 \pm 0.25\ ^{+0.16}_{-0.05}$	$2.47 \pm 0.29\ ^{+0.00}_{-0.17}$	$1.56 \pm 0.26\ ^{+0.10}_{-0.03}$
67.5	$3.09 \pm 0.25\ ^{+0.24}_{-0.13}$	$2.76 \pm 0.23\ ^{+0.09}_{-0.09}$	$2.43 \pm 0.23\ ^{+0.09}_{-0.06}$	$2.03 \pm 0.23\ ^{+0.02}_{-0.10}$	$1.48 \pm 0.19\ ^{+0.09}_{-0.04}$
82.5	$3.35 \pm 0.25\ ^{+0.11}_{-0.07}$	$2.48 \pm 0.23\ ^{+0.14}_{-0.05}$	$1.86 \pm 0.20\ ^{+0.07}_{-0.07}$	$1.82 \pm 0.20\ ^{+0.10}_{-0.06}$	$1.62 \pm 0.17\ ^{+0.03}_{-0.11}$
97.5	$2.88 \pm 0.24\ ^{+0.17}_{-0.09}$	$2.36 \pm 0.21\ ^{+0.05}_{-0.07}$	$2.15 \pm 0.21\ ^{+0.05}_{-0.05}$	$1.62 \pm 0.19\ ^{+0.12}_{-0.08}$	$1.17 \pm 0.15\ ^{+0.07}_{-0.02}$
112.5	$3.13 \pm 0.24\ ^{+0.03}_{-0.14}$	$1.96 \pm 0.19\ ^{+0.08}_{-0.06}$	$1.89 \pm 0.19\ ^{+0.02}_{-0.07}$	$1.39 \pm 0.18\ ^{+0.14}_{-0.04}$	$1.13 \pm 0.13\ ^{+0.03}_{-0.02}$
127.5	$2.93 \pm 0.22\ ^{+0.06}_{-0.04}$	$1.86 \pm 0.18\ ^{+0.12}_{-0.03}$	$1.42 \pm 0.17\ ^{+0.06}_{-0.10}$	$1.98 \pm 0.19\ ^{+0.07}_{-0.09}$	$1.08 \pm 0.11\ ^{+0.02}_{-0.04}$
142.5	$2.71 \pm 0.22\ ^{+0.03}_{-0.12}$	$1.97 \pm 0.19\ ^{+0.13}_{-0.02}$	$1.54 \pm 0.17\ ^{+0.06}_{-0.03}$	$1.44 \pm 0.17\ ^{+0.03}_{-0.01}$	$0.91 \pm 0.10\ ^{+0.04}_{-0.00}$
157.5	$2.68 \pm 0.22\ ^{+0.12}_{-0.12}$	$1.81 \pm 0.18\ ^{+0.11}_{-0.00}$	$1.78 \pm 0.18\ ^{+0.13}_{-0.08}$	$1.47 \pm 0.17\ ^{+0.04}_{-0.02}$	$1.14 \pm 0.12\ ^{+0.00}_{-0.07}$
172.5	$2.44 \pm 0.22\ ^{+0.07}_{-0.08}$	$2.18 \pm 0.20\ ^{+0.05}_{-0.12}$	$1.64 \pm 0.18\ ^{+0.08}_{-0.05}$	$1.61 \pm 0.19\ ^{+0.09}_{-0.05}$	$1.08 \pm 0.13\ ^{+0.06}_{-0.05}$
187.5	$2.59 \pm 0.22\ ^{+0.13}_{-0.02}$	$2.05 \pm 0.19\ ^{+0.05}_{-0.08}$	$1.75 \pm 0.19\ ^{+0.04}_{-0.09}$	$1.33 \pm 0.18\ ^{+0.22}_{-0.04}$	$1.06 \pm 0.12\ ^{+0.03}_{-0.04}$
202.5	$2.73 \pm 0.22\ ^{+0.14}_{-0.08}$	$2.21 \pm 0.20\ ^{+0.21}_{-0.08}$	$1.80 \pm 0.19\ ^{+0.04}_{-0.08}$	$1.27 \pm 0.18\ ^{+0.18}_{-0.07}$	$1.25 \pm 0.12\ ^{+0.01}_{-0.05}$
217.5	$2.63 \pm 0.21\ ^{+0.10}_{-0.04}$	$1.86 \pm 0.19\ ^{+0.09}_{-0.04}$	$1.51 \pm 0.19\ ^{+0.06}_{-0.03}$	$1.51 \pm 0.18\ ^{+0.09}_{-0.07}$	$0.86 \pm 0.11\ ^{+0.04}_{-0.04}$
232.5	$2.92 \pm 0.23\ ^{+0.12}_{-0.07}$	$2.31 \pm 0.22\ ^{+0.03}_{-0.14}$	$1.87 \pm 0.21\ ^{+0.07}_{-0.15}$	$1.61 \pm 0.19\ ^{+0.10}_{-0.02}$	$1.16 \pm 0.12\ ^{+0.02}_{-0.09}$
247.5	$2.92 \pm 0.23\ ^{+0.14}_{-0.05}$	$2.61 \pm 0.22\ ^{+0.06}_{-0.05}$	$1.80 \pm 0.20\ ^{+0.03}_{-0.06}$	$1.49 \pm 0.19\ ^{+0.05}_{-0.05}$	$1.46 \pm 0.14\ ^{+0.04}_{-0.05}$
262.5	$3.77 \pm 0.26\ ^{+0.03}_{-0.14}$	$2.57 \pm 0.22\ ^{+0.07}_{-0.09}$	$2.37 \pm 0.22\ ^{+0.05}_{-0.07}$	$1.79 \pm 0.20\ ^{+0.05}_{-0.09}$	$1.50 \pm 0.15\ ^{+0.06}_{-0.06}$
277.5	$3.62 \pm 0.27\ ^{+0.06}_{-0.13}$	$2.63 \pm 0.24\ ^{+0.16}_{-0.02}$	$2.51 \pm 0.24\ ^{+0.22}_{-0.09}$	$1.74 \pm 0.21\ ^{+0.04}_{-0.07}$	$1.84 \pm 0.17\ ^{+0.00}_{-0.09}$
292.5	$3.67 \pm 0.26\ ^{+0.10}_{-0.06}$	$3.29 \pm 0.25\ ^{+0.22}_{-0.11}$	$2.92 \pm 0.25\ ^{+0.05}_{-0.12}$	$2.47 \pm 0.25\ ^{+0.02}_{-0.10}$	$2.31 \pm 0.21\ ^{+0.05}_{-0.12}$
307.5	$3.65 \pm 0.26\ ^{+0.12}_{-0.13}$	$3.42 \pm 0.27\ ^{+0.15}_{-0.14}$	$2.96 \pm 0.27\ ^{+0.11}_{-0.03}$	$2.57 \pm 0.30\ ^{+0.13}_{-0.14}$	$2.10 \pm 0.27\ ^{+0.05}_{-0.09}$
322.5	$4.27 \pm 0.29\ ^{+0.11}_{-0.17}$	$3.75 \pm 0.29\ ^{+0.11}_{-0.06}$	$3.31 \pm 0.36\ ^{+0.11}_{-0.14}$	$2.84 \pm 0.46\ ^{+0.19}_{-0.11}$	$3.71 \pm 0.58\ ^{+0.16}_{-0.20}$
337.5	$4.19 \pm 0.28\ ^{+0.04}_{-0.08}$	$4.00 \pm 0.33\ ^{+0.08}_{-0.14}$	$3.28 \pm 0.44\ ^{+0.30}_{-0.08}$	$3.96 \pm 0.81\ ^{+0.31}_{-0.30}$	$2.05 \pm 1.33\ ^{+0.00}_{-0.50}$
352.5	$4.24 \pm 0.29\ ^{+0.12}_{-0.08}$	$4.13 \pm 0.36\ ^{+0.25}_{-0.05}$	$3.76 \pm 0.58\ ^{+0.19}_{-0.21}$	$2.91 \pm 1.16\ ^{+0.26}_{-0.27}$	$0.90 \pm 1.72\ ^{+0.95}_{-0.16}$

Table D.11: Unpolarized experimental cross section (pb) for kin483.

ϕ (deg)	$\langle x_{Bj}\rangle = 0.482$ $\langle Q^2\rangle = 5.331$ GeV^2 $\langle t'\rangle = -0.030$ GeV^2	$\langle x_{Bj}\rangle = 0.483$ $\langle Q^2\rangle = 5.339$ GeV^2 $\langle t'\rangle = -0.088$ GeV^2	$\langle x_{Bj}\rangle = 0.485$ $\langle Q^2\rangle = 5.360$ GeV^2 $\langle t'\rangle = -0.147$ GeV^2	$\langle x_{Bj}\rangle = 0.486$ $\langle Q^2\rangle = 5.371$ GeV^2 $\langle t'\rangle = -0.206$ GeV^2	$\langle x_{Bj}\rangle = 0.486$ $\langle Q^2\rangle = 5.379$ GeV^2 $\langle t'\rangle = -0.291$ GeV^2
7.5	-0.40 ± 0.38 $^{+0.14}_{-0.07}$	0.18 ± 0.22 $^{+0.18}_{-0.01}$	-0.06 ± 0.62 $^{+0.33}_{-0.21}$	0.13 ± 0.89 $^{+0.17}_{-0.24}$	1.63 ± 2.22 $^{+0.26}_{-0.89}$
22.5	0.39 ± 0.36 $^{+0.14}_{-0.02}$	0.27 ± 0.23 $^{+0.24}_{-0.07}$	0.60 ± 0.49 $^{+0.06}_{-0.16}$	-0.16 ± 0.57 $^{+0.14}_{-0.24}$	0.12 ± 0.88 $^{+0.21}_{-0.64}$
37.5	0.94 ± 0.33 $^{+0.16}_{-0.16}$	0.92 ± 0.24 $^{+0.14}_{-0.07}$	0.39 ± 0.39 $^{+0.17}_{-0.13}$	0.91 ± 0.42 $^{+0.07}_{-0.30}$	0.94 ± 0.42 $^{+0.02}_{-0.17}$
52.5	0.33 ± 0.35 $^{+0.04}_{-0.13}$	-0.06 ± 0.23 $^{+0.05}_{-0.08}$	1.29 ± 0.31 $^{+0.04}_{-0.09}$	0.81 ± 0.32 $^{+0.00}_{-0.18}$	0.13 ± 0.29 $^{+0.10}_{-0.07}$
67.5	0.38 ± 0.30 $^{+0.28}_{-0.07}$	0.37 ± 0.25 $^{+0.05}_{-0.06}$	1.25 ± 0.27 $^{+0.08}_{-0.05}$	1.15 ± 0.26 $^{+0.04}_{-0.09}$	0.82 ± 0.21 $^{+0.08}_{-0.11}$
82.5	0.45 ± 0.30 $^{+0.10}_{-0.03}$	0.51 ± 0.26 $^{+0.04}_{-0.16}$	0.08 ± 0.24 $^{+0.09}_{-0.07}$	0.24 ± 0.24 $^{+0.10}_{-0.07}$	0.22 ± 0.18 $^{+0.10}_{-0.05}$
97.5	0.47 ± 0.28 $^{+0.11}_{-0.08}$	0.35 ± 0.25 $^{+0.05}_{-0.13}$	0.37 ± 0.24 $^{+0.14}_{-0.06}$	0.21 ± 0.22 $^{+0.10}_{-0.03}$	0.36 ± 0.16 $^{+0.12}_{-0.00}$
112.5	0.20 ± 0.29 $^{+0.13}_{-0.03}$	0.98 ± 0.23 $^{+0.13}_{-0.14}$	0.45 ± 0.22 $^{+0.06}_{-0.05}$	0.35 ± 0.21 $^{+0.04}_{-0.06}$	0.02 ± 0.14 $^{+0.08}_{-0.08}$
127.5	0.57 ± 0.27 $^{+0.06}_{-0.06}$	0.31 ± 0.23 $^{+0.09}_{-0.06}$	-0.04 ± 0.18 $^{+0.08}_{-0.05}$	0.51 ± 0.22 $^{+0.05}_{-0.07}$	0.12 ± 0.12 $^{+0.05}_{-0.05}$
142.5	0.39 ± 0.26 $^{+0.06}_{-0.11}$	0.29 ± 0.23 $^{+0.08}_{-0.07}$	0.19 ± 0.17 $^{+0.17}_{-0.03}$	0.26 ± 0.20 $^{+0.02}_{-0.03}$	0.16 ± 0.10 $^{+0.01}_{-0.04}$
157.5	0.12 ± 0.27 $^{+0.05}_{-0.20}$	0.38 ± 0.22 $^{+0.11}_{-0.04}$	0.04 ± 0.17 $^{+0.07}_{-0.01}$	-0.09 ± 0.20 $^{+0.05}_{-0.07}$	-0.07 ± 0.11 $^{+0.06}_{-0.04}$
172.5	-0.14 ± 0.27 $^{+0.06}_{-0.08}$	0.08 ± 0.25 $^{+0.06}_{-0.06}$	0.21 ± 0.16 $^{+0.06}_{-0.02}$	0.14 ± 0.22 $^{+0.02}_{-0.12}$	-0.02 ± 0.12 $^{+0.08}_{-0.01}$
187.5	0.40 ± 0.25 $^{+0.04}_{-0.16}$	-0.14 ± 0.24 $^{+0.10}_{-0.07}$	-0.34 ± 0.17 $^{+0.02}_{-0.08}$	0.23 ± 0.22 $^{+0.07}_{-0.03}$	-0.16 ± 0.11 $^{+0.09}_{-0.02}$
202.5	-0.22 ± 0.26 $^{+0.07}_{-0.04}$	-0.22 ± 0.25 $^{+0.11}_{-0.09}$	-0.09 ± 0.17 $^{+0.04}_{-0.05}$	-0.51 ± 0.20 $^{+0.14}_{-0.05}$	-0.02 ± 0.12 $^{+0.03}_{-0.06}$
217.5	-0.11 ± 0.25 $^{+0.08}_{-0.06}$	-0.53 ± 0.22 $^{+0.11}_{-0.04}$	-0.13 ± 0.18 $^{+0.07}_{-0.03}$	-0.56 ± 0.21 $^{+0.07}_{-0.12}$	0.01 ± 0.10 $^{+0.03}_{-0.10}$
232.5	-0.12 ± 0.27 $^{+0.05}_{-0.10}$	-0.01 ± 0.26 $^{+0.04}_{-0.07}$	-0.60 ± 0.21 $^{+0.03}_{-0.12}$	-0.31 ± 0.23 $^{+0.04}_{-0.17}$	0.03 ± 0.13 $^{+0.05}_{-0.06}$
247.5	-0.54 ± 0.28 $^{+0.05}_{-0.05}$	-0.82 ± 0.27 $^{+0.08}_{-0.10}$	-0.36 ± 0.22 $^{+0.07}_{-0.05}$	-0.27 ± 0.22 $^{+0.01}_{-0.14}$	-0.38 ± 0.15 $^{+0.04}_{-0.04}$
262.5	-0.29 ± 0.31 $^{+0.08}_{-0.01}$	-0.35 ± 0.26 $^{+0.06}_{-0.11}$	-0.48 ± 0.26 $^{+0.13}_{-0.11}$	-0.60 ± 0.24 $^{+0.09}_{-0.05}$	-0.37 ± 0.17 $^{+0.02}_{-0.04}$
277.5	-0.24 ± 0.32 $^{+0.11}_{-0.08}$	-0.25 ± 0.27 $^{+0.06}_{-0.12}$	-0.72 ± 0.29 $^{+0.09}_{-0.27}$	-0.02 ± 0.25 $^{+0.01}_{-0.15}$	-0.65 ± 0.19 $^{+0.05}_{-0.05}$
292.5	-0.84 ± 0.32 $^{+0.09}_{-0.11}$	-0.33 ± 0.27 $^{+0.07}_{-0.11}$	-0.94 ± 0.30 $^{+0.09}_{-0.07}$	-0.38 ± 0.29 $^{+0.09}_{-0.07}$	-0.42 ± 0.24 $^{+0.03}_{-0.09}$
307.5	-0.08 ± 0.34 $^{+0.07}_{-0.13}$	0.23 ± 0.26 $^{+0.08}_{-0.26}$	-1.44 ± 0.34 $^{+0.06}_{-0.09}$	-0.75 ± 0.32 $^{+0.16}_{-0.06}$	-0.64 ± 0.31 $^{+0.12}_{-0.04}$
322.5	0.08 ± 0.35 $^{+0.10}_{-0.08}$	-0.33 ± 0.24 $^{+0.03}_{-0.19}$	-0.73 ± 0.43 $^{+0.08}_{-0.10}$	-0.65 ± 0.44 $^{+0.19}_{-0.23}$	0.49 ± 0.55 $^{+0.17}_{-0.08}$
337.5	-0.27 ± 0.35 $^{+0.13}_{-0.09}$	-0.28 ± 0.22 $^{+0.07}_{-0.11}$	0.33 ± 0.51 $^{+0.16}_{-0.14}$	0.54 ± 0.74 $^{+0.38}_{-0.30}$	0.30 ± 1.05 $^{+0.60}_{-0.01}$
352.5	-0.11 ± 0.34 $^{+0.22}_{-0.12}$	0.13 ± 0.21 $^{+0.09}_{-0.23}$	-0.08 ± 0.60 $^{+0.06}_{-0.09}$	-0.71 ± 0.88 $^{+0.56}_{-0.12}$	0.86 ± 1.32 $^{+0.12}_{-0.82}$

Table D.12: Helicity-dependent experimental cross section (pb) for kin483.

ϕ (deg)	$\langle x_{Bj}\rangle = 0.494$ $\langle Q^2\rangle = 7.044$ GeV^2 $\langle t'\rangle = -0.043$ GeV^2	$\langle x_{Bj}\rangle = 0.498$ $\langle Q^2\rangle = 7.093$ GeV^2 $\langle t'\rangle = -0.127$ GeV^2	$\langle x_{Bj}\rangle = 0.499$ $\langle Q^2\rangle = 7.115$ GeV^2 $\langle t'\rangle = -0.212$ GeV^2	$\langle x_{Bj}\rangle = 0.499$ $\langle Q^2\rangle = 7.106$ GeV^2 $\langle t'\rangle = -0.297$ GeV^2	$\langle x_{Bj}\rangle = 0.498$ $\langle Q^2\rangle = 7.102$ GeV^2 $\langle t'\rangle = -0.457$ GeV^2
7.5	$1.76 \pm 0.10\ ^{+0.08}_{-0.00}$	$1.87 \pm 0.19\ ^{+0.19}_{-0.00}$	$1.94 \pm 0.39\ ^{+0.09}_{-0.19}$	$2.40 \pm 1.00\ ^{+0.20}_{-0.32}$	$5.39 \pm 5.49\ ^{+1.51}_{-1.63}$
22.5	$1.95 \pm 0.11\ ^{+0.05}_{-0.12}$	$1.52 \pm 0.15\ ^{+0.04}_{-0.05}$	$1.34 \pm 0.27\ ^{+0.09}_{-0.11}$	$1.47 \pm 0.55\ ^{+0.11}_{-0.13}$	$1.03 \pm 1.39\ ^{+0.44}_{-0.11}$
37.5	$1.71 \pm 0.10\ ^{+0.03}_{-0.07}$	$1.47 \pm 0.12\ ^{+0.03}_{-0.04}$	$0.92 \pm 0.16\ ^{+0.07}_{-0.03}$	$0.93 \pm 0.27\ ^{+0.07}_{-0.18}$	$0.69 \pm 0.29\ ^{+0.02}_{-0.19}$
52.5	$1.59 \pm 0.09\ ^{+0.06}_{-0.02}$	$1.45 \pm 0.10\ ^{+0.00}_{-0.07}$	$1.15 \pm 0.11\ ^{+0.02}_{-0.05}$	$0.74 \pm 0.12\ ^{+0.04}_{-0.07}$	$0.52 \pm 0.10\ ^{+0.05}_{-0.04}$
67.5	$1.42 \pm 0.08\ ^{+0.06}_{-0.03}$	$1.20 \pm 0.08\ ^{+0.05}_{-0.04}$	$0.91 \pm 0.07\ ^{+0.03}_{-0.04}$	$0.74 \pm 0.07\ ^{+0.04}_{-0.01}$	$0.57 \pm 0.05\ ^{+0.01}_{-0.02}$
82.5	$1.40 \pm 0.08\ ^{+0.05}_{-0.02}$	$1.16 \pm 0.07\ ^{+0.04}_{-0.03}$	$0.86 \pm 0.07\ ^{+0.03}_{-0.03}$	$0.70 \pm 0.07\ ^{+0.01}_{-0.03}$	$0.53 \pm 0.04\ ^{+0.00}_{-0.01}$
97.5	$1.34 \pm 0.08\ ^{+0.05}_{-0.07}$	$0.98 \pm 0.07\ ^{+0.02}_{-0.03}$	$0.73 \pm 0.06\ ^{+0.03}_{-0.01}$	$0.71 \pm 0.06\ ^{+0.01}_{-0.05}$	$0.42 \pm 0.03\ ^{+0.02}_{-0.02}$
112.5	$1.22 \pm 0.07\ ^{+0.03}_{-0.05}$	$1.02 \pm 0.07\ ^{+0.04}_{-0.01}$	$0.63 \pm 0.06\ ^{+0.02}_{-0.03}$	$0.57 \pm 0.06\ ^{+0.01}_{-0.03}$	$0.32 \pm 0.03\ ^{+0.01}_{-0.02}$
127.5	$1.29 \pm 0.08\ ^{+0.09}_{-0.03}$	$0.91 \pm 0.07\ ^{+0.04}_{-0.00}$	$0.58 \pm 0.05\ ^{+0.01}_{-0.03}$	$0.53 \pm 0.05\ ^{+0.00}_{-0.03}$	$0.29 \pm 0.02\ ^{+0.01}_{-0.01}$
142.5	$1.38 \pm 0.08\ ^{+0.02}_{-0.05}$	$0.89 \pm 0.07\ ^{+0.03}_{-0.07}$	$0.63 \pm 0.06\ ^{+0.02}_{-0.04}$	$0.43 \pm 0.05\ ^{+0.01}_{-0.05}$	$0.32 \pm 0.03\ ^{+0.01}_{-0.01}$
157.5	$1.14 \pm 0.07\ ^{+0.05}_{-0.00}$	$0.80 \pm 0.06\ ^{+0.02}_{-0.02}$	$0.60 \pm 0.06\ ^{+0.03}_{-0.02}$	$0.46 \pm 0.05\ ^{+0.02}_{-0.01}$	$0.32 \pm 0.03\ ^{+0.01}_{-0.01}$
172.5	$1.21 \pm 0.08\ ^{+0.03}_{-0.02}$	$0.83 \pm 0.06\ ^{+0.05}_{-0.02}$	$0.61 \pm 0.05\ ^{+0.02}_{-0.03}$	$0.46 \pm 0.05\ ^{+0.01}_{-0.02}$	$0.35 \pm 0.03\ ^{+0.01}_{-0.01}$
187.5	$1.21 \pm 0.08\ ^{+0.04}_{-0.02}$	$0.80 \pm 0.06\ ^{+0.02}_{-0.02}$	$0.60 \pm 0.06\ ^{+0.01}_{-0.02}$	$0.46 \pm 0.05\ ^{+0.03}_{-0.01}$	$0.36 \pm 0.03\ ^{+0.00}_{-0.02}$
202.5	$1.32 \pm 0.08\ ^{+0.05}_{-0.05}$	$0.86 \pm 0.07\ ^{+0.02}_{-0.04}$	$0.71 \pm 0.06\ ^{+0.01}_{-0.00}$	$0.46 \pm 0.06\ ^{+0.01}_{-0.02}$	$0.38 \pm 0.03\ ^{+0.01}_{-0.01}$
217.5	$1.25 \pm 0.08\ ^{+0.05}_{-0.00}$	$0.94 \pm 0.07\ ^{+0.04}_{-0.00}$	$0.60 \pm 0.06\ ^{+0.03}_{-0.04}$	$0.53 \pm 0.06\ ^{+0.01}_{-0.04}$	$0.35 \pm 0.03\ ^{+0.01}_{-0.01}$
232.5	$1.36 \pm 0.08\ ^{+0.05}_{-0.05}$	$0.88 \pm 0.07\ ^{+0.02}_{-0.02}$	$0.73 \pm 0.06\ ^{+0.01}_{-0.03}$	$0.64 \pm 0.06\ ^{+0.03}_{-0.03}$	$0.41 \pm 0.03\ ^{+0.01}_{-0.01}$
247.5	$1.30 \pm 0.08\ ^{+0.01}_{-0.05}$	$1.07 \pm 0.07\ ^{+0.03}_{-0.02}$	$0.72 \pm 0.06\ ^{+0.05}_{-0.02}$	$0.60 \pm 0.06\ ^{+0.01}_{-0.02}$	$0.45 \pm 0.03\ ^{+0.01}_{-0.01}$
262.5	$1.38 \pm 0.08\ ^{+0.05}_{-0.04}$	$1.03 \pm 0.07\ ^{+0.02}_{-0.02}$	$0.82 \pm 0.07\ ^{+0.04}_{-0.02}$	$0.75 \pm 0.07\ ^{+0.03}_{-0.03}$	$0.53 \pm 0.04\ ^{+0.01}_{-0.03}$
277.5	$1.62 \pm 0.09\ ^{+0.07}_{-0.03}$	$1.17 \pm 0.08\ ^{+0.05}_{-0.04}$	$0.90 \pm 0.07\ ^{+0.02}_{-0.04}$	$0.68 \pm 0.07\ ^{+0.01}_{-0.03}$	$0.50 \pm 0.04\ ^{+0.02}_{-0.01}$
292.5	$1.62 \pm 0.09\ ^{+0.05}_{-0.07}$	$1.20 \pm 0.08\ ^{+0.03}_{-0.03}$	$0.88 \pm 0.08\ ^{+0.01}_{-0.04}$	$0.85 \pm 0.08\ ^{+0.04}_{-0.03}$	$0.55 \pm 0.05\ ^{+0.03}_{-0.03}$
307.5	$1.73 \pm 0.09\ ^{+0.09}_{-0.05}$	$1.53 \pm 0.10\ ^{+0.03}_{-0.06}$	$1.32 \pm 0.11\ ^{+0.08}_{-0.03}$	$1.06 \pm 0.13\ ^{+0.07}_{-0.02}$	$0.62 \pm 0.10\ ^{+0.02}_{-0.02}$
322.5	$1.89 \pm 0.10\ ^{+0.07}_{-0.07}$	$1.59 \pm 0.12\ ^{+0.05}_{-0.08}$	$1.19 \pm 0.16\ ^{+0.08}_{-0.03}$	$1.25 \pm 0.24\ ^{+0.11}_{-0.11}$	$0.52 \pm 0.25\ ^{+0.07}_{-0.07}$
337.5	$1.92 \pm 0.10\ ^{+0.01}_{-0.10}$	$2.04 \pm 0.16\ ^{+0.14}_{-0.03}$	$1.13 \pm 0.24\ ^{+0.09}_{-0.00}$	$0.77 \pm 0.40\ ^{+0.12}_{-0.08}$	$1.05 \pm 1.32\ ^{+0.24}_{-0.18}$
352.5	$2.12 \pm 0.11\ ^{+0.08}_{-0.03}$	$1.89 \pm 0.19\ ^{+0.08}_{-0.02}$	$1.80 \pm 0.39\ ^{+0.13}_{-0.15}$	$0.87 \pm 0.64\ ^{+0.16}_{-0.16}$	$-0.11 \pm 0.67\ ^{+0.02}_{-0.03}$

Table D.13: Unpolarized experimental cross section (pb) for kin484.

ϕ (deg)	$\langle x_{Bj}\rangle = 0.494$ $\langle Q^2\rangle = 7.044$ GeV^2 $\langle t'\rangle = -0.043$ GeV^2	$\langle x_{Bj}\rangle = 0.498$ $\langle Q^2\rangle = 7.093$ GeV^2 $\langle t'\rangle = -0.127$ GeV^2	$\langle x_{Bj}\rangle = 0.499$ $\langle Q^2\rangle = 7.115$ GeV^2 $\langle t'\rangle = -0.212$ GeV^2	$\langle x_{Bj}\rangle = 0.499$ $\langle Q^2\rangle = 7.106$ GeV^2 $\langle t'\rangle = -0.297$ GeV^2	$\langle x_{Bj}\rangle = 0.498$ $\langle Q^2\rangle = 7.102$ GeV^2 $\langle t'\rangle = -0.457$ GeV^2
7.5	0.31 ± 0.14 $^{+0.07}_{-0.02}$	0.19 ± 0.20 $^{+0.14}_{-0.05}$	-0.06 ± 0.33 $^{+0.04}_{-0.08}$	-0.06 ± 0.65 $^{+0.12}_{-0.27}$	2.02 ± 1.89 $^{+0.97}_{-0.49}$
22.5	0.37 ± 0.14 $^{+0.11}_{-0.06}$	0.41 ± 0.16 $^{+0.03}_{-0.09}$	0.53 ± 0.24 $^{+0.09}_{-0.09}$	0.12 ± 0.41 $^{+0.12}_{-0.10}$	0.33 ± 0.80 $^{+0.03}_{-0.24}$
37.5	0.28 ± 0.13 $^{+0.03}_{-0.05}$	0.10 ± 0.14 $^{+0.03}_{-0.01}$	-0.01 ± 0.16 $^{+0.03}_{-0.03}$	0.20 ± 0.24 $^{+0.05}_{-0.02}$	-0.15 ± 0.23 $^{+0.08}_{-0.07}$
52.5	0.03 ± 0.12 $^{+0.03}_{-0.03}$	0.26 ± 0.12 $^{+0.06}_{-0.05}$	0.59 ± 0.12 $^{+0.06}_{-0.07}$	0.17 ± 0.12 $^{+0.04}_{-0.04}$	0.28 ± 0.10 $^{+0.03}_{-0.02}$
67.5	0.29 ± 0.11 $^{+0.02}_{-0.03}$	0.18 ± 0.10 $^{+0.06}_{-0.03}$	0.34 ± 0.09 $^{+0.03}_{-0.02}$	0.26 ± 0.09 $^{+0.02}_{-0.01}$	0.15 ± 0.06 $^{+0.03}_{-0.00}$
82.5	0.28 ± 0.11 $^{+0.05}_{-0.03}$	0.28 ± 0.09 $^{+0.07}_{-0.03}$	0.25 ± 0.08 $^{+0.04}_{-0.02}$	0.27 ± 0.08 $^{+0.02}_{-0.04}$	0.29 ± 0.05 $^{+0.00}_{-0.04}$
97.5	0.25 ± 0.10 $^{+0.02}_{-0.02}$	0.29 ± 0.08 $^{+0.03}_{-0.02}$	0.28 ± 0.08 $^{+0.01}_{-0.02}$	0.16 ± 0.08 $^{+0.02}_{-0.02}$	0.13 ± 0.04 $^{+0.02}_{-0.02}$
112.5	0.18 ± 0.10 $^{+0.03}_{-0.03}$	0.28 ± 0.08 $^{+0.03}_{-0.01}$	0.05 ± 0.07 $^{+0.02}_{-0.01}$	0.18 ± 0.07 $^{+0.02}_{-0.03}$	0.07 ± 0.03 $^{+0.01}_{-0.01}$
127.5	0.18 ± 0.10 $^{+0.04}_{-0.03}$	0.05 ± 0.08 $^{+0.03}_{-0.05}$	0.10 ± 0.07 $^{+0.04}_{-0.01}$	0.18 ± 0.06 $^{+0.02}_{-0.01}$	0.08 ± 0.03 $^{+0.00}_{-0.01}$
142.5	0.16 ± 0.10 $^{+0.02}_{-0.03}$	0.17 ± 0.08 $^{+0.02}_{-0.02}$	0.24 ± 0.07 $^{+0.04}_{-0.03}$	-0.02 ± 0.06 $^{+0.01}_{-0.01}$	0.06 ± 0.03 $^{+0.01}_{-0.00}$
157.5	0.24 ± 0.10 $^{+0.02}_{-0.03}$	0.16 ± 0.08 $^{+0.03}_{-0.01}$	0.20 ± 0.07 $^{+0.02}_{-0.02}$	0.11 ± 0.06 $^{+0.02}_{-0.03}$	-0.01 ± 0.03 $^{+0.01}_{-0.02}$
172.5	-0.09 ± 0.10 $^{+0.02}_{-0.07}$	0.12 ± 0.08 $^{+0.03}_{-0.02}$	0.02 ± 0.07 $^{+0.01}_{-0.02}$	-0.01 ± 0.06 $^{+0.02}_{-0.00}$	0.04 ± 0.03 $^{+0.01}_{-0.01}$
187.5	0.10 ± 0.09 $^{+0.02}_{-0.04}$	-0.02 ± 0.07 $^{+0.05}_{-0.01}$	-0.03 ± 0.07 $^{+0.03}_{-0.02}$	0.05 ± 0.06 $^{+0.01}_{-0.01}$	-0.05 ± 0.04 $^{+0.00}_{-0.01}$
202.5	-0.04 ± 0.10 $^{+0.02}_{-0.02}$	-0.17 ± 0.08 $^{+0.06}_{-0.02}$	-0.00 ± 0.08 $^{+0.01}_{-0.03}$	0.03 ± 0.06 $^{+0.01}_{-0.02}$	-0.01 ± 0.04 $^{+0.02}_{-0.02}$
217.5	-0.09 ± 0.10 $^{+0.03}_{-0.02}$	-0.11 ± 0.09 $^{+0.02}_{-0.04}$	-0.13 ± 0.07 $^{+0.02}_{-0.03}$	0.01 ± 0.06 $^{+0.02}_{-0.03}$	-0.06 ± 0.03 $^{+0.01}_{-0.01}$
232.5	-0.18 ± 0.10 $^{+0.01}_{-0.03}$	-0.21 ± 0.08 $^{+0.04}_{-0.02}$	-0.23 ± 0.08 $^{+0.03}_{-0.04}$	-0.18 ± 0.07 $^{+0.02}_{-0.03}$	-0.08 ± 0.04 $^{+0.01}_{-0.00}$
247.5	-0.10 ± 0.11 $^{+0.03}_{-0.04}$	-0.23 ± 0.09 $^{+0.03}_{-0.03}$	-0.18 ± 0.08 $^{+0.04}_{-0.02}$	-0.26 ± 0.07 $^{+0.03}_{-0.02}$	-0.16 ± 0.04 $^{+0.01}_{-0.01}$
262.5	-0.34 ± 0.11 $^{+0.02}_{-0.09}$	-0.20 ± 0.09 $^{+0.02}_{-0.02}$	-0.34 ± 0.09 $^{+0.01}_{-0.01}$	-0.15 ± 0.09 $^{+0.06}_{-0.02}$	-0.10 ± 0.05 $^{+0.00}_{-0.02}$
277.5	-0.21 ± 0.11 $^{+0.02}_{-0.05}$	-0.30 ± 0.10 $^{+0.03}_{-0.03}$	-0.22 ± 0.09 $^{+0.01}_{-0.02}$	-0.15 ± 0.08 $^{+0.02}_{-0.03}$	-0.12 ± 0.05 $^{+0.02}_{-0.02}$
292.5	-0.09 ± 0.12 $^{+0.03}_{-0.02}$	-0.37 ± 0.10 $^{+0.04}_{-0.03}$	-0.19 ± 0.10 $^{+0.03}_{-0.02}$	-0.22 ± 0.09 $^{+0.03}_{-0.03}$	-0.23 ± 0.06 $^{+0.02}_{-0.02}$
307.5	-0.17 ± 0.12 $^{+0.05}_{-0.03}$	-0.37 ± 0.12 $^{+0.04}_{-0.03}$	-0.16 ± 0.13 $^{+0.04}_{-0.03}$	-0.24 ± 0.13 $^{+0.05}_{-0.05}$	-0.11 ± 0.10 $^{+0.04}_{-0.05}$
322.5	-0.36 ± 0.13 $^{+0.04}_{-0.01}$	-0.12 ± 0.13 $^{+0.02}_{-0.09}$	-0.03 ± 0.16 $^{+0.01}_{-0.04}$	-0.33 ± 0.21 $^{+0.06}_{-0.02}$	-0.26 ± 0.20 $^{+0.06}_{-0.04}$
337.5	0.05 ± 0.13 $^{+0.03}_{-0.02}$	-0.34 ± 0.17 $^{+0.11}_{-0.05}$	-0.10 ± 0.22 $^{+0.10}_{-0.03}$	0.52 ± 0.28 $^{+0.09}_{-0.07}$	0.16 ± 0.68 $^{+0.04}_{-0.02}$
352.5	0.13 ± 0.14 $^{+0.05}_{-0.01}$	-0.05 ± 0.19 $^{+0.06}_{-0.06}$	0.31 ± 0.30 $^{+0.11}_{-0.05}$	-0.56 ± 0.35 $^{+0.05}_{-0.13}$	0.05 ± 0.27 $^{+0.02}_{-0.01}$

Table D.14: Helicity-dependent experimental cross section (pb) for kin484.

ϕ (deg)	$\langle x_{Bj}\rangle = 0.610$ $\langle Q^2\rangle = 5.604$ GeV^2 $\langle t'\rangle = -0.068$ GeV^2	$\langle x_{Bj}\rangle = 0.612$ $\langle Q^2\rangle = 5.617$ GeV^2 $\langle t'\rangle = -0.200$ GeV^2	$\langle x_{Bj}\rangle = 0.615$ $\langle Q^2\rangle = 5.638$ GeV^2 $\langle t'\rangle = -0.333$ GeV^2	$\langle x_{Bj}\rangle = 0.617$ $\langle Q^2\rangle = 5.653$ GeV^2 $\langle t'\rangle = -0.467$ GeV^2	$\langle x_{Bj}\rangle = 0.616$ $\langle Q^2\rangle = 5.659$ GeV^2 $\langle t'\rangle = -0.654$ GeV^2
7.5	0.715 ± 0.039 $^{+0.021}_{-0.010}$	0.514 ± 0.042 $^{+0.025}_{-0.012}$	0.483 ± 0.070 $^{+0.016}_{-0.046}$	0.268 ± 0.132 $^{+0.054}_{-0.043}$	0.840 ± 0.361 $^{+0.000}_{-0.248}$
22.5	0.712 ± 0.038 $^{+0.008}_{-0.016}$	0.497 ± 0.039 $^{+0.025}_{-0.011}$	0.371 ± 0.052 $^{+0.031}_{-0.033}$	0.315 ± 0.088 $^{+0.031}_{-0.025}$	0.489 ± 0.159 $^{+0.065}_{-0.061}$
37.5	0.642 ± 0.037 $^{+0.017}_{-0.009}$	0.495 ± 0.036 $^{+0.001}_{-0.030}$	0.387 ± 0.042 $^{+0.025}_{-0.005}$	0.392 ± 0.056 $^{+0.015}_{-0.017}$	0.231 ± 0.064 $^{+0.020}_{-0.037}$
52.5	0.638 ± 0.037 $^{+0.017}_{-0.001}$	0.527 ± 0.035 $^{+0.009}_{-0.017}$	0.377 ± 0.035 $^{+0.036}_{-0.007}$	0.367 ± 0.040 $^{+0.051}_{-0.005}$	0.195 ± 0.038 $^{+0.017}_{-0.000}$
67.5	0.676 ± 0.037 $^{+0.008}_{-0.020}$	0.490 ± 0.034 $^{+0.008}_{-0.014}$	0.455 ± 0.035 $^{+0.008}_{-0.026}$	0.248 ± 0.033 $^{+0.028}_{-0.000}$	0.286 ± 0.032 $^{+0.018}_{-0.003}$
82.5	0.632 ± 0.036 $^{+0.020}_{-0.015}$	0.532 ± 0.035 $^{+0.002}_{-0.024}$	0.393 ± 0.034 $^{+0.004}_{-0.011}$	0.275 ± 0.033 $^{+0.040}_{-0.011}$	0.289 ± 0.029 $^{+0.026}_{-0.001}$
97.5	0.587 ± 0.035 $^{+0.013}_{-0.013}$	0.436 ± 0.033 $^{+0.004}_{-0.008}$	0.411 ± 0.034 $^{+0.021}_{-0.008}$	0.302 ± 0.032 $^{+0.015}_{-0.011}$	0.256 ± 0.027 $^{+0.010}_{-0.012}$
112.5	0.559 ± 0.035 $^{+0.011}_{-0.009}$	0.413 ± 0.032 $^{+0.021}_{-0.001}$	0.377 ± 0.033 $^{+0.005}_{-0.009}$	0.283 ± 0.031 $^{+0.015}_{-0.003}$	0.229 ± 0.024 $^{+0.007}_{-0.011}$
127.5	0.574 ± 0.035 $^{+0.009}_{-0.008}$	0.394 ± 0.032 $^{+0.007}_{-0.010}$	0.354 ± 0.032 $^{+0.020}_{-0.003}$	0.275 ± 0.030 $^{+0.000}_{-0.016}$	0.225 ± 0.024 $^{+0.015}_{-0.003}$
142.5	0.547 ± 0.035 $^{+0.007}_{-0.027}$	0.393 ± 0.032 $^{+0.009}_{-0.009}$	0.355 ± 0.032 $^{+0.016}_{-0.012}$	0.330 ± 0.033 $^{+0.000}_{-0.017}$	0.312 ± 0.027 $^{+0.006}_{-0.024}$
157.5	0.553 ± 0.035 $^{+0.000}_{-0.029}$	0.431 ± 0.033 $^{+0.021}_{-0.014}$	0.358 ± 0.032 $^{+0.003}_{-0.017}$	0.331 ± 0.034 $^{+0.001}_{-0.012}$	0.332 ± 0.029 $^{+0.000}_{-0.027}$
172.5	0.556 ± 0.035 $^{+0.022}_{-0.013}$	0.350 ± 0.032 $^{+0.026}_{-0.000}$	0.349 ± 0.034 $^{+0.006}_{-0.004}$	0.381 ± 0.036 $^{+0.020}_{-0.008}$	0.347 ± 0.030 $^{+0.010}_{-0.011}$
187.5	0.581 ± 0.036 $^{+0.020}_{-0.011}$	0.399 ± 0.034 $^{+0.055}_{-0.007}$	0.404 ± 0.036 $^{+0.008}_{-0.014}$	0.342 ± 0.036 $^{+0.012}_{-0.010}$	0.295 ± 0.028 $^{+0.031}_{-0.000}$
202.5	0.570 ± 0.036 $^{+0.024}_{-0.009}$	0.437 ± 0.035 $^{+0.002}_{-0.018}$	0.395 ± 0.036 $^{+0.000}_{-0.017}$	0.320 ± 0.036 $^{+0.017}_{-0.011}$	0.298 ± 0.028 $^{+0.011}_{-0.020}$
217.5	0.564 ± 0.037 $^{+0.021}_{-0.021}$	0.446 ± 0.036 $^{+0.021}_{-0.013}$	0.439 ± 0.038 $^{+0.011}_{-0.007}$	0.424 ± 0.039 $^{+0.008}_{-0.034}$	0.354 ± 0.028 $^{+0.010}_{-0.012}$
232.5	0.577 ± 0.038 $^{+0.006}_{-0.016}$	0.498 ± 0.039 $^{+0.024}_{-0.017}$	0.487 ± 0.040 $^{+0.010}_{-0.008}$	0.381 ± 0.038 $^{+0.022}_{-0.016}$	0.306 ± 0.028 $^{+0.018}_{-0.010}$
247.5	0.608 ± 0.038 $^{+0.004}_{-0.012}$	0.549 ± 0.041 $^{+0.011}_{-0.001}$	0.474 ± 0.042 $^{+0.001}_{-0.031}$	0.374 ± 0.041 $^{+0.018}_{-0.010}$	0.379 ± 0.032 $^{+0.011}_{-0.011}$
262.5	0.708 ± 0.040 $^{+0.013}_{-0.004}$	0.559 ± 0.041 $^{+0.005}_{-0.020}$	0.469 ± 0.042 $^{+0.024}_{-0.009}$	0.440 ± 0.043 $^{+0.018}_{-0.005}$	0.357 ± 0.035 $^{+0.009}_{-0.006}$
277.5	0.652 ± 0.038 $^{+0.002}_{-0.046}$	0.540 ± 0.038 $^{+0.003}_{-0.010}$	0.503 ± 0.041 $^{+0.011}_{-0.020}$	0.422 ± 0.040 $^{+0.040}_{-0.005}$	0.352 ± 0.034 $^{+0.011}_{-0.022}$
292.5	0.681 ± 0.038 $^{+0.015}_{-0.008}$	0.591 ± 0.039 $^{+0.011}_{-0.018}$	0.421 ± 0.037 $^{+0.029}_{-0.008}$	0.407 ± 0.039 $^{+0.016}_{-0.012}$	0.320 ± 0.033 $^{+0.004}_{-0.009}$
307.5	0.752 ± 0.039 $^{+0.018}_{-0.009}$	0.576 ± 0.037 $^{+0.011}_{-0.014}$	0.444 ± 0.037 $^{+0.012}_{-0.008}$	0.384 ± 0.042 $^{+0.045}_{-0.000}$	0.319 ± 0.042 $^{+0.007}_{-0.036}$
322.5	0.727 ± 0.038 $^{+0.010}_{-0.022}$	0.593 ± 0.037 $^{+0.008}_{-0.013}$	0.399 ± 0.043 $^{+0.032}_{-0.008}$	0.382 ± 0.053 $^{+0.000}_{-0.023}$	0.244 ± 0.070 $^{+0.024}_{-0.008}$
337.5	0.761 ± 0.039 $^{+0.005}_{-0.034}$	0.609 ± 0.041 $^{+0.005}_{-0.009}$	0.470 ± 0.055 $^{+0.026}_{-0.011}$	0.335 ± 0.089 $^{+0.055}_{-0.005}$	0.376 ± 0.160 $^{+0.040}_{-0.041}$
352.5	0.743 ± 0.040 $^{+0.020}_{-0.035}$	0.549 ± 0.043 $^{+0.007}_{-0.027}$	0.511 ± 0.070 $^{+0.057}_{-0.010}$	0.535 ± 0.139 $^{+0.095}_{-0.021}$	0.375 ± 0.379 $^{+0.075}_{-0.074}$

Table D.15: Unpolarized experimental cross section (pb) for kin601.

ϕ (deg)	$\langle x_{Bj}\rangle = 0.610$ $\langle Q^2\rangle = 5.604$ GeV^2 $\langle t'\rangle = -0.068$ GeV^2	$\langle x_{Bj}\rangle = 0.612$ $\langle Q^2\rangle = 5.617$ GeV^2 $\langle t'\rangle = -0.200$ GeV^2	$\langle x_{Bj}\rangle = 0.615$ $\langle Q^2\rangle = 5.638$ GeV^2 $\langle t'\rangle = -0.333$ GeV^2	$\langle x_{Bj}\rangle = 0.617$ $\langle Q^2\rangle = 5.653$ GeV^2 $\langle t'\rangle = -0.467$ GeV^2	$\langle x_{Bj}\rangle = 0.616$ $\langle Q^2\rangle = 5.659$ GeV^2 $\langle t'\rangle = -0.654$ GeV^2
7.5	0.017 ± 0.033 $^{+0.021}_{-0.011}$	-0.034 ± 0.042 $^{+0.009}_{-0.027}$	-0.000 ± 0.064 $^{+0.015}_{-0.057}$	-0.021 ± 0.114 $^{+0.092}_{-0.010}$	0.117 ± 0.338 $^{+0.030}_{-0.245}$
22.5	0.150 ± 0.041 $^{+0.000}_{-0.024}$	0.048 ± 0.045 $^{+0.010}_{-0.014}$	0.141 ± 0.056 $^{+0.000}_{-0.051}$	0.106 ± 0.089 $^{+0.035}_{-0.029}$	0.393 ± 0.171 $^{+0.023}_{-0.082}$
37.5	0.020 ± 0.042 $^{+0.018}_{-0.009}$	0.156 ± 0.043 $^{+0.007}_{-0.034}$	0.083 ± 0.047 $^{+0.022}_{-0.009}$	0.118 ± 0.060 $^{+0.018}_{-0.012}$	0.113 ± 0.072 $^{+0.028}_{-0.018}$
52.5	0.095 ± 0.042 $^{+0.010}_{-0.006}$	0.192 ± 0.042 $^{+0.003}_{-0.021}$	0.112 ± 0.040 $^{+0.008}_{-0.040}$	0.113 ± 0.046 $^{+0.029}_{-0.014}$	0.088 ± 0.043 $^{+0.011}_{-0.004}$
67.5	0.123 ± 0.043 $^{+0.014}_{-0.008}$	0.151 ± 0.040 $^{+0.008}_{-0.038}$	0.039 ± 0.039 $^{+0.005}_{-0.015}$	0.080 ± 0.038 $^{+0.013}_{-0.008}$	0.052 ± 0.037 $^{+0.002}_{-0.025}$
82.5	0.085 ± 0.043 $^{+0.016}_{-0.007}$	0.124 ± 0.040 $^{+0.004}_{-0.023}$	0.104 ± 0.038 $^{+0.000}_{-0.019}$	0.043 ± 0.037 $^{+0.018}_{-0.012}$	0.066 ± 0.032 $^{+0.002}_{-0.022}$
97.5	0.064 ± 0.042 $^{+0.023}_{-0.010}$	0.109 ± 0.038 $^{+0.018}_{-0.004}$	0.082 ± 0.037 $^{+0.018}_{-0.024}$	0.054 ± 0.035 $^{+0.012}_{-0.010}$	0.053 ± 0.029 $^{+0.004}_{-0.009}$
112.5	0.057 ± 0.041 $^{+0.006}_{-0.011}$	0.074 ± 0.037 $^{+0.025}_{-0.008}$	0.044 ± 0.036 $^{+0.006}_{-0.007}$	0.095 ± 0.034 $^{+0.013}_{-0.012}$	0.038 ± 0.026 $^{+0.008}_{-0.016}$
127.5	0.057 ± 0.041 $^{+0.032}_{-0.009}$	0.092 ± 0.035 $^{+0.003}_{-0.014}$	0.073 ± 0.034 $^{+0.005}_{-0.031}$	0.010 ± 0.033 $^{+0.023}_{-0.005}$	0.053 ± 0.025 $^{+0.004}_{-0.019}$
142.5	0.045 ± 0.040 $^{+0.006}_{-0.015}$	0.023 ± 0.035 $^{+0.018}_{-0.007}$	0.032 ± 0.034 $^{+0.021}_{-0.006}$	0.115 ± 0.035 $^{+0.009}_{-0.040}$	0.015 ± 0.028 $^{+0.001}_{-0.021}$
157.5	0.061 ± 0.038 $^{+0.023}_{-0.003}$	0.009 ± 0.035 $^{+0.017}_{-0.009}$	0.019 ± 0.033 $^{+0.010}_{-0.018}$	-0.017 ± 0.035 $^{+0.019}_{-0.009}$	-0.020 ± 0.029 $^{+0.022}_{-0.002}$
172.5	0.037 ± 0.031 $^{+0.015}_{-0.000}$	-0.012 ± 0.030 $^{+0.024}_{-0.014}$	-0.018 ± 0.030 $^{+0.013}_{-0.010}$	-0.028 ± 0.035 $^{+0.018}_{-0.009}$	0.017 ± 0.027 $^{+0.003}_{-0.019}$
187.5	-0.030 ± 0.074 $^{+0.048}_{-0.007}$	-0.024 ± 0.048 $^{+0.020}_{-0.000}$	-0.070 ± 0.044 $^{+0.025}_{-0.005}$	0.015 ± 0.045 $^{+0.013}_{-0.008}$	-0.001 ± 0.032 $^{+0.010}_{-0.008}$
202.5	-0.001 ± 0.052 $^{+0.018}_{-0.020}$	-0.038 ± 0.042 $^{+0.018}_{-0.020}$	0.025 ± 0.040 $^{+0.019}_{-0.005}$	0.001 ± 0.040 $^{+0.006}_{-0.020}$	0.009 ± 0.029 $^{+0.000}_{-0.023}$
217.5	0.021 ± 0.050 $^{+0.013}_{-0.027}$	-0.084 ± 0.042 $^{+0.011}_{-0.017}$	-0.066 ± 0.040 $^{+0.021}_{-0.028}$	-0.045 ± 0.042 $^{+0.038}_{-0.021}$	-0.019 ± 0.030 $^{+0.010}_{-0.014}$
232.5	-0.127 ± 0.050 $^{+0.022}_{-0.010}$	-0.101 ± 0.044 $^{+0.021}_{-0.010}$	-0.009 ± 0.042 $^{+0.005}_{-0.004}$	-0.075 ± 0.043 $^{+0.001}_{-0.016}$	-0.056 ± 0.030 $^{+0.013}_{-0.006}$
247.5	-0.165 ± 0.051 $^{+0.034}_{-0.000}$	-0.091 ± 0.047 $^{+0.037}_{-0.010}$	-0.077 ± 0.046 $^{+0.022}_{-0.006}$	-0.072 ± 0.045 $^{+0.040}_{-0.004}$	-0.069 ± 0.035 $^{+0.004}_{-0.007}$
262.5	-0.145 ± 0.052 $^{+0.027}_{-0.000}$	-0.097 ± 0.047 $^{+0.006}_{-0.025}$	-0.125 ± 0.046 $^{+0.029}_{-0.005}$	-0.142 ± 0.049 $^{+0.008}_{-0.022}$	-0.047 ± 0.039 $^{+0.006}_{-0.013}$
277.5	-0.130 ± 0.049 $^{+0.005}_{-0.028}$	-0.123 ± 0.045 $^{+0.002}_{-0.018}$	-0.170 ± 0.046 $^{+0.013}_{-0.010}$	-0.099 ± 0.046 $^{+0.017}_{-0.013}$	-0.083 ± 0.037 $^{+0.015}_{-0.011}$
292.5	-0.144 ± 0.050 $^{+0.024}_{-0.002}$	-0.159 ± 0.046 $^{+0.025}_{-0.007}$	-0.140 ± 0.042 $^{+0.002}_{-0.029}$	-0.062 ± 0.045 $^{+0.027}_{-0.000}$	-0.095 ± 0.037 $^{+0.010}_{-0.008}$
307.5	-0.076 ± 0.051 $^{+0.007}_{-0.020}$	-0.110 ± 0.044 $^{+0.013}_{-0.011}$	-0.113 ± 0.043 $^{+0.015}_{-0.017}$	-0.149 ± 0.049 $^{+0.016}_{-0.010}$	-0.154 ± 0.048 $^{+0.058}_{-0.007}$
322.5	-0.062 ± 0.051 $^{+0.009}_{-0.040}$	-0.109 ± 0.047 $^{+0.032}_{-0.000}$	-0.089 ± 0.050 $^{+0.046}_{-0.011}$	-0.154 ± 0.059 $^{+0.026}_{-0.008}$	-0.073 ± 0.080 $^{+0.065}_{-0.007}$
337.5	-0.017 ± 0.055 $^{+0.000}_{-0.036}$	-0.043 ± 0.053 $^{+0.015}_{-0.025}$	-0.041 ± 0.064 $^{+0.008}_{-0.025}$	-0.008 ± 0.093 $^{+0.026}_{-0.038}$	0.129 ± 0.184 $^{+0.001}_{-0.067}$
352.5	-0.113 ± 0.080 $^{+0.022}_{-0.032}$	-0.009 ± 0.064 $^{+0.033}_{-0.014}$	-0.014 ± 0.088 $^{+0.075}_{-0.001}$	-0.096 ± 0.157 $^{+0.058}_{-0.002}$	-0.356 ± 0.468 $^{+0.000}_{-0.175}$

Table D.16: Helicity-dependent experimental cross section (pb) for kin601.

ϕ (deg)	$\langle x_{Bj}\rangle = 0.608$ $\langle Q^2\rangle = 8.440$ GeV^2 $\langle t'\rangle = -0.060$ GeV^2	$\langle x_{Bj}\rangle = 0.609$ $\langle Q^2\rangle = 8.453$ GeV^2 $\langle t'\rangle = -0.177$ GeV^2	$\langle x_{Bj}\rangle = 0.611$ $\langle Q^2\rangle = 8.481$ GeV^2 $\langle t'\rangle = -0.294$ GeV^2	$\langle x_{Bj}\rangle = 0.613$ $\langle Q^2\rangle = 8.501$ GeV^2 $\langle t'\rangle = -0.412$ GeV^2	$\langle x_{Bj}\rangle = 0.613$ $\langle Q^2\rangle = 8.513$ GeV^2 $\langle t'\rangle = -0.577$ GeV^2
7.5	0.382 ± 0.020 $^{+0.008}_{-0.004}$	0.342 ± 0.023 $^{+0.006}_{-0.008}$	0.306 ± 0.036 $^{+0.017}_{-0.008}$	0.314 ± 0.070 $^{+0.014}_{-0.027}$	0.280 ± 0.136 $^{+0.055}_{-0.008}$
22.5	0.385 ± 0.020 $^{+0.009}_{-0.005}$	0.305 ± 0.021 $^{+0.013}_{-0.009}$	0.253 ± 0.028 $^{+0.006}_{-0.012}$	0.207 ± 0.046 $^{+0.006}_{-0.014}$	0.139 ± 0.072 $^{+0.045}_{-0.009}$
37.5	0.333 ± 0.018 $^{+0.005}_{-0.005}$	0.284 ± 0.019 $^{+0.007}_{-0.003}$	0.231 ± 0.022 $^{+0.016}_{-0.007}$	0.185 ± 0.028 $^{+0.004}_{-0.011}$	0.136 ± 0.029 $^{+0.006}_{-0.010}$
52.5	0.371 ± 0.019 $^{+0.010}_{-0.013}$	0.283 ± 0.018 $^{+0.006}_{-0.003}$	0.193 ± 0.017 $^{+0.003}_{-0.007}$	0.131 ± 0.017 $^{+0.005}_{-0.004}$	0.133 ± 0.017 $^{+0.003}_{-0.006}$
67.5	0.357 ± 0.018 $^{+0.010}_{-0.006}$	0.267 ± 0.017 $^{+0.009}_{-0.003}$	0.206 ± 0.016 $^{+0.010}_{-0.002}$	0.151 ± 0.015 $^{+0.004}_{-0.005}$	0.127 ± 0.014 $^{+0.005}_{-0.003}$
82.5	0.335 ± 0.018 $^{+0.006}_{-0.009}$	0.259 ± 0.016 $^{+0.010}_{-0.002}$	0.165 ± 0.014 $^{+0.010}_{-0.005}$	0.160 ± 0.015 $^{+0.005}_{-0.005}$	0.120 ± 0.012 $^{+0.005}_{-0.004}$
97.5	0.323 ± 0.017 $^{+0.002}_{-0.013}$	0.226 ± 0.015 $^{+0.003}_{-0.005}$	0.185 ± 0.014 $^{+0.003}_{-0.007}$	0.139 ± 0.013 $^{+0.006}_{-0.003}$	0.116 ± 0.011 $^{+0.005}_{-0.003}$
112.5	0.310 ± 0.017 $^{+0.002}_{-0.001}$	0.189 ± 0.014 $^{+0.008}_{-0.002}$	0.150 ± 0.013 $^{+0.006}_{-0.002}$	0.140 ± 0.013 $^{+0.007}_{-0.002}$	0.107 ± 0.010 $^{+0.003}_{-0.003}$
127.5	0.274 ± 0.016 $^{+0.012}_{-0.006}$	0.205 ± 0.014 $^{+0.008}_{-0.005}$	0.137 ± 0.012 $^{+0.005}_{-0.002}$	0.123 ± 0.012 $^{+0.005}_{-0.004}$	0.082 ± 0.008 $^{+0.002}_{-0.001}$
142.5	0.280 ± 0.017 $^{+0.009}_{-0.007}$	0.196 ± 0.014 $^{+0.006}_{-0.006}$	0.157 ± 0.013 $^{+0.003}_{-0.004}$	0.120 ± 0.012 $^{+0.001}_{-0.006}$	0.086 ± 0.008 $^{+0.002}_{-0.005}$
157.5	0.284 ± 0.016 $^{+0.005}_{-0.009}$	0.210 ± 0.014 $^{+0.003}_{-0.008}$	0.134 ± 0.012 $^{+0.005}_{-0.002}$	0.122 ± 0.012 $^{+0.004}_{-0.004}$	0.098 ± 0.009 $^{+0.005}_{-0.004}$
172.5	0.280 ± 0.016 $^{+0.005}_{-0.003}$	0.175 ± 0.014 $^{+0.006}_{-0.001}$	0.142 ± 0.013 $^{+0.005}_{-0.004}$	0.117 ± 0.012 $^{+0.003}_{-0.002}$	0.110 ± 0.010 $^{+0.003}_{-0.011}$
187.5	0.266 ± 0.016 $^{+0.012}_{-0.002}$	0.189 ± 0.014 $^{+0.003}_{-0.008}$	0.149 ± 0.013 $^{+0.002}_{-0.006}$	0.106 ± 0.012 $^{+0.002}_{-0.004}$	0.092 ± 0.010 $^{+0.002}_{-0.008}$
202.5	0.290 ± 0.016 $^{+0.005}_{-0.005}$	0.208 ± 0.015 $^{+0.001}_{-0.004}$	0.140 ± 0.013 $^{+0.005}_{-0.008}$	0.125 ± 0.013 $^{+0.008}_{-0.003}$	0.094 ± 0.009 $^{+0.006}_{-0.001}$
217.5	0.313 ± 0.017 $^{+0.001}_{-0.006}$	0.187 ± 0.014 $^{+0.007}_{-0.002}$	0.172 ± 0.014 $^{+0.007}_{-0.002}$	0.143 ± 0.014 $^{+0.000}_{-0.012}$	0.107 ± 0.009 $^{+0.001}_{-0.005}$
232.5	0.320 ± 0.017 $^{+0.020}_{-0.007}$	0.218 ± 0.016 $^{+0.005}_{-0.005}$	0.186 ± 0.015 $^{+0.006}_{-0.009}$	0.165 ± 0.015 $^{+0.003}_{-0.004}$	0.110 ± 0.009 $^{+0.000}_{-0.004}$
247.5	0.329 ± 0.018 $^{+0.013}_{-0.005}$	0.266 ± 0.017 $^{+0.003}_{-0.009}$	0.211 ± 0.015 $^{+0.005}_{-0.008}$	0.147 ± 0.014 $^{+0.009}_{-0.004}$	0.135 ± 0.011 $^{+0.004}_{-0.002}$
262.5	0.321 ± 0.018 $^{+0.004}_{-0.012}$	0.285 ± 0.017 $^{+0.003}_{-0.008}$	0.208 ± 0.016 $^{+0.006}_{-0.005}$	0.132 ± 0.014 $^{+0.006}_{-0.003}$	0.122 ± 0.011 $^{+0.002}_{-0.003}$
277.5	0.328 ± 0.018 $^{+0.012}_{-0.007}$	0.257 ± 0.016 $^{+0.007}_{-0.003}$	0.199 ± 0.015 $^{+0.005}_{-0.003}$	0.162 ± 0.015 $^{+0.007}_{-0.003}$	0.142 ± 0.012 $^{+0.004}_{-0.001}$
292.5	0.381 ± 0.019 $^{+0.007}_{-0.013}$	0.287 ± 0.018 $^{+0.004}_{-0.008}$	0.232 ± 0.016 $^{+0.008}_{-0.001}$	0.180 ± 0.016 $^{+0.003}_{-0.004}$	0.134 ± 0.014 $^{+0.008}_{-0.006}$
307.5	0.381 ± 0.019 $^{+0.008}_{-0.003}$	0.309 ± 0.018 $^{+0.004}_{-0.007}$	0.250 ± 0.017 $^{+0.010}_{-0.007}$	0.193 ± 0.018 $^{+0.003}_{-0.003}$	0.129 ± 0.018 $^{+0.006}_{-0.004}$
322.5	0.414 ± 0.020 $^{+0.016}_{-0.005}$	0.320 ± 0.019 $^{+0.005}_{-0.010}$	0.219 ± 0.019 $^{+0.010}_{-0.003}$	0.150 ± 0.024 $^{+0.013}_{-0.010}$	0.161 ± 0.031 $^{+0.001}_{-0.014}$
337.5	0.377 ± 0.020 $^{+0.013}_{-0.005}$	0.362 ± 0.021 $^{+0.009}_{-0.015}$	0.231 ± 0.026 $^{+0.016}_{-0.003}$	0.210 ± 0.046 $^{+0.025}_{-0.006}$	0.128 ± 0.063 $^{+0.013}_{-0.007}$
352.5	0.393 ± 0.020 $^{+0.010}_{-0.006}$	0.340 ± 0.023 $^{+0.005}_{-0.008}$	0.227 ± 0.032 $^{+0.023}_{-0.005}$	0.151 ± 0.065 $^{+0.007}_{-0.020}$	0.189 ± 0.171 $^{+0.014}_{-0.034}$

Table D.17: Unpolarized experimental cross section (pb) for kin603.

ϕ (deg)	$\langle x_{Bj}\rangle = 0.608$ $\langle Q^2\rangle = 8.440$ GeV^2 $\langle t'\rangle = -0.060$ GeV^2	$\langle x_{Bj}\rangle = 0.609$ $\langle Q^2\rangle = 8.453$ GeV^2 $\langle t'\rangle = -0.177$ GeV^2	$\langle x_{Bj}\rangle = 0.611$ $\langle Q^2\rangle = 8.481$ GeV^2 $\langle t'\rangle = -0.294$ GeV^2	$\langle x_{Bj}\rangle = 0.613$ $\langle Q^2\rangle = 8.501$ GeV^2 $\langle t'\rangle = -0.412$ GeV^2	$\langle x_{Bj}\rangle = 0.613$ $\langle Q^2\rangle = 8.513$ GeV^2 $\langle t'\rangle = -0.577$ GeV^2
7.5	-0.015 ± 0.020 $^{+0.005}_{-0.004}$	0.049 ± 0.026 $^{+0.005}_{-0.008}$	0.003 ± 0.030 $^{+0.005}_{-0.009}$	-0.033 ± 0.059 $^{+0.026}_{-0.031}$	0.292 ± 0.098 $^{+0.026}_{-0.012}$
22.5	-0.027 ± 0.022 $^{+0.007}_{-0.004}$	-0.009 ± 0.025 $^{+0.012}_{-0.004}$	0.016 ± 0.025 $^{+0.008}_{-0.016}$	0.076 ± 0.045 $^{+0.014}_{-0.018}$	-0.002 ± 0.061 $^{+0.015}_{-0.026}$
37.5	0.029 ± 0.021 $^{+0.002}_{-0.011}$	0.052 ± 0.023 $^{+0.007}_{-0.023}$	0.019 ± 0.022 $^{+0.007}_{-0.016}$	0.096 ± 0.032 $^{+0.013}_{-0.006}$	0.054 ± 0.029 $^{+0.004}_{-0.015}$
52.5	0.055 ± 0.023 $^{+0.005}_{-0.003}$	0.030 ± 0.022 $^{+0.013}_{-0.005}$	0.044 ± 0.019 $^{+0.010}_{-0.012}$	0.045 ± 0.022 $^{+0.004}_{-0.005}$	0.056 ± 0.019 $^{+0.008}_{-0.005}$
67.5	0.056 ± 0.023 $^{+0.003}_{-0.006}$	0.036 ± 0.020 $^{+0.006}_{-0.011}$	0.043 ± 0.018 $^{+0.007}_{-0.004}$	0.077 ± 0.019 $^{+0.004}_{-0.009}$	0.042 ± 0.015 $^{+0.003}_{-0.006}$
82.5	0.047 ± 0.023 $^{+0.010}_{-0.004}$	0.062 ± 0.019 $^{+0.005}_{-0.007}$	0.046 ± 0.017 $^{+0.007}_{-0.003}$	0.025 ± 0.017 $^{+0.002}_{-0.003}$	0.018 ± 0.014 $^{+0.004}_{-0.009}$
97.5	0.023 ± 0.022 $^{+0.006}_{-0.006}$	0.045 ± 0.018 $^{+0.004}_{-0.003}$	0.032 ± 0.017 $^{+0.008}_{-0.010}$	0.060 ± 0.016 $^{+0.001}_{-0.008}$	0.024 ± 0.013 $^{+0.006}_{-0.004}$
112.5	0.074 ± 0.022 $^{+0.020}_{-0.000}$	0.045 ± 0.017 $^{+0.005}_{-0.004}$	0.006 ± 0.015 $^{+0.006}_{-0.003}$	0.025 ± 0.014 $^{+0.005}_{-0.000}$	0.023 ± 0.011 $^{+0.006}_{-0.001}$
127.5	0.040 ± 0.021 $^{+0.005}_{-0.004}$	0.017 ± 0.017 $^{+0.008}_{-0.001}$	0.034 ± 0.015 $^{+0.004}_{-0.006}$	0.034 ± 0.013 $^{+0.005}_{-0.007}$	0.018 ± 0.009 $^{+0.001}_{-0.003}$
142.5	0.015 ± 0.021 $^{+0.010}_{-0.009}$	0.023 ± 0.016 $^{+0.008}_{-0.005}$	0.047 ± 0.015 $^{+0.000}_{-0.007}$	0.016 ± 0.012 $^{+0.003}_{-0.003}$	0.003 ± 0.009 $^{+0.006}_{-0.001}$
157.5	0.006 ± 0.021 $^{+0.009}_{-0.003}$	0.028 ± 0.016 $^{+0.006}_{-0.007}$	0.012 ± 0.014 $^{+0.001}_{-0.008}$	-0.006 ± 0.012 $^{+0.003}_{-0.003}$	-0.001 ± 0.010 $^{+0.003}_{-0.001}$
172.5	0.018 ± 0.019 $^{+0.004}_{-0.007}$	-0.004 ± 0.015 $^{+0.004}_{-0.003}$	0.005 ± 0.015 $^{+0.004}_{-0.002}$	-0.004 ± 0.011 $^{+0.002}_{-0.005}$	0.014 ± 0.011 $^{+0.001}_{-0.002}$
187.5	0.014 ± 0.023 $^{+0.011}_{-0.007}$	-0.025 ± 0.016 $^{+0.009}_{-0.000}$	0.012 ± 0.016 $^{+0.004}_{-0.007}$	-0.020 ± 0.012 $^{+0.002}_{-0.004}$	0.011 ± 0.011 $^{+0.002}_{-0.002}$
202.5	-0.057 ± 0.022 $^{+0.004}_{-0.004}$	-0.008 ± 0.017 $^{+0.000}_{-0.008}$	-0.042 ± 0.016 $^{+0.006}_{-0.001}$	0.006 ± 0.013 $^{+0.007}_{-0.005}$	-0.003 ± 0.011 $^{+0.000}_{-0.009}$
217.5	0.013 ± 0.023 $^{+0.002}_{-0.008}$	-0.000 ± 0.017 $^{+0.003}_{-0.002}$	-0.043 ± 0.018 $^{+0.002}_{-0.004}$	-0.006 ± 0.014 $^{+0.004}_{-0.003}$	-0.014 ± 0.011 $^{+0.001}_{-0.003}$
232.5	-0.049 ± 0.023 $^{+0.015}_{-0.004}$	-0.049 ± 0.018 $^{+0.002}_{-0.005}$	-0.045 ± 0.018 $^{+0.009}_{-0.006}$	-0.008 ± 0.015 $^{+0.002}_{-0.006}$	-0.035 ± 0.011 $^{+0.002}_{-0.006}$
247.5	-0.070 ± 0.023 $^{+0.003}_{-0.006}$	-0.071 ± 0.020 $^{+0.010}_{-0.002}$	-0.030 ± 0.019 $^{+0.005}_{-0.003}$	-0.040 ± 0.015 $^{+0.007}_{-0.004}$	-0.027 ± 0.012 $^{+0.003}_{-0.004}$
262.5	-0.033 ± 0.023 $^{+0.011}_{-0.004}$	-0.040 ± 0.020 $^{+0.005}_{-0.007}$	-0.042 ± 0.018 $^{+0.006}_{-0.003}$	-0.032 ± 0.016 $^{+0.006}_{-0.008}$	-0.045 ± 0.013 $^{+0.005}_{-0.002}$
277.5	-0.013 ± 0.023 $^{+0.005}_{-0.009}$	-0.065 ± 0.020 $^{+0.006}_{-0.005}$	-0.054 ± 0.018 $^{+0.006}_{-0.004}$	-0.031 ± 0.018 $^{+0.005}_{-0.001}$	-0.038 ± 0.014 $^{+0.004}_{-0.001}$
292.5	-0.041 ± 0.024 $^{+0.009}_{-0.008}$	-0.043 ± 0.021 $^{+0.014}_{-0.013}$	-0.079 ± 0.019 $^{+0.002}_{-0.012}$	-0.052 ± 0.020 $^{+0.007}_{-0.009}$	-0.054 ± 0.015 $^{+0.007}_{-0.004}$
307.5	-0.042 ± 0.024 $^{+0.010}_{-0.001}$	-0.024 ± 0.022 $^{+0.007}_{-0.002}$	-0.053 ± 0.019 $^{+0.002}_{-0.012}$	-0.073 ± 0.022 $^{+0.010}_{-0.005}$	-0.020 ± 0.019 $^{+0.004}_{-0.007}$
322.5	-0.005 ± 0.024 $^{+0.008}_{-0.008}$	-0.063 ± 0.023 $^{+0.005}_{-0.007}$	-0.016 ± 0.020 $^{+0.008}_{-0.006}$	-0.075 ± 0.029 $^{+0.012}_{-0.004}$	0.003 ± 0.030 $^{+0.014}_{-0.003}$
337.5	-0.027 ± 0.023 $^{+0.008}_{-0.001}$	-0.074 ± 0.026 $^{+0.006}_{-0.007}$	0.007 ± 0.024 $^{+0.012}_{-0.013}$	-0.069 ± 0.047 $^{+0.012}_{-0.018}$	0.082 ± 0.051 $^{+0.011}_{-0.020}$
352.5	0.009 ± 0.025 $^{+0.002}_{-0.015}$	-0.010 ± 0.028 $^{+0.009}_{-0.005}$	-0.052 ± 0.028 $^{+0.011}_{-0.010}$	-0.034 ± 0.061 $^{+0.012}_{-0.024}$	-0.193 ± 0.114 $^{+0.037}_{-0.008}$

Table D.18: Helicity-dependent experimental cross section (pb) for kin603.

Bibliography

[1] R. W. McAllister and R. Hofstadter. Elastic Scattering of 188-Mev Electrons from the Proton and the Alpha Particle. *Phys. Rev. 102, 851*, 1956.

[2] D. Marchand (on behalf of the PRAE collaboration). A new platform for research and applications with electrons: the PRAE project. In *Proceedings of XXIII International Baldin Seminar on High Energy Physics Problems (Baldin ISHEPP XXIII)*, 2017.

[3] D. Müller, D. Robaschik, B. Geyer, F. M. Dittes, and J. Horejsi. Wave Functions, Evolution Equations and Evolution Kernels from Light-Ray Operators of QCD. *Fortsch. Phys. 42, 101*, 1994.

[4] X. Ji. Gauge-Invariant Decomposition of Nucleon Spin and Its Spin-Off. *Phys. Rev. Lett. 78, 610*, 1996.

[5] A. V. Radyushkin. Nonforward parton distributions. *Phys. Rev. D 56, 5524*, 1997.

[6] A. W. Thomas and W. Weise. *The Structure of the Nucleon.* WILEY-VCH, Verlag Berlin GmbH, 2001.

[7] M. N. Rosenbluth. High Energy Elastic Scattering of Electrons on Protons. *Phys. Rev. 79, 615*, 1950.

[8] J. J. Kelly. Simple parametrization of nucleon form factors. *Phys. Rev. C 70, 068202*, 2004.

[9] J. C. Bernauer et al. The electric and magnetic form factors of the proton. *Phys. Rev. Lett. 105, 242001*, 2010.

[10] R. Pohl et al. The size of the proton. *Nature 466, 213*, 2010.

[11] H. W. Kendall. Deep inelastic scattering: Experiments on the proton and the observation of scaling. *Rev. Mod. Phys. 63, 597*, 1991.

[12] R. P. Feynman. Very High-Energy Collisions of Hadrons. *Phys. Rev. Lett. 23, 1415*, 1969.

[13] K. A. Olive et al. Review of Particle Physics. *Chin. Phys.*, C38:090001, 2014.

[14] M. Guidal, H. Moutarde, and M. Vanderhaeghen. Generalized Parton Distributions in the valence region from Deeply Virtual Compton Scattering. *Rept. Prog. Phys. 76, 066202*, 2013. arXiv:1303.6600.

[15] A. Bacchetta, U. D'Alesio, M. Diehl, and C. A. Miller. Single-spin asymmetries: the Trento conventions. *Phys. Rev. D70,117504*, 2004. arXiv:hep-ph/0410050.

[16] X. Ji and J. Osborne. One loop corrections and all order factorization in deeply virtual Compton scattering. *Phys. Rev. D 58, 094018*, 1998.

[17] J. C. Collins and A. Freund. Proof of factorization for deeply virtual Compton scattering in QCD. *Phys. Rev. D 59, 074009*, 1999.

[18] M. Defurne et al. (Jefferson Lab Hall A Collaboration). A Glimpse of Gluons through Deeply Virtual Compton Scattering on the Proton. *Nature Commun. 8 no.1, 1408*, 2017. arXiv:1703.09442.

[19] A. V. Belitsky, D. Müller, and A. Kirchner. Theory of deeply virtual Compton scattering on the nucleon. *Nucl. Phys. B 629, 323-392*, 2002. arXiv:hep-ph/0112108.

[20] K. Kumerički, S. Liuti, and H. Moutarde. GPD phenomenology and DVCS fitting. *Eur. Phys. J. A. 52, 157*, 2016. arXiv:1602.02763.

[21] H. Moutarde, B. Pire, F. Sabatie, L. Szymanowski, and J. Wagner. On timelike and spacelike deeply virtual Compton scattering at next to leading order. *Phys. Rev. D. 87, 054029*, 2013. arXiv:1301.3819.

[22] M. Burkardt. Impact Parameter Dependent Parton Distributions and Off-Forward Parton Distributions for $\zeta \to 0$. *Phys. Rev. D 62, 071503*, 2000. arXiv:hep-ph/0005108.

[23] A. V. Belitsky and D. Müller. Exclusive electroproduction revisited: treating kinematical effects. *Phys. Rev. D. 82, 074010*, 2010. arXiv:1005.5209.

[24] A. V. Belitsky, D. Müller, and Y. Ji. Compton scattering: from deeply virtual to quasi-real. *Nucl. Phys. B878, 214-268*, 2014. arXiv:1212.6674.

[25] N. d'Hose, S. Niccolai, and A. Rostomyan. Experimental overview of Deeply Virtual Compton Scattering. *Eur. Phys. J. A 52, 151*, 2016.

[26] A. Accardi et al. White paper: Electron Ion Collider: The Next QCD Frontier - Understanding the glue that binds us all, 2014. arXiv:1212.1701.

[27] C. Adloff et al. (H1 Collaboration). Measurement of Deeply Virtual Compton Scattering at HERA. *Phys. Lett. B 517, 47-58*, 2001. hep-ex/0107005.

[28] S. Chekanov (ZEUS Collaboration). Measurement of deeply virtual Compton scattering at HERA. *Phys. Lett. B 573, 46-62*, 2003. hep-ex/0305028.

[29] A. Aktas et al. (H1 Collaboration). Measurement of Deeply Virtual Compton Scattering at HERA. *Eur. Phys. J. C 44, 1-11*, 2005. hep-ex/0505061.

[30] F. D. Aaron et al. (H1 Collaboration). Measurement of Deeply Virtual Compton Scattering and its t-dependence at HERA. *Phys. Lett. B 659, 796-806*, 2007. arXiv:0709.4114.

[31] S. Chekanov (ZEUS Collaboration). A measurement of the Q^2, W and t dependencies of deeply virtual Compton scattering at HERA. *JHEP 0905:108*, 2009. arXiv:0812.2517.

[32] L. Schoeffel. Deeply Virtual Compton Scattering at HERA II. In *Proceedings of the International Workshop on Deep-Inelastic Scattering and Related Subjects (DIS 2007), Munich, Germany*, 2007. arXiv:0705.2925.

[33] F. D. Aaron et al. (H1 Collaboration). Deeply Virtual Compton Scattering and its Beam Charge Asymmetry in $e^{\pm}p$ Collisions at HERA. *Phys. Lett. B 681, 391-399*, 2009. arXiv:0907.5289.

[34] A. Airapetian et al. (HERMES Collaboration). Measurement of the Beam-Spin Azimuthal Asymmetry Associated with Deeply-Virtual Compton Scattering. *Phys. Rev. Lett. 87, 182001*, 2001. hep-ex/0106068.

[35] A. Airapetian et al. (HERMES Collaboration). Beam-helicity asymmetry arising from deeply virtual Compton scattering measured with kinematically complete event reconstruction. *JHEP 10, 042*, 2012. arXiv:1206.5683.

[36] A. Airapetian et al. (HERMES Collaboration). The Beam–Charge Azimuthal Asymmetry and Deeply Virtual Compton Scattering. *Phys. Rev. D 75, 011103*, 2007. hep-ex/0605108.

[37] A. Airapetian et al. (HERMES Collaboration). Separation of contributions from deeply virtual Compton scattering and its interference with the Bethe–Heitler process in measurements on a hydrogen target. *JHEP 0911:083*, 2009. arXiv:0909.3587.

[38] A. Airapetian et al. (HERMES Collaboration). Beam-helicity and beam-charge asymmetries associated with deeply virtual Compton scattering on the unpolarised proton. *JHEP 07, 032*, 2012. arXiv:1203.6287.

[39] A. Airapetian et al. (HERMES Collaboration). Exclusive Leptoproduction of Real Photons on a Longitudinally Polarised Hydrogen Target. *JHEP 1006:019*, 2010. arXiv:1004.0177.

[40] A. Airapetian et al. (HERMES Collaboration). Measurement of azimuthal asymmetries associated with deeply virtual Compton scattering on a longitudinally polarized deuterium target. *Nucl. Phys. B 842, 265-298*, 2011. arXiv:1008.3996.

[41] A. Airapetian et al. (HERMES Collaboration). Measurement of Azimuthal Asymmetries With Respect To Both Beam Charge and Transverse Target Polarization in Exclusive Electroproduction of Real Photons. *JHEP 0806, 066*, 2008. arXiv:0802.2499.

[42] S. Stepanyan et al. (CLAS Collaboration). Observation of exclusive DVCS in polarized electron beam asymmetry measurements. *Phys. Rev. Lett. 87,182002*, 2001. hep-ex/0107043.

[43] F. X. Girod et al. (CLAS Collaboration). Deeply Virtual Compton Scattering Beam-Spin Asymmetries. *Phys.Rev.Lett.100, 162002*, 2008. arXiv:0711.4805.

[44] H. S. Jo et al. (CLAS Collaboration). Cross sections for the exclusive photon electroproduction on the proton and Generalized Parton Distributions. *Phys. Rev. Lett. 115, 212003*, 2015. arXiv:1504.02009.

[45] S. Pisano et al. (CLAS Collaboration). Single and double spin asymmetries for deeply virtual Compton scattering measured with CLAS and a longitudinally polarized proton target. *Phys. Rev. D 91, 052014*, 2015. arXiv:1501.07052.

[46] E. Seder et al. (CLAS Collaboration). Longitudinal target-spin asymmetries for deeply virtual Compton scattering. *Phys. Rev. Lett.114, 032001*, 2015. arXiv:1410.6615.

[47] C. Muñoz Camacho et al. (Jefferson Lab Hall A Collaboration). Scaling Tests of the Cross Section for Deeply Virtual Compton Scattering. *Phys. Rev. Lett. 97, 262002*, 2006. nucl-ex/0607029.

[48] M. Defurne et al. (Jefferson Lab Hall A Collaboration). The E00-110 experiment in Jefferson Lab's Hall A: Deeply Virtual Compton Scattering off the Proton at 6 GeV. *Phys. Rev. C 92, 055202*, 2015. arXiv:1504.05453.

[49] M. Mazouz et al. (Jefferson Lab Hall A Collaboration). Deeply Virtual Compton Scattering off the neutron. *Phys. Rev. Lett. 99, 242501*, 2007. arXiv:0709.0450.

[50] M. Benali, M. Mazouz, and H. Fonvieille. Deeply virtual compton scattering on the neutron: Jlab experiment e08-025. *EPJ Web of Conferences 112, 01004*, 2016. https://doi.org/10.1051/epjconf/201611201004.

[51] F. Gautheron et al. (COMPASS Collaboration). COMPASS-II Proposal. *CERN/SPSC-2010-014, SPSC-P-340*, 2010.

[52] J. Roche, C. E. Hyde-Wright, B. Michel, C. Muñoz Camacho et al. (Jefferson Lab Hall A Collaboration). Measurements of the electron-helicity dependent cross sections of Deeply Virtual Compton Scattering with CEBAF at 12 GeV. *PR12-06-114*, 2006. http://hallaweb.jlab.org/experiment/DVCS/documents/proposals/E12-06-114_proposal.pdf.

[53] F. Sabatié et al. (CLAS12 Collaboration). Deeply Virtual Compton Scattering with CLAS at 11 GeV. *PR12-06-119*, 2006. https://www.jlab.org/exp_prog/proposals/06/PR12-06-119.pdf.

[54] S. Niccolai et al. (CLAS12 Collaboration). Deeply Virtual Compton Scattering on the Neutron with CLAS12 at 11 GeV. *PR12-11-003*, 2011. https://www.jlab.org/exp_prog/proposals/11/PR12-11-003.pdf.

[55] S. Niccolai et al. (CLAS12 Collaboration). Proposal of extension of the CLAS12 run-group Cb (ND_3 target). *C12-15-004*, 2016. https://www.jlab.org/exp_prog/proposals/16/C12-15-004.pdf.

[56] C. Muñoz Camacho et al. (Jefferson Lab Hall C Collaboration). Exclusive Deeply Virtual Compton and Neutral Pion Cross-Section Measurements in Hall C. *PR12-13-010*, 2013. https://www.jlab.org/exp_prog/proposals/13/PR12-13-010.pdf.

[57] E. Voutier et al. Nucleon and nuclear structure through dilepton production. *Acta Physica Polonica 49, 741*, 2018. arXiv:1712.04198.

[58] L. Cardman et al. White paper: The science driving the 12 GeV upgrade of CEBAF, February 2001. https://www.jlab.org/div_dept/physics_division/GeV/whitepaperv11/index.html.

[59] P. Adderley, M. Baylac, J. Clark, T. Day, J. Grames, J. Hanskneckt, M. Poelker, and M. Stutzman. Jefferson Lab Polarized Source, 2002. https://www.jlab.org/accel/inj_group/docs/2002/ori.pdf.

[60] M. Steigerwald. MeV Mott polarimetry at Jefferson Lab. In *Proceedings of the 14th International Spin Physics Symposium (SPIN 2000)*, 2001.

[61] J. Grames et al. Two Wien filter spin flipper. In *Proceedings of 2011 Particle Accelerator Conference*, 2011.

[62] J. Alcorn et al. Basic instrumentation for Hall A at Jefferson Lab. *Nuclear Instruments and Methods in Physics Research A 522, 294*, 2004.

[63] J. H. Mitchell et al. Hall A experimental equipment operations manual. http://hallaweb.jlab.org/document/OPMAN/.

[64] B. Karki. Internal note: BCMs and Charge for E12-06-114: DVCS, 2017. https://www.jlab.org/indico/event/197/session/0/contribution/2/material/slides/0.pdf.

[65] T. Gautam. Internal note: BPM Calibration for GMp/DVCS experiments, 2017. https://www.jlab.org/indico/event/197/session/3/contribution/9/material/slides/0.pdf.

[66] M. Baylac et al. First electron beam polarization measurements with a Compton polarimeter at Jefferson Laboratory. *Phys. Lett. B 539, 8*, 2002.

[67] https://hallaweb.jlab.org/dvcslog/12+GeV/496.

[68] F. Feinstein. The analogue ring sampler : A front-end chip for ANTARES. *Nuclear Instruments and Methods in Physics Research A504 258–261*, 2003.

[69] B. Schmookler. Internal note: Hall A 12 GeV Raster Calibration, 2017. https://www.jlab.org/indico/event/197/session/3/contribution/19/material/slides/0.pdf.

[70] C. Muñoz Camacho. *Diffusion Compton profondément virtuelle dans le Hall A au Jefferson Laboratory.* PhD thesis, Université Paris VI, 2005.

[71] M. Dlamini. Internal note: DVCS Calorimeter Analysis (Fall 2014 - Spring 2015): E12-06-114, 2016. https://hallaweb.jlab.org/dvcslog/12+GeV/348.

[72] H. Rashad. Internal note: Event Selection - DVCS3, 2017. https://hallaweb.jlab.org/dvcslog/12+GeV/417.

[73] N. Liyanage. Optics calibration of the Hall A High Resolution Spectrometers using the new optimizer. Technical Report JLAB-TN-02-012, Jefferson Lab, 2002. http://hallaweb.jlab.org/publications/Technotes/files/2002/02-012.pdf.

[74] B. Karki. Internal note, 2018. https://hallaweb.jlab.org/dvcslog/12+GeV/497.

[75] K. Makino and M. Bertz. COSY INFINITY version 8, 1999.

[76] B. Karki. Internal note: Optics for E12-06-114, 2018. https://hallaweb.jlab.org/dvcslog/12+GeV/512.

[77] R. T. Jones et al. A bootstrap method for gain calibration and resolution determination of a lead-glass calorimeter. *Nuclear Instruments and Methods in Physics Research A 566 366-374*, 2006.

[78] A. M. Martí Jiménez-Argüello. *Measurement of the photon electroproduction cross section at JLAB with the goal of performing a Rosenbluth separation of the DVCS contribution.* PhD thesis, Université Paris Sud - Paris XI ; Universidad de Valencia (Spain), 2014.

[79] V. Breton et al. Application of neural networks and cellular automata to interpretation of calorimeter data. *Nuclear Instruments and Methods in Physics Research A 362, 478-486*, 1995.

[80] A. Houcine. Reconstruction des quadrivecteurs des particules détectées dans le calorimètre électromagnétique de l'expérience DVCS. Master's thesis, Faculté des Sciences de Monastir (Tunisia), 2012.

[81] H. Rashad. Internal note: DVCS3_EventSelection (HRS), 2017. https://hallaweb.jlab.org/dvcslog/12+GeV/469.

[82] H. Rashad. Internal note: tracking, VDC multi cluster, 2017. https://hallaweb.jlab.org/dvcslog/12+GeV/402.

[83] A. Johnson. Internal note: R-Function for Hall A L-HRS Acceptance, 2016. https://hallaweb.jlab.org/dvcslog/12+GeV/399.

[84] M. Rvachev. Effective use of JLab Hall A HRS acceptance with R-functions. Technical Report JLAB-TN-01-055, Massachusetts Institute of Technology, 2001. http://hallaweb.jlab.org/publications/Technotes/files/2001/01-055.pdf.

[85] A. Johnson. Internal note: R-Function changes, 2017. https://hallaweb.jlab.org/dvcslog/12+GeV/457.

[86] A. Johnson. Internal note: R-Function Changes for Corrected Y, 2017. https://hallaweb.jlab.org/dvcslog/12+GeV/479.

[87] L. L. Frankfurt et al. Hard Exclusive Electroproduction of Decuplet Baryons in the Large Nc Limit. *Phys. Rev. Lett. 84, 2589*, 2000.

[88] H. Rashad. Internal note: DVCS collaboration meeting, updates on HRS efficiencies, 2018. https://www.jlab.org/indico/event/253/contribution/0/material/slides/0.pdf.

[89] B. Karki. Internal note: Systematic error evaluation of current and deadtime, 2018. https://hallaweb.jlab.org/dvcslog/12+GeV/536.

[90] J. C. Cornejo. Internal note: Compton Update for DVCS, 2018. https://www.jlab.org/indico/event/253/contribution/3/material/slides/0.pdf.

[91] S. Glamazdin and R. Pomatsalyuk. Internal note: Møller Polarimetry for DVCS, 2017. https://www.jlab.org/indico/event/197/session/3/contribution/11/material/slides/0.pdf.

[92] W. Henry. Internal note: Geant4 Geometry Update, 2018. https://hallaweb.jlab.org/dvcslog/12+GeV/498.

[93] L. W. Mo and Y. S. Tsai. Radiative corrections to elastic and inelastic ep and up scattering. *Rev. Mod. Phys. 41, 205–235*, 1969.

[94] M. Vanderhaeghen et al. QED radiative corrections to virtual Compton scattering. *Phys. Rev. C 62, 025501*, 2000. arXiv:hep-ph/0001100.

[95] C. E. Hyde-Wright. Comment on Radiative Corrections in Virtual Compton Scattering, 2006. https://hallaweb.jlab.org/dvcslog/DVCS2/235.

[96] D. Lhuillier. *Diffusion Compton Virtuelle à basse énergie*. PhD thesis, Université de Caen, 1997.

[97] C. E. Hyde-Wright. Non-Factorized Form of Radiative Corrections, 2015. https://hallaweb.jlab.org/dvcslog/Results/189.

[98] M. Defurne. *Photon and π electroproduction at Jefferson Laboratory-Hall A*. PhD thesis, Université Paris Sud - Paris XI, 2015.

[99] K. Kumerički and D. Müller. Description and interpretation of DVCS measurements. *EPJ Web of Conferences 112, 01012*, 2015. arXiv:1512.09014.

Résumé en Français

Introduites au milieu des années 90, les Distributions Généralisées de Partons (GPD) sont aujourd'hui un élément clé dans l'étude de la structure interne du nucléon. Les GPD sont la généralisation des Facteurs de Forme et des Fonctions de Distribution de Partons. Elles englobent la distribution spatiale et la distribution en impulsion des partons à l'intérieur du nucléon, ce qui permet d'en effectuer une tomographie en trois dimensions. De plus, elles permettent d'obtenir le moment orbital angulaire total des quarks grâce à la règle de somme de Ji, ce qui est un élément crucial dans l'élucidation de l'énigme de la structure en spin du nucléon. En décrivant de manière plus complète la structure des hadrons en termes de quarks et gluons, il est possible d'approfondir notre compréhension de la Chromodynamique Quantique.

Les GPD sont accessibles expérimentalement à travers les processus d'électro-production exclusifs profonds, et l'un des canaux les plus simples est la Diffusion Compton Profondément Virtuelle (DVCS) $ep \to e'p'\gamma$. Un programme expérimental mondial a été lancé au début des années 2000 afin d'extraire ces GPD. L'expérience DVCS E12-06-114 qui est le sujet de cette thèse a été effectuée dans le Hall A du Jefferson Laboratory (Virginie, États-Unis) entre 2014 et 2016 et est incluse dans ce programme.

Le but de cette expérience est de mesurer avec grande précision la section efficace DVCS dépendante de l'hélicité en fonction du transfert d'impulsion Q^2, pour des valeurs fixes de la variable de Bjorken x_{Bj}, sur une cible de proton. La récente amélioration à 12 GeV de l'accélérateur d'électron du Jefferson Lab permet d'obtenir un bras de levier en Q^2 plus important que lors des expériences précédentes et de sonder des régions cinématiques encore inexplorées, tandis que le faisceau polarisé d'électrons permet de séparer les contributions des parties réelles et imaginaires de l'amplitude DVCS à la section efficace totale.

Au cours de l'expérience, un faisceau d'électrons polarisé est envoyé sur une cible d'hydrogène liquide. Dans la limite de Bjorken, l'électron interagit avec un unique quark d'un proton de la cible par l'intermédiaire d'un photon virtuel. Le quark émet alors un photon réel avant de retourner dans le proton (voir Fig. E.1). L'électron diffusé est détecté par un spectromètre de haute résolution tandis que le photon émis est détecté dans un calorimètre électromagnétique composé de 208 cristaux de PbF_2 (voir Fig. E.2). Le proton de recul quant à lui n'est pas détecté, mais il est identifié grâce à la masse manquante $M_X^2 = (e + p - e' - \gamma)^2$ qui dans ce cas doit être égale au carré de la masse du proton. L'identification des trois particules de l'état final permet alors d'assurer l'exclusivité de la réaction DVCS.

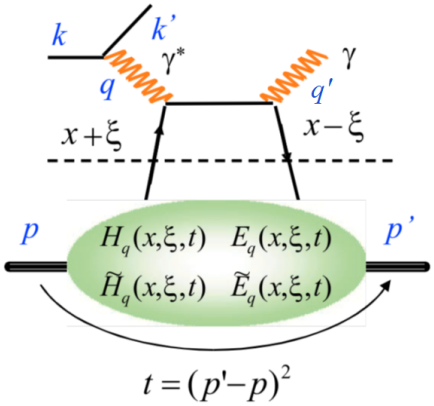

Figure E.1: Diagramme du "sac à main" du processus DVCS.

L'élément déclencheur de la sauvegarde des données est la détection en coïncidence d'un électron dans le spectromètre et d'un photon dans le calorimètre. Par ailleurs, chaque voie du calorimètre est connectée à une électronique d'acquisition (Analog Ring Samplers: ARS) échantillonnant le signal de sorti à une

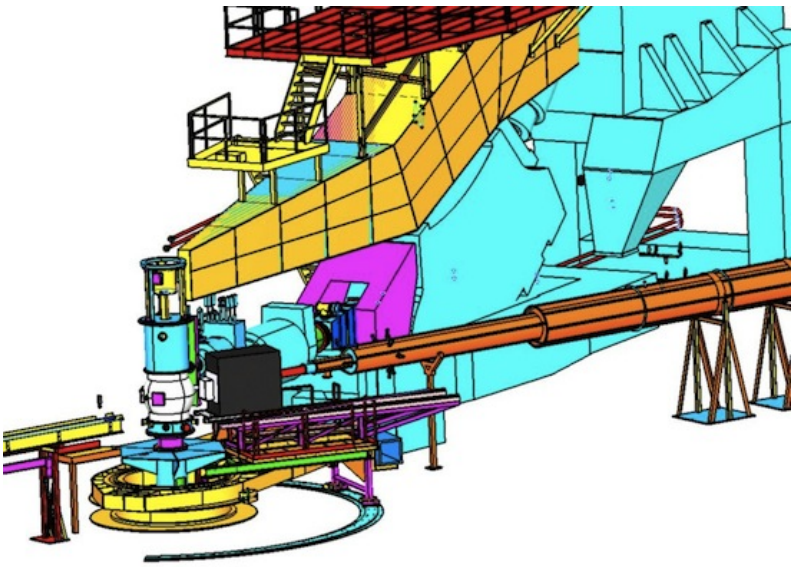

Figure E.2: Représentation schématique du dispositif expérimental DVCS. La cible est représentée par la sphère blanche. Les électrons diffusés sont détectés dans le spectromètre de haute résolution (bleu clair) et les photons émis sont détectés dans un calorimètre électromagnétique (noir). Les protons de recul ne sont pas détectés.

fréquence de 1 GHz. Cet échantillonnage à haute fréquence des données permet de séparer et identifier des évènements très rapprochés en temps.

Afin d'assurer la reconstruction précise des variables associées aux particules de l'état final, une grande attention a été portée sur l'étalonnage des détecteurs. En ce qui concerne le spectromètre, des difficultés sont apparues pendant le Printemps 2016 en raison du vieillissement et de la dégradation des propriétés supraconductrices de l'un de ses aimants. Afin d'accélérer l'étalonnage de l'optique du détecteur, le spectromètre a été positionné à petit angle afin d'augmenter le taux de comptage. Cependant, en contrepartie, l'optique du spectromètre s'en est retrouvée dégradée pour les évènements provenant des bords de la cible lorsque les données DVCS étaient prises avec le détecteur positionné à grand angle. Puis, durant l'Automne 2016, il fut découvert que l'aimant installé en remplacement souffrait d'un problème de saturation. Ces différents contre-temps ont eu pour conséquence que la procédure standard d'étalonnage de l'optique du spectromètre ne permettait pas d'obtenir des résultats suffisants. Cependant, la conception et l'application de corrections empiriques ou calculées à partir de simulations, ainsi que des modifications à la procédure d'étalonnage de l'optique du détecteur ont permis d'outrepasser ces difficultés et d'obtenir une résolution satisfaisante.

En ce qui concerne l'étalonnage du gain en énergie du calorimètre, des difficultés sont apparues en raison d'importants dégâts d'irradiation dus à une forte luminosité, l'importante énergie du faisceau, et le vieillissement des blocs du détecteur. Outre la méthode standard d'étalonnage utilisant la diffusion élastique $ep \to e'p'$ qui a permis d'obtenir une résolution en énergie de 3% à 7.0 GeV, une nouvelle procédure basée sur la reconstruction de la masse invariante des π^0 a également été mise en œuvre. Appliquée quotidiennement, cette nouvelle méthode a permis d'étalonner le gain du calorimètre avec une précision de 1% à 2% et de corriger la perte de gain continue provoquée par les dégâts d'irradiation. Bien qu'après de longues périodes sans faisceau, les dégâts d'irradiation pouvaient avoir des effets non négligeables sur des échelles de temps aussi courtes que quelques heures, une correction empirique utilisée en complément a été employée avec succès afin de compenser l'assombrissement rapide des blocs du calorimètre.

Le contrôle détaillé de la qualité des données a permis de rejeter celles qui pourraient conduire à des résultats peu fiables. Par ailleurs, une quantité importante de données d'une configuration cinématique à été compromise par la désynchronisation du spectromètre et du calorimètre. Cependant, une méthode a été développée avec succès afin de corriger la synchronisation des détecteurs et a permis la restauration des données endommagées.

Les ARS ont été essentiels à l'obtention de la résolution en énergie citée précédemment, ainsi qu'une résolution en temps inférieure à la nanoseconde. Afin d'exploiter pleinement leurs propriétés, les principaux paramètres de l'analyse en forme du signal des ARS ont été optimisés afin d'assurer une extraction

précise des informations en temps et énergie contenues dans les données. Le traitement des évènements fortement rapprochés en temps a également été contrôlé. Les résultats montrent que de tels évènements sont relativement rares et qu'ils ne contribuent que très faiblement à la résolution en énergie du calorimètre.

La détection en coïncidence d'un électron dans le spectromètre et d'un photon dans le calorimètre n'est pas suffisante pour assurer qu'il s'agit bien d'un évènement DVCS. L'électron et le photon peuvent provenir de deux évènements distincts ayant eu lieu simultanément de manière fortuite. On parle alors d'évènements fortuits. Le photon peut également provenir de la désintégration d'un π^0 produit au cours du processus $ep \to e'p'\pi^0$. Dans 99% des cas, le π^0 se désintègre en deux photons, et si l'un des deux photons n'est pas détecté par le calorimètre, l'évènement peut-être mépris pour un évènement DVCS. On parle alors de contamination π^0. Enfin, des Diffusions Profondément Inélastiques Semi-Inclusives (SIDIS) $ep \to e'p'\gamma X$ peuvent être méprises pour des évènements DVCS si les particules supplémentaires X de l'état final ne sont pas détectés.

Les méthodes employées au cours d'expériences précédentes du Hall A afin de soustraire la contamination π^0 et les évènements fortuits ont été adaptées et utilisées pour cette expérience. En ce qui concerne la soustraction des évènements fortuits, les évènements ont été sélectionnés dans des fenêtres en temps hors coïncidences de même largeur que pour la sélection des vraies coïncidences tout en respectant la structure temporelle de 4 ns du faisceau. La soustraction de la contamination π^0 quant à elle est basée sur une simulation de Monte Carlo des évènements π^0 mépris pour des évènements DVCS. L'efficacité de la méthode a été contrôlée à l'aide d'une simulation Géant4. La méthode a été validée pour toute la surface du calorimètre à l'exception des bords et des coins où la détection des π^0 est inefficace en raison d'effets d'acceptance.

Les évènements DVCS ont été sélectionnés en appliquant une série de coupures visant à assurer l'efficacité de détection, la reconstruction précise des variables, et l'exclusivité de la réaction grâce à l'identification des particules. En particulier, de nouvelles coupures ont été définies pour l'acceptance du spectromètre suite aux calibrations de son optique [83], et pour l'acceptance du calorimètre afin de certifier l'efficacité de la soustraction de la contamination π^0. De plus, des coupures strictes sur la masse manquante $M_X^2 = (e + p - e' - \gamma)^2$ permettent simultanément d'assurer l'exclusivité du processus DVCS et de rejeter presque toute la contamination des résonances et SIDIS (voir Fig. E.3). Par ailleurs, des corrections ont été appliquées afin de tenir compte de l'efficacité des détecteurs, des mesures de polarisation du faisceau, et du temps mort expérimental. Une méthode développée dans [98] pour tenir compte des évènements à plusieurs clusters dans le calorimètre a également été adaptée et appliquée à cette expérience.

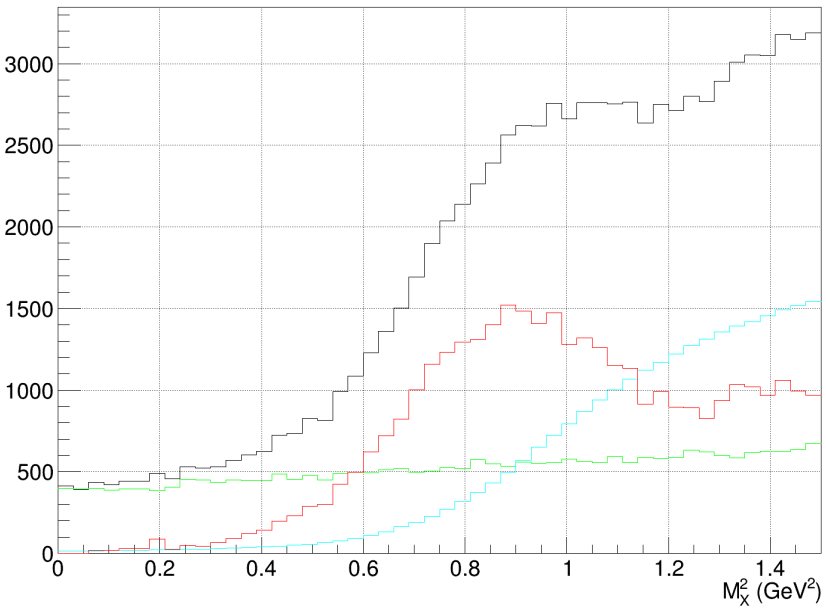

Figure E.3: Distribution de la masse manquante DVCS $M_X^2 = (e + p - e' - \gamma)^2$ pour les données de la configuration cinématique kin48_1. Noir : masse manquante DVCS avant soustraction des contaminations fortuites et π^0. Rouge : masse manquante DVCS après soustraction des contaminations fortuites et π^0. Vert : évènements fortuits. Bleu : contamination π^0.

L'utilisation d'une simulation de Monte Carlo permet d'extraire avec une grande précision l'acceptance des détecteurs. À cette fin, la géométrie du dispositif expérimentale implémenté dans Géant4 a été mise à jour de façon à être une réplique exacte de l'équipement installé dans le Hall A [92]. Par ailleurs, les corrections radiatives réelles sont également implémentées dans la simulation afin d'inclure dans le calcul de l'acceptance les effets combinés de la queue radiative et de la résolution des détecteurs. En revanche, les corrections radiatives virtuelles n'ont pas encore été calculées pour cette expérience. Cependant, il est raisonnable de supposer que ces corrections devraient être extrêmement similaires à celles calculées pour l'expérience E00-110.

En raison du fait que la simulation ne peut pas reproduire parfaitement le gain et la résolution en énergie du calorimètre, une procédure de calibration et d'élargissement de la distribution en énergie de la simulation développée dans [98] a été adaptée et mise en œuvre pour cette expérience de façon à ce que le spectre en masse manquante de la simulation reproduise du mieux possible les données expérimentales. De cette façon, la perte d'évènements DVCS due aux coupures appliquées à la masse manquante sont compensées en appliquant des coupures identiques à la simulation. Cependant, l'élargissement Gaussien de la simulation ne permet pas de reproduire parfaitement la queue de la distribution de la masse manquante observée dans les données. En fonction de la configuration cinématique, une incertitude comprise entre 2.8% et 5.6% en résulte. Un élargissement non-Gaussien de la simulation devrait permettre de grandement minimiser cette incertitude.

Des sections efficaces préliminaires ont été extraites sur un ensemble de 9 configurations cinématiques, chacune divisée en 120 bins expérimentaux (voir Fig. E.4 et E.5). Les sections efficaces polarisées et non polarisées ont permis de séparer les parties réelles et imaginaires de l'amplitude DVCS. La méthode d'extraction est basée sur une paramétrisation des sections efficaces par des combinaisons linéaires et bilinéaires de Facteurs de Forme Compton (CFF). Plusieurs combinaisons ont été testées, et deux d'entre elles ont pu être ajustées aux données de manière satisfaisante. Dans le cas non polarisé, il a été possible de clairement distinguer les sections efficaces DVCS du pure Bethe-Heitler, et les amplitudes des termes DVCS et d'interférence ont pu être mesurées. En particulier, avec la paramétrisation employée, pour des valeurs de ϕ proches de 180°, le terme DVCS a été trouvé dominant par rapport aux termes d'interférence, tandis que pour des valeurs de ϕ proches de 0° ou 360°, la valeur absolue du terme d'interférence devenait d'une taille comparable, voire supérieure, au terme DVCS. Que la section efficace soit polarisée ou non, en moyenne, les termes d'interférence et DVCS de twist 2 ont été trouvés dominants, tandis que les termes de twist-3 étaient proches de zéro. Pour certaines configurations cinématiques, des termes de twist 3 ont été extraits avec des contributions non négligeables, mais cela est peut-être une conséquence des incertitudes statistiques et systématiques.

Les sections efficaces préliminaires ont été comparées aux modèles KM10a et KM15 qui résultent d'ajustements aux données DVCS mondiales. En ce qui concerne les sections efficaces non polarisées (voir Fig. E.4), un très bon accord entre le modèle KM15 et les données a été observé pour toutes les configurations cinématiques. En revanche, il a été observé que le modèle KM10a sous-estime les sections efficaces expérimentales. Il a également été constaté que l'accord entre les modèles et les données se dégradait pour des valeurs croissantes de x_{Bj}, ce qui n'est pas surprenant car les modèles ont été conçus pour des valeurs plus faibles de x_{Bj}. En ce qui concerne les sections efficaces polarisées (voir Fig. E.5), les deux modèles décrivent relativement bien les données. L'accord entre le modèle KM15 et les résultats expérimentaux n'est pas aussi bon que dans le cas non-polarisé, mais l'incertitude expérimentale est plus grande dans le cas polarisé.

La dépendance en Q^2 des combinaisons de CFF utilisées pour paramétrer la section efficace a été étudiée pour chaque valeur de x_{Bj}, intégrée sur t. Le terme de twist-2 $\mathcal{I}m\mathcal{C}^I(\mathcal{F}_{++})$ a été trouvé indépendant de Q^2 (voir Fig. E.6), ce qui est cohérent avec les résultats de la précédente expérience du Hall A et qui est une indication en faveur de la dominance du twist-2. De manière surprenante, en revanche, une dépendance en Q^2 a été observée pour les termes de twist-2 $\mathcal{C}^{DVCS}(\mathcal{F}_{++}, \mathcal{F}^*_{++} \mid \mathcal{F}_{-+}, \mathcal{F}^*_{-+})$ et $\mathcal{R}e\mathcal{C}^I(\mathcal{F}_{++})$ (voir Fig. E.7). Cependant, il est probable que les deux termes soient corrélés et que la dépendance en ϕ de la section efficace ne soit pas suffisante pour les séparer complètement. Par conséquent, l'interprétation de ce résultat est non triviale. Enfin, il a été observé que les termes de twist-3 $\mathcal{R}e\mathcal{C}^I(\mathcal{F}_{0+})$ et $\mathcal{I}m\mathcal{C}^I(\mathcal{F}_{0+})$ semblent petits, mais ne sont pas nécessairement compatibles avec 0 (voir Fig. E.8), ce qui pourrait soutenir l'existence d'une contribution de twist-3.

Les incertitudes systématiques associées aux coupures sur la masse manquante ont été évaluées entre 2% et 5%. Afin de réduire d'avantage cette incertitude, l'amélioration de la procédure de calibration et d'élargissement de la distribution en énergie de la simulation est nécessaire: un élargissement non-Gaussien et l'ajustement de la fenêtre en masse manquante employée pour calculer les paramètres de l'élargissement pourraient réduire l'incertitude de manière non négligeable. Par ailleurs, l'incertitude systématique associée au choix de la paramétrisation de la section efficace DVCS par les CFF a été

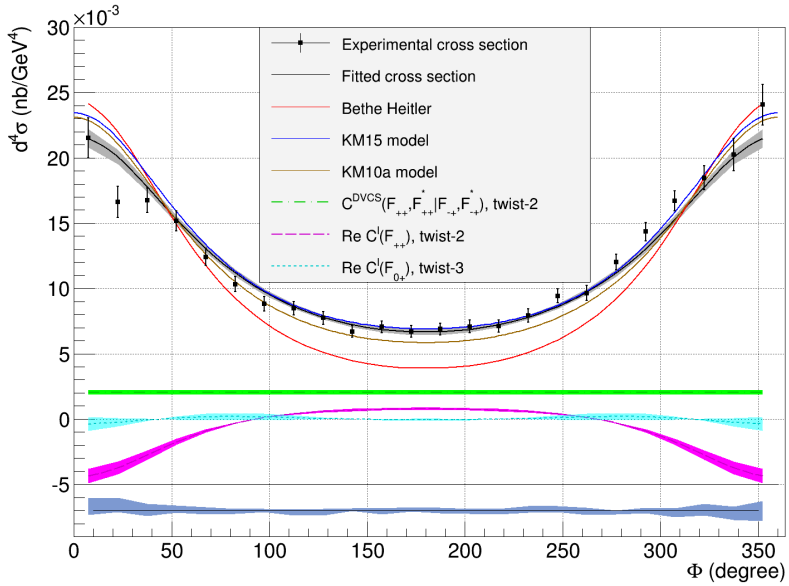

Figure E.4: Section efficace non polarisée pour la configuration cinématique kin36_2, avec une énergie de faisceau $E_{beam} = 8.5$ GeV, $\langle Q^2 \rangle = 3.6$ GeV^2, $\langle x_{Bj} \rangle = 0.36$ et -0.186 GeV^2 $< t - t_{min} < -0.124$ GeV^2. Les points noirs représentent la section efficace expérimentale tandis que la courbe noire correspond à la section efficace ajustée, avec incertitudes statistiques. La contribution Bethe-Heitler est représentée en rouge tandis que les modèles KM10a et KM15 sont respectivement en marron et en bleu. Les contributions des combinaisons de CFF $\langle X_n \rangle_v$ paramétrisant la section efficace non polarisée, multipliées par les facteurs cinématiques $F_n(E, \langle Q^2 \rangle_v, \langle x_{Bj} \rangle_v, \langle t \rangle_v, \phi_r, \lambda)$ sont représentées en vert, magenta et cyan, avec leurs bandes d'incertitude statistique respectives. La bande d'incertitude en bas de la figure représente l'incertitude systématique totale introduite par les coupures sur la masse manquante.

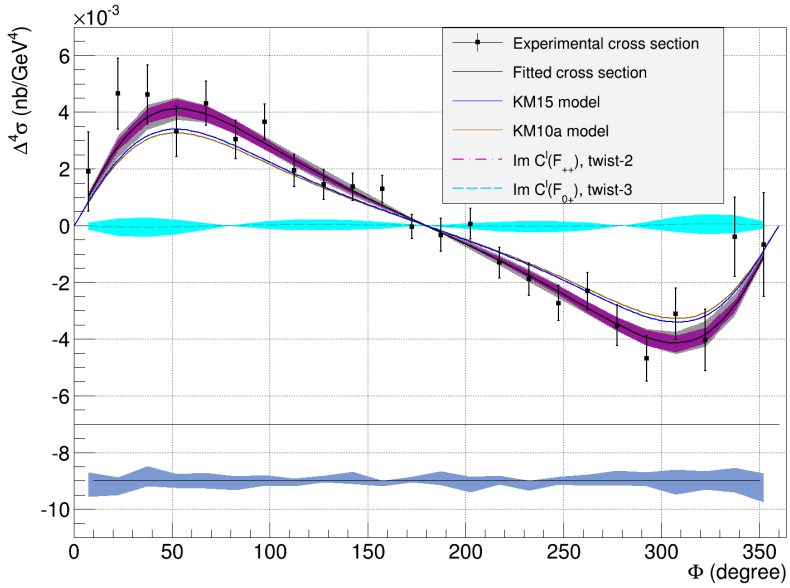

Figure E.5: Section efficace dépendante de l'hélicité du faisceau pour la configuration cinématique kin36_2, avec une énergie de faisceau $E_{beam} = 8.5$ GeV, $\langle Q^2 \rangle = 3.6$ GeV^2, $\langle x_{Bj} \rangle = 0.36$ et -0.186 GeV^2 $< t - t_{min} < -0.124$ GeV^2. Les points noirs représentent la section efficace expérimentale tandis que la courbe noire correspond à la section efficace ajustée, avec incertitudes statistiques. Les modèles KM10a et KM15 sont respectivement en marron et en bleu. Les contributions des combinaisons de CFF $\langle X_n \rangle_v$ paramétrisant la section efficace polarisée, multipliées par les facteurs cinématiques $F_n(E, \langle Q^2 \rangle_v, \langle x_{Bj} \rangle_v, \langle t \rangle_v, \phi_r, \lambda)$ sont représentées en magenta et en cyan, avec leurs bandes d'incertitude statistique respectives. La bande d'incertitude en bas de la figure représente l'incertitude systématique totale introduite par les coupures sur la masse manquante.

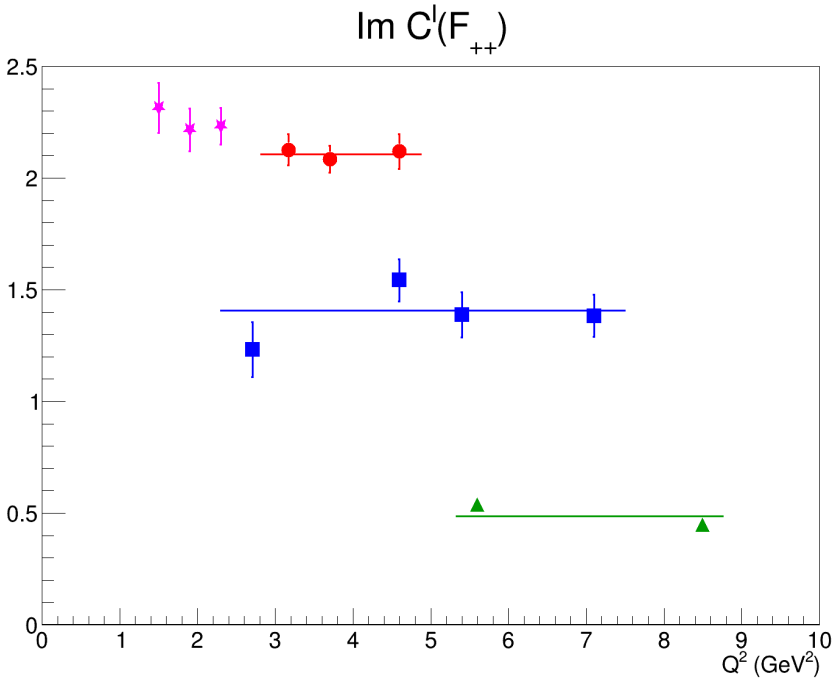

Figure E.6: Dépendance en Q^2 du terme de twist-2 $\mathcal{I}m\mathcal{C}^I(\mathcal{F}_{++})$ employé dans la paramétrisation de la section efficace, intégré sur t, pour $x_{Bj} = 0.36$ et $\langle t \rangle = -0.35$ GeV^2 (rouge), $x_{Bj} = 0.48$ et $\langle t \rangle = -0.47$ GeV^2 (bleu) et $x_{Bj} = 0.60$ et $\langle t \rangle = -1.06$ GeV^2 (vert), avec incertitudes statistiques. Les étoiles magenta correspondent aux résultats précédents du Hall A à $x_{Bj} = 0.36$ et $\langle t \rangle = -0.27$ GeV^2 [48].

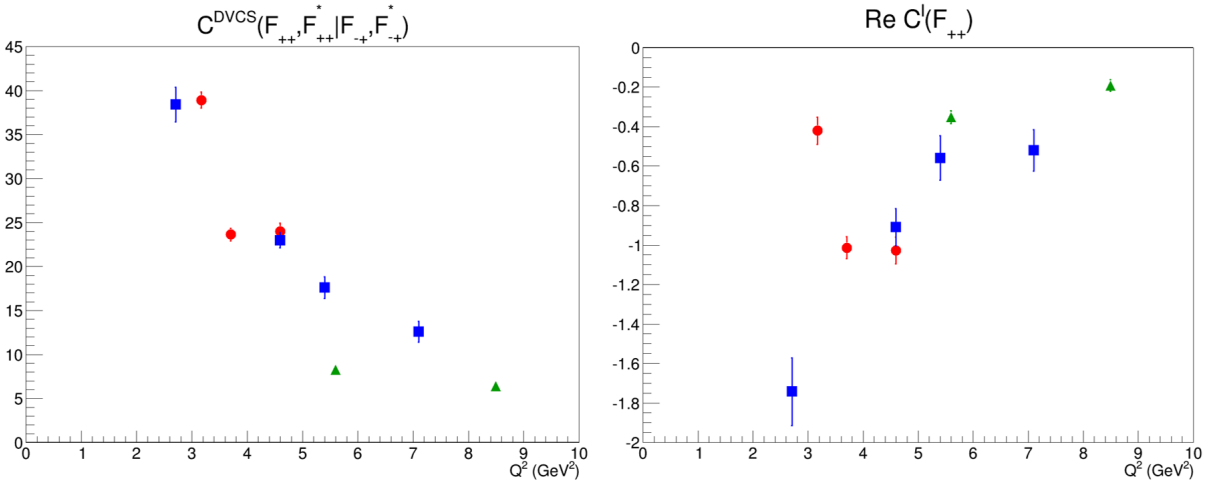

Figure E.7: Dépendance en Q^2 des termes de twist-2 $\mathcal{C}^{DVCS}(\mathcal{F}_{++}, \mathcal{F}^*_{++} \mid \mathcal{F}_{-+}, \mathcal{F}^*_{-+})$ et $\mathcal{R}e\mathcal{C}^I(\mathcal{F}_{++})$ employés dans la paramétrisation de la section efficace, intégré sur t, pour $x_{Bj} = 0.36$ et $\langle t \rangle = -0.35$ GeV^2 (rouge), $x_{Bj} = 0.48$ et $\langle t \rangle = -0.47$ GeV^2 (bleu) et $x_{Bj} = 0.60$ et $\langle t \rangle = -1.06$ GeV^2 (vert), avec incertitudes statistiques.

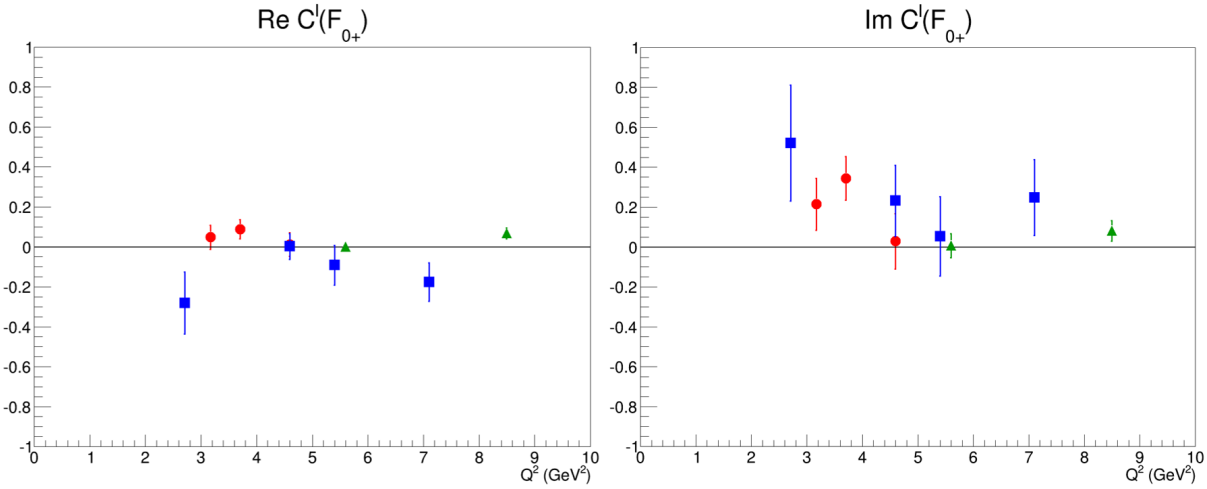

Figure E.8: Dépendance en Q^2 des termes de twist-3 $\mathcal{R}e\mathcal{C}^I(\mathcal{F}_{0+})$ et $\mathcal{I}m\mathcal{C}^I(\mathcal{F}_{0+})$ employés dans la paramétrisation de la section efficace, intégré sur t, pour $x_{Bj} = 0.36$ et $\langle t \rangle = -0.35$ GeV^2 (rouge), $x_{Bj} = 0.48$ et $\langle t \rangle = -0.47$ GeV^2 (bleu) et $x_{Bj} = 0.60$ et $\langle t \rangle = -1.06$ GeV^2 (vert), avec incertitudes statistiques.

évaluée à 1.0%, celle reliée à la luminosité et au temps mort a été évaluée à 1.6%, et l'incertitude associée aux mesures de polarisation est de 1.0%, à l'exception de la configuration cinématique kin36_1 où l'incertitude a été estimée à 2.2%. Enfin, les incertitudes systématiques associées aux corrections radiatives virtuelles et aux coupures sur le spectromètre n'ont pas encore été évaluées précisément, mais il est estimé qu'elles seront fortement similaires à celles de l'expérience E00-110.

université PARIS-SACLAY | ÉCOLE DOCTORALE PHENIICS

Titre: Diffusion Compton Profondément Virtuelle au Jefferson Lab

Mots clés: Diffusion Compton Profondément Virtuelle (DVCS) ; Distributions de Partons Généralisées (GPD) ; Jefferson Lab (CEBAF) ; Physique hadronique ; Structure du Nucléon ; Simulation

Résumé: Introduites au milieu des années 90, les Distributions Généralisées de Partons (GPD) sont aujourd'hui un élément clé dans l'étude de la structure interne du nucléon. Les GPD sont la généralisation des Facteurs de Forme et des Fonctions de Distribution de Partons. Elles englobent la distribution spatiale et la distribution en impulsion des partons à l'intérieur du nucléon, ce qui permet d'en effectuer une tomographie en trois dimensions. De plus, elles permettent d'obtenir le moment orbital angulaire total des quarks grâce à la règle de somme de Ji, ce qui est un élément crucial dans l'élucidation de l'énigme de la structure en spin du nucléon. En décrivant de manière plus complète la structure des hadrons en termes de quarks et gluons, il est possible d'approfondir notre compréhension de la Chromodynamique Quantique. Les GPD sont accessibles expérimentalement à travers les processus d'électro-production exclusifs profonds, et l'un des canaux les plus simples est la Diffusion Compton Profondément Virtuelle (DVCS). Un programme expérimental mondial a été lancé au début des années 2000 afin d'extraire ces GPD. L'expérience DVCS E12-06-114 qui a été effectuée dans le Hall A du Jefferson Laboratory (Virginie, États-Unis) entre 2014 et 2016 est incluse dans ce programme. Le but de cette expérience est de mesurer avec grande précision la section efficace DVCS dépendante de l'hélicité en fonction du transfert d'impulsion Q^2, pour des valeurs fixes de la variable de Bjorken x_{Bj}, sur une cible de proton. La récente amélioration à 12 GeV de l'accélérateur permet d'obtenir un bras de levier en Q^2 plus important que lors des expériences précédentes et de sonder des régions cinématiques encore inexplorées, tandis que le faisceau polarisé d'électrons permet de séparer les contributions des parties réelles et imaginaires de l'amplitude DVCS à la section efficace totale. Dans ce document, un bref résumé du programme expérimental mondial sur l'étude des GPD va être fourni, suivi par la description de l'appareillage et l'analyse des données de l'expérience E12-06-114. Enfin, les résultats des mesures de sections efficaces polarisées et non-polarisées sont présentés et comparés à une sélection de modèles.

Title: Deeply Virtual Compton Scattering at Jefferson Lab

Keywords: Deeply Virtual Compton Scattering (DVCS) ; Generalized Parton Distributions (GPDs) ; Jefferson Lab (CEBAF) ; Hadronic physics ; Nucleon structure ; Simulation

Abstract: Introduced in the mid 90's, Generalized Parton Distributions (GPDs) are now a key element in the study of the nucleon internal structure. GPDs are a generalization of Form Factors and Parton Distribution Functions. They encapsulate both spatial and momentum distributions of partons inside a nucleon, allowing to perform its three-dimensional tomography. Furthermore, they allow to derive the total orbital angular momentum of quarks through the Ji sum rule, which is a crucial point to unravel the nucleon spin structure. By providing a more complete description of hadrons in terms of quarks and gluons, a deeper understanding of Quantum Chromodynamics can be reached. GPDs are experimentally accessible through deeply exclusive electro-production processes, and one of the simplest channels available is Deeply Virtual Compton Scattering (DVCS). A worldwide experimental program was started in the early 2000's to extract these GPDs. The DVCS experiment E12-06-114 performed at Jefferson Laboratory Hall A (Virginia, USA) between 2014 and 2016, is encompassed in this program. The aim of this experiment is to extract with high precision the DVCS helicity-dependent cross sections as a function of the momentum transfer Q^2, for fixed values of the Bjorken variable x_{Bj}, on a proton target. The recent upgrade of the accelerator facility to 12 GeV allows to cover a larger Q^2 range than in previous measurements and probe yet unexplored kinematic regions, while the polarized electron beam allows the separation of the contributions from the real and imaginary parts of the DVCS amplitude to the total cross section. In this document, a brief summary of the worldwide experimental program for the study of GPDs will be provided, followed by a description of the E12-06-114 apparatus and data analysis. Finally, the results of the unpolarized and polarized cross-section measurements are presented and compared to a few selected models.

Université Paris-Saclay
Espace Technologique / Immeuble Discovery
Route de l'Orme aux Merisiers RD 128 / 91190 Saint-Aubin, France